

INFORMATION TO USERS

While the most advanced technology has been used to photograph and reproduce this manuscript, the quality of the reproduction is heavily dependent upon the quality of the material submitted. For example:

- Manuscript pages may have indistinct print. In such cases, the best available copy has been filmed.
- Manuscripts may not always be complete. In such cases, a note will indicate that it is not possible to obtain missing pages.
- Copyrighted material may have been removed from the manuscript. In such cases, a note will indicate the deletion.

Oversize materials (e.g., maps, drawings, and charts) are photographed by sectioning the original, beginning at the upper left-hand corner and continuing from left to right in equal sections with small overlaps. Each oversize page is also filmed as one exposure and is available, for an additional charge, as a standard 35mm slide or as a 17"x 23" black and white photographic print.

Most photographs reproduce acceptably on positive microfilm or microfiche but lack the clarity on xerographic copies made from the microfilm. For an additional charge, 35mm slides of 6"x 9" black and white photographic prints are available for any photographs or illustrations that cannot be reproduced satisfactorily by xerography.

8716834

Vijayaraghavan, S. B.

EFFECTS OF FREE STREAM TURBULENCE, REYNOLDS NUMBER, AND
INCIDENCE ANGLE ON AXIAL TURBINE CASCADE PERFORMANCE

Iowa State University

PH.D. 1987

**University
Microfilms
International** 300 N. Zeeb Road, Ann Arbor, MI 48106

PLEASE NOTE:

In all cases this material has been filmed in the best possible way from the available copy. Problems encountered with this document have been identified here with a check mark .

1. Glossy photographs or pages _____
2. Colored illustrations, paper or print _____
3. Photographs with dark background
4. Illustrations are poor copy _____
5. Pages with black marks, not original copy _____
6. Print shows through as there is text on both sides of page _____
7. Indistinct, broken or small print on several pages
8. Print exceeds margin requirements _____
9. Tightly bound copy with print lost in spine _____
10. Computer printout pages with indistinct print _____
11. Page(s) _____ lacking when material received, and not available from school or author.
12. Page(s) _____ seem to be missing in numbering only as text follows.
13. Two pages numbered _____. Text follows.
14. Curling and wrinkled pages _____
15. Dissertation contains pages with print at a slant, filmed as received _____
16. Other _____

University
Microfilms
International

**Effects of free stream turbulence, Reynolds number, and incidence
angle on axial turbine cascade performance**

by

S. B. Vijayaraghavan

**A Dissertation Submitted to the
Graduate Faculty in Partial Fulfillment of the
Requirements for the Degree of
DOCTOR OF PHILOSOPHY**

Major: Mechanical Engineering

Approved:

Signature was redacted for privacy.

In Charge of Major Work

Signature was redacted for privacy.

For the Major Department

Signature was redacted for privacy.

For the Graduate College

**Iowa State University
Ames, Iowa**

1987

TABLE OF CONTENTS

	PAGE
SYMBOLS AND NOTATION	xii
I. INTRODUCTION	1
II. REVIEW OF THEORY OF STABILITY AND TRANSITION IN BOUNDARY LAYERS	4
A. Theory of Stability of Laminar Flows	5
B. Factors Influencing Transition	21
1. Effects of pressure gradient	21
2. Effects of free-stream turbulence level	25
3. Effects of wall suction	29
4. Effects of heat transfer	30
5. Effects of compressibility	32
6. Effects of surface roughness	33
7. Effects of body forces	35
III. DESIGN OF THE TEST CASCADE	38
A. Review of Cascade Design Program	38
1. Cascade geometry design	40
2. Inviscid analysis	40
3. Integral boundary layer analysis	43
B. Test Cascade	43
IV. CASCADE TEST FACILITY	54
A. Test Cascade Pack	54
B. Test Section	56
C. Endwall Suction System	62
D. Data Acquisition System	64
V. EXPERIMENTAL TEST PROGRAM	68
A. Test Conditions	68
B. Inlet Flow Measurements	69
C. Test Measurements	70
1. Five-hole probe and static pressure measurements	70
a. Initial data and calibration constants	72
b. Data taking and data reduction	76
c. Airfoil static pressure measurements	78
2. Mass-averaged and mixed-out flow calculations	78
3. Hot-wire measurements	80
4. Glue-on hot-film gage measurements	82

5.	Flow visualizations	88
D.	Experimental Accuracy	89
VI.	RESULTS AND DISCUSSION	91
A.	Inlet Angle, $\beta_1 = 45^\circ$ (-7° design incidence)	92
1.	Static pressure measurements	92
2.	Flow visualizations	93
3.	Five-hole probe traverse results	116
a.	Secondary velocity vector plots	116
b.	Total pressure loss coefficient	117
4.	Hot-wire traverse results	130
5.	Hot-film gage results	149
a.	Time-domain analysis	149
b.	Frequency-domain analysis	169
B.	Inlet Angle, $\beta_1 = 52^\circ$ (-14° incidence)	171
1.	Static pressure measurements	171
2.	Flow visualizations	175
3.	Five-hole probe traverse results	188
a.	Secondary velocity vector plots	188
b.	Total pressure loss coefficient	188
4.	Hot-film gage results	189
C.	Inlet Angle, $\beta_1 = 38^\circ$ (0° incidence)	210
1.	Static pressure measurements	210
2.	Flow visualizations	210
3.	Five-hole probe traverses	222
a.	Secondary velocity vector plots	222
b.	Total pressure loss coefficient	222
4.	Hot-film gage results	223
D.	Comparison of measured and predicted results	230
VII.	CONCLUSIONS	252
VIII.	REFERENCES	257
IX.	ACKNOWLEDGMENTS	263
X.	APPENDIX A: COMPARISON OF STAN5 AND DISSIPATION INTEGRAL ANALYSIS METHODS	264
XI.	APPENDIX B: PRINCIPLE OF HOT-FILM GAGES FOR USE IN WALL SHEAR STRESS MEASUREMENTS	271

LIST OF TABLES

	PAGE
TABLE 1. Predicted results of integral boundary layer analysis for the test cascade at design incidence of -7° and axial chord Reynolds number of 830,000	48
TABLE 2. Predicted results of integral boundary layer analysis for the test cascade at design inlet turbulence level of 1.0% and inlet Mach number of 0.1	50
TABLE 3. Predicted results of STAN5 boundary layer analysis for the test cascade at design incidence of -7° and axial chord Reynolds number of 830,000	52
TABLE 4. Comparison of measured and predicted (STAN5) results at midspan for axial chord Reynolds number 700,000 (REL)	245

LIST OF FIGURES

	PAGE
FIGURE 1. Curve of neutral stability as a function of Reynolds number for the Blasius profile	10
FIGURE 2. Curves of constant temporal amplification for the Blasius profile over a wide range of Reynolds number . .	11
FIGURE 3. Curves of neutral stability for a 2-D boundary layer with 2-D disturbances - (a) non-viscous instability (b) viscous instability	12
FIGURE 4. Plan view of flat plate and spanwise variation of wave amplitude at various distances downstream from vibrating ribbon	15
FIGURE 5. Progressive movement and deformation of a U-shaped vortex loop due to self-induction	16
FIGURE 6. Plan and side views of a turbulence spot generated by an electric spark	18
FIGURE 7. Idealized sketch of transition process on a flat plate	19
FIGURE 8. Curves of neutral stability for laminar boundary layer profiles with pressure decrease ($\Lambda > 0$) and pressure increase ($\Lambda < 0$)	23
FIGURE 9. Critical Reynolds number of boundary layer velocity profiles with pressure gradient as a function of Λ . . .	24
FIGURE 10. Momentum thickness Reynolds number at the start of transition for nonzero pressure gradient	28
FIGURE 11. Curves of neutral stability for velocity profiles with suction -- (A) - Asymptotic suction profile, (B) - profile without suction -- ξ denotes the dimensionless inlet length	31
FIGURE 12. Neutral curves in supersonic adiabatic flow over a flat plate (perfect gas)	34

FIGURE 13. Distance between the point of transition and the position of tripping wire for "fully effective" operation	36
FIGURE 14. Turbine cascade design flow diagram	39
FIGURE 15. Coordinate system and turbine cascade geometry parameters	41
FIGURE 16. Computer generated design for the test cascade	45
FIGURE 17. Predicted pressure distribution at design incidence	46
FIGURE 18. Test cascade pack	55
FIGURE 19. Central airfoil of test cascade pack with static pressure taps	57
FIGURE 20. Test cascade airfoil internal passages and pressure tap tubing	58
FIGURE 21. Plenum tank and frame inserts	60
FIGURE 22. Probe positioners and adjustable linkage arrangement	61
FIGURE 23. Endwall suction system and auxiliary blower	63
FIGURE 24. Schematic of data acquisition and experiment control system	66
FIGURE 25. Schematic of hot-wire anemometer system	67
FIGURE 26. Turbulence decay measurements obtained for three turbulence generator grids	71
FIGURE 27. Five-hole probe angle and traverse direction conventions	73
FIGURE 28. Flow diagram of data acquisition program MASTER	74
FIGURE 29. Sample printout for five-hole probe measurements	77
FIGURE 30. Hot-film gages glued to the airfoil suction surface	84
FIGURE 31. Transition curves from hot-film and hot-wire measurements	87
FIGURE 32. Static pressure distribution at midspan and at 20% from endwalls, $\beta_1 = 45^\circ$, NGRID, RE2	94
FIGURE 33. Static pressure distribution, $\beta_1 = 45^\circ$, RE1	95
FIGURE 34. Static pressure distribution, $\beta_1 = 45^\circ$, RE2	96
FIGURE 35. Static pressure distribution, $\beta_1 = 45^\circ$, RE3	97

FIGURE 36. Static pressure distribution, $\beta_1 = 45^\circ$, NGRID	98
FIGURE 37. Static pressure distribution, $\beta_1 = 45^\circ$, GRID1	99
FIGURE 38. Static pressure distribution, $\beta_1 = 45^\circ$, GRID2	100
FIGURE 39. Static pressure distribution, $\beta_1 = 45^\circ$, GRID3	101
FIGURE 40. Flow pattern, Suction surface, $\beta_1 = 45^\circ$, NGRID, RE1 . . .	105
FIGURE 41. Flow pattern, Suction surface, $\beta_1 = 45^\circ$, NGRID, RE2 . . .	106
FIGURE 42. Flow pattern, Suction surface, $\beta_1 = 45^\circ$, NGRID, RE1 (No endwall suction)	107
FIGURE 43. Flow pattern, Suction surface, $\beta_1 = 45^\circ$, GRID1, RE1 . . .	108
FIGURE 44. Flow pattern, Suction surface, $\beta_1 = 45^\circ$, GRID1, RE2 . . .	109
FIGURE 45. Flow pattern, Suction surface, $\beta_1 = 45^\circ$, GRID1, RE3 . . .	110
FIGURE 46. Flow pattern, Suction surface, $\beta_1 = 45^\circ$, GRID3, RE1 . . .	111
FIGURE 47. Flow pattern, Suction surface, $\beta_1 = 45^\circ$, GRID3, RE3 . . .	112
FIGURE 48. Flow pattern, Pressure surface, $\beta_1 = 45^\circ$, NGRID, RE1 . . .	113
FIGURE 49. Flow pattern, Endwall, $\beta_1 = 45^\circ$ (No endwall suction) . . .	114
FIGURE 50. Flow pattern, Endwall, $\beta_1 = 45^\circ$ (With endwall suction)	115
FIGURE 51. Secondary velocity vectors, $\beta_1 = 45^\circ$, NGRID, RE1 (No endwall suction)	118
FIGURE 52. Secondary velocity vectors, $\beta_1 = 45^\circ$, GRID1, RE1 (No endwall suction)	119
FIGURE 53. Secondary velocity vectors, $\beta_1 = 45^\circ$, GRID2, RE1 (No endwall suction)	120
FIGURE 54. Secondary velocity vectors, $\beta_1 = 45^\circ$, GRID3, RE1 (No endwall suction)	121
FIGURE 55. Secondary velocity vectors, $\beta_1 = 45^\circ$, NGRID, RE1	122
FIGURE 56. Secondary velocity vectors, $\beta_1 = 45^\circ$, NGRID, RE2	123
FIGURE 57. Secondary velocity vectors, $\beta_1 = 45^\circ$, NGRID, RE3	124
FIGURE 58. Secondary velocity vectors, $\beta_1 = 45^\circ$, GRID1, RE1	125
FIGURE 59. Secondary velocity vectors, $\beta_1 = 45^\circ$, GRID2, RE1	126
FIGURE 60. Secondary velocity vectors, $\beta_1 = 45^\circ$, GRID3, RE1	127
FIGURE 61. Total pressure loss contours, $\beta_1 = 45^\circ$, NGRID, RE1 (No endwall suction)	131

FIGURE 62. Total pressure loss contours, $\beta_1 = 45^\circ$, GRID1, RE1 (No endwall suction)	132
FIGURE 63. Total pressure loss contours, $\beta_1 = 45^\circ$, GRID2, RE1 (No endwall suction)	133
FIGURE 64. Total pressure loss contours, $\beta_1 = 45^\circ$, GRID3, RE1 (No endwall suction)	134
FIGURE 65. Pitch-averaged loss coefficient, $\beta_1 = 45^\circ$ (No endwall suction)	135
FIGURE 66. Total pressure loss contours, $\beta_1 = 45^\circ$, NGRID, RE1 . . .	136
FIGURE 67. Total pressure loss contours, $\beta_1 = 45^\circ$, NGRID, RE2 . . .	137
FIGURE 68. Total pressure loss contours, $\beta_1 = 45^\circ$, NGRID, RE3 . . .	138
FIGURE 69. Total pressure loss contours, $\beta_1 = 45^\circ$, GRID1, RE1 . . .	139
FIGURE 70. Total pressure loss contours, $\beta_1 = 45^\circ$, GRID2, RE1 . . .	140
FIGURE 71. Total pressure loss contours, $\beta_1 = 45^\circ$, GRID3, RE1 . . .	141
FIGURE 72. Pitch-averaged loss coefficient, $\beta_1 = 45^\circ$ (With endwall suction)	142
FIGURE 73. Turbulence level contours, $\beta_1 = 45^\circ$, NGRID, RE1	144
FIGURE 74. Turbulence level contours, $\beta_1 = 45^\circ$, GRID1, RE1	145
FIGURE 75. Turbulence level contours, $\beta_1 = 45^\circ$, GRID2, RE1	146
FIGURE 76. Turbulence level contours, $\beta_1 = 45^\circ$, GRID3, RE1	147
FIGURE 77. Hot-film gage locations plotted against the pressure distribution for $\beta_1 = 45^\circ$	155
FIGURE 78. Hot-film gage results, $\beta_1 = 45^\circ$, NGRID, RE1	156
FIGURE 79. Hot-film gage results, $\beta_1 = 45^\circ$, NGRID, RE2	157
FIGURE 80. Hot-film gage results, $\beta_1 = 45^\circ$, NGRID, RE3	158
FIGURE 81. Hot-film gage results, $\beta_1 = 45^\circ$, GRID1, RE1	159
FIGURE 82. Hot-film gage results, $\beta_1 = 45^\circ$, GRID1, RE2	160
FIGURE 83. Hot-film gage results, $\beta_1 = 45^\circ$, GRID1, RE3	161
FIGURE 84. Hot-film gage results, $\beta_1 = 45^\circ$, GRID2, RE1	162
FIGURE 85. Hot-film gage results, $\beta_1 = 45^\circ$, GRID2, RE2	163
FIGURE 86. Hot-film gage results, $\beta_1 = 45^\circ$, GRID2, RE3	164
FIGURE 87. Hot-film gage results, $\beta_1 = 45^\circ$, GRID3, RE1	165
FIGURE 88. Hot-film gage results, $\beta_1 = 45^\circ$, GRID3, RE2	166

FIGURE 89. Hot-film gage results, $\beta_1 = 45^\circ$, GRID3, RE3	167
FIGURE 90. Power spectrum results, $\beta_1 = 45^\circ$, NGRID, RE1	172
FIGURE 91. Power spectrum results, $\beta_1 = 45^\circ$, GRID2, RE1	173
FIGURE 92. Power spectrum of hot-film gage#14, $\beta_1 = 45^\circ$, GRID2, RE1	174
FIGURE 93. Static pressure distribution, $\beta_1 = 52^\circ$, RE1	177
FIGURE 94. Static pressure distribution, $\beta_1 = 52^\circ$, RE1	178
FIGURE 95. Static pressure distribution, $\beta_1 = 52^\circ$, NGRID	179
FIGURE 96. Static pressure distribution, $\beta_1 = 52^\circ$, GRID1	180
FIGURE 97. Static pressure distribution, $\beta_1 = 52^\circ$, GRID2	181
FIGURE 98. Static pressure distribution, $\beta_1 = 52^\circ$, GRID3	182
FIGURE 99. Flow pattern, Suction surface, $\beta_1 = 52^\circ$, NGRID, RE1	183
FIGURE 100. Flow pattern, Suction surface, $\beta_1 = 52^\circ$, GRID1, RE1	184
FIGURE 101. Flow pattern, Suction surface, $\beta_1 = 52^\circ$, GRID3, RE1	185
FIGURE 102. Flow pattern, Pressure surface, $\beta_1 = 52^\circ$, GRID3, RE1	186
FIGURE 103. Flow pattern, Endwall, $\beta_1 = 52^\circ$	187
FIGURE 104. Secondary velocity vectors, $\beta_1 = 52^\circ$, NGRID, RE1	190
FIGURE 105. Total pressure loss contours, $\beta_1 = 52^\circ$, NGRID, RE1	191
FIGURE 106. Total pressure loss contours, $\beta_1 = 52^\circ$, NGRID, RE2	192
FIGURE 107. Total pressure loss contours, $\beta_1 = 52^\circ$, NGRID, RE3	193
FIGURE 108. Pitch-averaged loss coefficient, $\beta_1 = 52^\circ$	194
FIGURE 109. Hot-film gage locations plotted against the pressure distribution for $\beta_1 = 52^\circ$	197
FIGURE 110. Hot-film gage results, $\beta_1 = 52^\circ$, NGRID, RE1	198
FIGURE 111. Hot-film gage results, $\beta_1 = 52^\circ$, NGRID, RE2	199
FIGURE 112. Hot-film gage results, $\beta_1 = 52^\circ$, NGRID, RE3	200
FIGURE 113. Hot-film gage results, $\beta_1 = 52^\circ$, GRID1, RE1	201
FIGURE 114. Hot-film gage results, $\beta_1 = 52^\circ$, GRID1, RE2	202
FIGURE 115. Hot-film gage results, $\beta_1 = 52^\circ$, GRID1, RE3	203
FIGURE 116. Hot-film gage results, $\beta_1 = 52^\circ$, GRID2, RE1	204
FIGURE 117. Hot-film gage results, $\beta_1 = 52^\circ$, GRID2, RE2	205
FIGURE 118. Hot-film gage results, $\beta_1 = 52^\circ$, GRID2, RE3	206
FIGURE 119. Hot-film gage results, $\beta_1 = 52^\circ$, GRID3, RE1	207

FIGURE 120. Hot-film gage results, $\beta_1 = 52^\circ$, GRID3, RE2	208
FIGURE 121. Hot-film gage results, $\beta_1 = 52^\circ$, GRID3, RE3	209
FIGURE 122. Static pressure distribution, $\beta_1 = 38^\circ$, RE1	211
FIGURE 123. Static pressure distribution, $\beta_1 = 38^\circ$, NGRID	212
FIGURE 124. Static pressure distribution, $\beta_1 = 38^\circ$, GRID1	213
FIGURE 125. Static pressure distribution, $\beta_1 = 38^\circ$, GRID2	214
FIGURE 126. Static pressure distribution, $\beta_1 = 38^\circ$, GRID3	215
FIGURE 127. Flow pattern, Suction surface, $\beta_1 = 38^\circ$, NGRID, RE1	217
FIGURE 128. Flow pattern, Suction surface, $\beta_1 = 38^\circ$, GRID1, RE1	218
FIGURE 129. Flow pattern, Suction surface, $\beta_1 = 38^\circ$, GRID3, RE1	219
FIGURE 130. Flow pattern, Pressure surface, $\beta_1 = 38^\circ$, NGRID, RE1	220
FIGURE 131. Flow pattern, Endwall, $\beta_1 = 38^\circ$	221
FIGURE 132. Secondary velocity vectors, $\beta_1 = 38^\circ$, NGRID, RE1	224
FIGURE 133. Total pressure loss contours, $\beta_1 = 38^\circ$, NGRID, RE1	225
FIGURE 134. Total pressure loss contours, $\beta_1 = 38^\circ$, NGRID, RE2	226
FIGURE 135. Total pressure loss contours, $\beta_1 = 38^\circ$, NGRID, RE3	227
FIGURE 136. Pitch-averaged loss coefficient, $\beta_1 = 38^\circ$	228
FIGURE 137. Hot-film gage locations plotted against the pressure distribution for $\beta_1 = 38^\circ$	231
FIGURE 138. Hot-film gage results, $\beta_1 = 38^\circ$, NGRID, RE1	232
FIGURE 139. Hot-film gage results, $\beta_1 = 38^\circ$, NGRID, RE2	233
FIGURE 140. Hot-film gage results, $\beta_1 = 38^\circ$, NGRID, RE3	234
FIGURE 141. Hot-film gage results, $\beta_1 = 38^\circ$, GRID1, RE1	235
FIGURE 142. Hot-film gage results, $\beta_1 = 38^\circ$, GRID1, RE2	236
FIGURE 143. Hot-film gage results, $\beta_1 = 38^\circ$, GRID1, RE3	237
FIGURE 144. Hot-film gage results, $\beta_1 = 38^\circ$, GRID2, RE1	238
FIGURE 145. Hot-film gage results, $\beta_1 = 38^\circ$, GRID2, RE2	239
FIGURE 146. Hot-film gage results, $\beta_1 = 38^\circ$, GRID2, RE3	240
FIGURE 147. Hot-film gage results, $\beta_1 = 38^\circ$, GRID3, RE1	241
FIGURE 148. Hot-film gage results, $\beta_1 = 38^\circ$, GRID3, RE2	242
FIGURE 149. Hot-film gage results, $\beta_1 = 38^\circ$, GRID3, RE3	243
FIGURE 150. Comparison of STAN5 and dissipation integral analysis-- zero pressure gradient	266

FIGURE 151. Comparison of STAN5 and dissipation integral analysis-- favorable pressure gradient	269
FIGURE 152. Comparison of STAN5 and dissipation integral analysis-- adverse pressure gradient	270
FIGURE 153. Comparison of hot-film signal and predicted shear-stress distribution for $\beta_1 = 45^\circ$, RE1, NGRID	274
FIGURE 154. Comparison of hot-film signal and predicted shear-stress distribution for $\beta_1 = 45^\circ$, RE1, GRID2	275

SYMBOLS AND NOTATION

- B_x - Airfoil axial chord
 C_f - Skin friction coefficient = τ_w/q
 C_p - Static pressure coefficient = $(P-P_1)/q_1$
 C_{PT} - Total pressure loss coefficient = $(P_{T1}-P_{T2})/q_1$
 C_{PT2} - Total pressure loss coefficient = $(P_{T1}-P_{T2})/q_2$
 E - Hot-wire/hot-film DC output voltage
 H - Shape factor
 I - Sensor current
 P - Pressure
 Q - Hot-film gage heat transfer rate
 R - Reynolds number or hot-wire/hot-film resistance
 Ri - Richardson number
 T - Temperature
 Tu - Turbulence level, $\{[(u^2+v^2+w^2)^{1/2}/U] \times 100$
 U - Streamwise velocity component (Chapter I)
 V - Cascade inlet/exit flow velocity or transverse velocity component (Chapter I)
 c - Complex eigenvalue of Orr-Sommerfeld Equation (Chapter I)
 e - Hot-wire/hot-film AC output voltage
 h - Airfoil span
 p - Disturbance pressure (Chapter I)
 q - Velocity head = $\rho v^2/2$
 t - Time (Chapter I)
 u,v,w - Disturbance velocities (Chapter I)

- x, y, z - Cartesian coordinates
- Γ - Uncovered turning angle
- Λ - Pressure gradient parameter = $(\delta^2/\nu)(dU/dx)$
- Ψ - Zweifel loading coefficient = $2 \tau/B_x \sin^2\beta_2(\cot \beta_1 + \cot \beta_2)$
- a - Wave number
- β - Falkner-Skan parameter or flow angle
- β_λ - Gaging angle = $\sin^{-1}(\lambda/\tau)$
- β^* - Metal angle at leading or trailing edge
- $\Delta\beta^*$ - Wedge angle at leading or trailing edge
- γ - Intermittency
- δ - Boundary layer thickness
- δ_1 - Displacement thickness
- η - Dimensionless length parameter (Chapter I)
- θ - Momentum thickness
- λ - Throat length
- μ - Absolute viscosity
- ν - Kinematic viscosity
- ξ - Dimensionless inlet length = $(-v_0/U)^2 Ux/\nu$ [3] (Chapter I)
- ρ - Density
- τ - Cascade pitch or shear stress
- ϕ - Flow pitch angle

Subscripts

- 1 - Upstream station or leading edge
- 2 - Downstream station or trailing edge

- 3 - Mixed-out conditions
- E - End of transition
- L - Length of transition
- S - Start of transition
- T - Total
- i - Imaginary
- r - Real
- x - Streamwise direction
- w - Wall

I. INTRODUCTION

The design of a modern gas turbine engine for aircraft applications is a challenging problem due to the increasing demand for reduced size and weight. To meet this demand, the turbine has to be operated with fewer stages and at higher temperatures and pressure ratios. Since fewer stages lead to increased loading for each stage, it is necessary for the blade rows to be designed for minimal losses in order to maintain or even improve engine efficiency and performance. In addition, due to the higher operating temperatures, accurate prediction of temperature distribution on the blade surfaces is necessary to provide efficient cooling.

The flow losses occurring across a blade row can generally be classified as profile losses and secondary losses. Profile losses result from 2-D boundary layers developing over the blade surface and account for a major portion of the total losses. Secondary losses result from endwall boundary layers and their interaction with the blade passage flow. To control these losses and to predict blade surface temperatures, which depend on the heat transfer taking place between the flow and the blades, a detailed and thorough understanding of the aerodynamics of the gas flow in the blade passages is necessary.

The profile boundary layers are highly transitional in the Reynolds number range encountered in gas turbines. For such transitional boundary layers, the skin friction and the heat transfer coefficients change dramatically as the boundary layer undergoes

transition from a laminar to a turbulent one. Hence, it becomes essential to predict the state of the boundary layer on the blade surface accurately. Because of the limited understanding of the exact nature of transition, theoretical or numerical analyses have not been successful in predicting transition, except for the simple case of low turbulence level flow over uniform pressure gradients. Most of the currently available transition models based on experimental results have also been taken from flow measurements on flat plates under conditions of uniform pressure gradients. However, in a gas turbine, the inlet gas to the turbine from the combustion chamber has high turbulence levels, and the flow over the blade surfaces experiences strongly varying pressure gradient conditions.

As an attempt to obtain transition data on the blade surface, a highly loaded, high-turning, large-scale cascade was designed using a fast interactive design code and tested at Reynolds number ranges typically present in gas turbines. With the use of turbulence-generating grids, various inlet turbulence levels were made available in the test flow. In addition, the cascade was tested at different incidence angles. Since the primary interest in the cascade testing was on profile boundary layers, endwall suction was applied to provide a 2-D flow over a large spanwise region of the airfoil. Transition on the suction surface of the blade was identified with glue-on hot-film gages. Surface oil-flow visualization results were also used to assist with interpreting the hot-film gage output signals. In addition,

static pressure distributions on the airfoil and detailed five-hole pressure probe and hot-wire traverses were made in an exit plane of the cascade. Results from the traverse measurements were used to determine the overall cascade performance, including mass-averaged losses.

A brief review on the theory of stability of laminar flows which forms the usual basis for a theoretical understanding of transition is presented, followed by a discussion of the factors influencing transition and the currently available experimental correlations for predicting transition. The experimental cascade investigation is then presented, covering the design and fabrication of the test cascade and the testing procedures used. Finally, the experimental results obtained are discussed and comparisons are made between the predicted and measured results. Also included in the concluding section are discussions on the merits and shortcomings of the transition model used in the cascade design program and suggestions for reducing the cascade profile losses.

II. REVIEW OF THEORY OF STABILITY AND TRANSITION IN BOUNDARY LAYERS

Transition is the process by which a well-ordered laminar flow becomes a fully disordered turbulent flow. A transitional flow is extremely difficult to analyze since it is affected by various factors such as pressure gradient, free-stream turbulence, surface roughness, heat transfer, surface curvature, Mach number, acoustic radiation, injection or suction of the fluid at the wall, and other factors. Since all of these factors may act simultaneously, it is difficult to develop a general theory for the transition process that takes into account all of the influencing factors.

Besides being a challenging problem in theoretical fluid mechanics, the prediction of transition is important in a practical engineering sense because of the important role transition plays in the lift and drag developed by airfoils, in flow losses produced in turbomachinery, and in heat and mass transfer in various engineering equipment. The transition from laminar to turbulent flow in boundary layers is important because it significantly increases wall shear stresses and heat transfer rates. Since it has been observed that as much as 50% to 80% of the suction surface of a turbine blade may be covered by transitional flow, it is essential to predict accurately the nature of the boundary layer on the blade surface in order to estimate the blade profile losses and the heat transfer rates for design calculations. The usual simplifying assumption that the profile boundary layer is turbulent from the blade leading edge onward is generally wrong and not necessarily conservative [1].

Inspite of the complexity of the transition process, several attempts have been made to study transition with the goal of predicting and/or controlling the transition process under largely simplified conditions. Some of these attempts are reviewed in the following sections.

A. Theory of Stability of Laminar Flows

The theoretical investigation of transition is based on the assumption that laminar flows are affected by small disturbances. In the case of a boundary layer, these disturbances could arise from the velocity or pressure fluctuations in the main flow, or from the effects of wall roughness. The theory regards such disturbances in time, and, if they tend to decay, the flow is said to be stable. If the disturbances increase with time, then the flow is considered unstable, and the possibility exists for transition to a turbulent type of flow. It should be noted that the instability of a flow does not imply that the flow becomes turbulent; the flow may change from one type of laminar flow to another. An example of this is the formation of Taylor vortices in the flow between annular rotating cylinders for a certain combination of rotational speeds and cylinder radii (Stuart [2]).

The initial work on stability was the development of a linear theory by Reynolds and Lord Rayleigh (cited in Schlichting [3]) nearly a century ago. However, it was not until 1930 that Tollmien [4] succeeded in predicting a critical Reynolds number based on the theory

for the Blasius profile. The flow model usually employed in developing the linear theory of stability consists of a parallel, incompressible flow in the x,y plane described by a mean flow

$$U = U(y), \quad V = 0, \quad P = P(x,y)$$

and an unsteadiness

$$u = u(x,y,t), \quad v = v(x,y,t), \quad p = p(x,y,t)$$

superimposed on the mean flow. Here U is the mean velocity component in the streamwise direction, V is the mean velocity component in the transverse direction, and P is the mean static pressure. The disturbance velocities u and v and the disturbance pressure p are dependent on x and y and on time t .

A first or so-called energy method used in the investigation of the stability of a disturbed flow was developed primarily by Orr and Lorentz (cited in Stuart [2]). This method considers the energy transferred between the mean motion and the disturbances. If the energy of the disturbances is found to increase in time, the flow is considered to be unstable. This method has given results in poor agreement with experimental results because, in this approach, the disturbance velocities are made to satisfy only the continuity equation, but not the momentum equations.

In another method, the method of small disturbances, the disturbance velocities satisfy the 2-D Navier-Stokes equation in

addition to the continuity equation. Here the disturbance velocities and pressure are considered to be very small compared to the mean velocity and pressure so that the Navier-Stokes equations can be linearized. With the introduction of a stream function for the disturbance velocities, the linearized Navier-Stokes equations are reduced to a fourth-order ordinary differential equation. This is the fundamental stability equation known as the Orr-Sommerfeld equation. The stream function represents a single oscillation of the disturbance. Since any arbitrary 2-D disturbance can be assumed to be expanded in a Fourier series, each term of the series represents a component of the oscillation. More details on the development of the Orr-Sommerfeld equation can be found in Schlichting [3]. A boundary layer type of flow has homogeneous boundary conditions for the Orr-Sommerfeld equation, and, hence, the equation yields an eigenfunction and an eigenvalue when the mean flow and the wavelength of the disturbance are specified. The sign of the imaginary component of the eigenvalue determines whether the disturbance waves are damped or amplified; i.e., a positive sign corresponds to an amplification of the waves and hence an unstable disturbance, while a negative sign corresponds to a damped wave and a stable disturbance. The limiting case of a zero value corresponds to a neutral disturbance.

In the first attempts to study the Orr-Sommerfeld equation, Lord Rayleigh (cited in Schlichting [3]) neglected the terms containing viscosity, using the argument that transition occurs at very high

Reynolds numbers. He obtained what is called the frictionless stability or Rayleigh equation. This equation does not yield a critical Reynolds number but does indicate whether or not a given laminar profile is stable. The main result of the studies on the Rayleigh equation has been that velocity profiles possessing a point of inflection are unstable.

Tollmien [4] employed the Orr-Sommerfeld equation to investigate the stability of the Blasius profile. He determined a critical Reynolds number of 420 based on displacement thickness. The results of such an analysis can be plotted in an $\alpha\delta_1 - R\delta_1$ diagram, where α is the wave number, δ_1 is the displacement thickness, and $R\delta_1$ is the Reynolds number based on displacement thickness. Each point of the diagram corresponds to an eigenvalue of the Orr-Sommerfeld equation. The locus of the points corresponding to the imaginary component of the eigenvalue equal to zero is the neutral stability curve. This curve separates the region of stable disturbances from that of unstable disturbances. The point on this curve at which the Reynolds number has its least value indicates the critical Reynolds number, thus representing the limiting Reynolds number below which all disturbances are damped out, and above which at least some disturbances are amplified. Figure 1, from the results of Jordinson [5], shows the neutral stability curve for a 2-D disturbance. Ombrewski et al. [6] also obtained curves of constant amplification rates as seen in Figure 2. Figure 2 shows that the maximum amplification rates occur in a

moderate Reynolds number range of 10^3 to 10^4 , and not at high Reynolds numbers.

Figure 3 shows the neutral stability curves for two types of velocity profiles. Curve (a), known as the non-viscous instability curve, is for a velocity profile having a point of inflection, and curve (b), known as the viscous instability curve, is for a velocity profile without a point of inflection. As can be seen, velocity profiles having a point of inflection have a much lower critical Reynolds number.

At this stage of the discussion, the difference between the point of instability and the point of transition in a boundary layer should be emphasized. While the point of instability denotes the point at which the amplification of small disturbances begins and proceeds downstream, the point of actual transition is still further downstream. The distance between the two points depends greatly on numerous free-stream flow conditions, as mentioned previously.

The two important assumptions made in the above analysis--namely, that the disturbance velocities are only 2-D and that there exists only one component of mean velocity that also remains constant along the flow direction (parallel flow)--have been justified by Squire [7] and Pretsch (cited in Schlichting [3]) in the application of the theory to boundary layer flows. Squire proved that a 2-D disturbance causes instability at a lower Reynolds number than a 3-D disturbance; i.e., a 2-D disturbance is the more critical one from the point of instability.

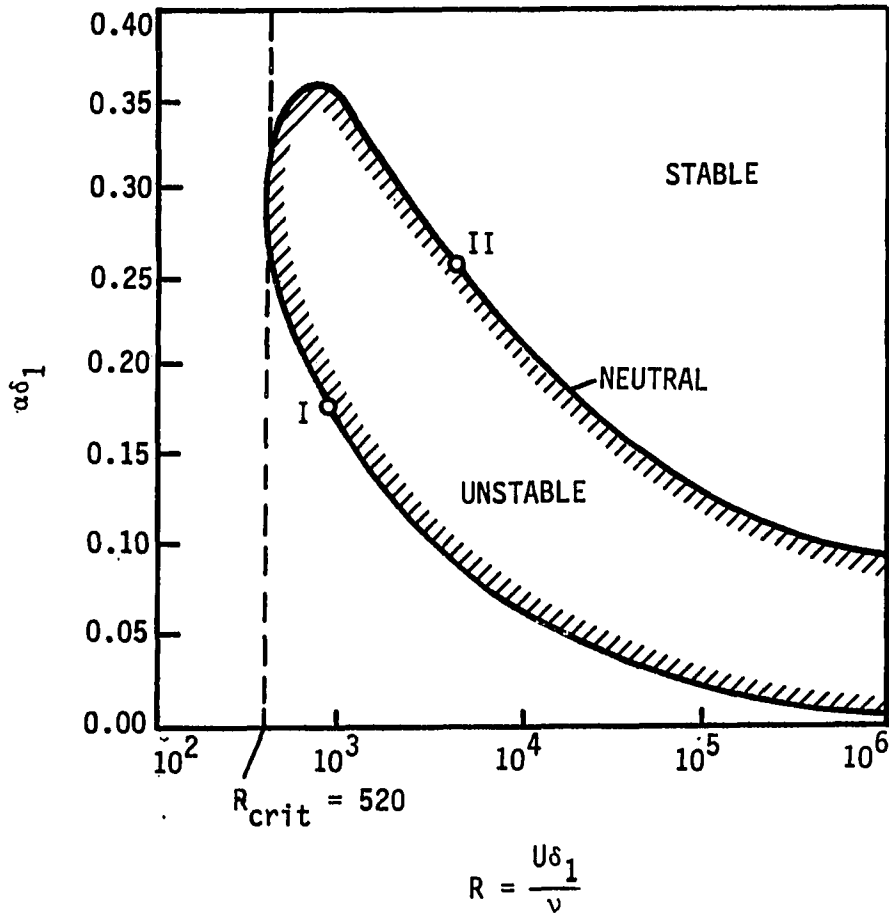


FIGURE 1. Curve of neutral stability as a function of Reynolds number for the Blasius profile [5]

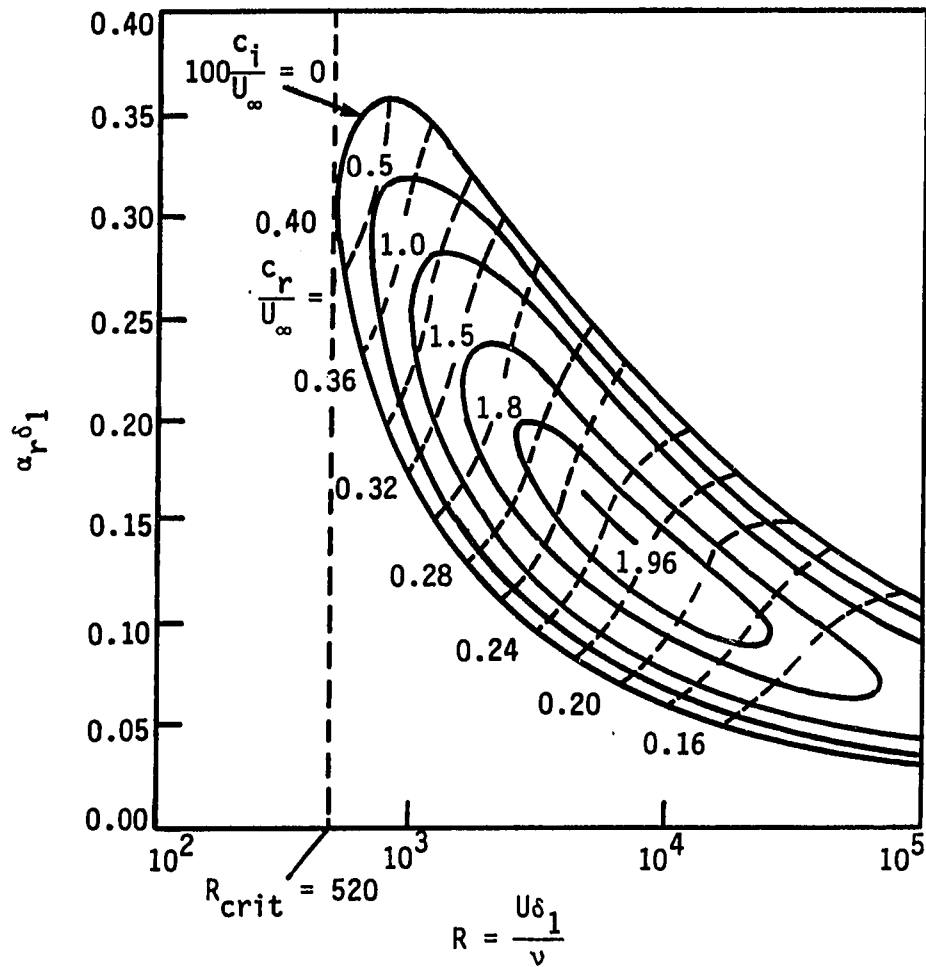


FIGURE 2. Curves of constant temporal amplification for the Blasius profile over a wide range of Reynolds number [6]

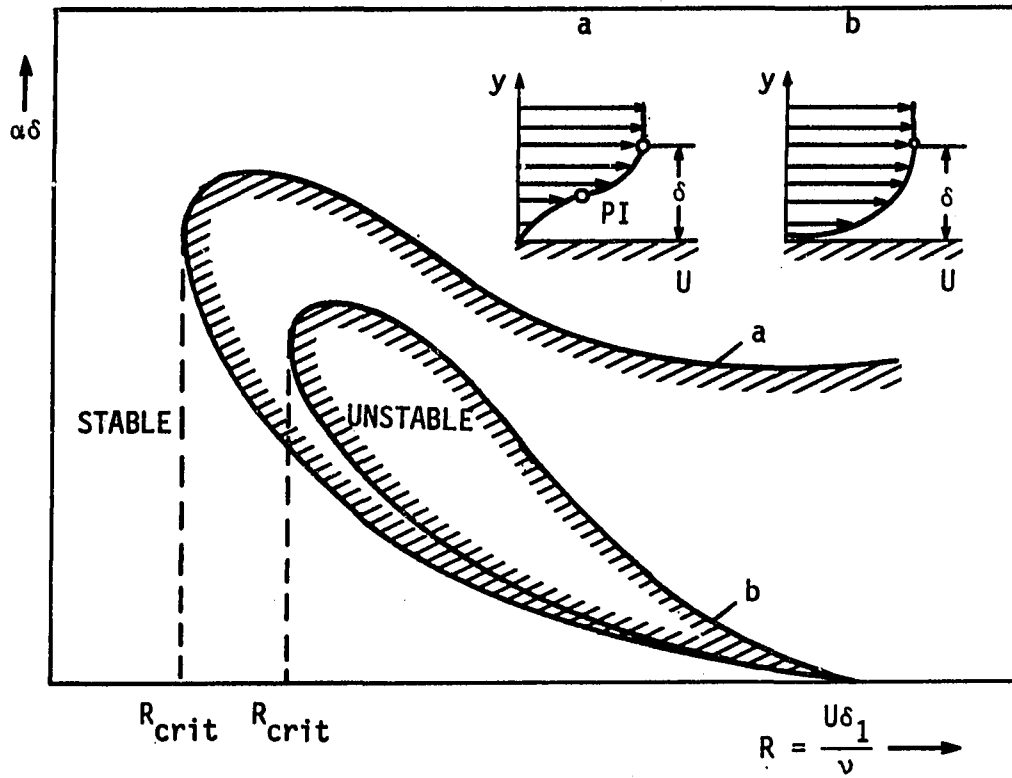


FIGURE 3. Curves of neutral stability for a 2-D boundary layer with 2-D disturbances - (a) non-viscous instability (b) viscous instability

Pretsch has shown that the terms in the stability equation resulting from the inclusion of other mean velocity components, such as those in a boundary layer flow, are unimportant to stability.

The first experimental verification of the above linear stability theory was obtained by Schubauer and Skramstad [8]. Earlier attempts to verify the theory had failed due to the high free-stream disturbances in the test flows. Schubauer and Skramstad constructed a wind tunnel of extremely low free-stream turbulence level (0.02%) to eliminate this problem. By vibrating a thin metallic strip using a magnetic field, they were able to introduce artificial 2-D disturbances at specified frequencies inside the boundary layer. These disturbances gave rise to amplified, damped, or neutral oscillations. The amplified 2-D instability waves are called Tollmien-Schlichting waves. The experimental results from hot-wire anemometer measurements were found to be in excellent agreement with the stability theory.

The 2-D Tollmien-Schlichting waves soon tend to become 3-D as the waves begin to show spanwise variations. The development of these variations has been confirmed experimentally by Klebanoff et al. [9], who introduced in their vibrating ribbon experiment small, initial, spanwise variations in wave amplitude by using spacers. Figure 4 from their results shows the development of the spanwise variations in the streamwise velocity fluctuations downstream of a vibrating ribbon with spacers. As seen in Figure 4, the variations intensify as the wave progresses downstream. Associated with this variation is also a

variation in the local mean velocity, which gives rise to a system of secondary streamwise vortices. By now the transition process becomes non-linear, and the velocity induced by this system of secondary vortices in the streamwise direction distorts the vorticity filaments. Figure 5 from Hinze [10] shows the hairpin shape of such a vorticity filament being deformed because of self induction. This non-linear development is terminated by an abrupt increase in the wave amplitude followed by a subsequent concentration of vorticity in a thin layer called the "high shear layer". Vortex breakdown into fully 3-D fluctuations occurs at these regions of highly localized shear. From these local peaks of vorticity variations, true turbulence bursts forth, proceeds downstream, and grows into a fully turbulent spot. These spots were first noticed by Emmons [11]. Later Michener [12], and Schubauer and Klebanoff [13] studied such turbulent spots in more detail by generating them artificially using electric sparks. Figure 6 shows a turbulent spot generated by an electric spark. The shape of these spots has also been studied in more detail by Criminale and Kovaszany [14] who showed, according to linear stability theory, that the local disturbance develops into a kidney-shaped patch. This has also been verified experimentally by Vasudeva [15].

Flow outside the turbulent spots is still essentially laminar, and, since the laminar flow ahead of the spot itself travels at a much slower velocity, the passage of the spot causes the fluid to become turbulent and then laminar again; that is, the flow undergoes a

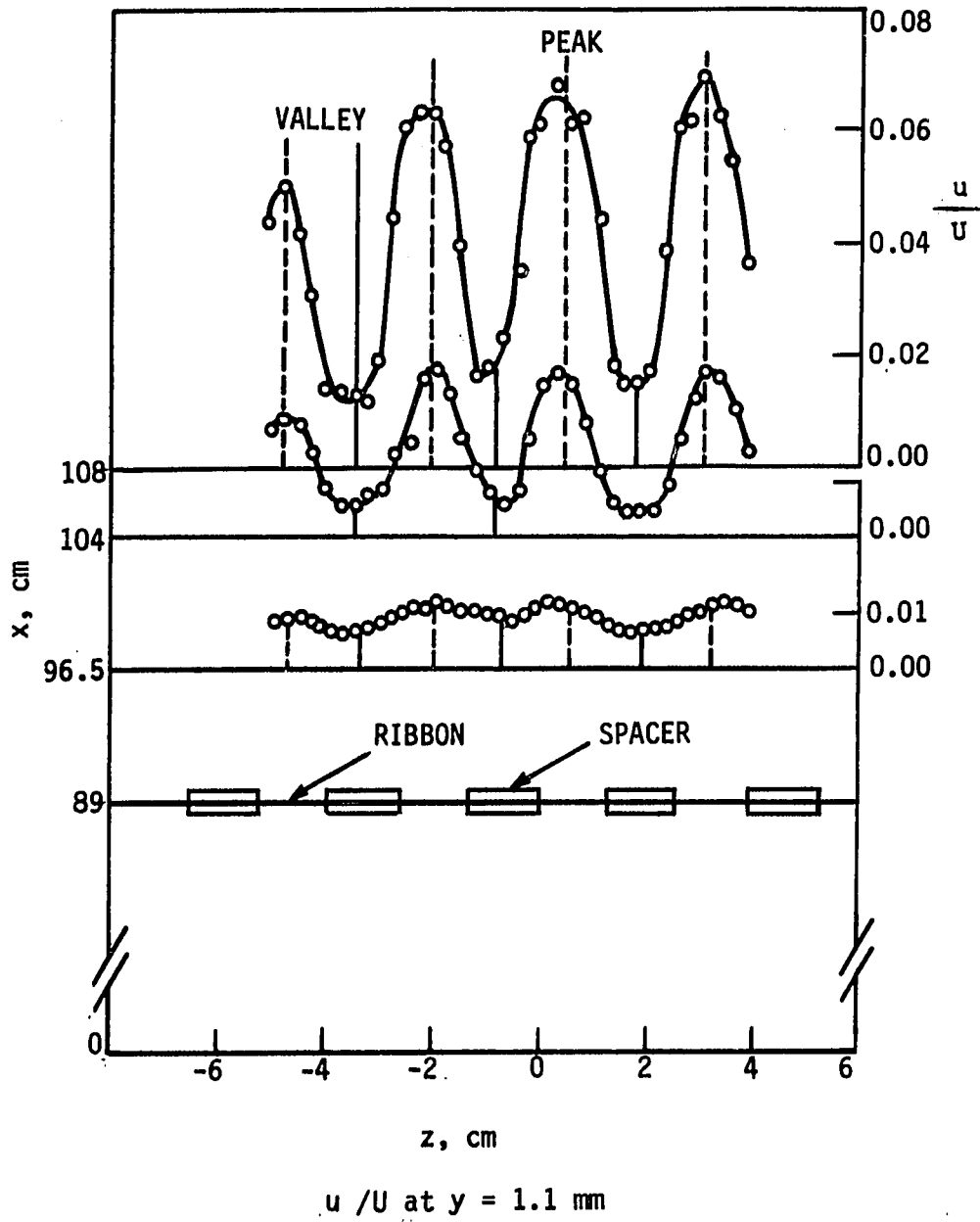


FIGURE 4. Plan view of flat plate and spanwise variation of wave amplitude at various distances downstream from vibrating ribbon [9]

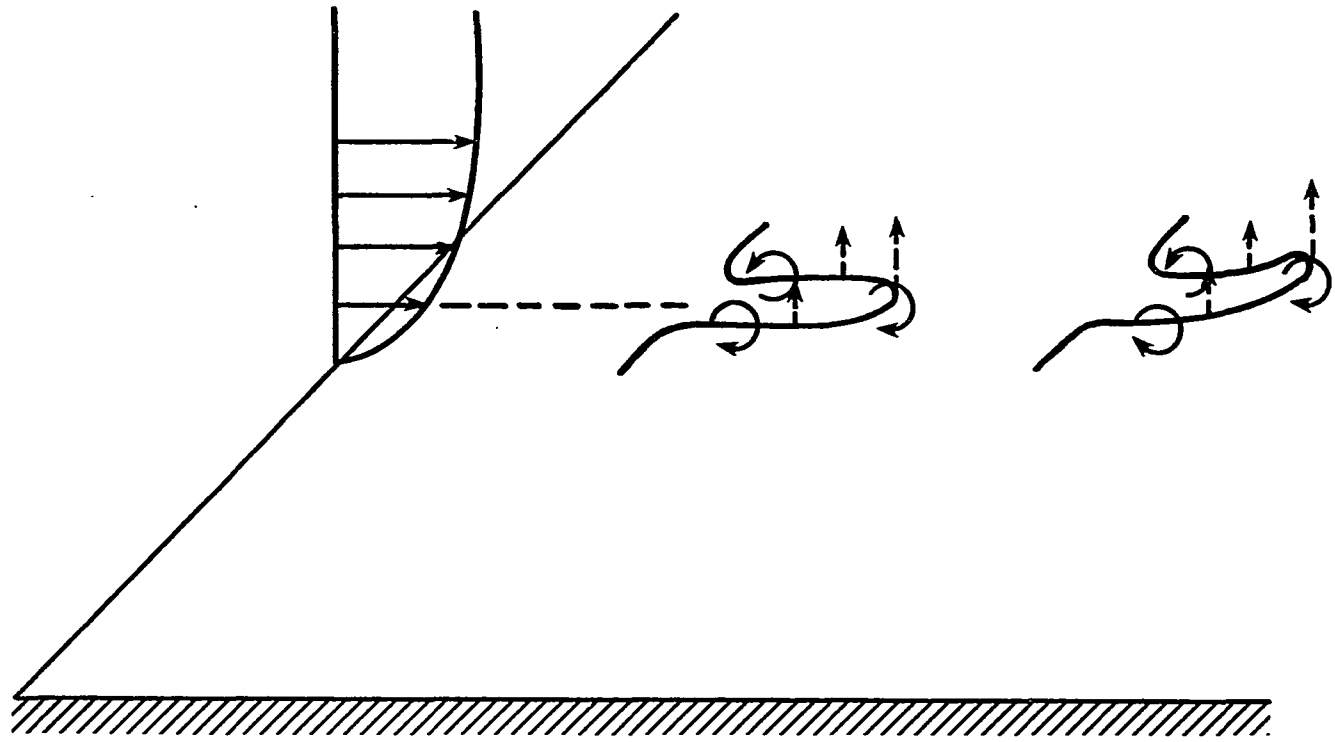


FIGURE 5. Progressive movement and deformation of a U-shaped vortex loop due to self-induction [10]

relaminarization. However, the turbulent spots formed ultimately coalesce into a fully turbulent flow. Extensive measurements in the transition region by Dhawan and Narasimha [16] have shown that the actual region in which these spots appear before coalescing into a fully turbulent boundary layer is small compared to the transition length.

In summary, the overall picture of the transition process in a quiet flow past a smooth plate consists of the following (see Figure 7):

1. Region of stable laminar flow near the leading edge
2. Occurrence of unstable 2-D Tollmien-Schlichting waves
3. Development of 3-D unstable waves and hairpin eddies
4. Vortex break down at regions of highly localized shear
5. Cascading vortex breakdown into fully 3-D fluctuations
6. Formation of turbulent spots at locally intense fluctuations
7. Coalescence of spots into fully turbulent flow.

Although the process of transition described above (at least starting with the formation of Tollmien-Schlichting waves and proceeding up through the formation of 3-D waves and hairpin eddies) has been verified experimentally, this process has not been widely accepted as the only one by which transition occurs. As one example, the formation of separation bubbles in unfavorable pressure gradients may lead also to transition and the production of a turbulent boundary layer.

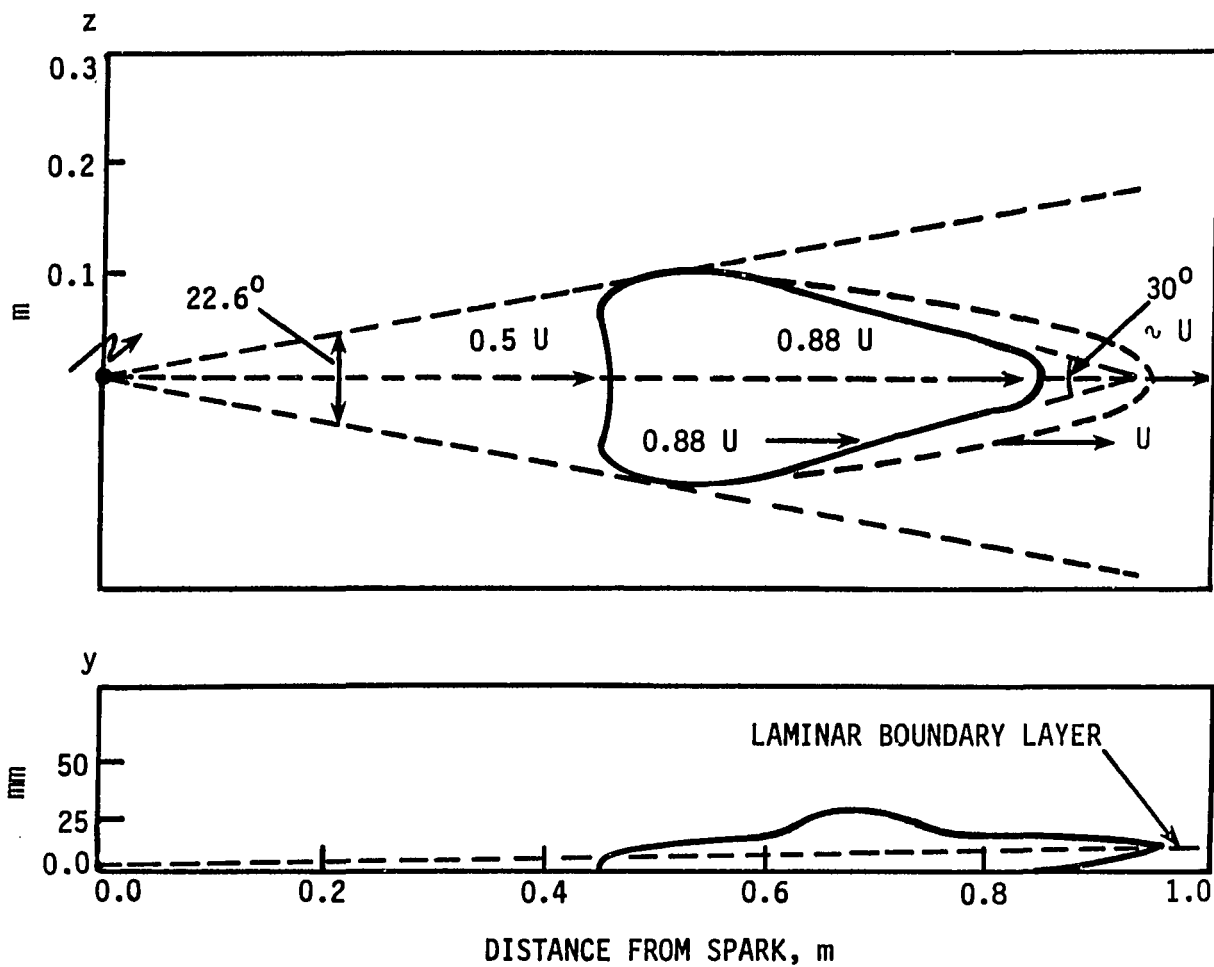


FIGURE 6. Plan and side views of a turbulence spot generated by an electric spark [13]

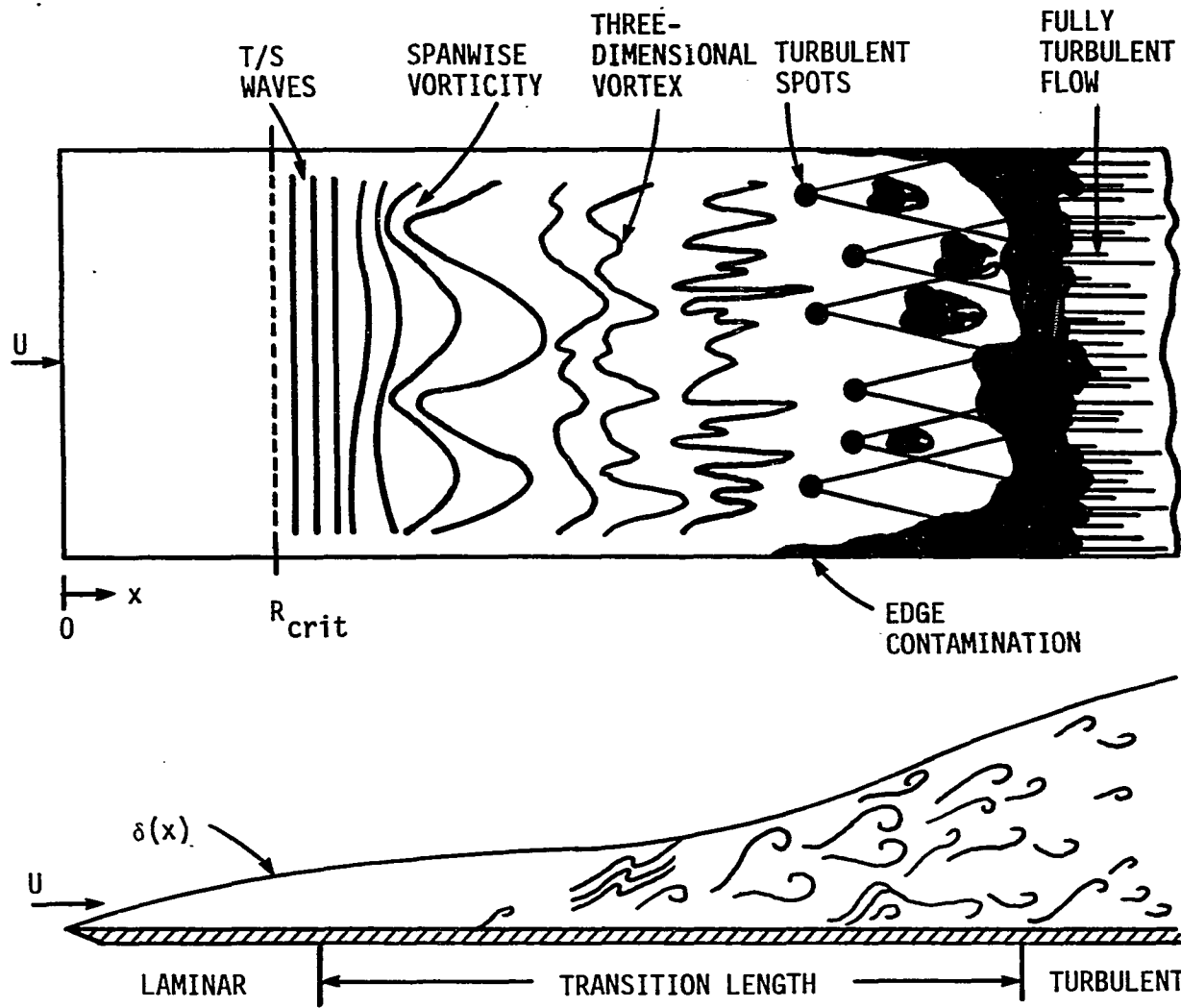


FIGURE 7. Idealized sketch of transition process on a flat plate

Theoretical analysis on stability and transition has so far been confined mostly to linear analysis. The resulting linear theories cannot accurately predict nor describe transition for the most general case. Only qualitatively correct indications of the relative stability of flows of practical interest are available. At best, such linear theories describe only the onset and early evolution of infinitesimal perturbations.

As a more generalized way of looking at transition, a laminar boundary layer can be considered as a very complicated oscillator, with transition as a non-linear response of the oscillator (laminar boundary layer) to a random forcing function. The response depends upon the receptivity of the boundary layer to particular disturbances assumed and their amplification. If the initial disturbances are small, they tend to excite free disturbances in the boundary layer, which are the normal modes of oscillation in the boundary layer or the Tollmien-Schlichting waves. On the other hand, if the disturbances are sufficiently large, they can grow by forcing mechanisms to non-linear levels leading directly to turbulent flow. One example to lend support to this theory is the transition in a Poiseuille pipe flow. Although such a flow is stable to Tollmien-Schlichting waves, it has been verified that transition does occur due to finite disturbances introduced at the inlet (see Reshotko [17]).

The concept of receptivity was first discussed by Morkovin [18]. Physically, receptivity is the signature in the boundary layer of some

externally imposed disturbance. Mathematically, the problem is posed not as an eigenvalue problem, but as one involving a non-homogeneous equation with non-homogeneous boundary conditions.

From the discussion so far, it can be seen that the process of transition is an extremely complex phenomenon, and it is highly unlikely that it will ever be solved completely. Experimental correlations are still being extensively used to predict transition in practical engineering applications. These correlations are discussed next.

B. Factors Influencing Transition

In this section, the factors influencing transition and the various correlations available to take them into account for predicting the properties of transitional boundary layers are discussed.

1. Effects of pressure gradient

For flows taking place in the presence of a pressure gradient, the velocity profile does not remain constant in the flow direction. When a favorable pressure gradient exists (pressure decreasing in flow direction), inflections in the velocity profile do not occur and the critical Reynolds number increases. On the other hand, when an adverse pressure gradient exists, the velocity profile possesses points of inflection, and the critical Reynolds number correspondingly reduces. In addition to influencing the location of the point of instability, a pressure gradient in the flow also influences the rate of amplification

of the unstable disturbances, thereby influencing the distance between the point of instability and the point of transition (transition length). As a result, a favorable pressure gradient increases the transition length, while an unfavorable one decreases it.

Figure 8 from Schlichting [3] shows the curves of neutral stability for laminar boundary layers with pressure gradients. In these plots, Λ is a shape factor defined by $\Lambda = (\delta^2/\nu)(dU/dx)$. Figure 8 shows that, for favorable pressure gradients ($\Lambda > 0$), the curves of neutral stability are of the viscous instability type as discussed previously, and, for adverse pressure gradients ($\Lambda < 0$), the curves are of the non-viscous instability type. Figure 9 shows the effect of pressure gradient on critical Reynolds number as determined from Figure 8. The strong dependence of critical Reynolds number on the pressure gradient can be seen, with the critical Reynolds number ranging from about 100 for $\Lambda = -6$ to over 10,000 for $\Lambda = +7$. Schubauer and Skramstaad [8] have also verified experimentally the strong influence of pressure gradient on stability and on the amplification of small disturbances. Using Figures 8 and 9, Schlichting [3] has calculated the point of instability on a Zhukovskii airfoil as a function of lift coefficient and Reynolds number. On a similar basis, it is possible to calculate the point of instability and hence the point of transition for any arbitrary airfoil shape.

In turbomachines, pressure gradients may be accompanied by turbulence intensity levels in the flow that range from 4% to as high

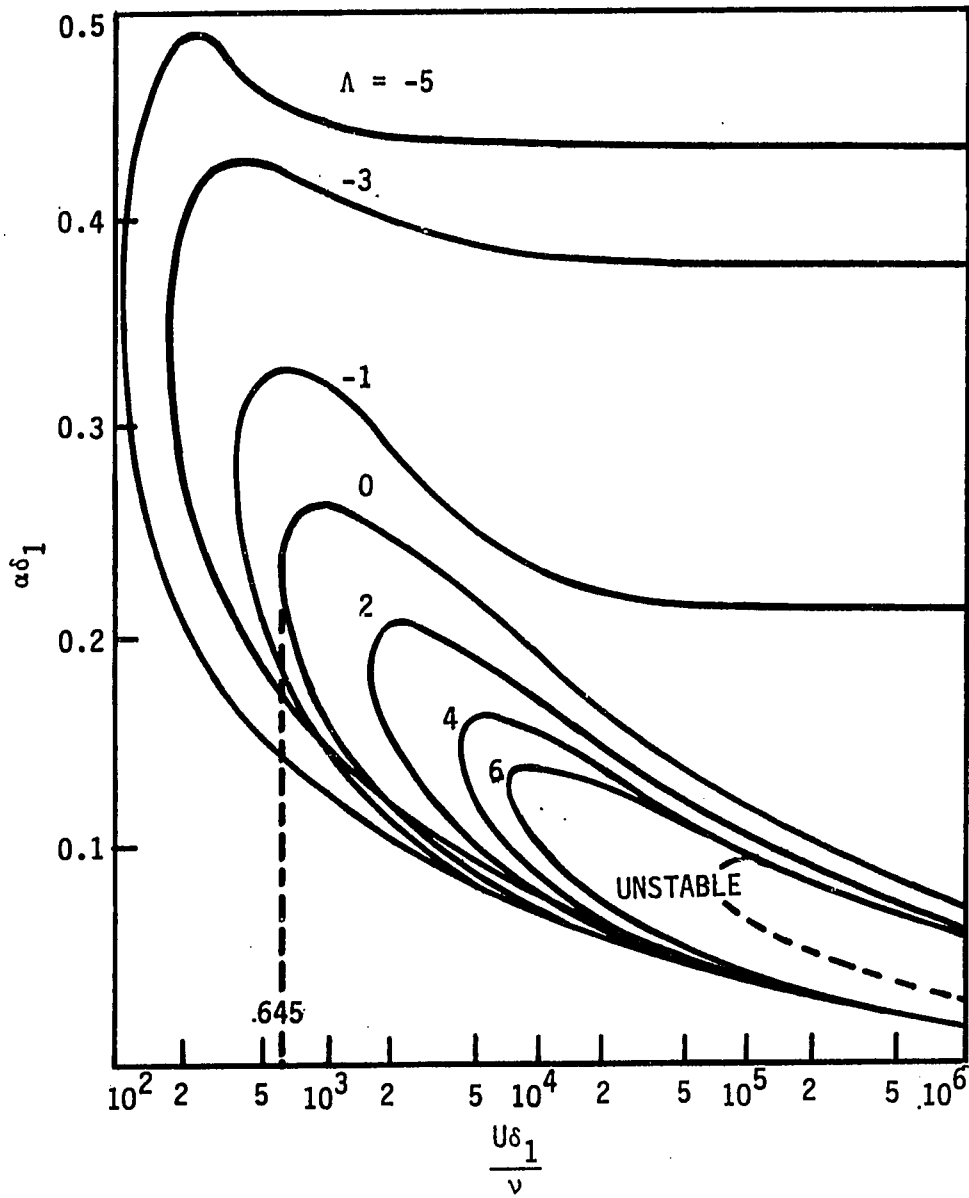


FIGURE 8. Curves of neutral stability for laminar boundary layer profiles with pressure decrease ($\Lambda > 0$) and pressure increase ($\Lambda < 0$) [3]

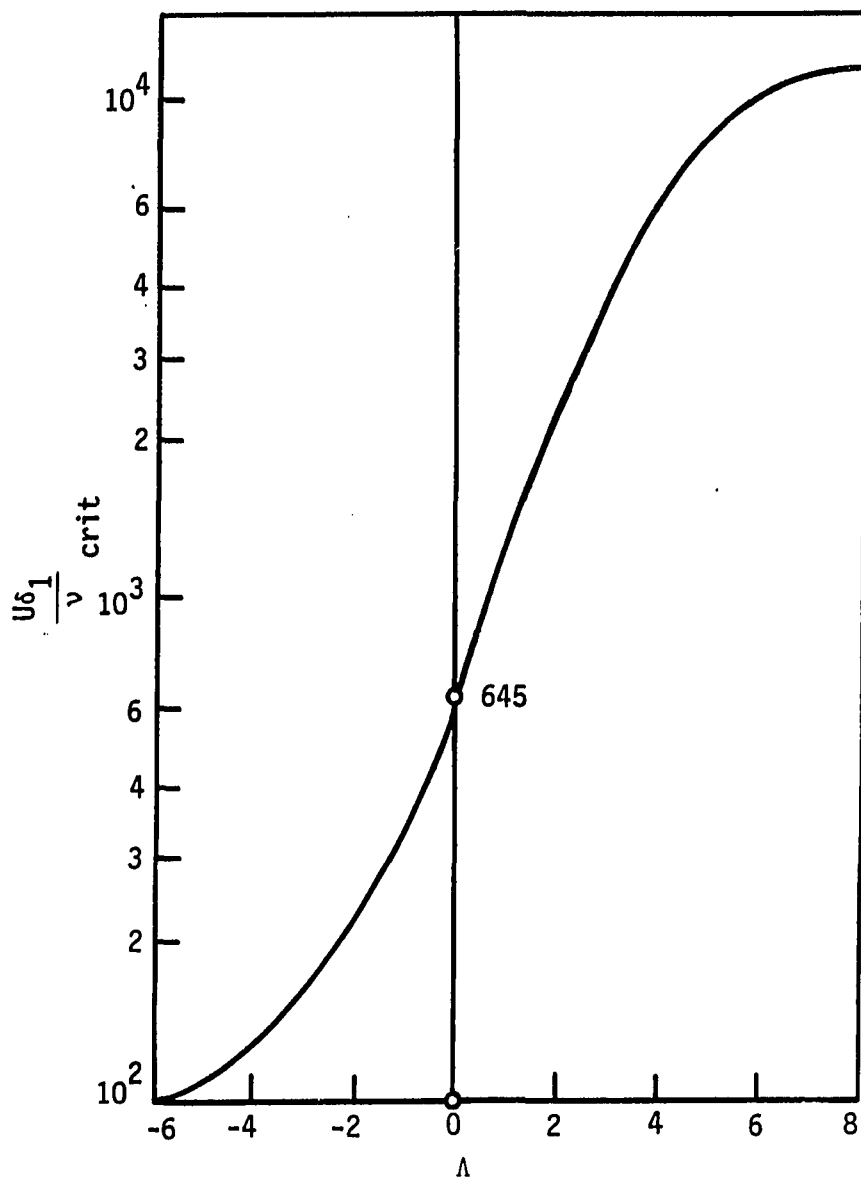


FIGURE 9. Critical Reynolds number of boundary layer velocity profiles with pressure gradient as a function of Λ

as 20%. Experimental correlations which include both the effects of pressure gradient and turbulence level have been developed for use in boundary layer analysis and design calculations as discussed below.

2. Effects of free-stream turbulence level

The effects of free-stream turbulence do not lend itself to analytical or numerical predictions. It is generally presumed that free-stream turbulence level influences only the final breakdown of the amplified Tollmien-Schlichting waves and does not affect the initial linear amplification of these waves. An earlier theory by Taylor [19] proposed that, at high turbulence levels, transition is produced by fluctuating pressure gradients which cause momentary boundary layer separation. This theory has not been verified experimentally, although it seems highly improbable that at high turbulence levels transition can be initiated only by the Tollmien-Schlichting waves (see Morkovin [18] and Reshotko [17]).

A semi-empirical vorticity Reynolds number theory by Van Driest and Blumer [20] postulates that transition occurs at a critical vorticity Reynolds number, which is a function of the free-stream turbulence level. For flow along a flat plate, their correlation is

$$R_{xS}^{1/2} = \frac{-1 + \sqrt{1 + 132,500(Tu/100)^2}}{39.2(Tu/100)^2}$$

where R_{xS} is the Reynolds number at the start of transition and Tu is the turbulence level defined as $Tu = [\{(u^2 + v^2 + w^2)/3\}^{1/2}/U] \times 100$. For the Falkner-Skan velocity profile $U = Cx^m$, Van Driest and Blumer modified their formula as

$$\frac{1690}{R_{x_S}^{1/2}} = 0.312(m + 0.11)^{-0.323} + 1.6\eta_\delta^2 R_{x_S}^{1/2} \frac{Tu^2}{100}$$

where η is a dimensionless normal coordinate, and η_δ is the coordinate value at the edge of the boundary layer. Values of η for different m values can be obtained from tables for the Falkner-Skan similarity flows (see, for instance, White [21]).

Abu-Ghanaam and Shaw [22] have also produced useful correlations for free-stream turbulence level by combining their own experimental results with those of a number of other investigators to give an expression for momentum thickness Reynolds number (for zero pressure gradient) at the start of transition as

$$R_{\theta_S} = 163 + \exp(6.91 - Tu)$$

and at the end of the transition

$$R_{\theta_E} = 2.667 R_{\theta_S}.$$

For non-zero pressure gradients, the expression for the start of transition has been further modified by Abu-Ghanaam and Shaw [22] to give

$$R_{\theta_S} = 163 + \exp(F(\Lambda_\theta) - F(\Lambda_\theta)Tu/6.91)$$

in which

$$F(\Lambda_\theta) = 6.91 + 12.75(\Lambda_\theta) + 63.34(\Lambda_\theta)^2, \quad \text{for } \Lambda_\theta < 0$$

$$F(\Lambda_\theta) = 6.91 + 2.48(\Lambda_\theta) - 12.27(\Lambda_\theta)^2, \quad \text{for } \Lambda_\theta > 0$$

and where Λ_θ is a pressure gradient parameter defined as

$\Lambda_\theta = (\theta^2/\nu)(dU/dx)$. This correlation is plotted in Figure 10. Figure 10 also shows that, at a given turbulence level, the effect of adverse

pressure gradient in promoting transition is greater than the effect of favorable pressure gradient in retarding it, and that smaller pressure gradients are relatively more influential than larger ones in promoting or delaying transition. Also, it is apparent that the effect of pressure gradient is less significant as the turbulence level increases.

The expression given above for the end of transition, also modified for the effect of pressure gradient, is

$$R_{\theta_E} = 540 + 183.5(R_L \times 10^{-5} - 1.5)(1 - 1.4\Lambda\theta)$$

in which R_L is the length of transition Reynolds number given by Dhawan and Narasimha [16] as,

$$R_L = 16.8 (R_{x_S})^{0.8}$$

The above expression for R_{θ_E} is quadratic in θ_E and can be solved for θ_E since x , U , and $(dU/dx)_E$ are all known, once the length of transition has been determined from R_{x_S} .

In addition to the correlations for the start and end of transition, Abu-Ghanaam and Shaw [22] have presented correlations for the boundary layer parameters during transition. These are:

Momentum thickness

$$\theta' = \frac{\theta - \theta_S}{\theta_E - \theta_S} = \eta^{1.35}$$

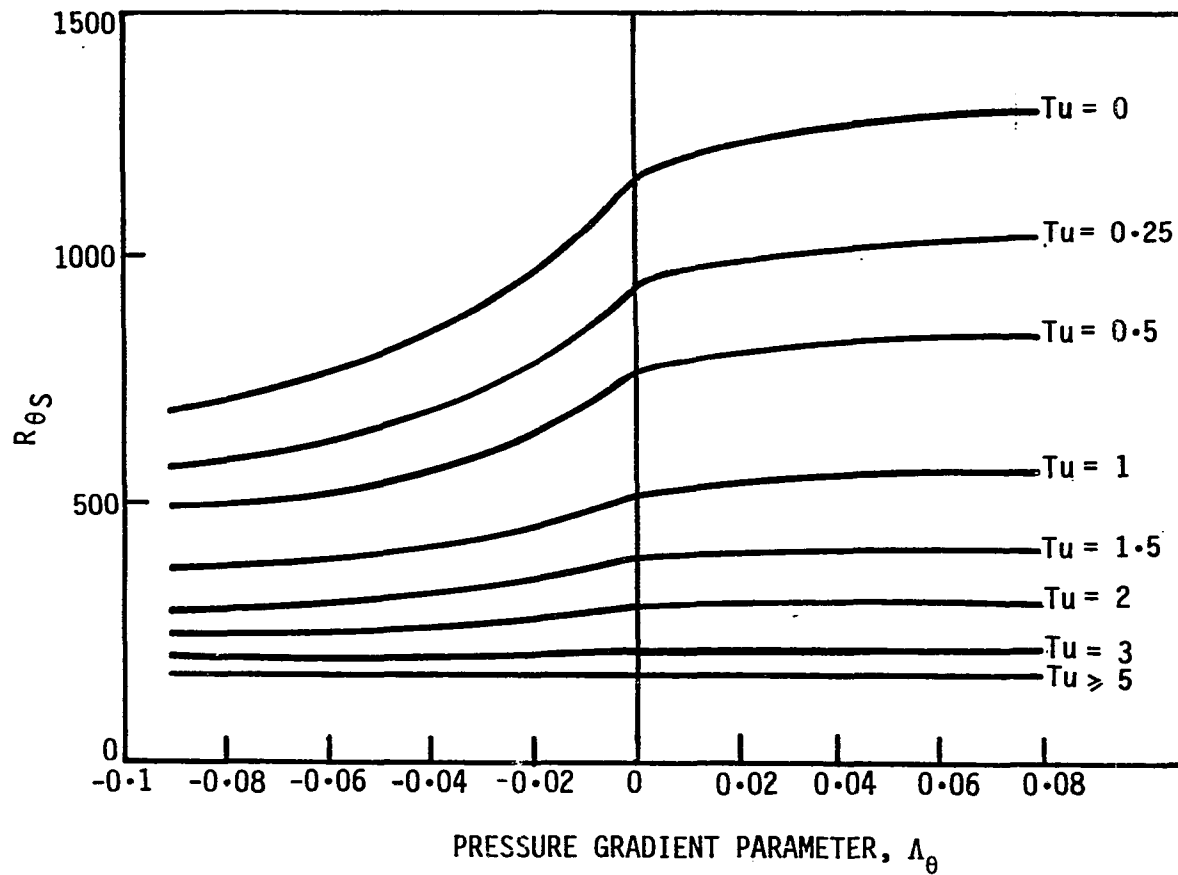


FIGURE 10. Momentum thickness Reynolds number at the start of transition for nonzero pressure gradient [22]

Shape factor

$$H' = \frac{H_S - H}{H_S - H_E} = \sin \frac{\pi}{2}\eta$$

Skin friction

$$C_f' = \frac{C_{fS} - C_{fE}}{C_{fE} - C_{fS}} = 1 - \exp(-5.645\eta^2)$$

Intermittency

$$\gamma = 1 - \exp(-5\eta^3)$$

in which η is a non-dimensional length parameter defined as

$$\eta = \frac{R_x - R_{xS}}{R_{xE} - R_{xS}}$$

Turbulence scale as well as turbulence level may influence transition. However, with the lack of experimental data, this effect has not been included in transition modelling.

3. Effects of wall suction

The effect of wall suction on a boundary layer flow is to stabilize the boundary layer in a way similar to that of a favorable pressure gradient. Wall suction reduces the boundary layer thickness and creates a more stable laminar velocity profile. Qualitatively, we can say that wall suction, by removing low energy fluid close to the wall, stabilizes the boundary layer as a whole.

Bussmann and Muenz (cited in Schlichting [3]) investigating the stability of an asymptotic suction profile (a boundary layer whose thickness remains constant along the flow direction) found that the critical Reynolds number was more than 130 times that for flow along a flat plate with out suction. Schlichting [3], in estimating the amount of suction necessary to maintain an asymptotic suction profile, found the ratio of suction velocity to free-stream velocity to be less than $1/70,000$. In a practical application, this velocity ratio can be expected to be higher when the region in which the asymptotic suction profile develops is also considered. It has been found that savings of up to 65% to 85% in drag can be achieved by employing suction and delaying transition on airfoils in the Reynolds number range of 10^6 to 10^8 [3]. Figure 11 shows curves of neutral stability for a velocity profile with suction. It is seen that the limit of stability is increased for the velocity profile with suction as compared to the case with no suction, and the range of unstable disturbance wavelengths encompassed by the curve of neutral stability is reduced considerably for the case with suction.

4. Effects of heat transfer

The effects of heat transfer on transition are mainly through the changing of the shape of the velocity profile, which is brought about by the dependence of fluid viscosity on temperature. It can be shown that, for flow along a flat plate with zero pressure gradient, the curvature of the velocity profile at the wall is [3]

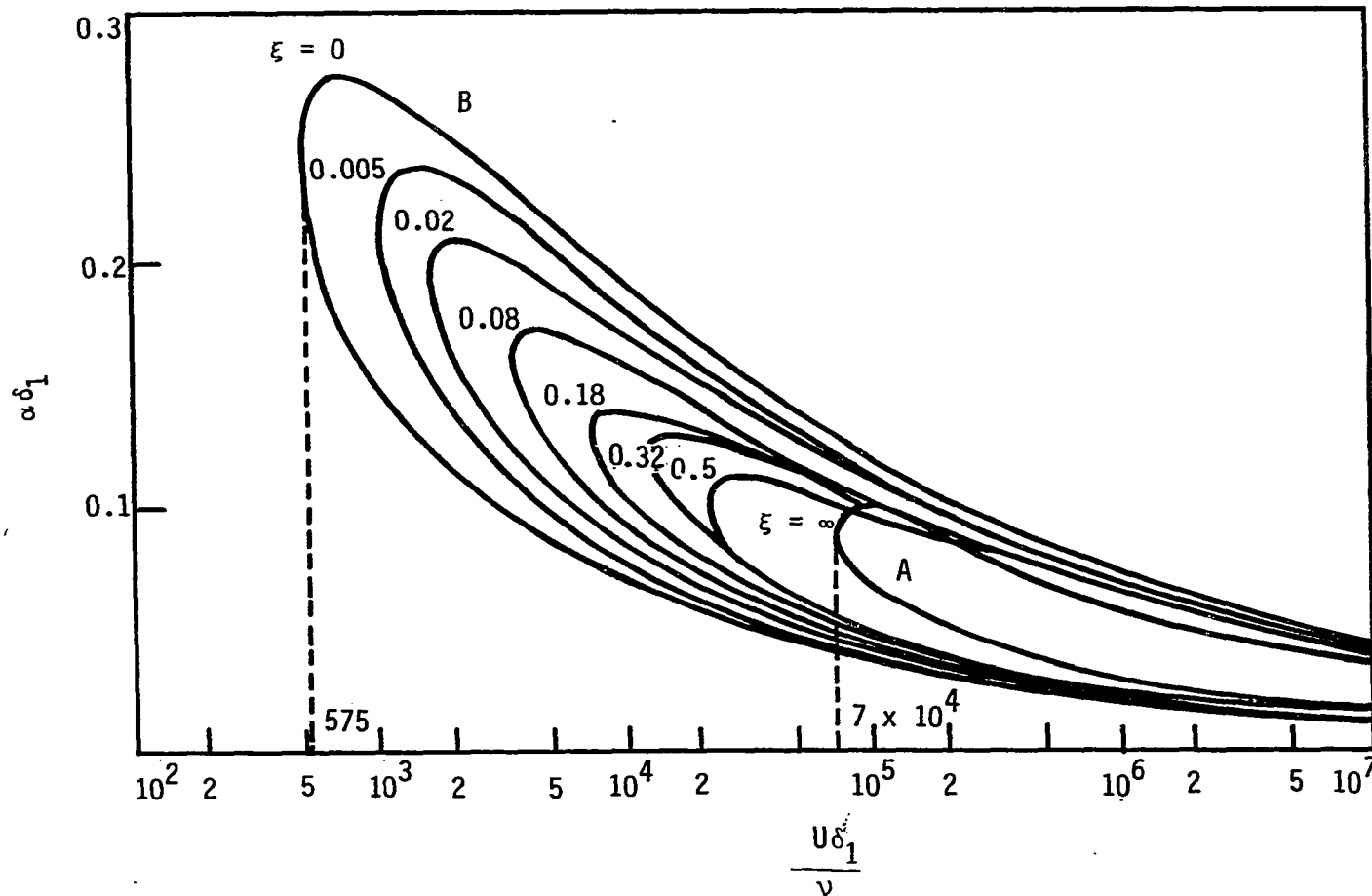


FIGURE 11. Curves of neutral stability for velocity profiles with suction -- (A) - Asymptotic suction profile, (B) - profile without suction -- ξ denotes the dimensionless inlet length

$$\frac{d^2U}{dy_{\text{wall}}^2} = \frac{-1}{\mu_{\text{wall}}} \frac{d\mu}{dy_{\text{wall}}} \frac{dU}{dy_{\text{wall}}}$$

If heat transfer takes place from the wall to a gas flowing over it, the curvature of the velocity profile is seen from the above relationship to be positive at the wall, implying that there is a point of inflection in the velocity profile. This is the case since, for a gas, viscosity increases with temperature. On the other hand, heat transfer from the gas to the wall would make the boundary layer more stable. This effect is analogous to that of adverse or favorable pressure gradients in the flow. In a liquid flow, since the viscosity decreases as the temperature increases, the effect is reversed.

5. Effects of compressibility

The effect of compressibility is to increase the complexity of the boundary layer stability problem through the addition of density, temperature, viscosity, thermal conductivity, specific heat and entropy variations to the flow. The earliest compressible stability analysis was carried out by Landau (cited in White [21]). His theory, and those of others who have followed him, are only approximate. A numerical solution approach was first initiated by Mack [23] to analyze the fully compressible stability equation. From Mack's results (shown in Figure 12) it appears that the effect of compressibility is to stabilize the flow. However, in this situation, the character of the instabilities themselves is changing. For a free-stream Mach number

greater than 3.0, higher modes of instability appear. These modes arise when the disturbance velocities are supersonic relative to the wall. Another aspect of compressibility is that Squire's theorem [7] no longer holds for the first mode: i.e., the most unstable waves no longer move parallel to the wall (x -axis), but at an angle away from it [7]. It has been also observed by Kendall [24] that at high Mach numbers, sound field radiation from the wind-tunnel turbulent-wall boundary layers creates disturbances in the boundary layers under study, causing transition in a region that would be stable according to stability theory.

6. Effects of surface roughness

The presence of roughness, in general, favors transition at a lower Reynolds number under otherwise similar conditions. From the viewpoint of stability theory, existence of roughness elements would give rise to additional disturbances in the laminar stream that have to be added to those already present in the boundary layer because of turbulence. However, if the roughness elements are sufficiently small, the resulting disturbances lie below the threshold of those generated by turbulence and do not influence transition.

Although surface roughness effects are of great practical importance, it has not yet been possible to treat them theoretically. Earlier studies by Schiller, Tani et al. and Goldstein (cited in Schlichting [3]) have generally assumed that if the roughness elements are large, transition occurs at the point of the element itself. On

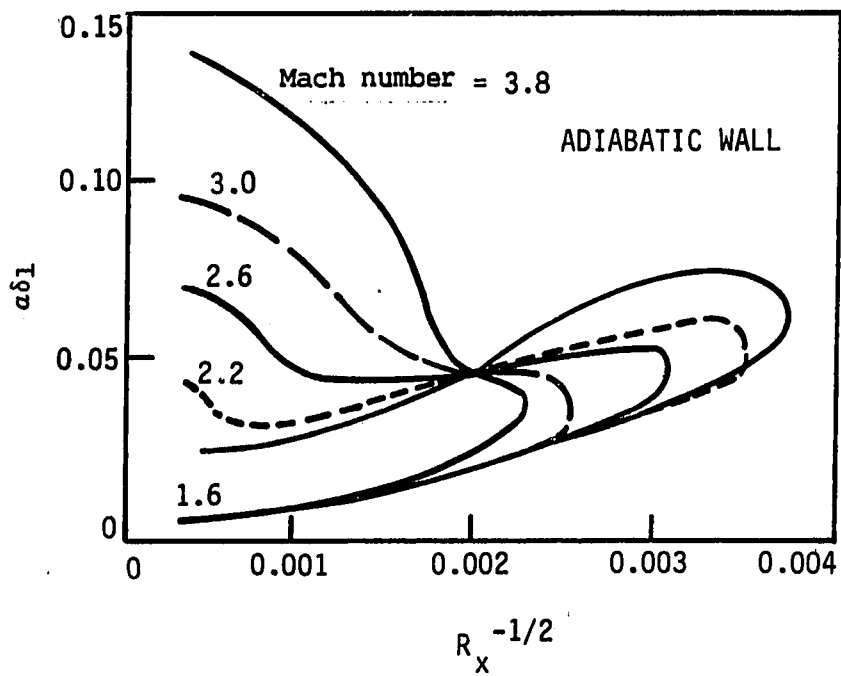


FIGURE 12. Neutral curves in supersonic adiabatic flow over a flat plate (perfect gas) [23]

the other hand, if the roughness elements are small, they assumed the elements have no influence on transition. However, studies by Fage and Preston [25] have shown that the point of transition, which lies downstream of the roughness element, moves continuously upstream as the height of the element is increased, until it reaches the position of the roughness element itself. Figure 13, from Schlichting [3], shows the experimental results for the effect of roughness element height on the transition length. It is apparent that as the size of the roughness element increases, the distance between the location of the roughness element and the point of transition decreases until it reaches a certain minimum value.

7. Effects of body forces

Flow over a horizontal plate with a varying density across the boundary layer is stable if the density decreases away from the wall towards the free-stream (upward); the flow is unstable if the density variation is reversed. Prandtl (cited in Schlichting [3]) has shown that in addition to the Reynolds number, the stability of a stratified flow depends on a stratification parameter, the Richardson number, defined as

$$Ri = \frac{-g}{\rho} \frac{d\rho}{dy} \frac{d^2U}{dy_{wall}^2}$$

Here g is the acceleration due to gravity, ρ is the density, and y is positive upward. $Ri = 0$ corresponds to homogeneous fluids, $Ri > 0$ denotes stable and $Ri < 0$ denotes unstable stratification.

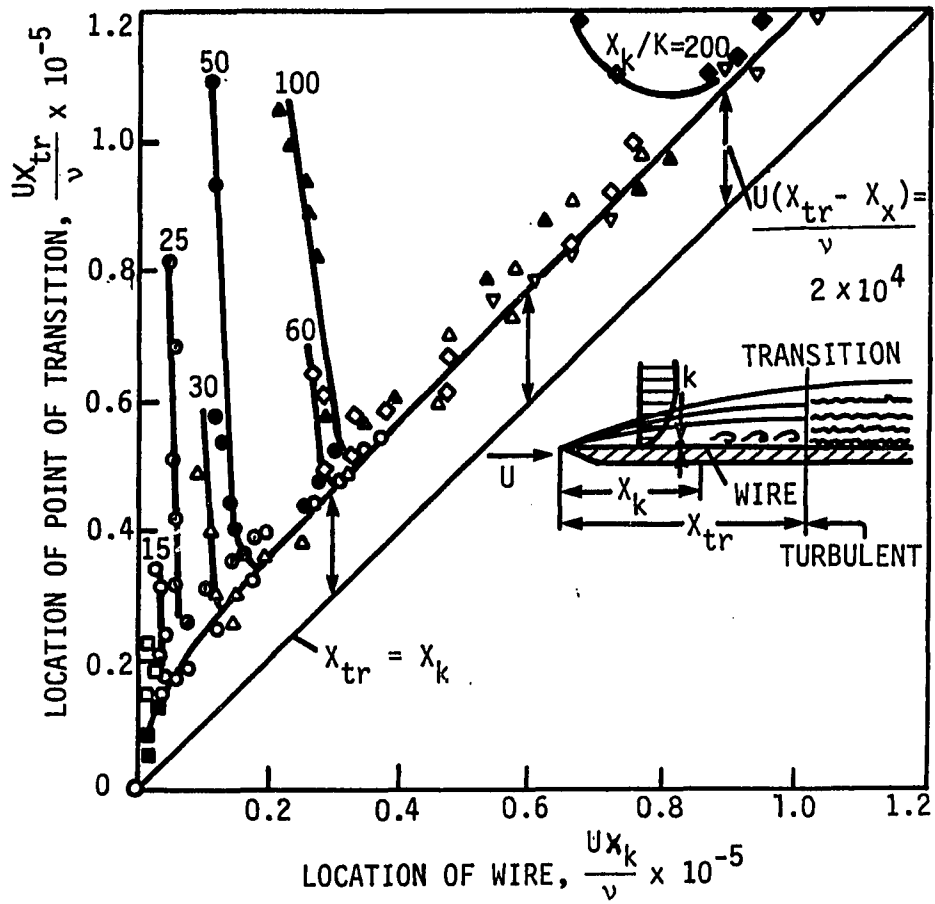


FIGURE 13. Distance between the point of transition and the position of tripping wire for "fully effective" operation [3]

Calculations by Schlichting [3] for the Blasius profile have shown that for $Re = 0.42$, the critical Reynolds number becomes infinite; i.e., the flow remains stable everywhere on the flat plate.

Görtler (cited in Schlichting [3]) generalized Tollmien's inviscid stability criteria for velocity profiles containing a point of inflection to show that the change of sign of $[(d^2U/dy^2) + (1/R)(dU/dy)]$ should be considered for instability, instead of just the change of sign of (d^2U/dy^2) . Here R is the radius of curvature, $R > 0$ denotes a convex wall and $R < 0$ a concave wall. In general, however, the influence of wall curvature is relatively small if the ratio of boundary layer thickness to the radius of curvature is small. With concave walls, a different kind of instability of a 3-D nature arises, leading to longitudinal vortices (Görtler vortices).

III. DESIGN OF THE TEST CASCADE

The test cascade was designed using the cascade design/analysis program originally developed by Alarcon [26]. This program is based on iterative calculations in which airfoil profiles are designed from velocity diagram requirements and specified geometry parameters. With a proposed design, an inviscid blade-to-blade flow calculation and a leading edge reanalysis is performed to obtain airfoil pressure or Mach number distributions. From these results, the profile boundary layer calculations are carried out and cascade losses are estimated using a wake mixing analysis. A brief review of the cascade design program and the design parameters used for the test cascade are presented in the following sections. In the concluding section, the predicted performance of the cascade with varying inlet turbulence levels and incidence angles is presented.

A. Review of Cascade Design Program

A flow diagram for the turbine cascade design program is shown in Figure 14. As seen in the Figure, the design process consists of four major steps, which are the cascade geometry design, the global inviscid blade-to-blade analysis, the leading edge reanalysis, and the profile boundary layer analysis. The entire cascade design program is an interactive program with graphic outputs of airfoil profile, static pressure and Mach number distributions, and leading edge reanalysis mesh.

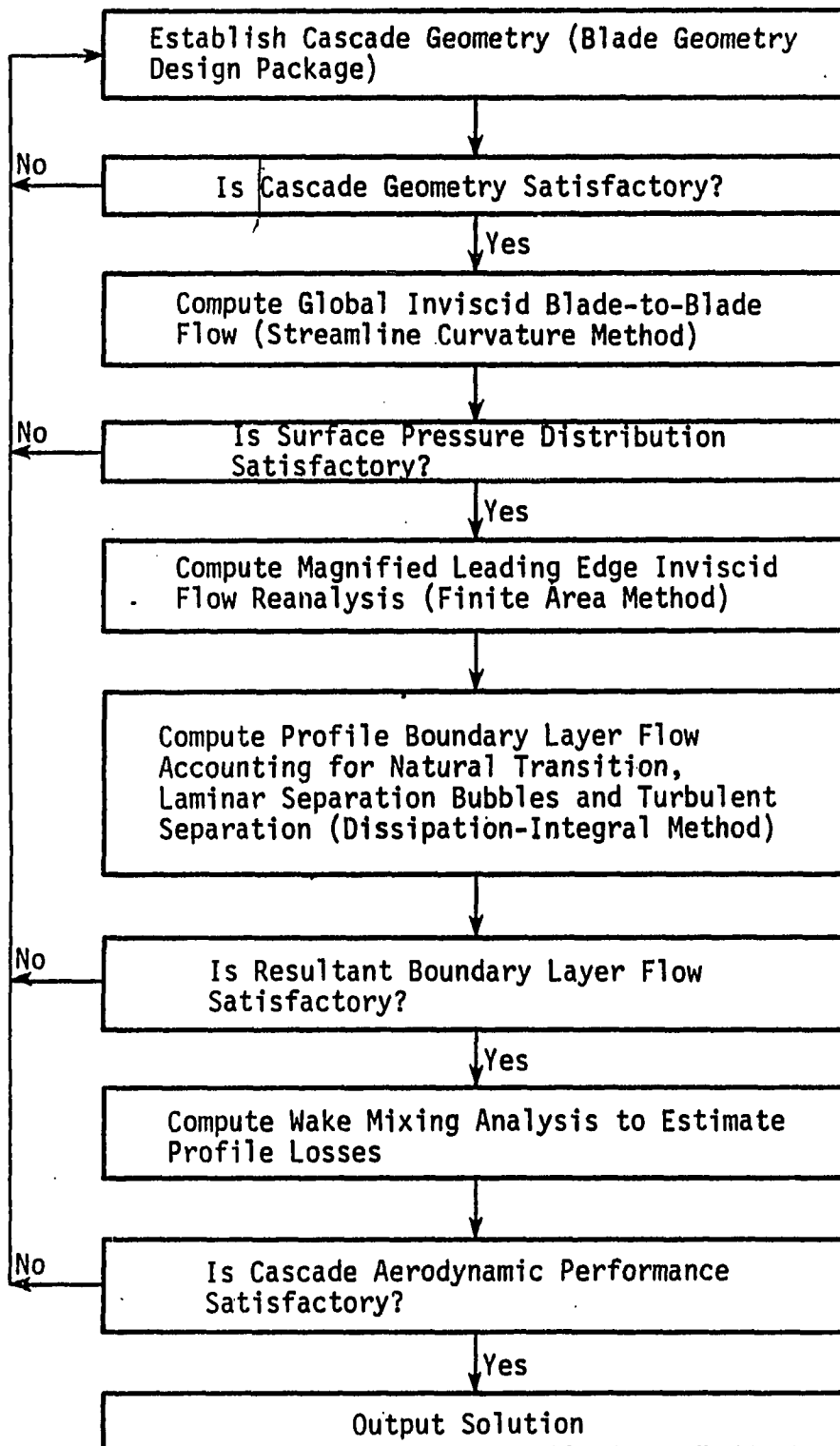


FIGURE 14. Turbine cascade design flow diagram

1. Cascade geometry design

The airfoil profile is generated with third and fourth-order polynomials, and with leading edge and trailing edge circles. The analytical description of the profile makes it possible to locally change the profile without substantially affecting other portions of the profile, and to maintain a continuous curvature variation.

The basic geometric parameters required to define the airfoil are shown in Figure 15. R_{LE} and R_{TE} are the leading and trailing edge radii, B_x is the axial chord, H/L is the height to length ratio, β_1^* , β_2^* are the inlet and exit metal angles, $\Delta\beta_1^*$, $\Delta\beta_2^*$ are the leading and trailing edge wedge angles, τ is the blade pitch, β_λ is the gaging angle, Γ is the uncovered turning, S_2 , S_4 , P_2 , P_3 are the suction and pressure surface auxiliary defining points. Once the geometry parameters are supplied, the program applies the matching conditions to the defining polynomials and solves for the polynomial coefficients. More details on the governing equations for the polynomials can be found in Ye and Kavanagh [27].

2. Inviscid analysis

After the airfoil profile had been designed from the velocity diagram requirements and the specified geometry parameters, an inviscid flow calculation is made to obtain the pressure and Mach number distributions. This inviscid analysis consists of two parts, a global streamline curvature analysis and a detailed leading edge reanalysis.

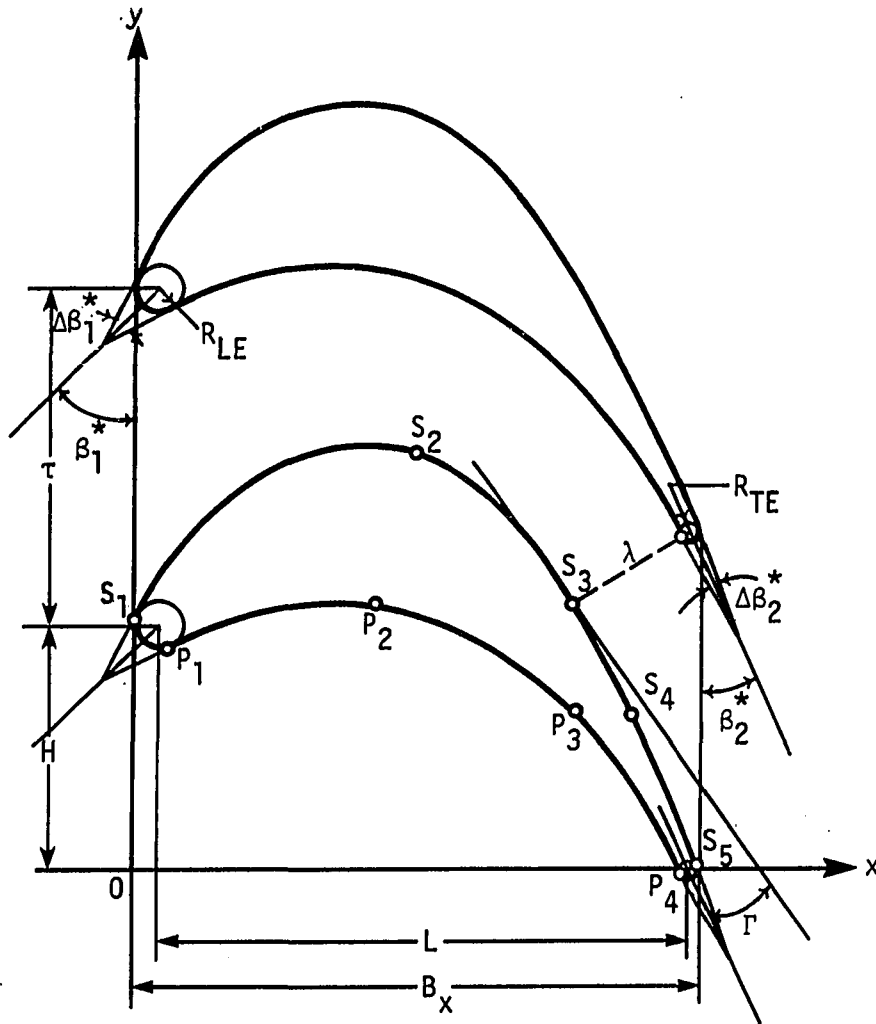


FIGURE 15. Coordinate system and turbine cascade geometry parameters

The streamline curvature analysis consists of two nested iteration loops, the inner loop solving the velocity gradient and the continuity equations inside the channel formed by the stagnation streamlines and the cascade passage, and the outer loop correcting the stagnation streamlines to achieve flow periodicity for the next inner loop calculation. The computational grid is formed by streamlines and uniformly spaced quasi-orthogonals. Since the streamlines are not known in advance but are determined as a part of the solution, the grid is a floating type and the streamlines are changed until a solution satisfying the flow periodicity conditions is obtained. In the calculations, limits are placed on the number of iterations performed and specific tolerances applied for convergence of the solution. More details on the streamline curvature analysis can be found in Ye and Kavanagh [27] and Alarcon [26].

Once the results from the global analysis are obtained, a leading edge reanalysis is performed using a finite area technique. A body fitted orthogonal mesh is constructed around the leading edge of the airfoil geometry, and the results obtained from the global analysis are interpolated on the boundaries of the computational mesh. The continuity equation and the irrotationality condition are used to obtain the equation to be approximated with the finite area technique. The solution is carried out for the stream function. More details on the leading edge reanalysis are given in Alarcon [26].

3. Integral boundary layer analysis

The profile boundary layer calculations in the design program are performed using the dissipation-integral method of Walz [28]. Different sets of auxiliary relations from analytical and experimental results are used in the laminar and turbulent analyses for closure of the system of boundary layer equations. In addition, the effects of wall curvature and free stream turbulence level on the development of the turbulent boundary layer are included. Transition models presented by Crimi and Reeves [29] (with Dhawan and Narasimha transition length model [16]), Dunham [30], and Abu-Ghanaam and Shaw [22] are available in the program to predict natural transition and to determine transition length. Models to predict laminar separation and turbulent reattachment as presented by Roberts [31], or to predict turbulent separation as presented by Föttner [32], are also employed. Finally, profile losses for the cascade are estimated using the Stewart [33] wake mixing analysis.

B. Test Cascade

For the test cascade, a Zweifel loading coefficient of 1.18, and inlet and exit gas angles of 45.0° and 27.7° , giving a turning angle of 107.3° , were used. The axial chord Reynolds number was 830,000 on the basis of the selected axial chord of 8.0 inches. The design inlet turbulence level was taken as 1.0%, the inlet Mach number as 0.1, and the design incidence angle as -7.0° . Several versions of the cascade

design, each having different airfoil profiles satisfying the design conditions, were developed before a satisfactory airfoil pressure distribution was obtained. The factors considered with regard to pressure distribution were the avoidance of overspeeding around the leading edge, moderate diffusion rate through the blade passage, and, in general, a smooth, well-behaved pressure distribution along the airfoil suction surface to prevent separation. The geometric parameters of the designed cascade, non-dimensionalized with respect to axial chord, were as follows (see Figure 15):

R_{LE}	= 0.070	$XS2$	= 0.200
R_{TE}	= 0.030	$YS2$	= 0.910
H/L	= 0.650	$XP2$	= 0.325
β_1^*	= 38.0°	$YP2$	= 0.588
$\Delta\beta_1^*$	= 42.0°	r	= 1.12
β_2^*	= 23.7°	β_λ	= 24.0°
$\Delta\beta_2^*$	= 2.5°	Γ	= 17.0°

Figure 16 shows the test cascade generated by the design program, and Figure 17 shows the predicted pressure distribution for the cascade at design incidence.

The results of the integral boundary layer analysis are summarized in Table 1 for design incidence and Reynolds number, and for a range of inlet turbulence levels of 1% to 7%. As noted, both the Crimi and Reeves and the Abu-Ghanaam and Shaw transition models predicted natural transition on the suction surface, followed by a fully turbulent

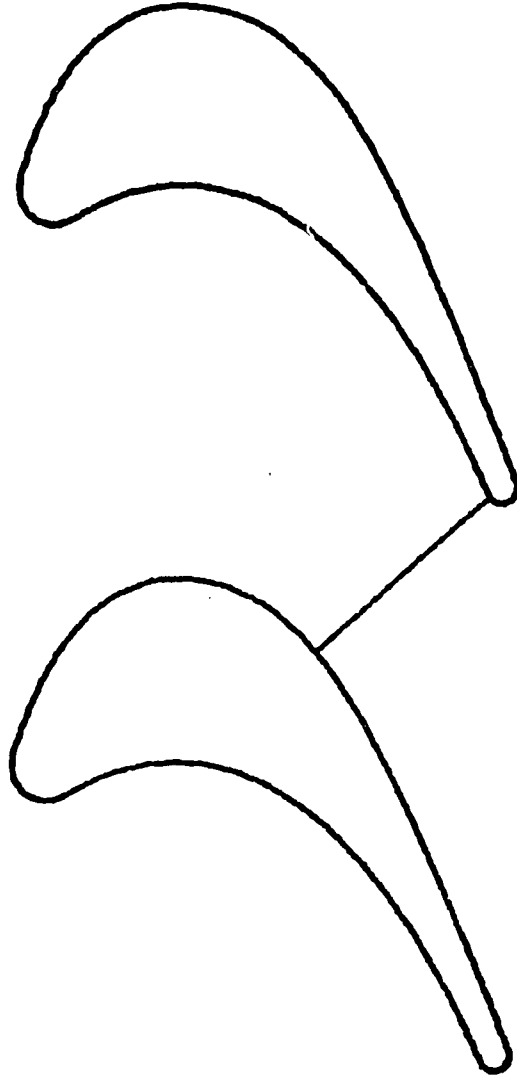


FIGURE 16. Computer generated design for the test cascade

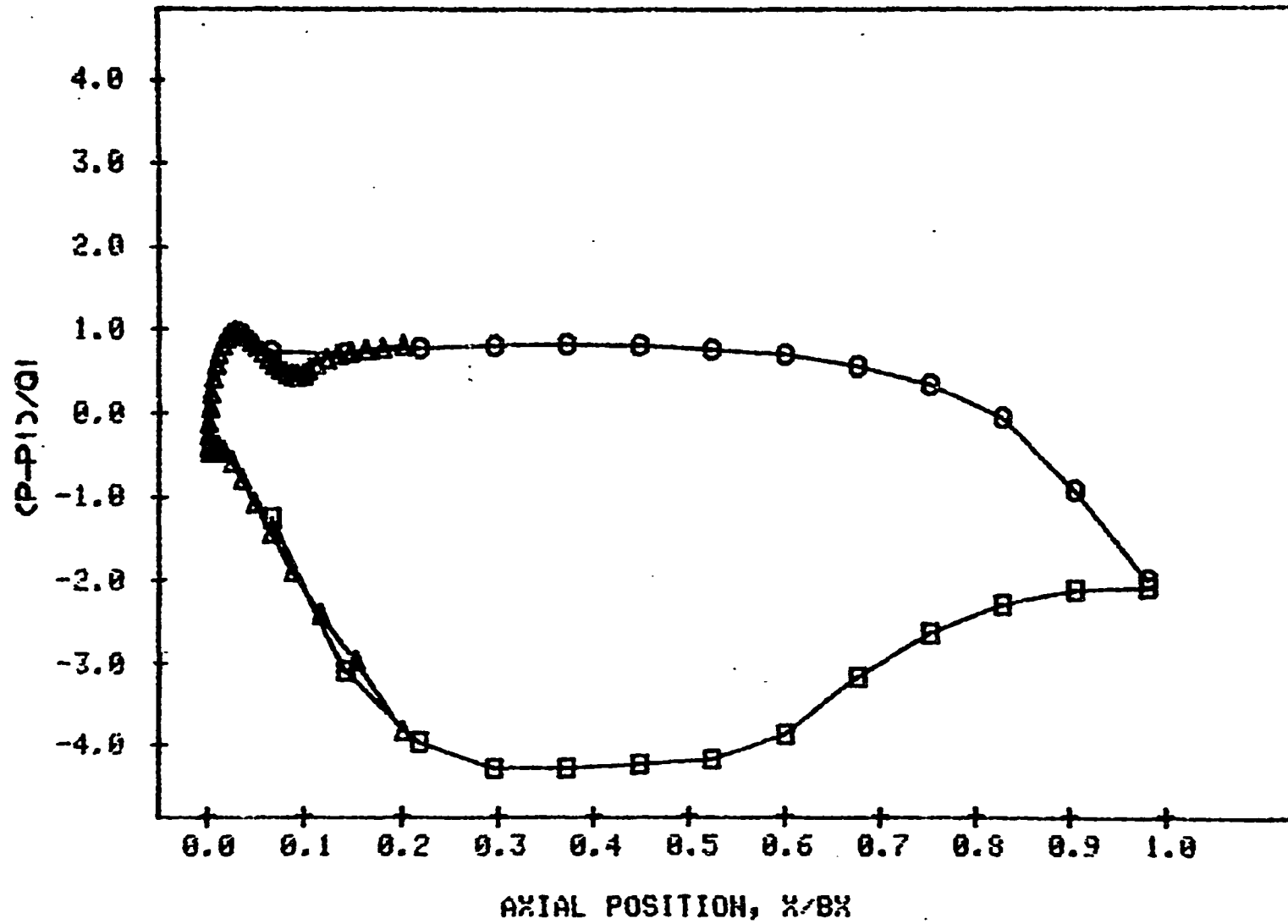


FIGURE 17. Predicted pressure distribution at design incidence

boundary layer, at all values of inlet turbulence level. However, the Crimi and Reeves model predicted transition closer to the leading edge than did the Abu-Ghanaam and Shaw model. On the pressure surface, the Crimi and Reeves model predicted laminar separation followed by a turbulent reattachment for turbulence levels up to 5%; above that value, natural transition followed by a fully turbulent boundary layer occurred. Turbulent separation was also predicted at the 4% and 7% turbulence levels. On the other hand, the Abu-Ghanaam and Shaw model predicted laminar separation, followed by turbulent reattachment, for all turbulence levels, with turbulent separation predicted for turbulence levels over 4%. These results show that, for both transition models, the location of transition and the transition length changed considerably with turbulence level. However, at the same time, predicted losses did not change appreciably. For the Crimi and Reeves model, losses remained nearly constant as turbulence level increased from 1% to 6%. For the Abu-Ghanaam and Shaw model, losses increased as turbulence level increased from 1% to 4%, then decreased until a turbulence level of 6% was reached, beyond which losses increased again. In those cases where turbulent separation was predicted, the analysis assumed a constant momentum thickness Reynolds number equal to that at the point of separation in calculating the loss coefficient. With such an assumption, the loss coefficient can only be approximate.

In reviewing the results in Table 1, it is seen that on the suction surface, the Crimi and Reeves model which is based mostly on

TABLE 1. Predicted results of integral boundary layer analysis for the test cascade at design incidence of -7° and axial chord Reynolds number of 830,000

NT - Natural transition, FT - Fully turbulent, LS - Laminar separation, TR - Turbulent reattachment, TS - Turbulent separation denoted as a percentage of suction or pressure surface length from the stagnation point; C_{PT2} is the mixed-out loss coefficient

Tu	Suction Surface		Pressure Surface					C_{PT2}
	%	NT	FT	NT	FT	LS	TR	
<u>Crimi and Reeves model</u>								
1	23.1	35.8	-	-	5.7	12.8	-	0.019
2	23.1	35.8	-	-	5.7	10.0	-	0.019
3	7.5	13.5	-	-	5.7	8.5	-	0.021
4	6.5	11.9	-	-	5.7	7.6	18.3	0.020
5	5.6	10.2	-	-	5.7	7.1	-	0.020
6	5.1	9.4	5.7	13.5	-	-	-	0.020
7	4.6	8.6	5.2	12.1	-	-	47.3	0.022
<u>Abu-Ghanaam and Shaw model</u>								
1	46.0	97.2	-	-	5.7	12.6	-	0.015
2	29.5	78.8	-	-	5.7	9.8	-	0.018
3	27.1	60.9	-	-	5.7	8.4	-	0.019
4	20.2	47.8	-	-	5.7	7.4	7.4	0.024
5	14.4	36.6	-	-	5.7	6.8	17.8	0.020
6	12.9	33.1	-	-	5.7	6.5	15.8	0.019
7	11.9	31.7	-	-	5.7	6.3	46.8	0.025

theoretical reasoning, predicted transition closer to the stagnation point than did the Abu-Ghanaam and Shaw model. The Abu-Ghanaam and Shaw model, which is based on a large number of experimental results and hence may be expected to be more representative of actual experimental conditions, predicted transition to occur almost twice as

far downstream. However, it was noted in using the Abu-Ghanaam and Shaw model that, at certain turbulence levels, the predicted results were extrapolations of the model; i.e., no experimental data were available in the range of pressure gradients present on the airfoil surface. It is also important to note that most of the experimental data used in the development of the transition models were for a uniform pressure gradient, whereas for the cascade airfoil the pressure gradient was continuously changing. Another factor not considered in the transition models was the curvature effect. More discussion on the transition models follows after the discussion of the experimental results.

Table 2 shows the predicted results from the integral boundary layer analysis for the test cascade as a function of the incidence angle. For all the cases, the transition model used was the Crimi and Reeves model. As observed in Table 2, at incidence angles of $+8^\circ$ and $+3^\circ$, laminar separation followed by turbulent reattachment was predicted on both the suction and pressure surfaces. For incidence angles of -2° and -7° (design incidence), natural transition followed by a fully turbulent boundary layer was predicted on the suction surface, whereas on the pressure surface, laminar separation followed by turbulent reattachment was predicted. For incidence angles of -12° and -17° , natural transition followed by a fully turbulent boundary layer was predicted on the suction surface; on the pressure surface, laminar separation, turbulent reattachment, and turbulent separation

were predicted. The predicted loss coefficient was a minimum near the design incidence angle of -7° . However, losses increased rapidly as the incidence angle decreased below -12° because of turbulent separation on the pressure surface.

TABLE 2. Predicted results of integral boundary layer analysis for the test cascade at design inlet turbulence level of 1.0% and inlet Mach number of 0.1

NT - Natural transition, FT - Fully turbulent, LS - Laminar separation, TR - Turbulent reattachment, TS - Turbulent separation denoted as a percentage of suction or pressure surface length from the stagnation point; C_{PT2} is the mixed-out loss coefficient

Incid deg	Suction Surface				Pressure Surface			C_{PT2}
	NT	FT	LS	TR	LS	TR	TS	
8	-	-	6.7	8.5	7.1	20.5	-	0.031
3	-	-	6.1	8.1	4.2	19.2	-	0.027
-2	22.3	34.8	-	-	4.7	14.3	-	0.020
-7	23.1	35.8	-	-	5.7	12.8	-	0.019
-12	23.9	36.9	-	-	6.2	12.2	19.5	0.017
-17	24.3	37.1	-	-	7.2	11.9	19.4	0.066

As an alternative to the dissipation integral method used in the design analysis program, the STAN5 boundary layer code based on finite-difference computation and incorporating improvements by Gaugler [34] was used to perform the profile boundary layer analysis for the cascade. In this analysis, the momentum equation for the boundary layer plus any number of diffusion equations may be solved for either

laminar or turbulent boundary layers. The program may also be started as a laminar boundary layer calculation and shifted to a turbulent boundary layer through appropriate transition models. In turbulent boundary layer calculations, the eddy viscosity concept is used to model the turbulent stresses with turbulent viscosity calculated using either Prandtl's mixing length scheme, or a one-differential-equation kinetic energy scheme. In transitional boundary layer calculations, the turbulent viscosity is modified using the Abu-Ghanaam and Shaw [22] intermittency factor. In the present analysis, constant fluid properties were assumed and the turbulence kinetic energy scheme was used. Also, the start of transition was located using the Abu-Ghanaam and Shaw transition model [22], and the end using Dhawan and Narasimha model [16]. Stewart's wake mixing analysis [33] was again used to calculate the mixed-out losses.

Table 3 summarizes the results of the boundary layer analysis using the STAN5 code for design incidence and design Reynolds number. As noted in Table 3, on the suction surface, with an increase in turbulence level, the start of transition point moved further upstream and the transition length was reduced. Also, for a given change in turbulence level, the change in the start of transition point location (or the transition length) was smaller at higher turbulence levels than at lower turbulence levels. On the pressure surface, the flow was assumed to be fully turbulent from the laminar separation point obtained from the integral analysis. Without this assumption, negative

velocities were calculated in the separated region and the program was unable to calculate further. This occurred because the STAN5 analysis did not model laminar separation and turbulent reattachment.

Table 3 shows that, for turbulence levels of 2% and above, the predicted losses increased with turbulence level and tended to a constant value at high turbulence. Such a trend was not observed in the results from the dissipation integral analysis in Table 1. Also, the loss levels predicted by the STAN5 analysis are, in general, higher than those predicted by the dissipation integral analysis.

TABLE 3. Predicted results of STAN5 boundary layer analysis for the test cascade at design incidence of -7° and axial chord Reynolds number of 830,000

NT - Natural transition, FT - Fully turbulent, denoted as a percentage of suction or pressure surface length from the stagnation point; C_{PT2} is the mixed-out loss coefficient

Tu	Suction Surface		Pressure Surface ^a		C_{PT2}
	NT	FT	NT	FT	
1	51.0	98.2	5.7	5.7	0.029
2	42.8	80.7	5.7	5.7	0.026
3	35.4	65.4	5.7	5.7	0.029
4	29.5	52.8	5.7	5.7	0.032
5	23.6	40.3	5.7	5.7	0.035
6	21.2	35.4	5.7	5.7	0.036
7	20.1	33.4	5.7	5.7	0.036

^aTurbulent calculations were started at the laminar separation point obtained from the integral analysis.

In order to evaluate and compare the dissipation integral and the STAN5 methods, the development of a boundary layer on a flat plate was also studied using the two methods for three different cases: a zero pressure gradient, a favorable pressure gradient, and an adverse pressure gradient. In general, the results showed rate of growth in momentum thickness to be higher in the STAN5 analysis than in the integral analysis. This was particularly true in the adverse pressure gradient case. Further details of the three cases examined are included in Appendix A. Since severe adverse pressure gradient regions occur on the suction surface of the cascade airfoil, the smaller growth rate of momentum thickness in the integral analysis might explain the consistently low and slowly varying losses predicted by the integral method.

IV. CASCADE TEST FACILITY

A. Test Cascade Pack

The test cascade pack, pictured in Figure 18 consisted of five airfoils with Plexiglas upper and lower endwalls. Each airfoil was built up from three or four mahogany sections, with each section having been machined individually in an N.C. milling machine. Accuracy of the machined profile was confirmed visually by overlaying the produced sections on an accurate plot of the profile. Each airfoil assembled from the individual sections had a span of 10 in., which resulted in an aspect ratio of 1.25 based on the axial chord of 8.0 in. Details on producing the N.C. control tapes and machining of the airfoil can be found in Vijayaraghavan and Kroneman [35].

Rows of static pressure taps were drilled in the central airfoil of the test pack to be used for static pressure distribution measurements. One row at midspan of the airfoil consisted of 30 pressure taps, and two more rows at sections 20% of span from either endwall had 24 taps each. The rows of taps can be seen in the views of the central airfoil in Figure 19. Either airfoil adjacent to the central airfoil also contained taps around the leading and trailing edges for use in setting flow periodicity in the cascade. Leads for all the pressure taps passed through inner passages in the airfoil and up through the upper endwall. In all 111 pressure taps were used. Figure 20 shows the hypodermic tubing for the taps, connecting tubing,

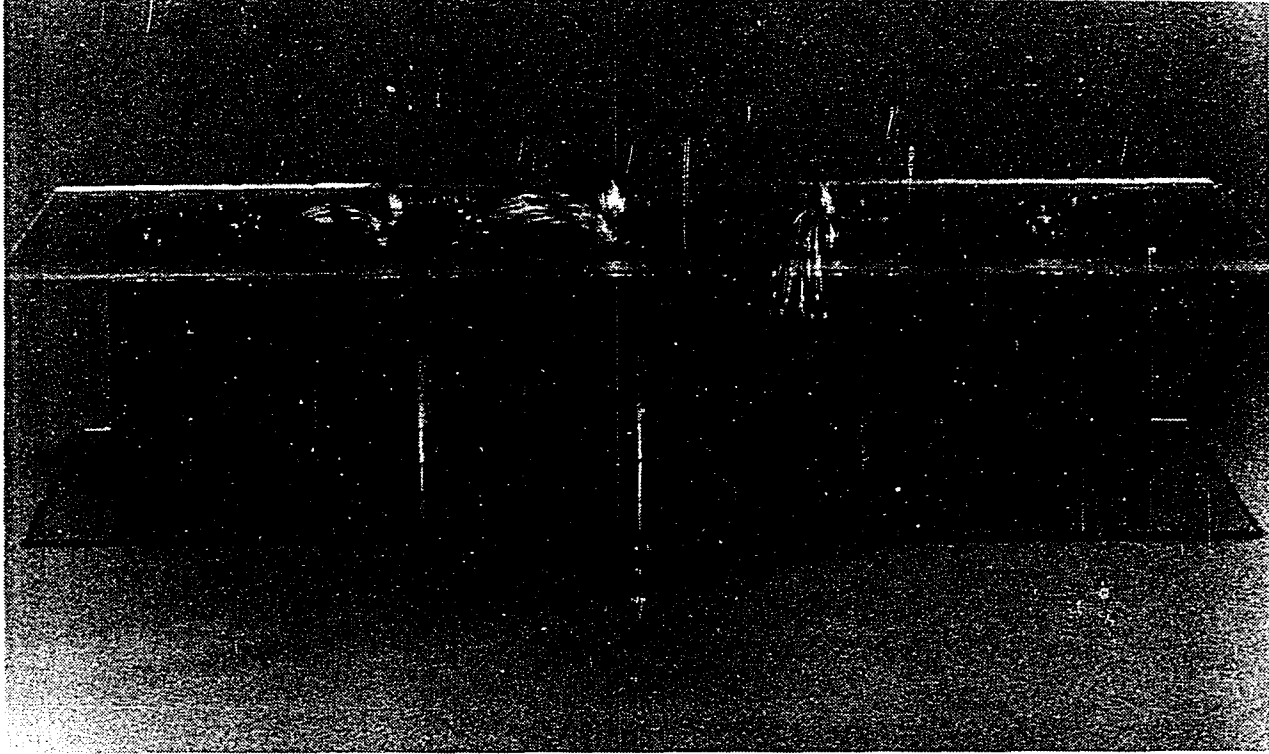


FIGURE 18. Test cascade pack

and the internal passages of the airfoil prior to the assembly. The entire cascade pack was assembled from the individual airfoils and Plexiglas endwalls using a template to set the design pitch and stagger angle.

B. Test Section

The test section consisted of a horizontal base table which formed the lower endwall, a removable upper endwall, and flexible sidewalls with tailboards attached. The assembled cascade pack was clamped and bolted down in position in the test section at the required inlet angle. Flow periodicity was achieved by adjusting the sidewalls and tailboards to control the bleed-flow at either side of the cascade. A manometer bank connected to the leading and trailing edge pressure taps was used to examine the pressure distribution while this adjustment was done.

Airflow to the cascade and test section was supplied by the laboratory low-speed flow loop which consisted of a large centrifugal blower having a design flow rate of 20,000 cfm at 40 in. water head rise, a variable-speed drive and electric motor (200 hp), and a suspended piping system made up of 30 in. diameter pipe. The flow was introduced to the test section from one of the down-runners of the flow loop through a round-to-square transition section, a plenum box and a 3.3:1 2-D contraction section. The plenum box contained honeycomb, screens, perforated plates for flow straightening, and turbulence

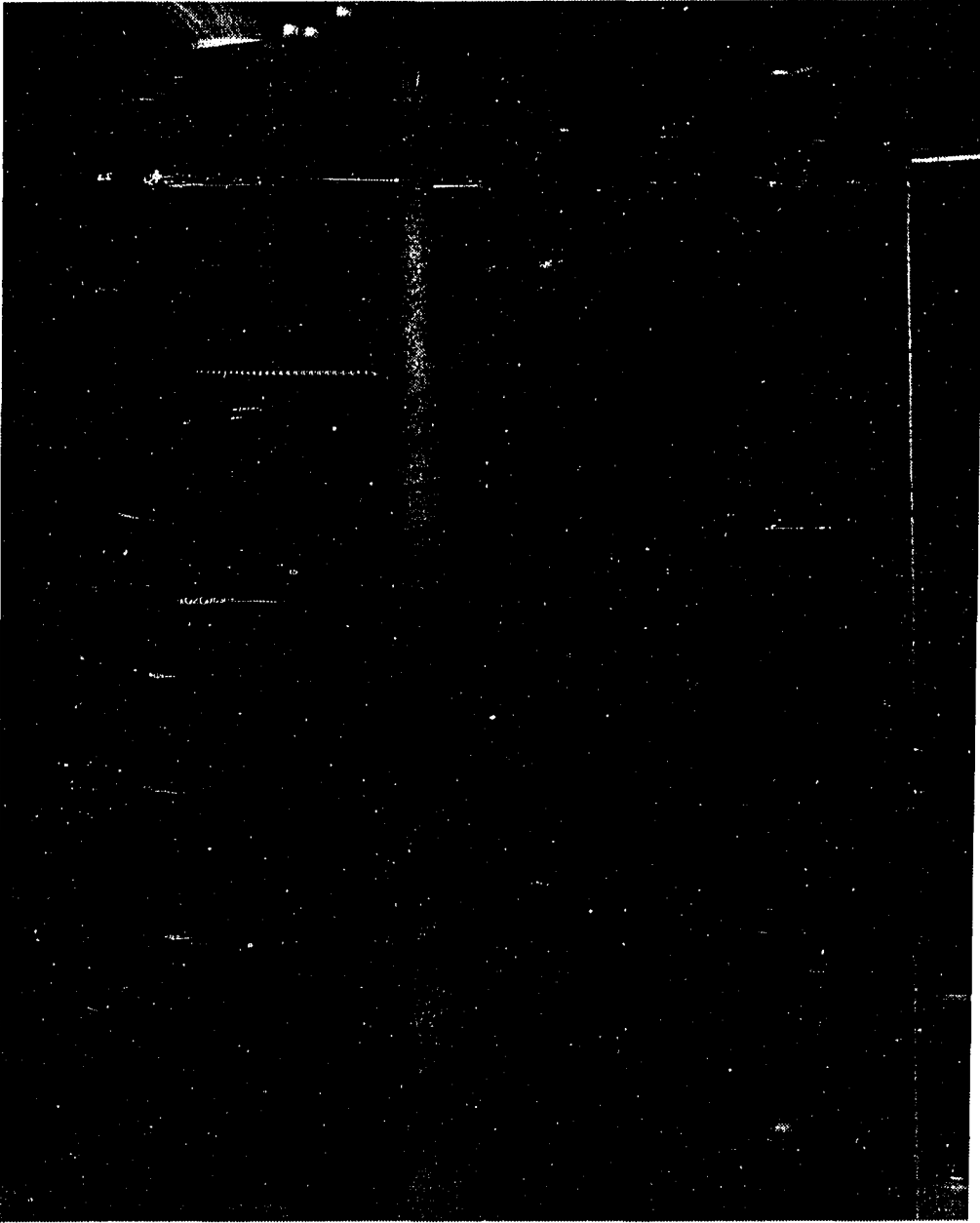


FIGURE 19. Central airfoil of test cascade pack with static pressure taps

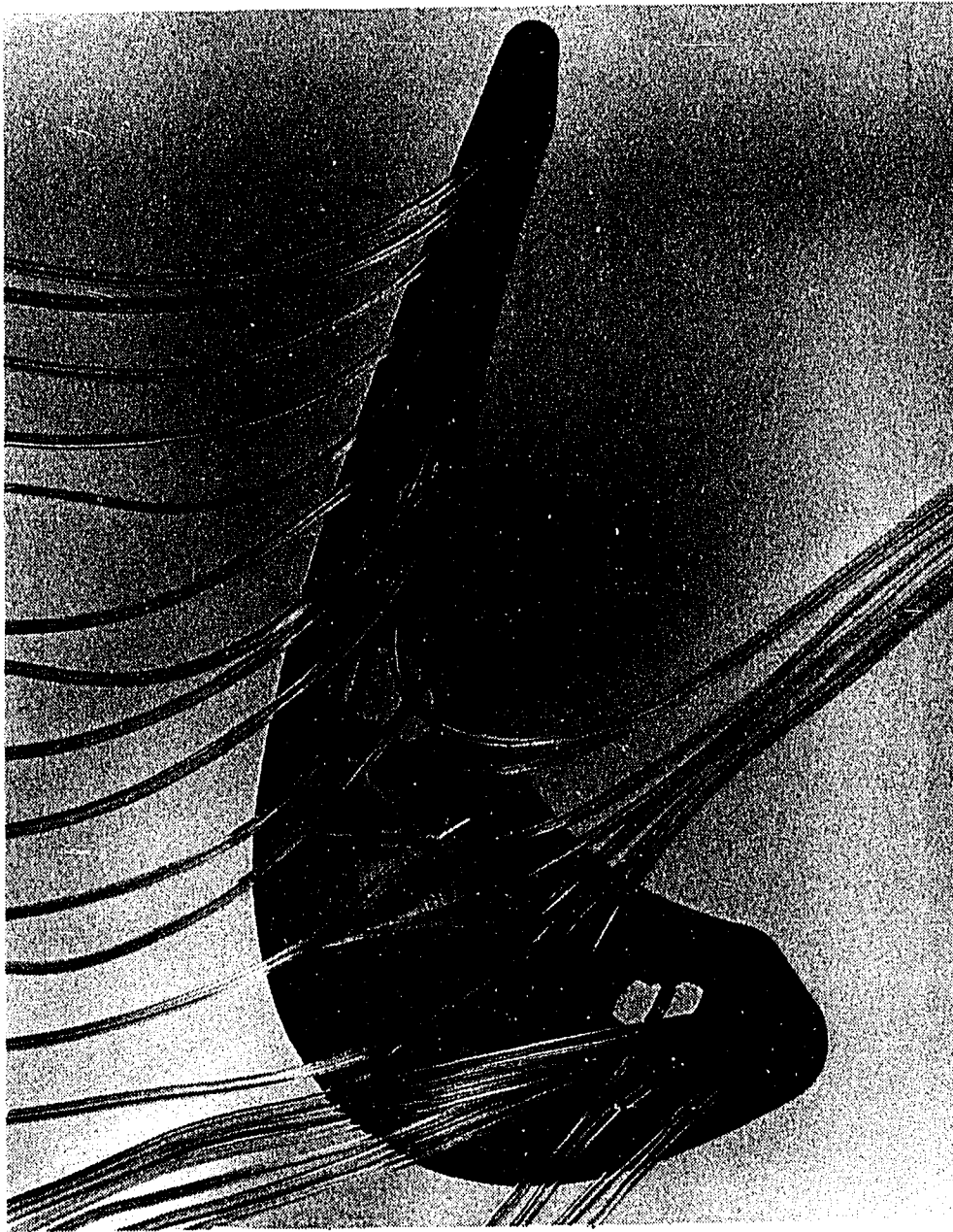


FIGURE 20. Test cascade airfoil internal passages and pressure tap tubing

generating grids. The plenum box had removable side walls to facilitate changing of the turbulence grids to obtain different turbulence levels in the test section. Figure 21 shows a view of the plenum box with its side wall removed, displaying the turbulence grid, screen, and the honeycomb insert frames. This type of plenum design has also been used successfully by Blair and Werle [36] for their boundary layer tunnel. Design information from Mehta and Bradshaw [37] was referred to in building the plenum box. The entire test section including the sidewalls, endwalls, and contraction section were made of Plexiglas to facilitate flow visualization.

A special linkage arrangement was used for supporting the probe positioning system. This arrangement, shown in Figure 22, consisted of two slotted aluminum brackets bolted down to a Unistrut frame over the upper endwall of the test section. The brackets could be adjusted to comply with the inlet angle setting of the cascade pack so that the probe could be translated parallel to the cascade inlet or exit plane. The probe positioning system consisted of the five-hole or hot-wire probes mounted on a linear actuator (L.C. Smith model BBR 18-180) which in turn was mounted on a third-motion positioner (L.C. Smith model L3M12). The linear actuator was used for yawing the probe and traversing it in a spanwise direction, while the third-motion positioner was used for traversing the probe in the pitchwise direction. With this linkage arrangement, pitchwise and spanwise traverses could be made in the cascade exit plane at any arbitrary distance downstream of the cascade.

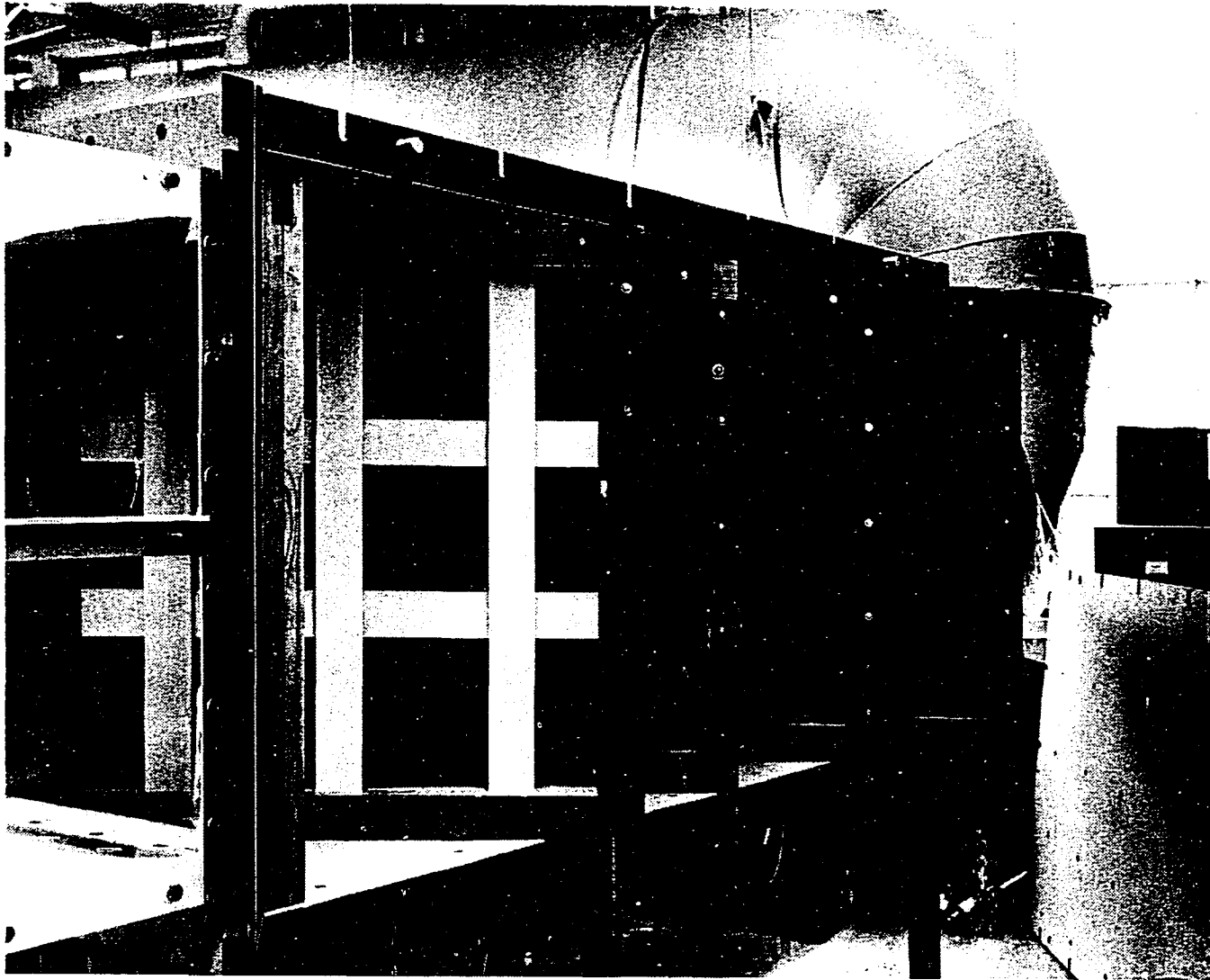


FIGURE 21. Plenum tank and frame inserts

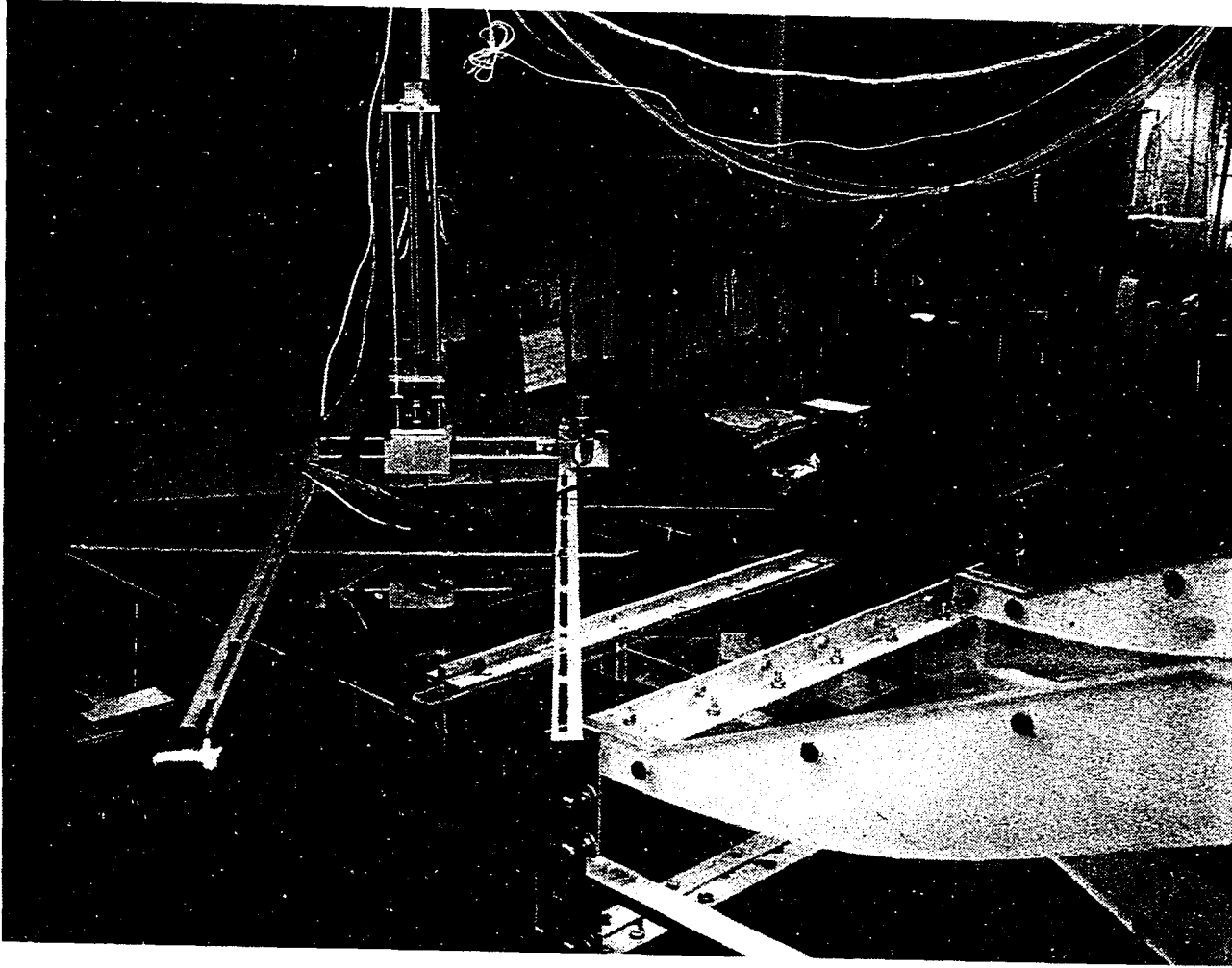


FIGURE 22. Probe positioners and adjustable linkage arrangement

C. Endwall Suction System

To provide a 2-D flow over the airfoil span, endwall suction was employed for three central blade passages of the cascade. At both the upper and lower endwalls, 1/4 in. slots were cut in the suction surface-endwall corner of each passage, starting at a point about 25% along the surface and extending to the trailing edge. In addition, endwall slots were cut in the middle of the passage starting at about 50% axial chord from the leading edge plane and extending to the trailing edge plane. These slots were connected to a suction box and blower through a manifold attached to the upper and lower endwalls of the cascade (see Figure 23). With the outlet of the blower throttled to control the suction flow rate for different inlet velocities, the blower created sufficient vacuum to suck most of the endwall boundary layer and passage vortex from the blade passages. Small woolen tufts glued along the airfoil span were observed to determine if the right suction flow rate was being provided. At the right flow rate, these tufts were horizontal and parallel, neither pointing towards midspan (insufficient suction) nor towards the endwall (over suction). Typically, suction flow rates between 10% and 15% of the main flow rate were required to achieve a satisfactory 2-D flow. Axial velocity ratios across the cascade in the range of 0.93 to 0.97 were maintained at these flow conditions.

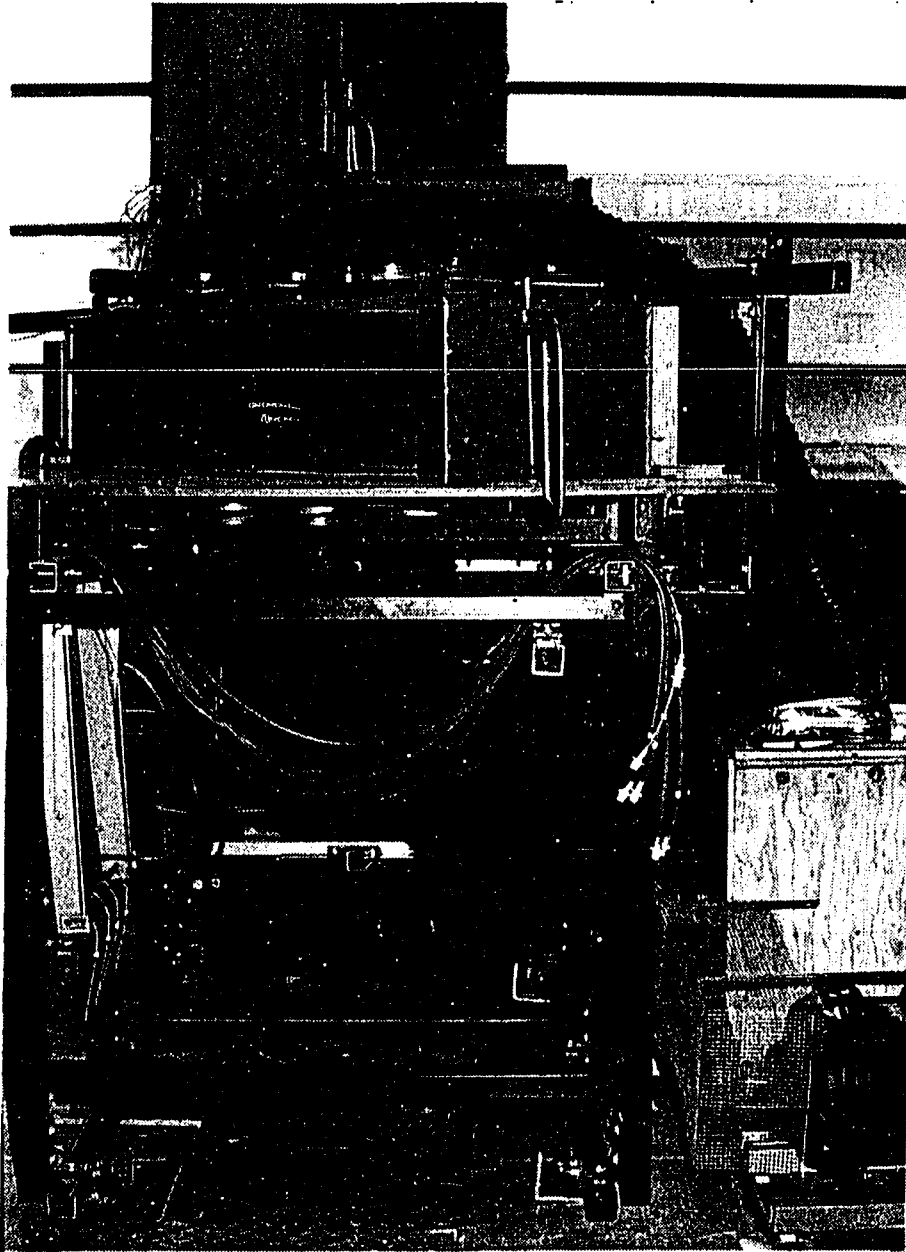


FIGURE 23. Endwall suction system and auxiliary blower

D. Data Acquisition System

The laboratory data acquisition and experiment control system was used to control the cascade testing and to record and reduce the experimental data. Figure 24 shows a schematic layout of the data acquisition system. A 32K Commodore PET microcomputer controlled the various components of the system and collected and reduced the data. Connected to the PET through an IEEE 488 interface were a Hewlett-Packard 3455A digital voltmeter and a Hewlett-Packard 3495A voltage scanner. The pressure measuring system consisted of a Scanivalve 48D3-1023 pressure scanner driven by a Scanivalve solenoid controller CTRL2/S2-S6, a Druck 1.0 psid PDCR pressure transducer, an Endevco model 4476.2 bridge conditioner mounted in an Endevco 4470 universal conditioning module (for signal amplification), and a pressure reference system providing four reference water column pressures with a high degree of accuracy for online calibration of the transducer. Three inclined manometers (Meriam Instrument model 40HE35) were also used to check periodically the pressure measurements made by the transducer. Power to the linear and angular drives of the two probe positioners was supplied from an L.C. Smith model D1-3R position indicator. Through appropriate programming of the PET, the proper channel of the voltage scanner was selected to perform any pressure measurement, probe positioning, or data collection. Collected data were stored on a CBM 4040 dual disk drive and printed out on a Digital Corporation Decwriter II. Also through the use of an RS 232 serial

adaptor, the PET could be operated as a remote terminal for the university mainframe computer for complete data acquisition and computing capabilities. Further details on this data acquisition system can be found in Hottman [38].

Figure 25 shows separately a schematic of the instrumentation set-up used to collect and process the hot-wire/hot-film signals. This sub-system consisted of a TSI 1050 anemometer system including signal conditioner (1057) and linearizer (1052) connected to the voltage scanner. Also connected to the anemometer was a Norland 3001A dual channel processing digital oscilloscope, connected in turn to a Digital Equipment Corporation PRO 380 microcomputer through IEEE 488 interface and to a Hewlett-Packard 7035-B x-y recorder.

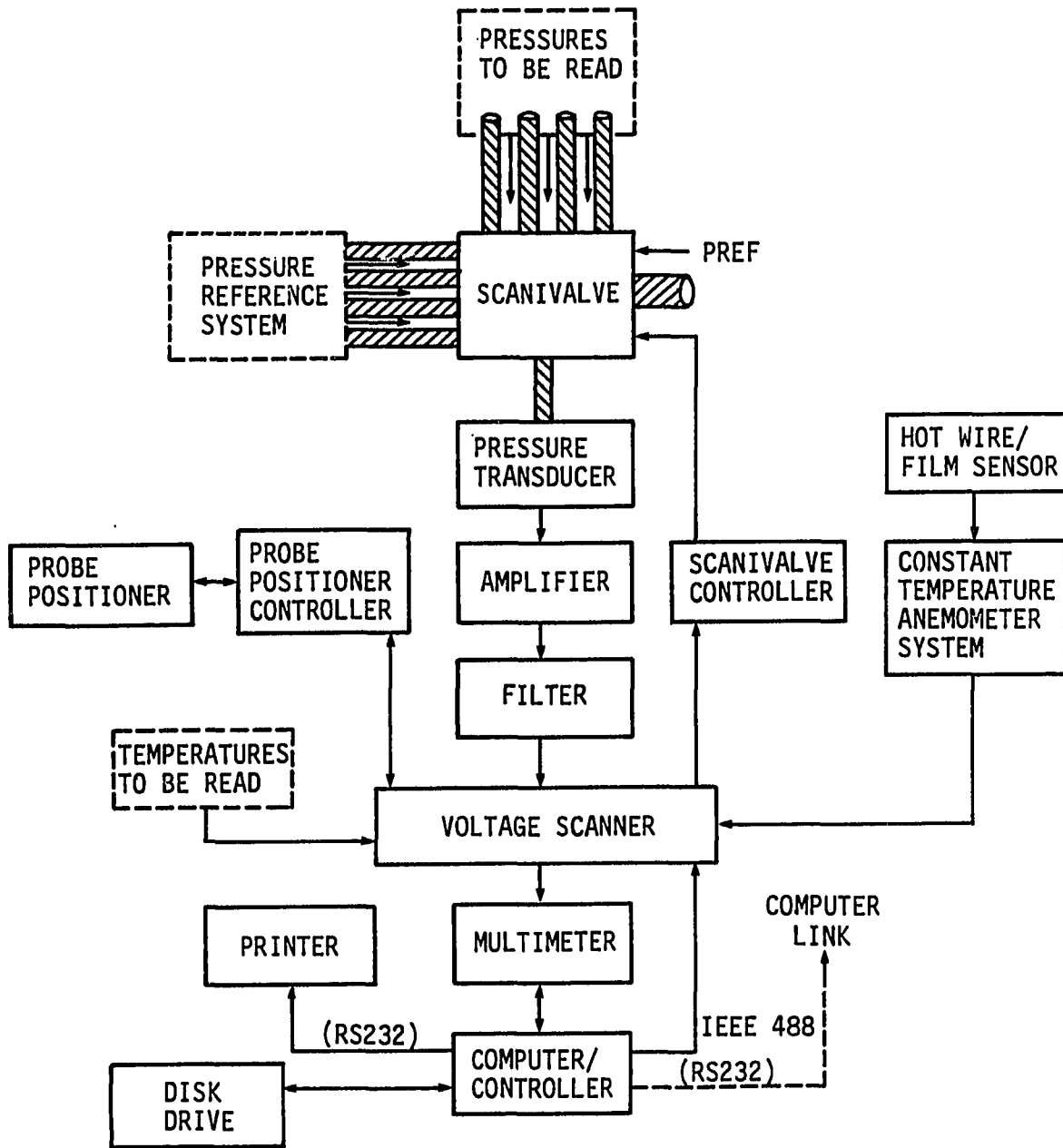


FIGURE 24. Schematic of data acquisition and experiment control system

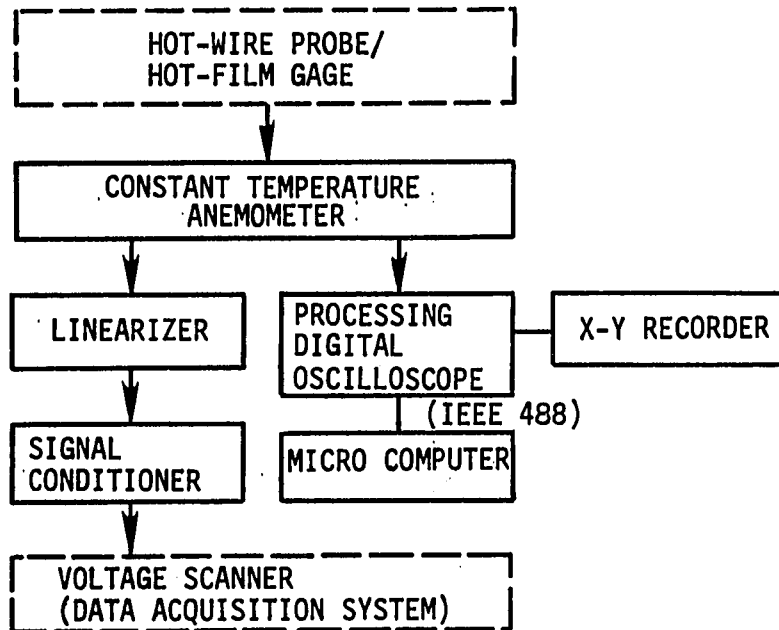


FIGURE 25. Schematic of hot-wire anemometer system

V. EXPERIMENTAL TEST PROGRAM

The experimental test program consisted of determining the cascade performance and studying the profile boundary layer development on the suction surface of the airfoil. In all, the cascade was tested at three incidence angles, four turbulence levels, and three Reynolds numbers, resulting in a total of thirty-six test flow conditions. This chapter describes the test conditions and procedures used. Details of data acquisition and data reduction programs and the calibrations involved in using the probes and gages are discussed. Also included are details on the flow visualization technique used to obtain the flow patterns on the airfoil surface and endwalls. Finally, an uncertainty analysis on the measurements made is presented.

A. Test Conditions

The cascade was tested at the design inlet angle $\beta_1 = 45^\circ$ (-7° incidence) and at inlet angles of $\beta_1 = 52^\circ$ (-14° incidence) and $\beta_1 = 38^\circ$ (0° incidence). Different test turbulence levels were obtained by inserting the turbulence generator grids in the plenum box. The lowest level, 0.8%, was obtained when a fine wire mesh was inserted instead of a turbulence grid. The higher turbulence levels of 2.0%, 4.8%, and 6.4% were obtained with the three grids, the coarsest grid producing the highest turbulence level.

The test Reynolds number was varied by changing the speed of the blower supplying air to the test section. The three test Reynolds

numbers were 700,000, 540,000, and 330,000, based on the exit velocity and axial chord. Since each test Reynolds number was obtained by maintaining the blower speed control at a constant setting, a slight drop in the flow Reynolds number during a typical test-run extending over 10 hours was observed due the heating of the motor. However, the drop in Reynolds number was less than 5% and at lower test Reynolds numbers, the drop was still smaller.

B. Inlet Flow Measurements

Preliminary flow measurements were made with a five-hole pressure probe (United Sensor model #DC125) across the test section entrance to confirm that the supplied inlet flow to the cascade was straight and uniform. It was observed that the variation in inlet flow angle was less than $\pm 0.5^\circ$ in both yaw and pitch, and the variation in flow velocity was less than 1%. With the turbulence grids installed, single hot-wire traverses (using TSI model 1210-20 sensors) were also made across the entrance to confirm that the generated turbulence was homogeneous. The variation in the inlet turbulence level was found to be within the uncertainty of measurement at a given point.

In addition, hot-wire measurements were made along the flow direction in the test section to measure turbulence decay rates. The measured rates were found to agree well with the concept of an apparent origin of turbulence (to account for contraction) as proposed by Blair and Werle [36]. Figure 26 shows the measured streamwise turbulence

intensity in the test section for the three turbulence grids, along with the results of Blair and Werle [36] which are based on the streamwise and the two transverse components. Since the streamwise component of the turbulence intensity is smaller than either transverse component after a 2-D contraction (Oberoi [39]), the measured intensity values, as may be expected, are lower than those of Blair and Werle.

C. Test Measurements

To determine the total pressure, velocity, flow angles, and turbulence intensity, probe traverses were conducted in an exit plane of the cascade using a five-hole pressure probe and a hot-wire probe. The probes were mounted in pitch and spanwise positioners which in turn were supported by the adjustable linkage arrangement described earlier. Inlet total pressure and velocity required to determine the loss coefficient were measured by a pitot static tube located upstream of the cascade. Finally the state of the profile boundary layer on the airfoil suction surface was determined from the glue-on hot-film gages.

1. Five-hole probe and static pressure measurements

The laboratory data acquisition system described in Chapter 3 was used to perform five-hole probe and static pressure measurements. The system was controlled by the data acquisition program MASTER, written in BASIC language for the controller, the Commodore PET microcomputer. The program positioned the five-hole probe at required locations in a traverse plane downstream of the cascade, yaw-nulled the probe and

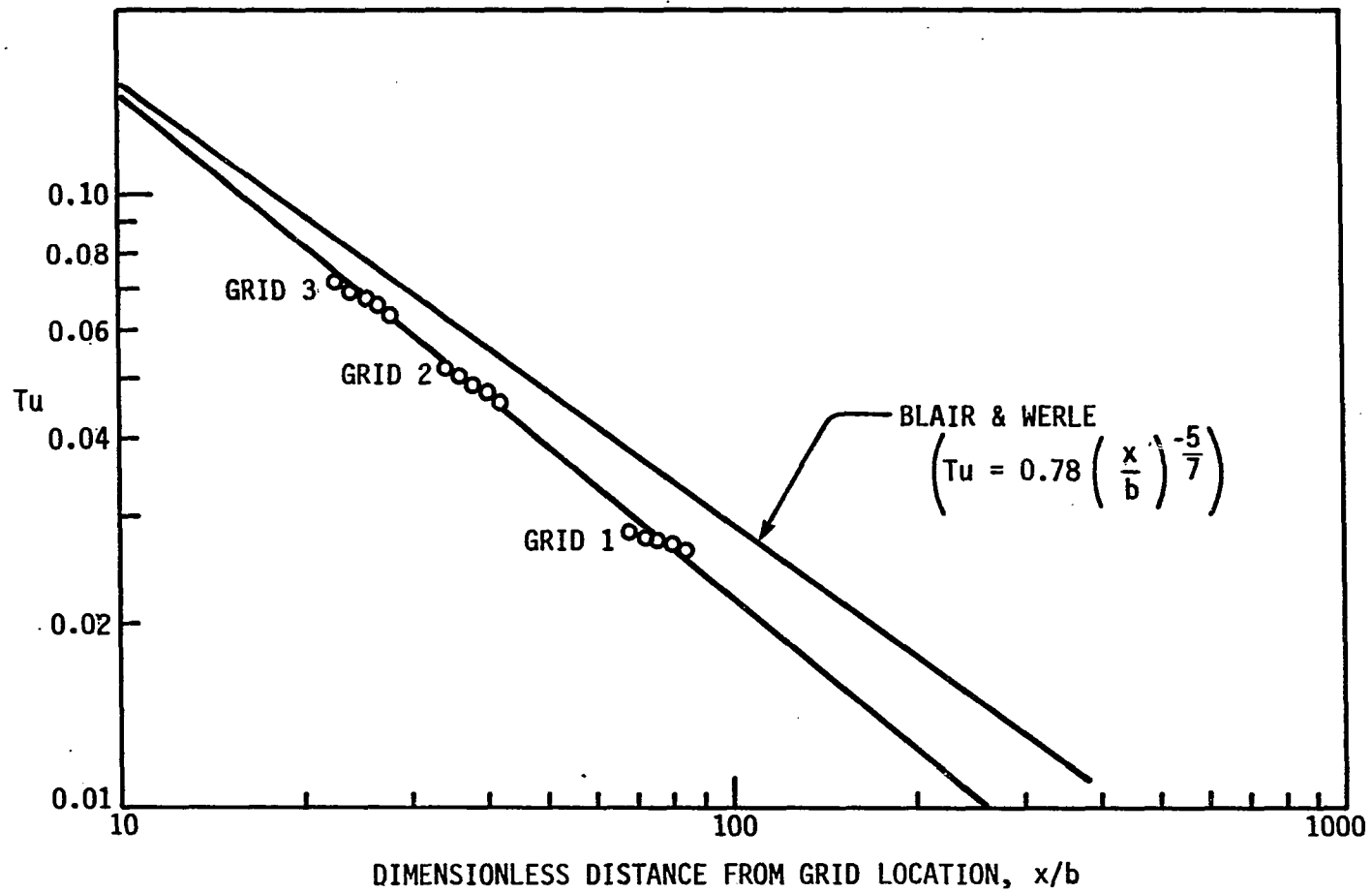


FIGURE 26. Turbulence decay measurements obtained for three turbulence generator grids

recorded the five-hole and upstream pitot-static probe pressures, plenum pressure and temperature. From these data, the program calculated exit flow velocity, angles and total pressure based on the five-hole probe calibration, and calculated total pressure loss coefficients. In a separate part of the program, static pressures obtained from the static taps on the airfoil were recorded and reduced to coefficient form.

Figure 27 shows the angle and direction conventions used in the five-hole probe traverses. Exit flow angle β_2 is measured from the cascade trailing edge plane (y-z plane), while the pitch angle ϕ_2 is measured in the plane of velocity V_2 and velocity component V_{z2} , as shown. The y-direction corresponds to the pitchwise direction and the z-direction to the spanwise direction.

The general arrangement of the program MASTER and its specific functions are shown in the flow diagram in Figure 28. The numbers shown in the boxes and beside the branch points in the diagram refer to line numbers in the program listing (for a complete listing and description of the program see Vijayaraghavan and Kavanagh [40]). The program is made up of three major parts, indicated by the three major branches in the diagram. The functions or requirements of these three branches are discussed below.

a. Initial data and calibration constants To operate the system, the program requires the following initial data and calibration constants.

- Barometric pressure

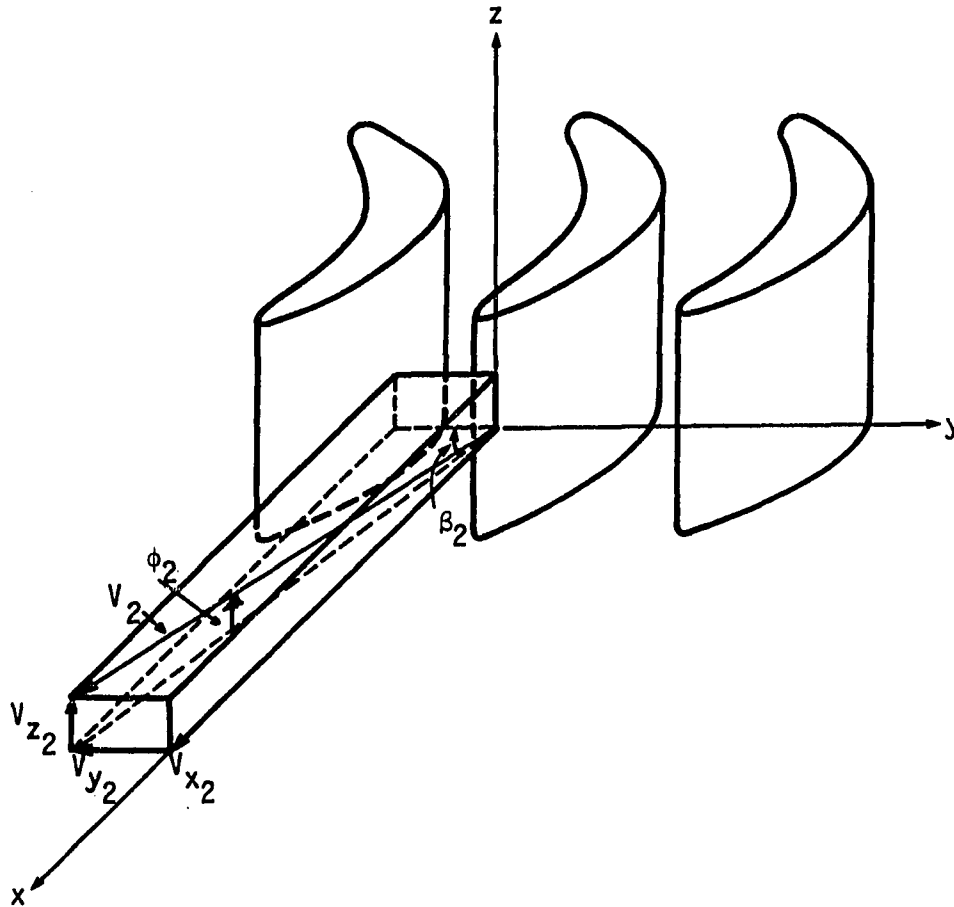


FIGURE 27. Five-hole probe angle and traverse direction conventions

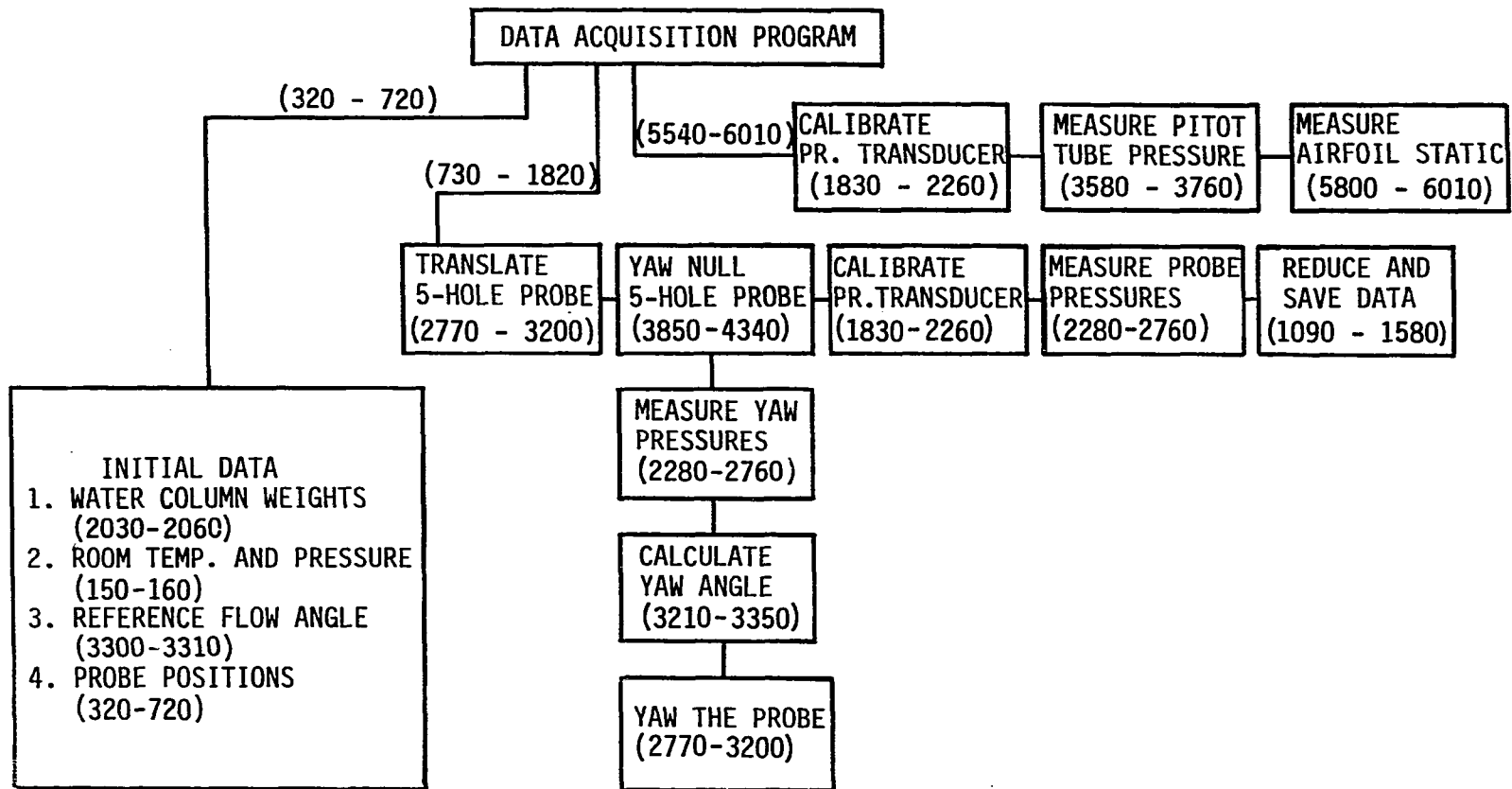


FIGURE 28. Flow diagram of data acquisition program MASTER

- **Pressure reference system calibration constants**

The pressure reference system used for on-line calibration of the pressure transducer consists of four water columns to provide four reference pressures. These water columns are calibrated against a micro-manometer to relate their weight to the pressure represented. The pressure transducer is calibrated against these reference pressures each time a pressure measurement is to be made. For more details on the pressure reference system refer to Morgan [41].

- **Probe positioner calibration constants**

All probe positions for pitchwise, spanwise and yaw actuators are calculated using voltages read from their potentiometers. Hence these actuators are calibrated in volts/inch (pitchwise and spanwise) or volts/degree (yaw).

- **Five-hole probe calibration data**

The five-hole probe is calibrated in a separate calibration flow to relate the measured probe pressures to the pitch angle, local dynamic pressure, local total pressure, and to correct measured yaw angle for pitch. More details on the five-hole probe calibration can be found in Smith [42].

- **Reference flow angle**

This is the undisturbed fluid angle for the five-hole probe in the absence of the cascade pack in the test section.

- **Probe positions in the traverse plane**

The number of probe positions and the intervals between probe positions in the pitchwise and spanwise directions in the traverse plane must be supplied to the program.

b. Data taking and data reduction The probe is initially positioned by the operator at the first data taking point. From pitchwise and spanwise positioner voltages at this initial point and the input number of probe positions, the program calculates the positioner voltages for all the required positions. After moving the probe to each position, the program yaw-nulls the five-hole probe. From the pressure measurements and probe calibration data, the program calculates the total pressure, velocity and flow pitch angle. The flow yaw angle is determined from the yaw reference angle and the yaw positioner voltage. Upstream total and static pressure are measured with the reference pitot static tube, and plenum pressure and temperature are also recorded. Figure 29 is a sample printout showing at each data taking point the plenum pressure (P0), inlet total pressure (PT), exit total pressure (P1), along with the reduced data consisting of exit dynamic pressure (q2), exit velocity (U2), yaw (BETA2) and pitch (PITCH) angles, inlet velocity (U1) and total pressure loss coefficient (CPT). At the end of each pitchwise traverse, the data for that traverse are saved on disk. After the traverse cycle is completed for the pitchwise and spanwise directions, the probe is brought back to the starting point.

Y IN	Z IN	U2 FPS	BETA2 DEG	PITCH DEG	U1 FPS	CPT	F0-ATH IN H2O	D2 IN H2O	F1-ATH IN H2O	F0-F1 IN H2O
AT= 80.4228334										
0	0	62.351	24.683	.891	46.784	-7E-03	.944	.97	.99	-.049
.5	0	62.678	24.687	.915	46.569	4E-03	.939	.979	.991	-.05
1	0	67.755	25.16	.932	46.623	3E-03	.944	.981	.991	-.045
1.5	0	68.021	25.168	.796	46.651	.029	.946	.989	1.006	-.047
2	0	67.845	25.862	.898	46.481	-3E-03	.94	.984	.989	-.051
2.5	0	67.659	26.268	1.129	46.577	-6E-03	.943	.979	.987	-.047
3	0	65.763	26.889	.935	46.567	.138	.942	.924	1	6E-03
3.5	0	58.414	27.341	.582	46.507	.556	.943	.729	.995	.205
4	0	52.642	26.205	.066	46.611	.806	.943	.592	.995	.322
4.5	0	59.465	25.613	.101	46.886	.338	.952	.756	.995	.116
5	0	64.418	25.354	.537	46.733	.017	.943	.887	.999	-.048
5.5	0	64.423	24.362	.412	46.898	-1E-03	.952	.887	.998	-.047
6	0	65.253	23.601	.279	46.603	4E-03	.946	.91	1.002	-.055
6.5	0	66.297	23.085	.219	46.753	-2E-03	.95	.939	.997	-.048
7	0	67.275	23.093	.103	46.511	.015	.944	.967	1.008	-.058
7.5	0	67.843	23.342	.267	46.764	-3E-03	.917	.984	.969	-.054
8	0	68.029	23.867	.191	47.057	7E-03	.945	.989	1	-.052
8.5	0	68.281	23.869	.154	46.798	.011	.954	.997	1	-.041
9	0	68.819	24.293	.251	46.784	.013	.958	1.012	1.009	-.045
9.5	0	69.569	24.59	.289	47.302	3E-03	.974	1.035	1.02	-.045
10	0	69.357	25.035	.219	47.235	.023	.95	1.028	1.016	-.055
10.5	0	68.758	25.425	-.294	46.94	6E-03	.965	1.011	1.016	-.049
11	0	68.463	25.901	-.535	47.112	.021	.967	1.002	1.029	-.052

77

FIGURE 29. Sample printout for five-hole probe measurements

c. Airfoil static pressure measurements

Here the static

pressures are measured from pressure taps on the airfoil surface, and a static pressure coefficient is calculated. Rows of static pressure taps were available on the central airfoil at three spanwise locations: at midspan, and at 20% of span from either endwall. Since the number of ports reserved on the scanivalve for static pressure measurements was limited, pressure measurements on the airfoil could be done only one spanwise location at a time.

2. Mass-averaged and mixed-out flow calculations

From the total pressure, velocity and flow angle measurements made by the program MASTER, the mass-averaged loss coefficient, and the mixed-out exit flow velocity and angle were calculated for comparison with the predicted results. The mass-averaged total pressure loss coefficient was calculated for each pitchwise traverse and for the complete traverse plane (the upper-half of the span for one blade pitch). For one pitchwise traverse, the mass averaged total pressure loss coefficient is defined as

$$\bar{C}_{PT} = \frac{\int_0^{\tau} C_{PT} V_2 \sin \beta_2 dy}{\int_0^{\tau} V_2 \sin \beta_2 dy}$$

where C_{PT} is the local value, and V_2 , β_2 the measured velocity and flow angle. For the complete traverse we have,

$$\bar{C}_{PT} = \frac{\int_0^{(h/2)} \int_0^{\tau} C_{PT} V_2 \sin \beta_2 dy dz}{\int_0^{(h/2)} \int_0^{\tau} V_2 \sin \beta_2 dy dz}$$

The mixed-out exit velocity V_3 and angle β_3 downstream of the traverse plane were calculated at mid-span from the conservation of mass and of pitchwise momentum as follows: The conservation of mass gives the result,

$$\int_0^1 v_2 \sin \beta_2 d(y/r) = v_3 \sin \beta_3$$

and the conservation of pitchwise momentum,

$$\int_0^1 v_2^2 \sin \beta_2 \cos \beta_2 d(y/r) = v_3^2 \sin \beta_3 \cos \beta_3$$

From these results, the mixed out flow angle and exit velocity are,

$$\beta_3 = \tan^{-1} \frac{\left[\int_0^1 v_2 \sin \beta_2 d(y/r) \right]^2}{\int_0^1 v_2^2 \sin \beta_2 \cos \beta_2 d(y/r)}$$

$$v_3 = \frac{\int_0^1 v_2 \sin \beta_2 d(y/r)}{\sin \beta_3}$$

It should be noted in the above calculations, that a local value of the total pressure loss coefficient was determined at each data-taking point in the traverse plane. This was done by calculating the difference in measured total pressures upstream and downstream of the cascade and then computing the local coefficient values. The overall total pressure loss coefficient was then formed by mass averaging the local values in the traverse plane. An alternative method would be to compute a mass-averaged total pressure itself in the traverse plane, based on assumed constant upstream total and dynamic pressures. From the mass-averaged total pressure thus formed, the overall total

pressure loss coefficient could be calculated. This alternative approach is, however, entirely equivalent to the one described above using the mass-averaged local coefficient values. Different methods based on area, momentum, energy or entropy averaging may be used to obtain an averaged total pressure in the traverse plane. From this averaged total pressure, an overall total pressure loss coefficient could be calculated. The various averaging methods would yield slightly different results, the difference becoming smaller as the traverse plane is moved further downstream of the trailing edge plane. More details on the averaging techniques can be found in Schimming and Starcken [43].

3. Hot-wire measurements

The data acquisition program HFMASTER was used to make hot wire traverses for velocity and turbulence intensity measurements in the cascade exit plane. This program was similar to MASTER described earlier for five-hole probe measurements and, hence, is not discussed in detail.

The TSI anemometer system described in Chapter IV was used for the hot wire measurements. The bridge output for a constant temperature anemometer, E , is related to the flow velocity, V , as follows [10]:

$$\frac{E^2/R_s}{R_s - R_e} = A + B/V$$

Here A and B are constants, and R_s and R_e are the wire resistance at the probe operating and fluid temperatures, respectively. A fourth-order polynomial was used to linearize the relationship between E and V. The hot-wire probe (TSI model 1210-20W) was first calibrated against a pitot static tube in a calibration flow to determine the polynomial coefficients for the linearizer (see [44] for details). With the coefficients set, and the span and zero-suppress adjusted in the linearizer to correspond to the maximum and zero velocity, the output voltage of the linearizer was proportional to the measured flow velocity. To account for temperature differences between the calibration and test flows, the linearizer output was multiplied by a factor $[(T_s - T_c)/(T_s - T_e)]^2$, where T_c was the calibration temperature, T_e the test flow temperature, and T_s the probe operating temperature.

The anemometer output voltage, being a function of the angle between the flow direction and the probe orientation, was a maximum when the hot-wire was normal to the flow. Hence, in the program HFMMASTER at the beginning of each pitchwise traverse, the hot-wire was aligned normal to the flow as follows: The anemometer output voltage was measured for seven different angular positions of the probe evenly distributed about the approximate flow direction. By fitting a least-square polynomial through these seven points, the maximum voltage and the corresponding angular position of the hot-wire was obtained [45]. This direction was taken to be the nominal flow direction for that spanwise location, and the hot-wire probe was yawed to this angle.

Since the change in turbulence intensity due to the variation in flow angle over a pitchwise traverse was negligible, the hot-wire was not yaw-nulled for each data point in a pitchwise traverse.

Once the input data specifying the number of datapoints in the pitchwise and spanwise directions had been entered in program HFMASTER, the program positioned the hot-wire probe at the specified locations and measured the linearizer output voltage (both AC and DC) along with the flow temperature from the thermocouple located in the plenum. The DC component of the linearizer output multiplied by the proportionality constant relating the flow velocity and the linearizer output and corrected for the flow temperature gave the flow velocity. The ratio of the AC component (true RMS) and the DC component gave the turbulence intensity of the flow.

4. Glue-on hot-film gage measurements

Hot-film gages glued to the suction surface of one of the airfoils in the cascade were used to determine the state of the suction-surface boundary layer. These gages (Micro-Measurements ETG-50A), consisting of a high purity nickel foil coating on a 1 mil flexible polyimide film backing, measured 0.06 in by 0.1 in. A total of 14 gages were positioned at 1-in intervals along the suction surface, starting at 1 in from the leading edge. The gages were also staggered in order to minimize the influence of a given gage on the gage measurements further downstream. Particular care was taken in applying the gages and soldering the lead connections to produce a minimum disruption to the

suction surface profile. The gage leads were passed through small holes immediately downstream of the gages into the interior of the airfoil or, in some cases, to the pressure side of the airfoil, and then out through the endwall. Figure 30 shows a view of the hot-film gages glued to the airfoil suction surface.

The TSI anemometer system along with the Norland digital oscilloscope and the PRO 380 microcomputer described in Chapter IV was used to collect and process the hot-film signal (see Figure 25). The hot-film gages had a nominal resistance of 50 ohms and were operated at a temperature of 90° C by the anemometer system.

The principle involved in the operation of a hot-film gage was based on the relationship between the rate of heat transfer of the heated sensor in the colder test flow and the shear stress at the wall. This relationship has the form [see Appendix B]:

$$\frac{I^2 R}{\Delta T} = a(\tau_w)^{1/3} + b$$

here I is the sensor current, R the resistance of the sensor, ΔT the temperature difference between the sensor and fluid, and τ_w the wall shear stress. The constant a in the relationship depends upon the the geometry of the sensor and on the fluid properties, and the constant b represents the heat loss from the sensor to the substrate. Since the state of the boundary layer could be recognized by comparing signals from all the gages, no attempts were made in the present investigation to evaluate the constants a and b, or to actually determine the wall

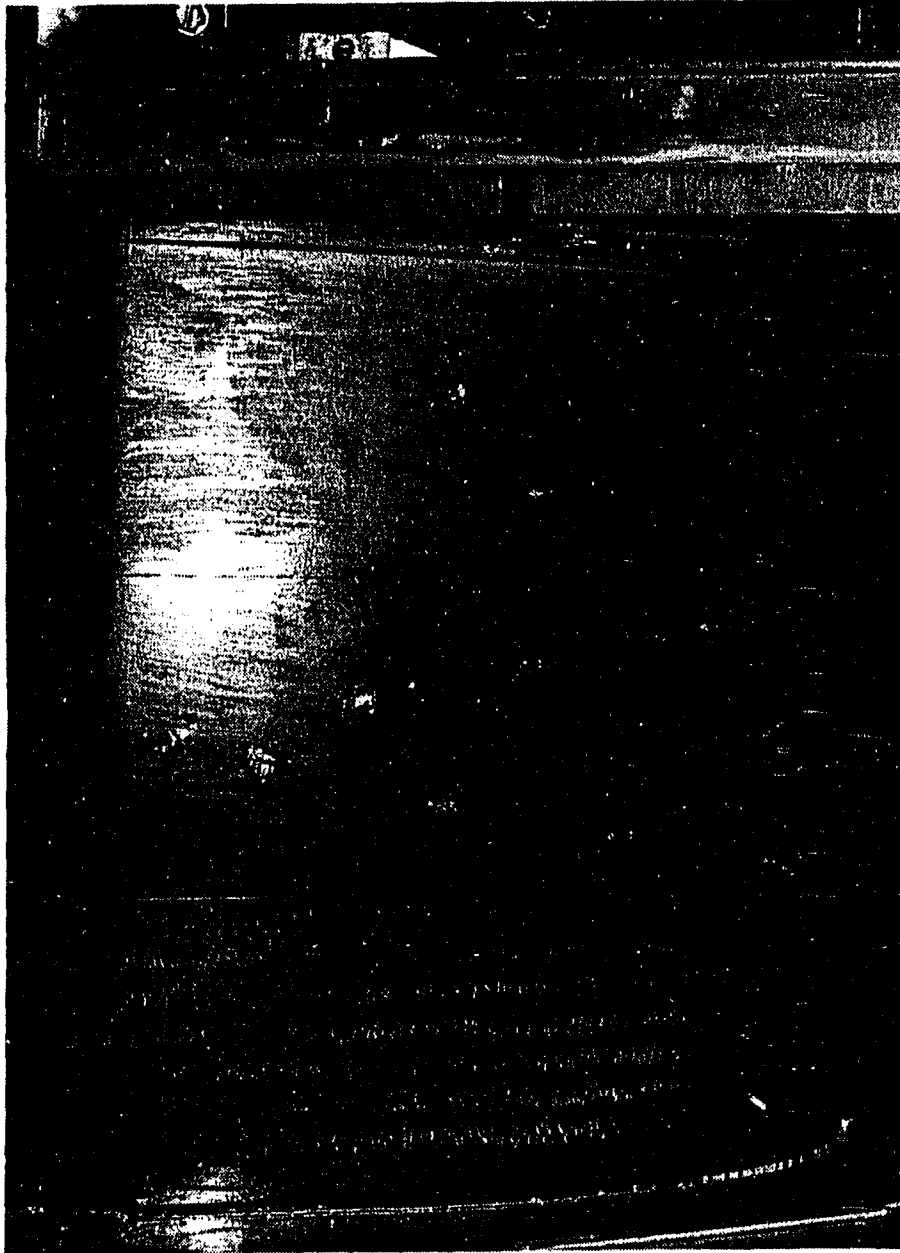


FIGURE 30. Hot-film gages glued to the airfoil suction surface

shear stress. In the hot-film gage output, the DC component corresponds to the time averaged heat transfer or wall shear stress, and the AC component to the fluctuating heat transfer or wall shear stress.

Transition was located by examining the AC signals from the hot-film gages. In the transitional region, the fluctuations in shear stress were much higher than those present in a fully turbulent boundary layer [46, 47]. Since these shear stress fluctuations related to the heat transfer fluctuations in the hot-film gages, transition was detected by observing the AC signals of the gages. At that point where the AC signal suddenly increased, transition was said to have begun; where the signal tends to a steady value, transition was said to have been completed.

To determine the accuracy of transition measurements, a glue-on hot-film gage was first tested against a boundary layer hot-wire probe (TSI model 1218 T1.5) in a flat plate boundary layer flow. The hot-wire was immersed in the boundary layer at a given streamwise location along the flat plate, and Reynolds number at the probe location was varied by changing the free stream velocity. By plotting the ratio of velocity measured by the hot-wire to free stream velocity, v/V , against free stream velocity, V , transition could be detected due to the change in the boundary layer velocity profile shape. Results from Figure 31 show the start of transition at $V = 42.5$ ft/sec where v/V shows a sudden increase, and the end of transition at $V = 75$ ft/sec, where v/V

reaches a constant value. Also plotted in Figure 31 are the results from hot-film gage measurements at the same streamwise location along the flat plate. The start of transition is identified as the point where the ratio of the RMS to DC signals shows a sudden increase, and the end where this ratio tends to a constant value. As seen in Figure 31, the results from the hot-wire and hot-film gage are in good agreement, confirming that the RMS signal from the hot-film gage can be used to determine the state of the boundary layer.

Another method to identify transition was based on the examination of the power spectrum of the hot-film gage output. A transitional signal has a higher power spectral density at low frequencies than does either a fully laminar or a fully turbulent signal [48].

Hot-film gage output signals were digitized and processed by the digital oscilloscope to obtain the RMS and mean voltages and the power spectral density. A sampling rate of 10 KHz was used in digitizing the signal and the digitized data were collected and processed in blocks of 1024 data points. At this sampling rate, and with a sampling time of 0.1023 seconds, a resolution of 9.76 Hz and a frequency range of 0 to 5 kHz was obtained for the power spectrum. The RMS voltage, the DC voltage, and the power spectral density were calculated individually for each data block. The mean of the results for ten data blocks was taken as the output for that hot-film gage. The output of each hot-film gage (both in time domain and frequency domain) was transferred to the microcomputer through the IEEE 488 interface and stored in a diskette.

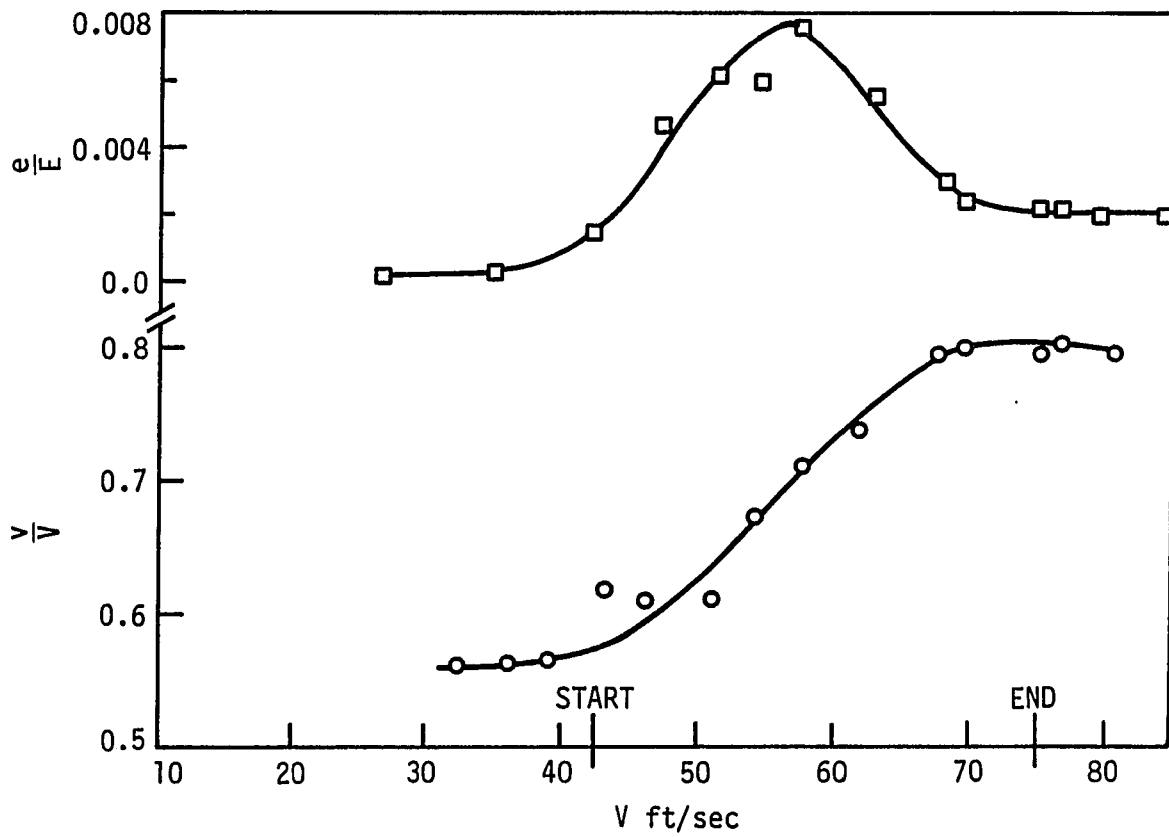


FIGURE 31. Transition curves from hot-film and hot-wire measurements

5. Flow visualizations

Surface oil-flow visualizations were made on the airfoil surface and the cascade endwall to obtain flow patterns and locate separation zones. With this flow visualization technique, information about the nature of the flow was obtained quickly and easily. By taking photographs of the flow patterns, a permanent record was obtained.

The surface to be tested was coated with a specially prepared paint consisting of a finely powdered pigment dispersed in a suitable oil medium. The air flowing over the surface carried the oil with it and a streaky deposit of the pigment was left behind to mark the flow direction. A mixture of kerosene and a fluorescent pigment (Dayglo Rocket Red AX-13) was used. The patterns produced by this pigment were clearly visible in natural light and photographed very well in ultra-violet light. The exact composition of the oil-pigment mixture was arrived at by trial and error. In general, different compositions had to be used for different flow velocities to produce acceptable flow patterns. For a few cases, when the mixture was too thin, a few drops of 10W-30 motor oil were added to increase the viscosity. More details on the oil-flow visualization technique can be found in Maltby [49].

For ease in photographing, a mylar sheet was attached to the surface to be tested and the flow patterns were obtained on the sheet. The surface was covered with the mylar sheet, and, after removing any wrinkles and unevenness, the sheet was firmly attached to the surface with tape. The sheet was then wetted with kerosene by rubbing it with

a soaked rag. Next, a thin and even coating of the oil-pigment mixture was applied with a fine brush over the mylar sheet. The blower was quickly started and brought to the test speed. After the kerosene has been completely driven away by the flow, the blower was turned off and the mylar sheet containing the flow pattern was carefully removed and photographed under black light. An U-V filter was used to increase the contrast in the flow pattern.

D. Experimental Accuracy

An uncertainty analysis was performed to estimate the accuracy of the measured data. The mean and uncertainty levels (odds 20 to 1) of pressure and turbulence intensity were calculated from a sample of 25 data values, all of which were measured at the same location and flow speed. The following results were obtained for the primary measurement values.

Pressure measurements in terms of q_2 ,

Five-hole probe pressures	$\pm 0.003 \times q_2$
Pitot-static probe pressures	$\pm 0.005 \times q_2$
Airfoil static pressures	$\pm 0.004 \times q_2$
Flow temperature	$\pm 0.13^\circ \text{ F}$
Turbulence intensity	$\pm 0.12 \%$
Yaw angle, β	$\pm 0.2^\circ$
Pitch angle, ϕ	$\pm 0.1^\circ$

Using the propagation of error method of Kline and McClintock [50], uncertainty of reduced data was estimated. The results obtained were:

Total pressure loss coefficient, C_{PT}	± 0.02
Total pressure loss coefficient, C_{PT2}	± 0.007
Static pressure coefficient, C_p	± 0.017
Flow velocity	$\pm 1.1 \%$

VI. RESULTS AND DISCUSSION

Test results for the cascade obtained from airfoil static pressure measurements, flow visualizations, five-hole probe and hot-wire traverses, and glue-on hot-film gage measurements are presented and discussed in the following sections. Results for flow inlet angle $\beta_1 = 45^\circ$ (-7° design incidence) are presented first, followed by those for $\beta_1 = 52^\circ$ (-14° incidence) and $\beta_1 = 38^\circ$ (0° incidence). For each inlet angle setting of the cascade, testing was carried out at four inlet turbulence levels, Tu , and three axial chord Reynolds numbers, Re . These testing conditions are identified as:

<u>Tu, %</u>	<u>Re</u>
0.8 (NGRID)	700,000 (RE1)
2.0 (GRID1)	540,000 (RE2)
4.8 (GRID2)	330,000 (RE3)
6.4 (GRID3)	

The indicated notation NGRID, RE1, etc., for turbulence level and axial chord Reynolds number is used for convenience in representing the testing conditions in the results. Testing was done more extensively for the design inlet angle case to include five-hole probe and hot-wire traverses in the upper half of the cascade exit plane at all test conditions. The testing at the two other inlet angles was done similar to the design inlet angle, except that no hot-wire traverses were performed and five-hole probe traverses were limited to midspan only for the GRID1, GRID2, and GRID3 turbulence levels. Results from off-

design inlet angle tests were used primarily to support or further clarify those obtained for the design inlet angle case.

A. Inlet Angle, $\beta_1 = 45^\circ$ (-7° design incidence)

1. Static pressure measurements

Figure 32 shows the results of static pressure measurements made at midspan, and at 20% of span from either endwall, along with the predicted 2-D pressure distribution (the solid line). The flow conditions were NGRID and RE2. No endwall suction was applied to the cascade. As seen in Figure 32, the agreement between the measured and predicted distributions is quite good indicating that the flow was symmetric about the midspan. The measured pressure distribution at 20% span deviated little from that measured at midspan, except for a slight increase in loading on the suction surface close to the trailing edge. Similar results were obtained in comparing the midspan and 20% span pressure distributions at the other testing conditions.

The measured static pressure distribution at midspan for the three test Reynolds numbers are given in Figures 33, 34, and 35. Here the pressure distributions are plotted for each turbulence level against the fraction of suction or pressure surface length from the stagnation point. Also shown for comparison is the predicted 2-D distribution. In general, it is seen that as turbulence level increases, the loading tends to decrease on the suction surface. The measured distribution on the suction surface fails to follow the underspeeding predicted near

the leading edge, and also shows lower values than those predicted up to the minimum pressure point. On the pressure surface there is little change in pressure distribution with turbulence level for Reynolds numbers RE1 and RE2. Only for the case of RE3, shown in Figure 35, is there a slight deviation for high turbulence levels at the 30% position on the pressure surface. However, for all the cases, the leading edge overspeeding on the pressure side closely follows the predicted pattern.

Figures 36 through 39 show the pressure distributions for the four different turbulence levels. In each Figure, results are plotted for the three Reynolds numbers. As can be seen, for the range of Reynolds numbers tested, the measured pressure distribution is independent of Reynolds number.

The measured static pressure distributions were used later to calculate the boundary layer development on the airfoil surface and to determine profile losses.

2. Flow visualizations

Results from surface oil-flow visualizations are shown in Figures 40 through 50 for the range of test turbulence levels and Reynolds numbers used. Figures 40 and 41 show the flow pattern on the suction surface of the airfoil for flow conditions NGRID, and Reynolds numbers RE1 and RE2. Here endwall suction has been applied to the cascade, and the flow, as pictured, is from right to left with gravity acting from top to bottom. In both Figures 40 and 41, a laminar separation bubble

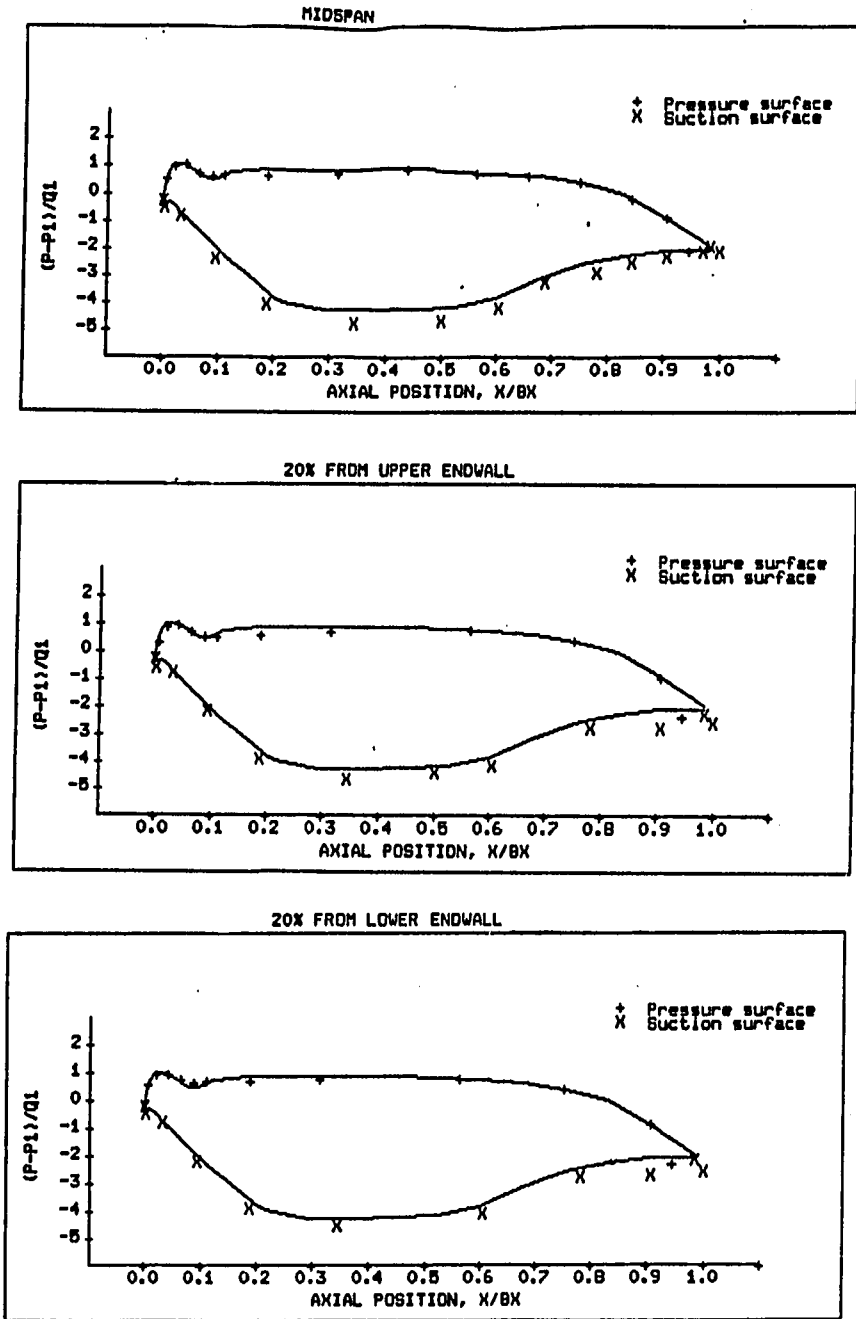


FIGURE 32. Static pressure distribution at midspan and at 20% from endwalls, $\beta_1 = 45^\circ$, NGRID, RE2

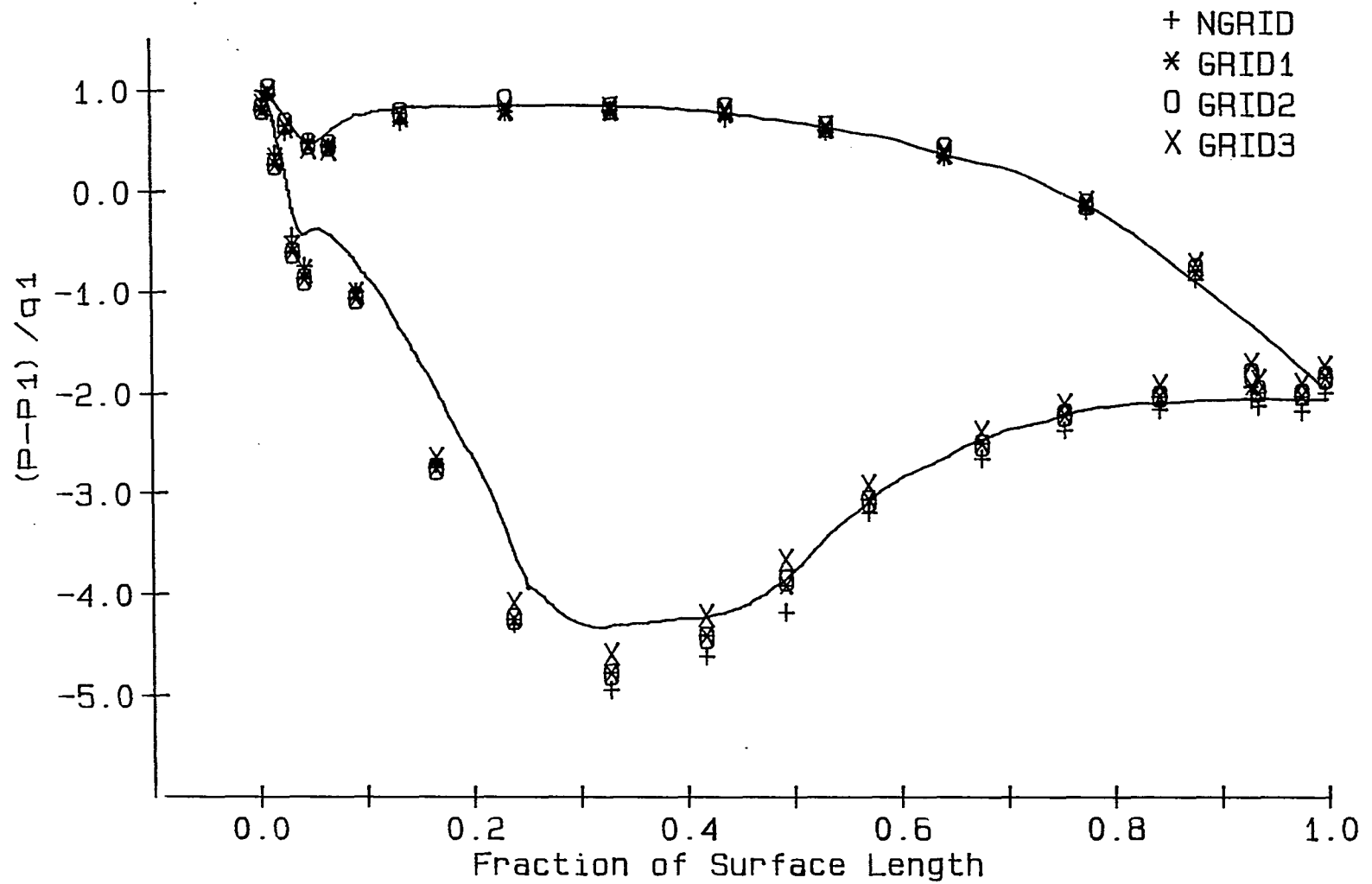


FIGURE 33. Static pressure distribution, $\beta_1 = 45^\circ$, RE1

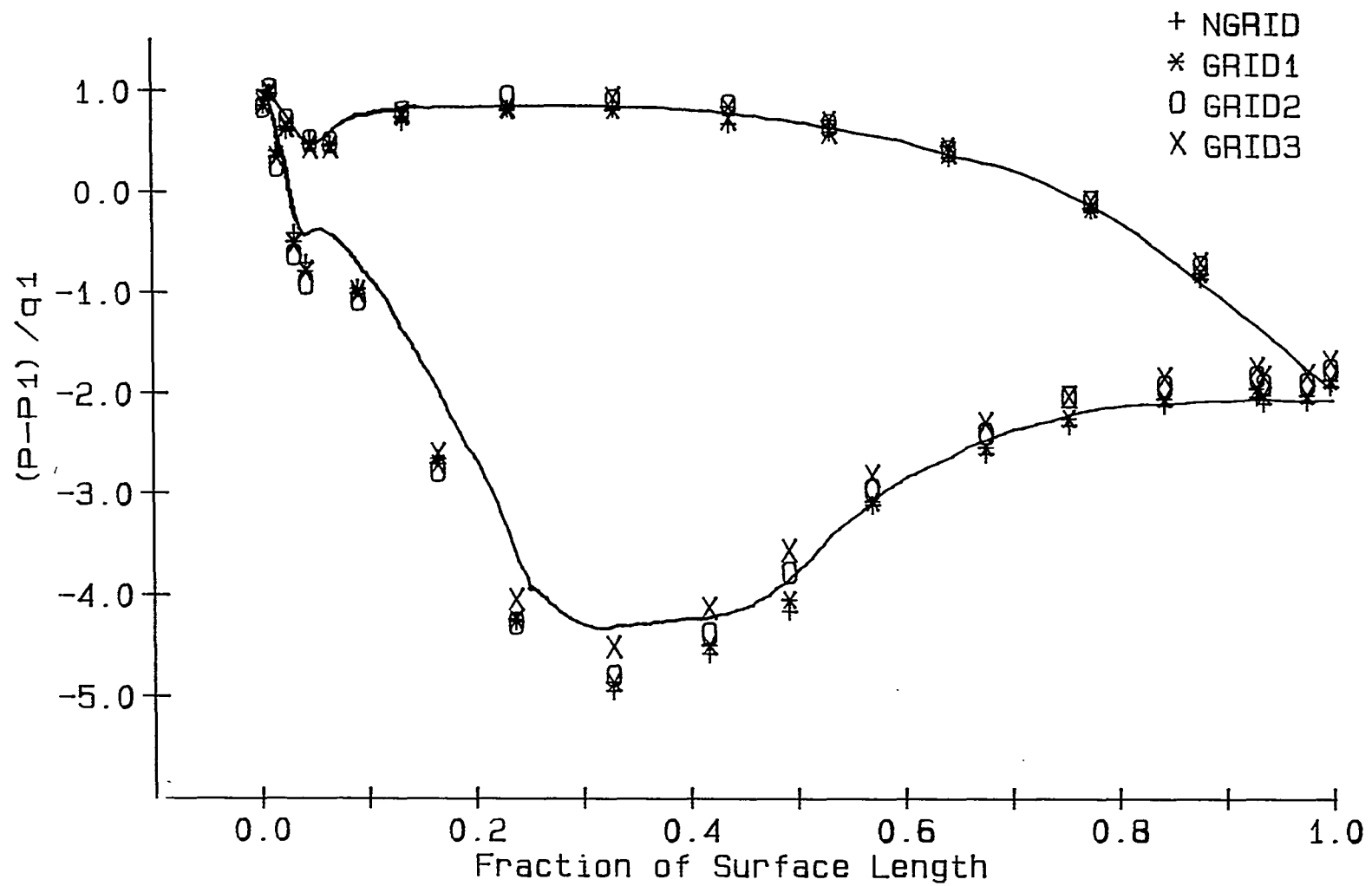


FIGURE 34. Static pressure distribution, $\beta_1 = 45^\circ$, RE2

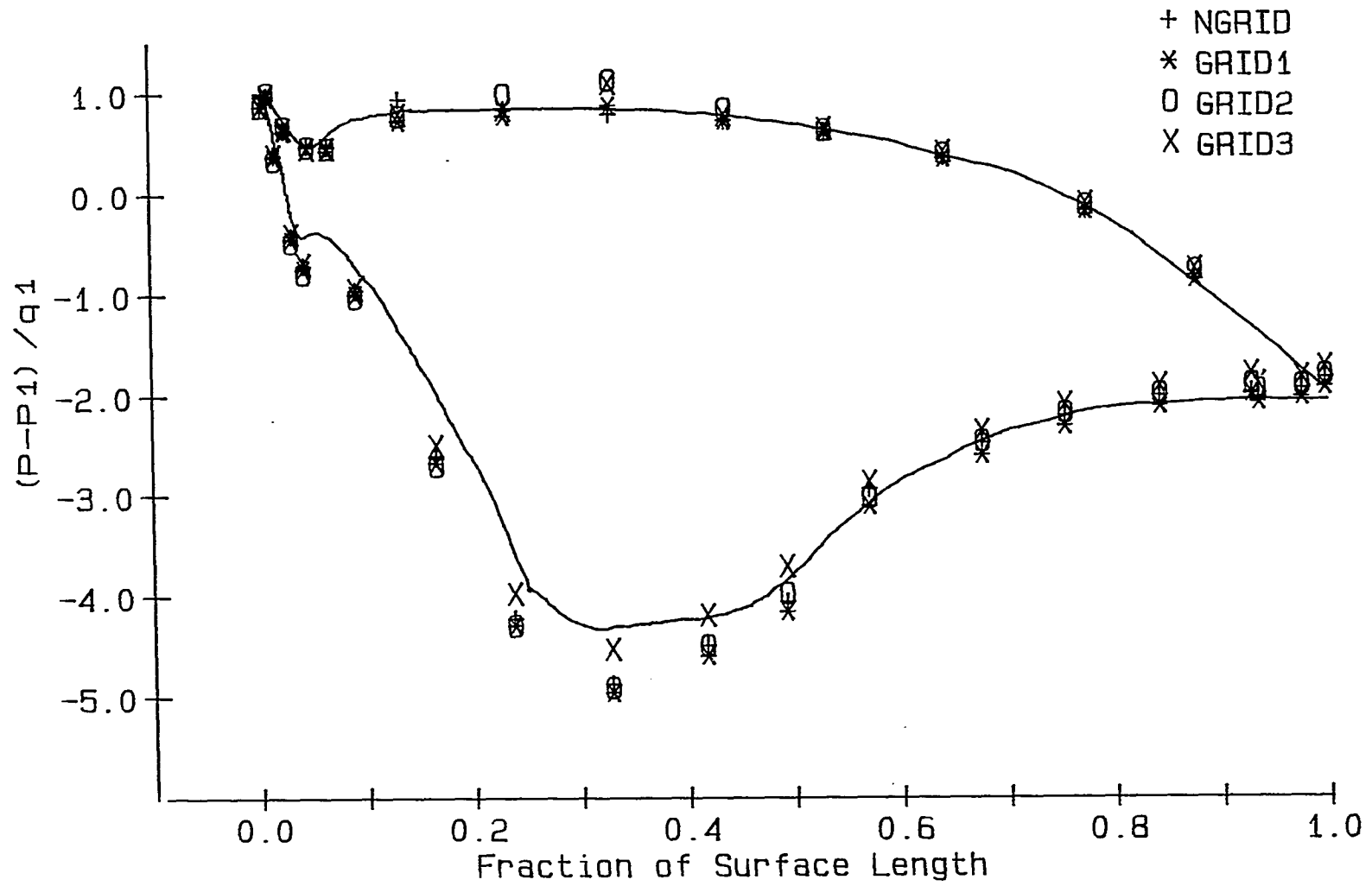


FIGURE 35. Static pressure distribution, $\beta_1 = 45^\circ$, RE3

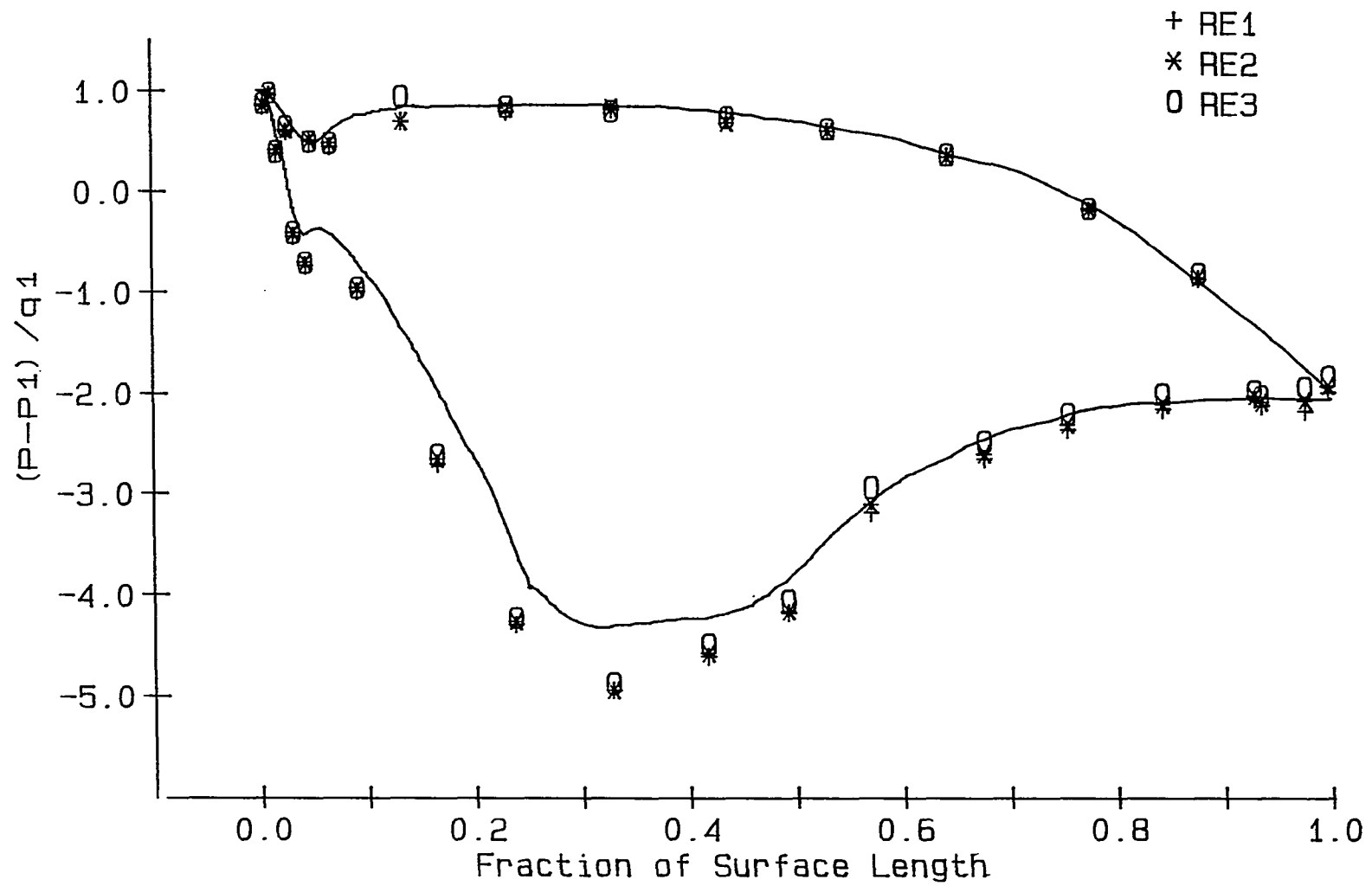


FIGURE 36. Static pressure distribution, $\beta_1 = 45^\circ$, NGRID

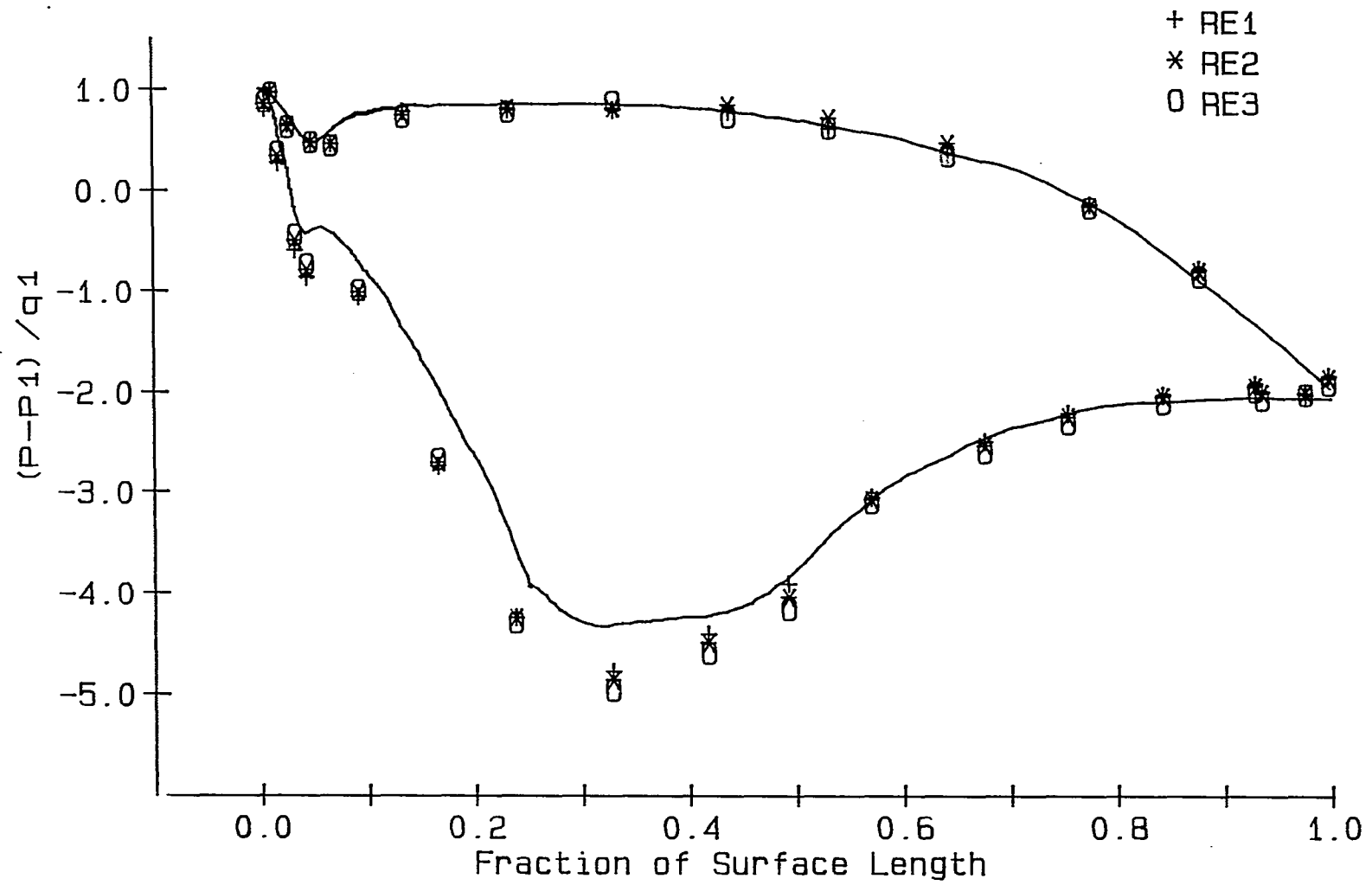


FIGURE 37. Static pressure distribution, $\beta_1 = 45^\circ$, GRID1

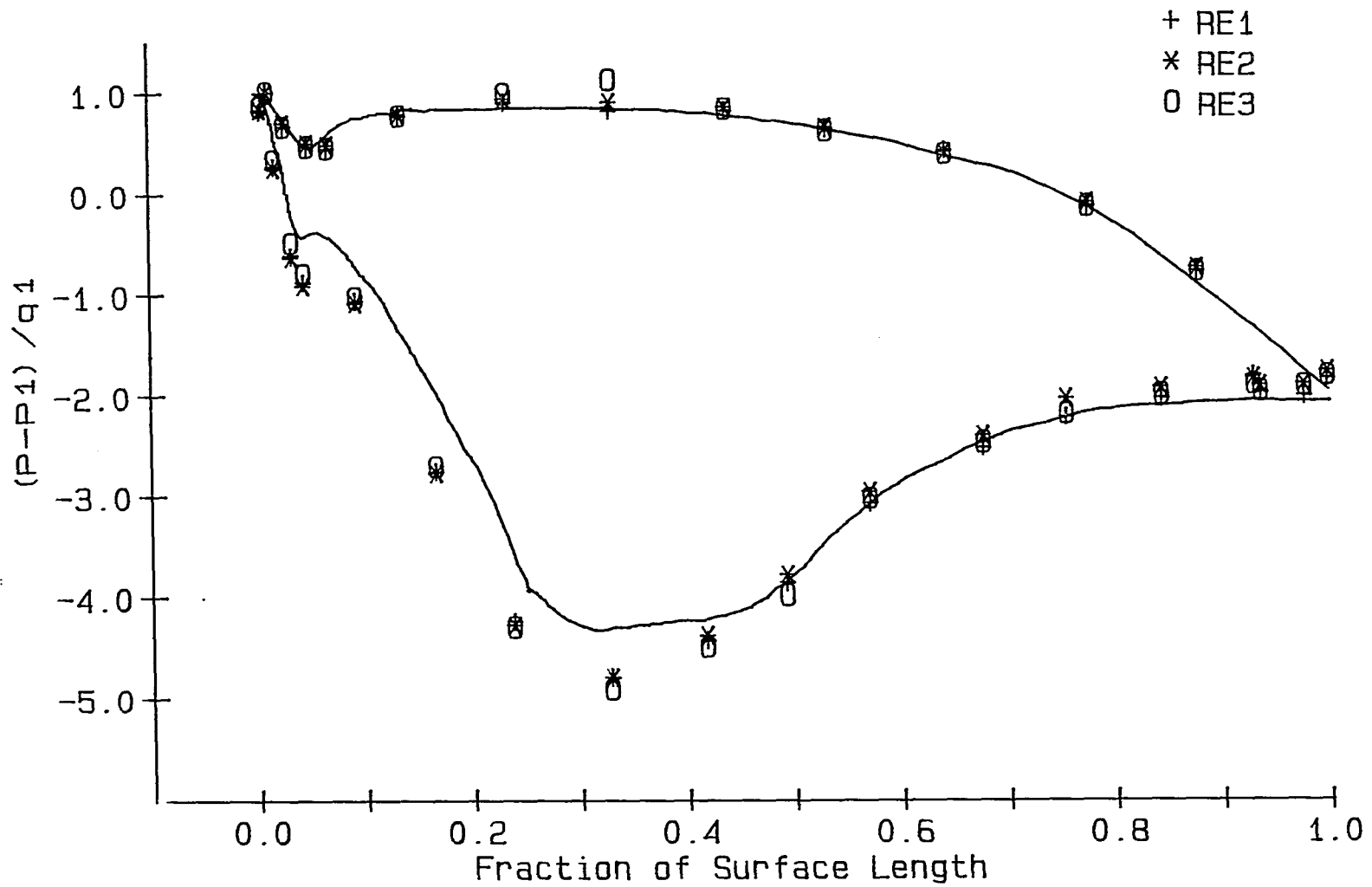


FIGURE 38. Static pressure distribution, $\beta_1 = 45^\circ$, GRID2

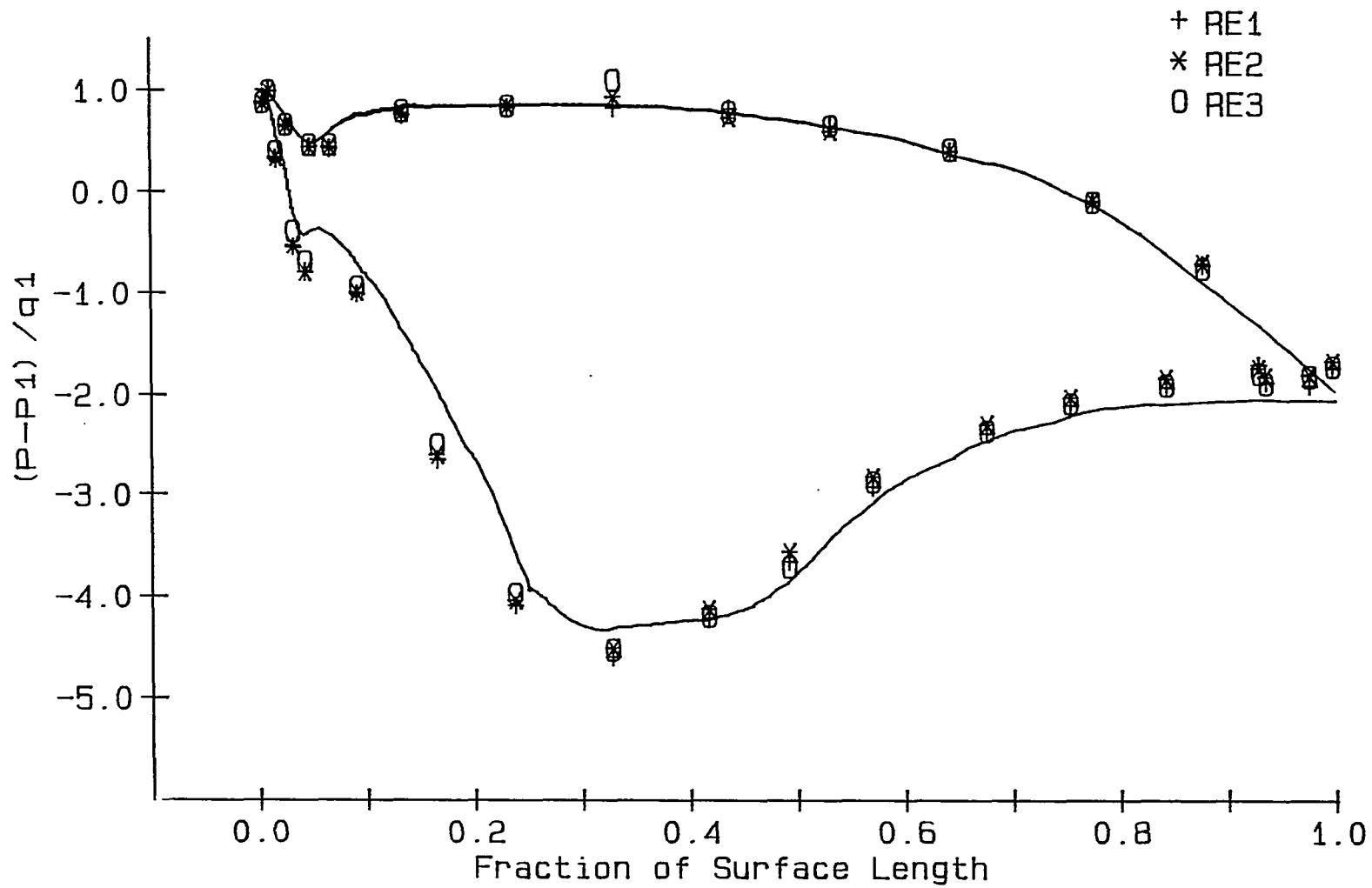


FIGURE 39. Static pressure distribution, $\beta_1 = 45^\circ$, GRID3

located at about 45% along the surface length is evident. The bubble reattaches as a turbulent boundary layer, and the flow from there on to the trailing edge remains turbulent. Also, at the lower endwall, the limiting streamline is seen to move towards midspan due to the passage vortex and endwall flow interference.

Figure 42 shows the flow pattern on the suction surface for the same testing conditions as in Figure 40, but without endwall suction applied. Here the limiting streamlines are seen to converge strongly towards midspan in a symmetric fashion from either endwall. Also, the separation bubble is seen to be at approximately the same streamwise location as before, indicating that squeezing of the suction surface boundary layer by the passage vortex and endwall flow does not affect the separation bubble location.

Figures 43, 44, and 45 show the flow pattern on the suction surface for the flow conditions GRID1, and Reynolds numbers, RE1, RE2 and RE3. Figure 43, for Reynolds number RE1, shows no separation bubble, while Figure 44, for Reynolds number RE2, shows a separation bubble pattern similar to that in Figures 40 and 41, although the bubble appears to be weaker. The absence of the separation bubble in Figure 43 indicates that the boundary layer has undergone natural transition upstream of the location of the separation bubble for the RE1 case. In Figure 45, for Reynolds number RE3, the low flow velocities are barely able to drive the oil and create a flow pattern, especially in the region close to the leading edge. However, a

separation bubble and reattachment line can still be clearly seen. Gravity effects causing a downward flow of the oil ahead of the separation bubble and near the trailing edge are apparent.

Figures 46 and 47 show the flow patterns for flow conditions GRID3, and Reynolds numbers RE1 and RE3. Figure 46 for RE1 shows no evidence of a separation bubble, indicating a natural transition similar to GRID1 case. Figure 47 for RE3 shows signs of flow separation near a point 40% along the suction surface, but without a distinct separation bubble indicated. Hence, in this case, we have a weak separation similar to that seen for conditions GRID1 and RE2 in Figure 44. It should be noted, however, that at low Reynolds numbers, as in Figure 47, thin oil-pigment mixtures were required in order for the flow to drive the mixture and produce discernible flow patterns. Due to this, gravity effects in the flow visualizations were more dominant at low Reynolds numbers, causing some distortions in the flow patterns.

In Figure 48, the flow pattern on the pressure surface of the airfoil is shown for flow conditions NGRID and RE1. Here, the flow is seen proceeding from left to right. The leading edge stagnation region, and a separation bubble near the leading edge can be clearly seen. Again, gravity effects in the thin oil-pigment mixture used are evident.

To complete the flow visualizations for the $\beta_1 = 45^\circ$ case, endwall flow patterns were obtained and are shown in Figures 49 and 50. Figure

49 is without endwall suction applied, while Figure 50 is with endwall suction. As can be seen, the flow patterns are the same and are apparently not affected by the endwall suction flow. The saddle points of separation ahead of the airfoil leading edges are clearly indicated, with the distance between them measuring one blade pitch. Also, the inlet angle setting of 45° for the cascade and the measured angle from the flow pattern ahead of the saddle points are in excellent agreement. The separation line caused by the pressure side leg of the horseshoe vortex can be seen stretching from the saddle point to the suction surface of the adjacent airfoil. The suction side leg is seen to wrap around the leading edge of the airfoil and attach to the airfoil suction surface. These endwall flow patterns and their various features agree with those observed by Langston et al. [51].

In summary, the flow visualizations indicate that on the suction surface of the airfoil, laminar bubbles are formed at low turbulence levels and low Reynolds numbers, and that the profile boundary layer reattaches as a fully turbulent layer. At higher turbulence levels, no separation bubbles are formed on the suction surface, with the profile boundary layer undergoing natural transition. Results from hot-film gage measurements (to be discussed later) further support these conclusions about transition and separation on the airfoil suction surface. On the pressure surface, a separation bubble close to the leading edge was clearly identified. Also, flow visualizations confirmed the existence of a large region of 2-D flow over the airfoil surface when endwall suction was applied.

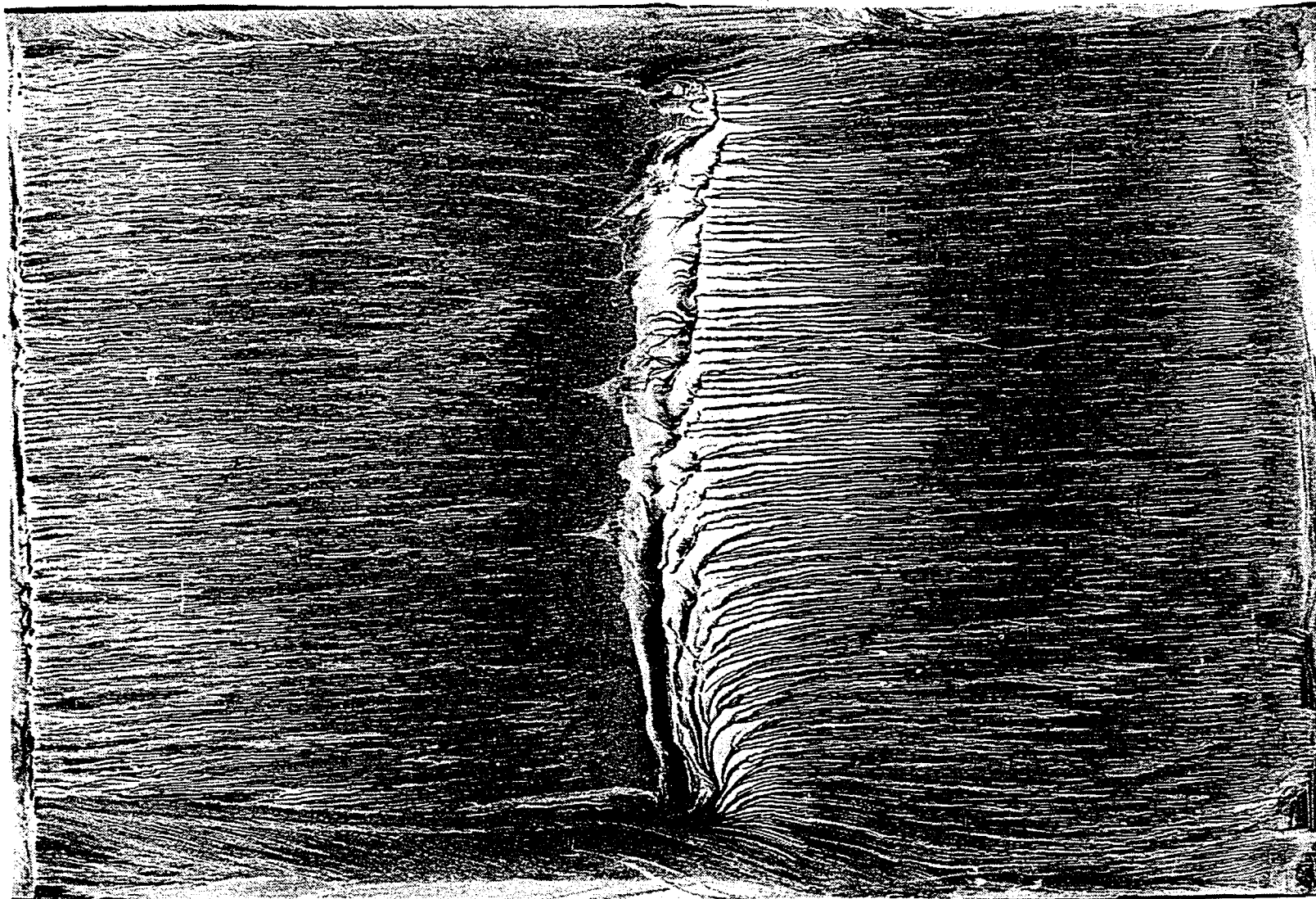


FIGURE 40. Flow pattern, Suction surface, $\beta_1 = 45^\circ$, NGRID, REL

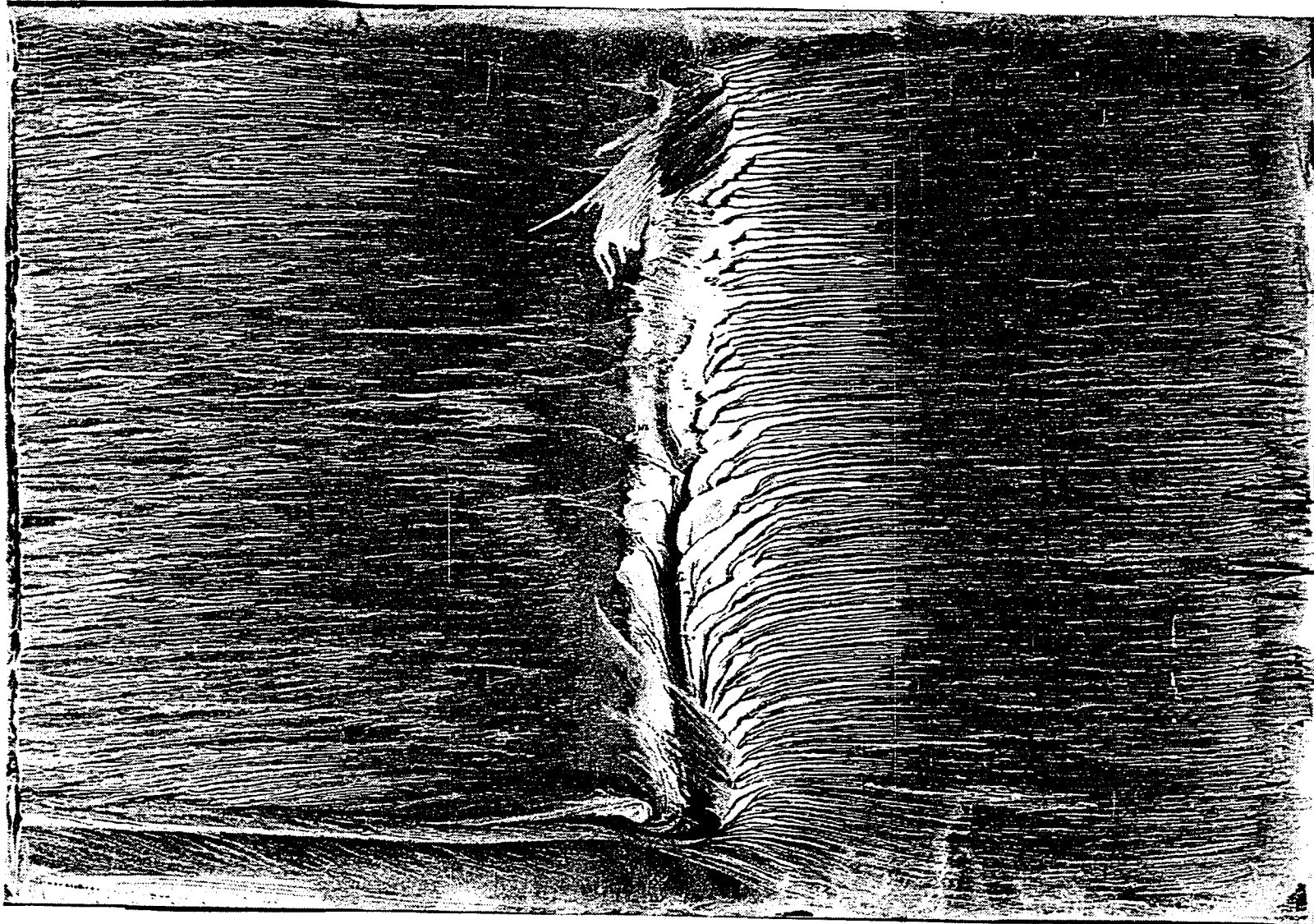


FIGURE 41. Flow pattern, Suction surface, $\beta_1 = 45^\circ$, NGRID, RE2

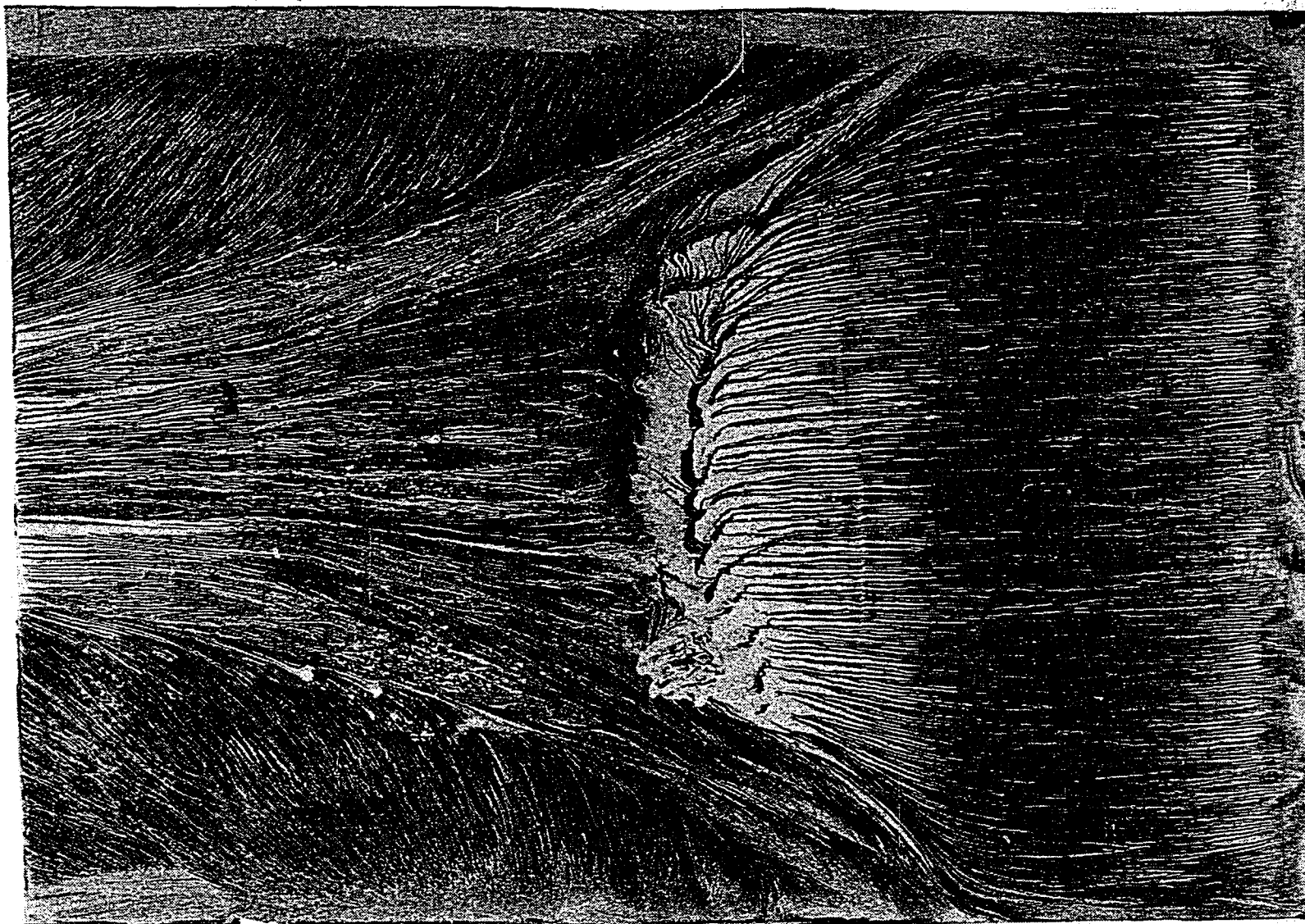


FIGURE 42. Flow pattern, Suction surface, $\beta_1 = 45^\circ$, NGRID, REL. (No endwall suction)

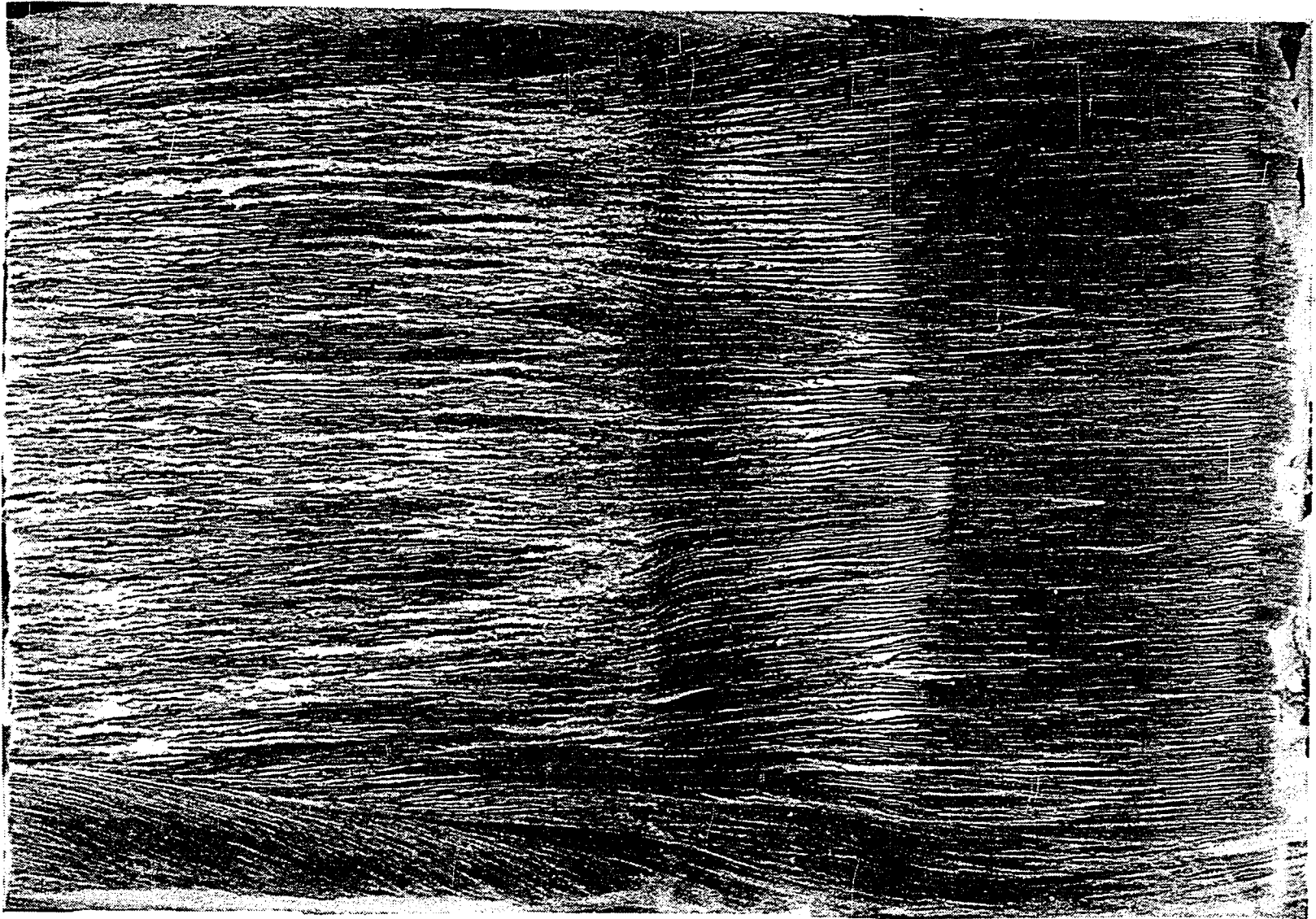


FIGURE 43. Flow pattern, Suction surface, $\beta_1 = 45^\circ$, GRID1, RE1

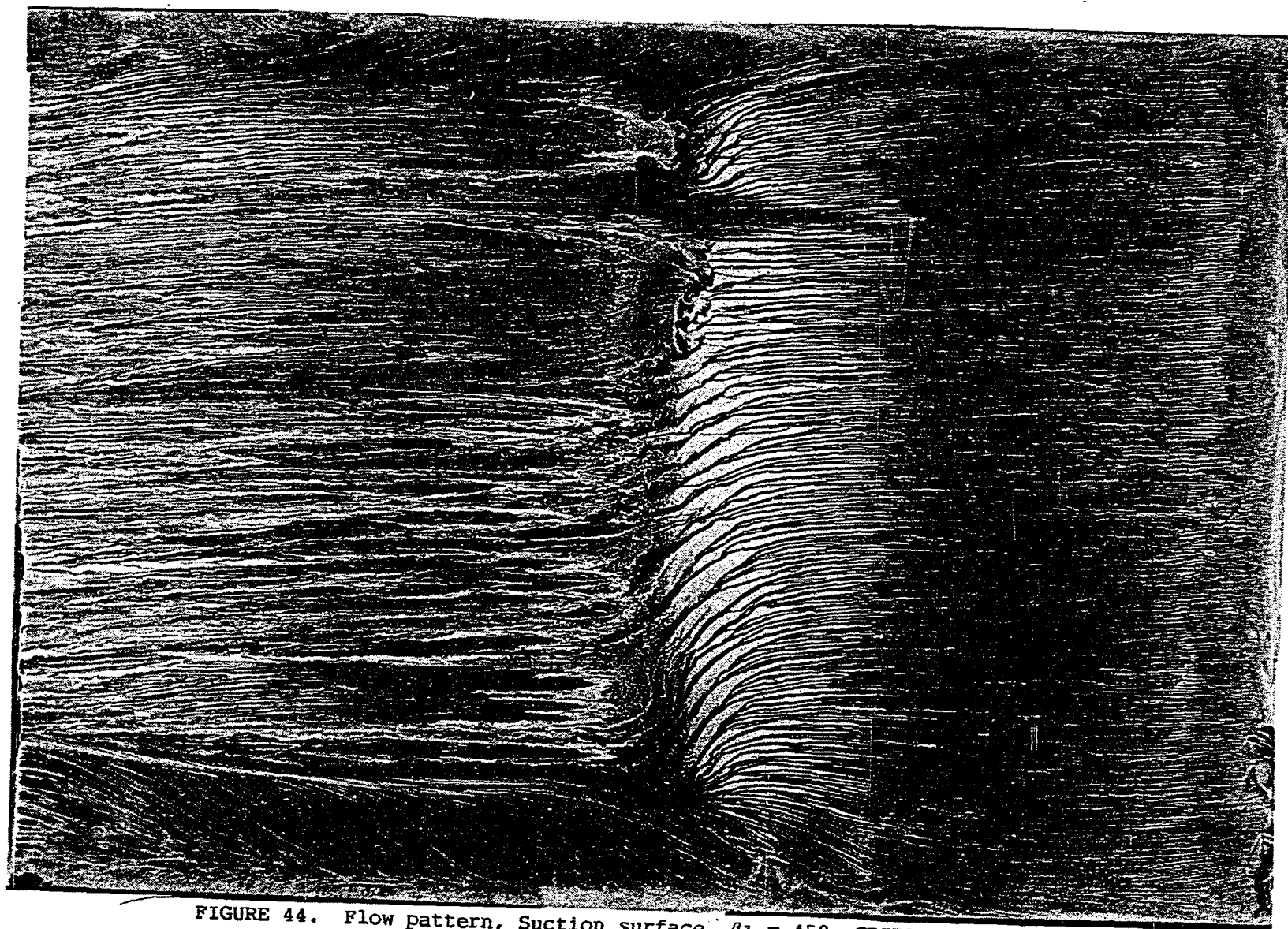


FIGURE 44. Flow pattern, Suction surface, $\beta_1 = 45^\circ$, GRID1, RE2

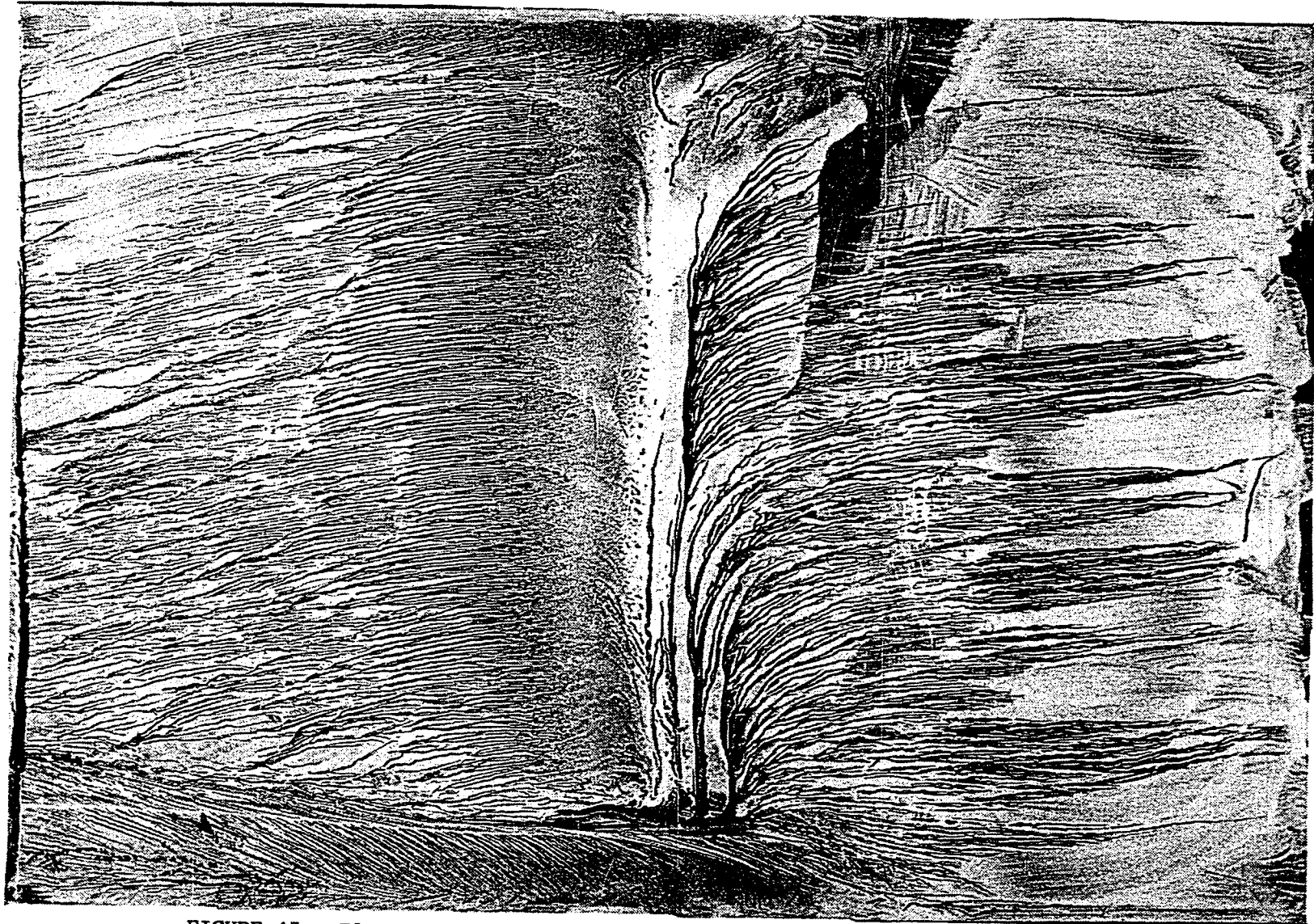


FIGURE 45. Flow pattern, Suction surface, $\beta_1 = 45^\circ$, GRID1, RE3

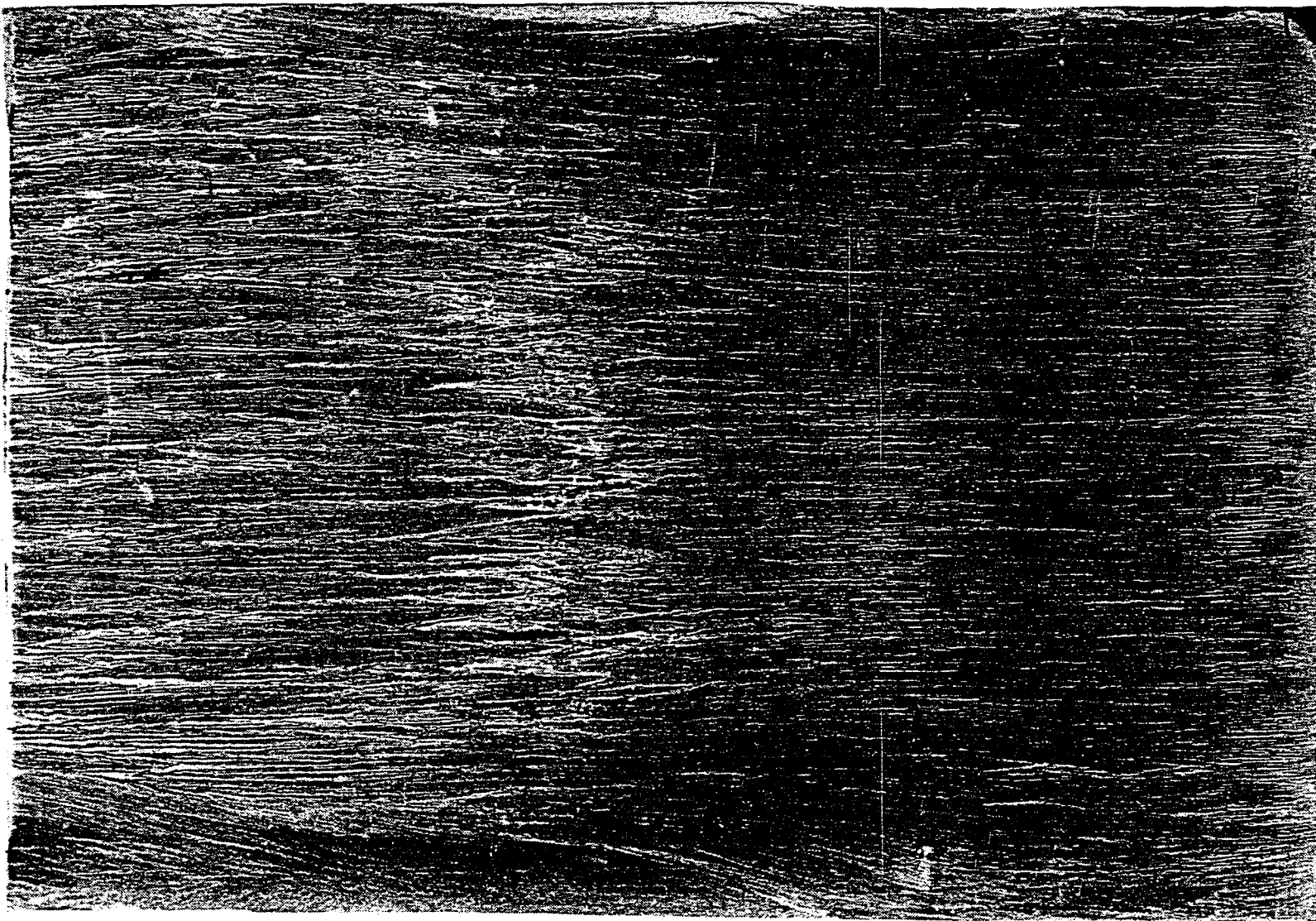


FIGURE 46. Flow pattern, Suction surface, $\beta_1 = 45^\circ$, GRID3, REL

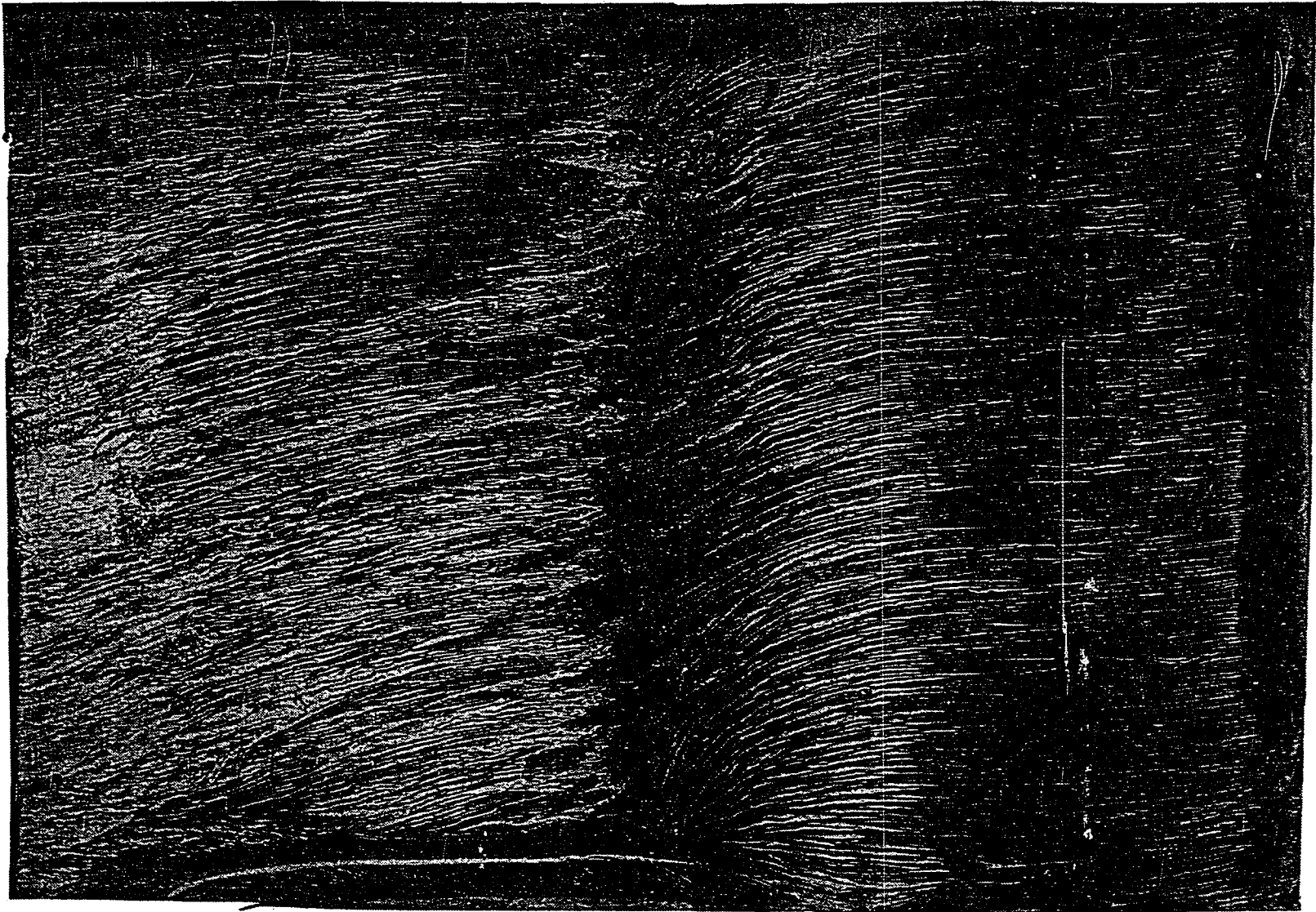


FIGURE 47. Flow pattern, Suction surface, $\beta_1 = 45^\circ$, GRID3, RE3

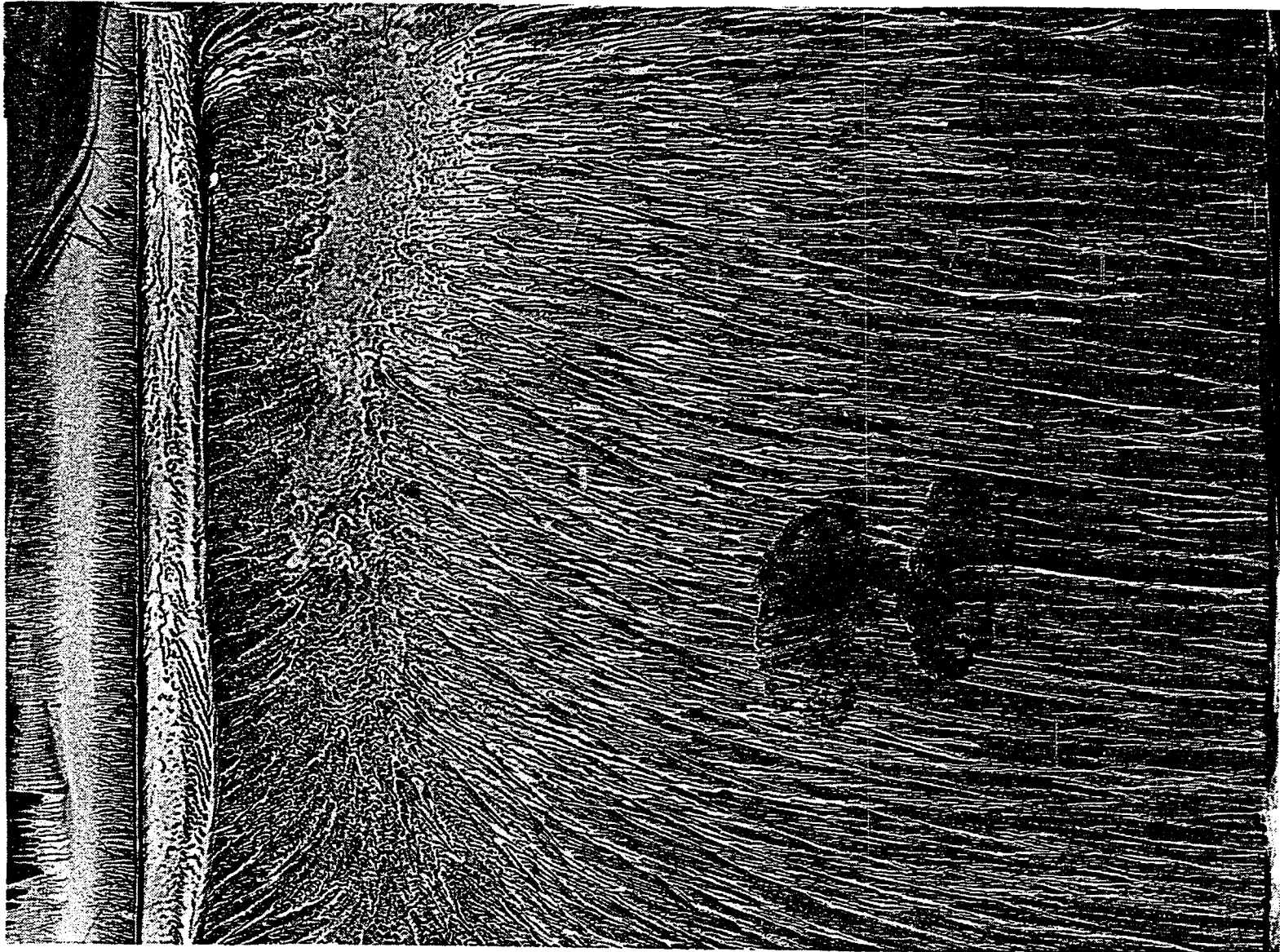


FIGURE 48. Flow pattern, Pressure surface, $\beta_1 = 45^\circ$, NGRID, RE1

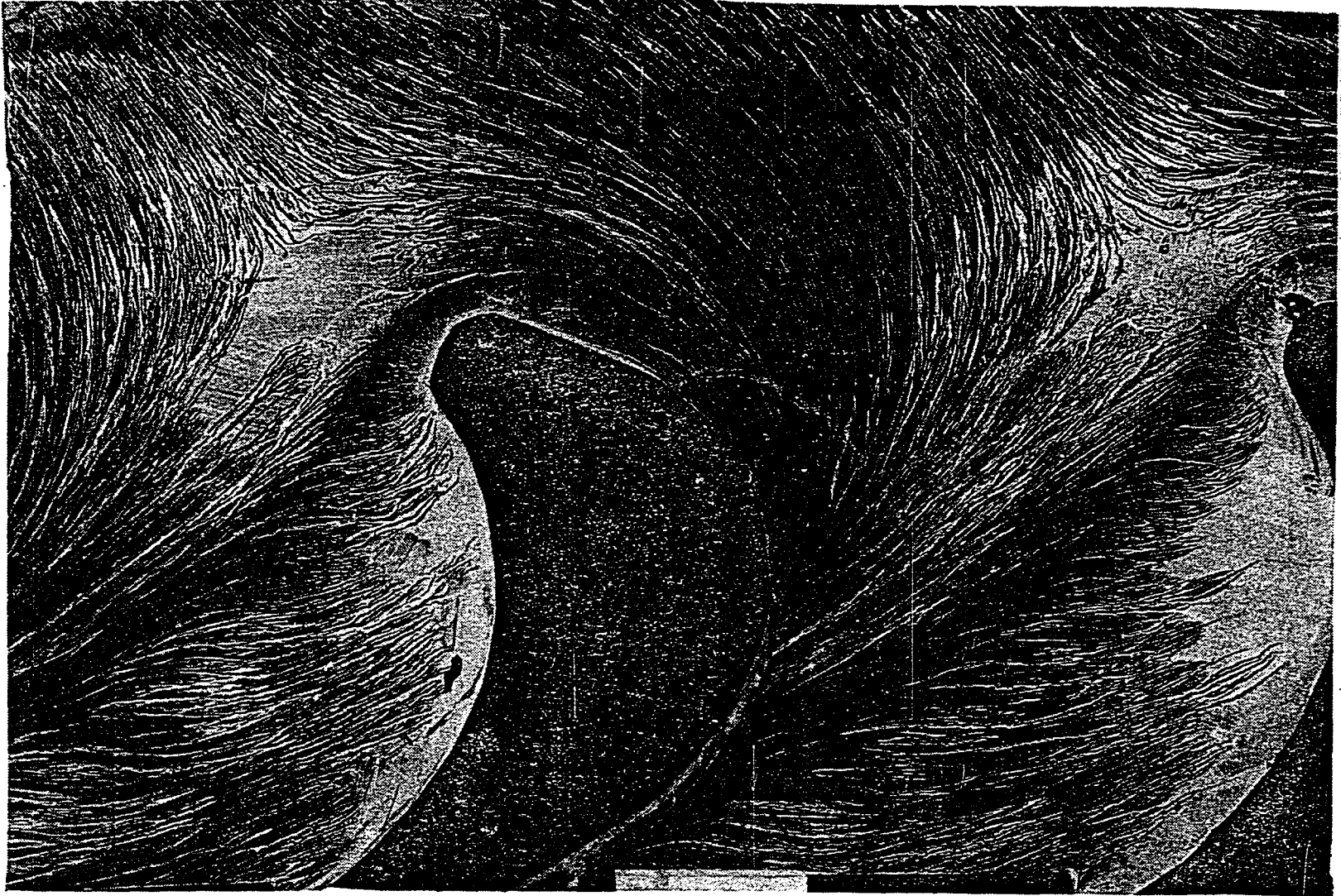


FIGURE 49. Flow pattern, Endwall, $\beta_1 = 45^\circ$ (No endwall suction)

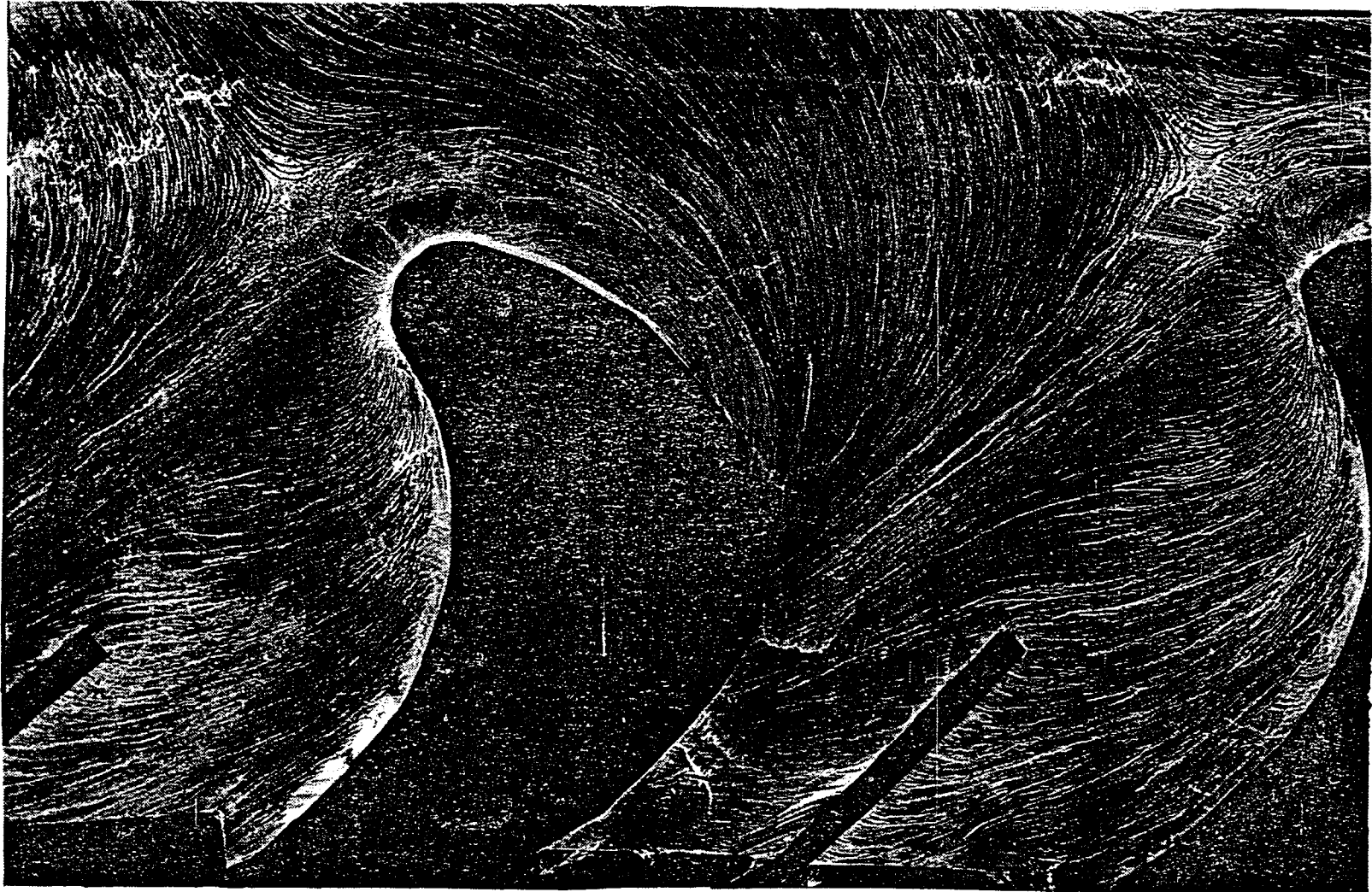


FIGURE 50. Flow pattern, Endwall, $\beta_1 = 45^\circ$ (With endwall suction)

3. Five-hole probe traverse results

Results from five-hole probe traverses conducted in the cascade exit plane are presented in the form of secondary velocity vector plots, contour plots of total pressure loss coefficient, and mass averaged total pressure loss coefficients.

a. Secondary velocity vector plots From the flow yaw and pitch angles measured by the five-hole probe, pitchwise and spanwise components of the exit flow velocity were calculated. Figures 51 through 54 show the secondary velocity vectors in a plane normal to the mean camberline at the airfoil trailing edge. These plots are for NGRID through GRID3 with Reynolds number RE1, and for no endwall suction. The plots show half of the blade span for one blade pitch, with the upper endwall at the top of the plots. The presence of a strong passage vortex can be seen at about 25% of span from the upper endwall. Since the velocity vectors are drawn in a plane normal to the mean camber line at the trailing edge of the airfoil, the vectors represent the deviation from potential flow. At midspan the vectors are directed away from the suction side towards the pressure side, indicating underturning. Near the endwall, overturning is indicated. On examining the size of the passage vortex in each of the Figures 51 through 54, it can be seen that as turbulence level increases, the strength of the vortex is reduced. This is due to the larger diffusion of the vortex at higher turbulence levels. Also, it is to be noted that, at the different turbulence levels, the underturning or deviation

at midspan does not change, indicating that turning through the cascade is not affected by turbulence level.

Additional plots of secondary velocities are shown in Figures 55 through 60, but with endwall suction applied. Figures 55, 56, and 57 present the results for flow conditions NGRID and Reynolds numbers RE1, RE2 and RE3. The velocity vectors shown are scaled according to the inlet velocity. As can be seen, Reynolds number has little influence on the secondary velocity vector pattern. Also in these cases, the passage vortex has almost disappeared, with only a trace of it present in the suction side corner of the endwall. The spanwise component of the velocity vectors away from the passage vortex is directed towards the upper endwall due to endwall suction.

In Figures 58, 59, and 60, secondary velocities are shown for flow conditions GRID1, GRID2, GRID3, and Reynolds number RE1. Again, there are few noticeable differences in the vector patterns, and the passage vortex is barely observable.

In general, endwall suction is seen to have removed most of the passage vortex, and has provided for a 2-D flow over a large portion of the airfoil span. Whatever is left of the passage vortex has been moved close to the suction surface endwall corner.

b. Total pressure loss coefficient Total pressure loss
coefficient contour plots for flow conditions NGRID, GRID1, GRID2, GRID3, and Reynolds number RE1 are shown in Figures 61 through 64. No endwall suction was applied in these cases. As seen in the Figures,

NO-GRID

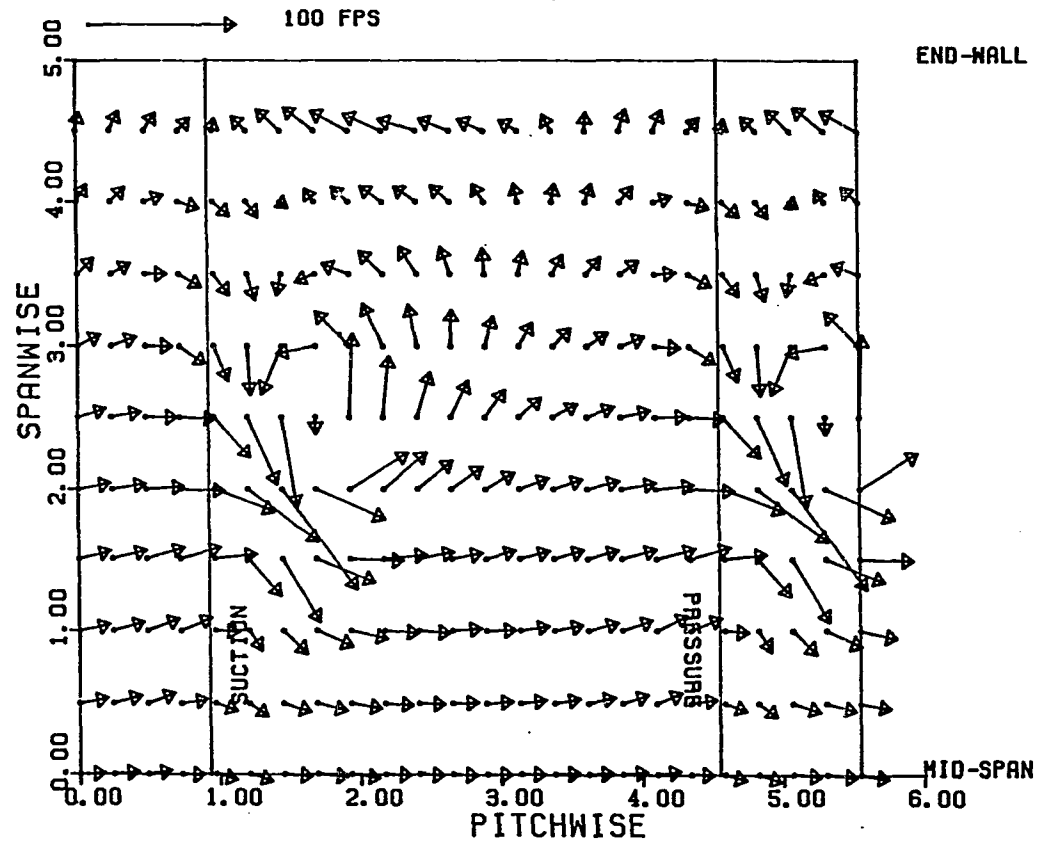


FIGURE 51. Secondary velocity vectors, $\beta_1 = 45^\circ$, NGRID, RE1 (No endwall suction)

GRID1

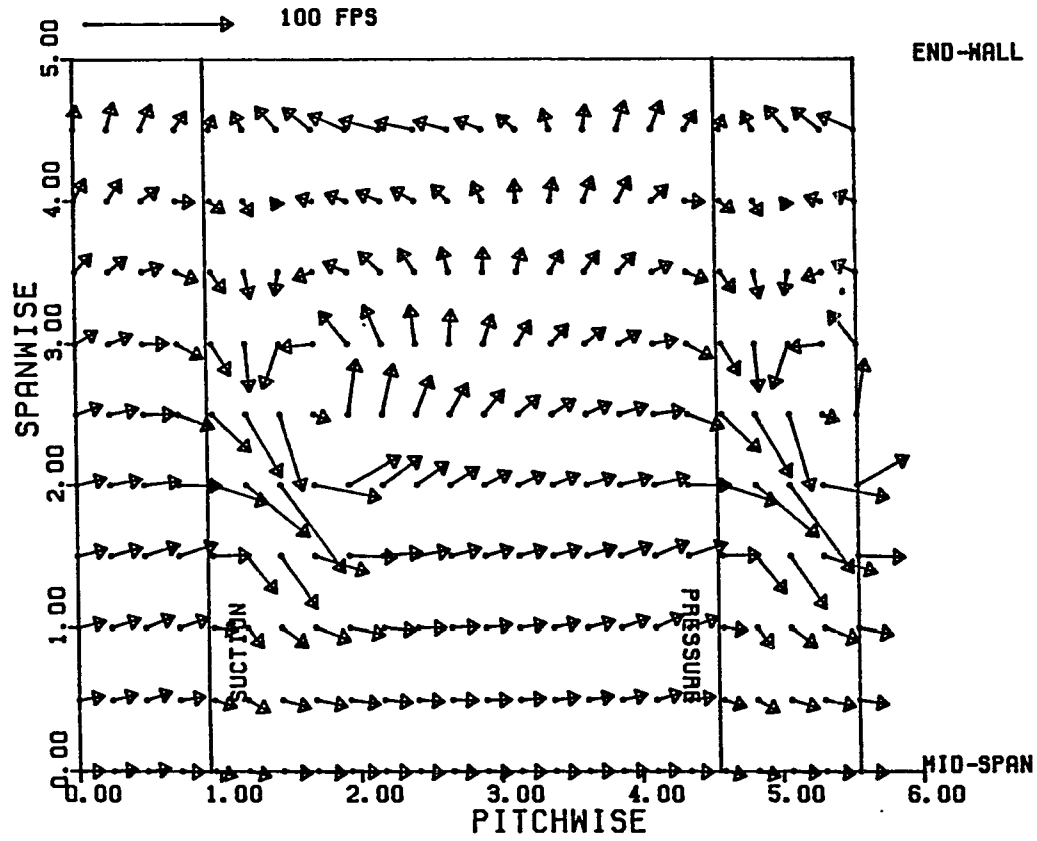


FIGURE 52. Secondary velocity vectors, $\beta_1 = 45^\circ$, GRID1, REL (No endwall suction)

GRID2

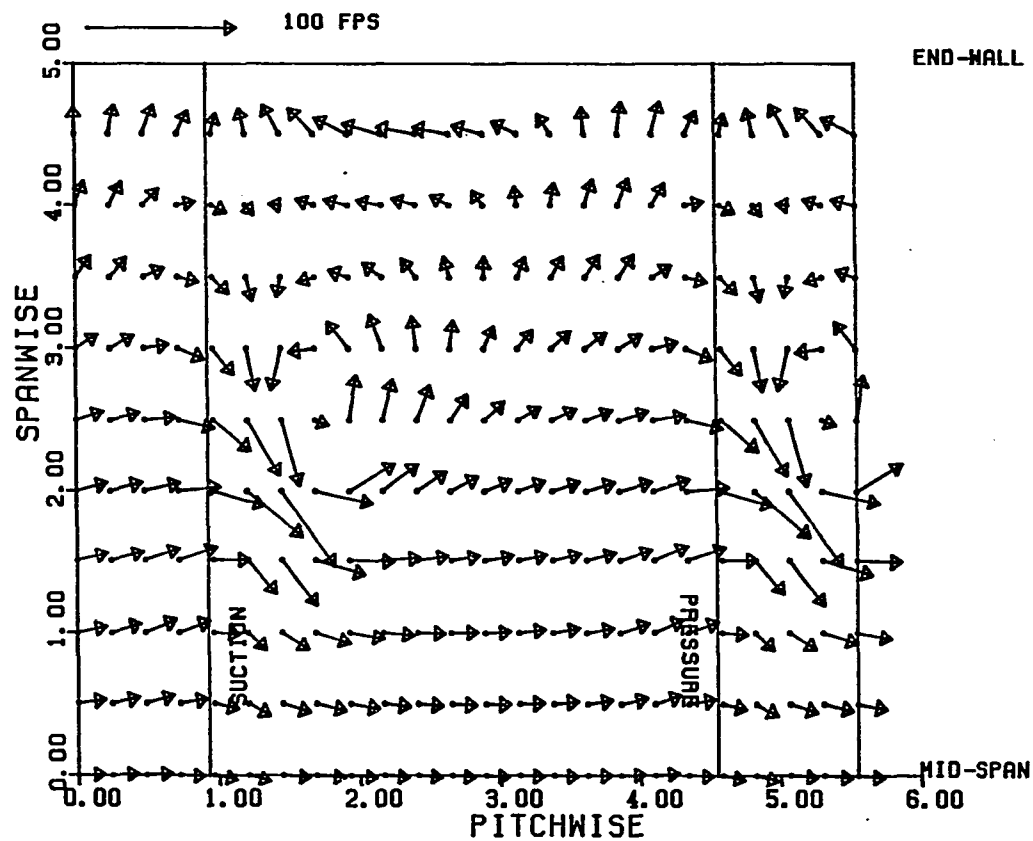


FIGURE 53. Secondary velocity vectors, $\beta_1 = 45^\circ$, GRID2, RE1 (No endwall suction)

GRID3

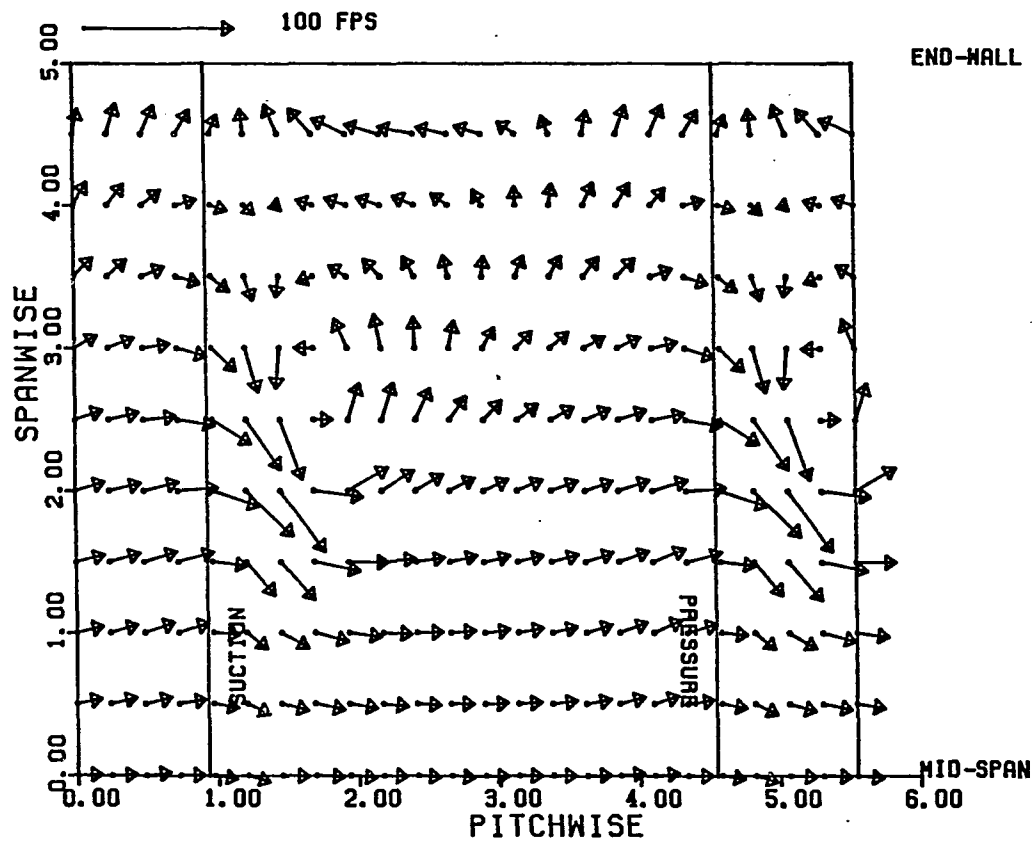


FIGURE 54. Secondary velocity vectors, $\beta_1 = 45^\circ$, GRID3, RE1 (No endwall suction)

NO-GRID

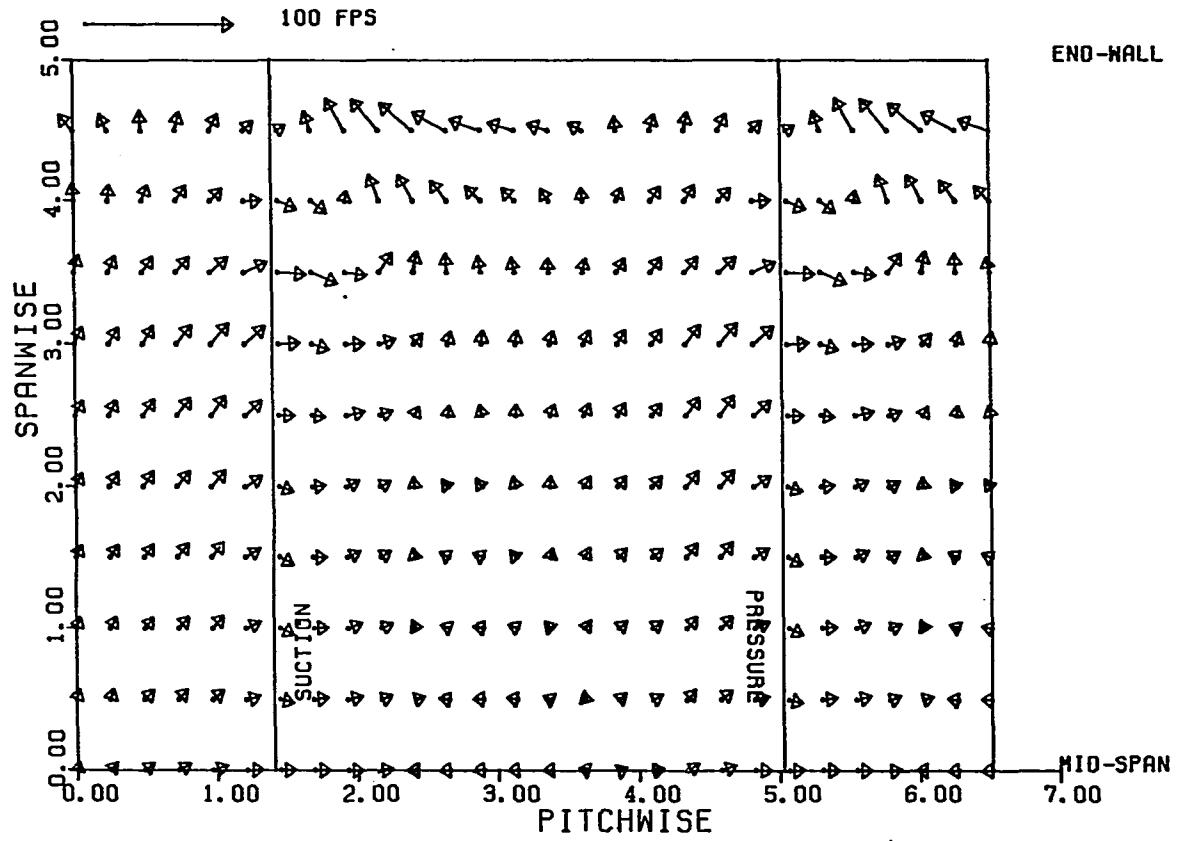


FIGURE 55. Secondary velocity vectors, $\beta_1 = 45^\circ$, NGRID, REL

NO-GRID

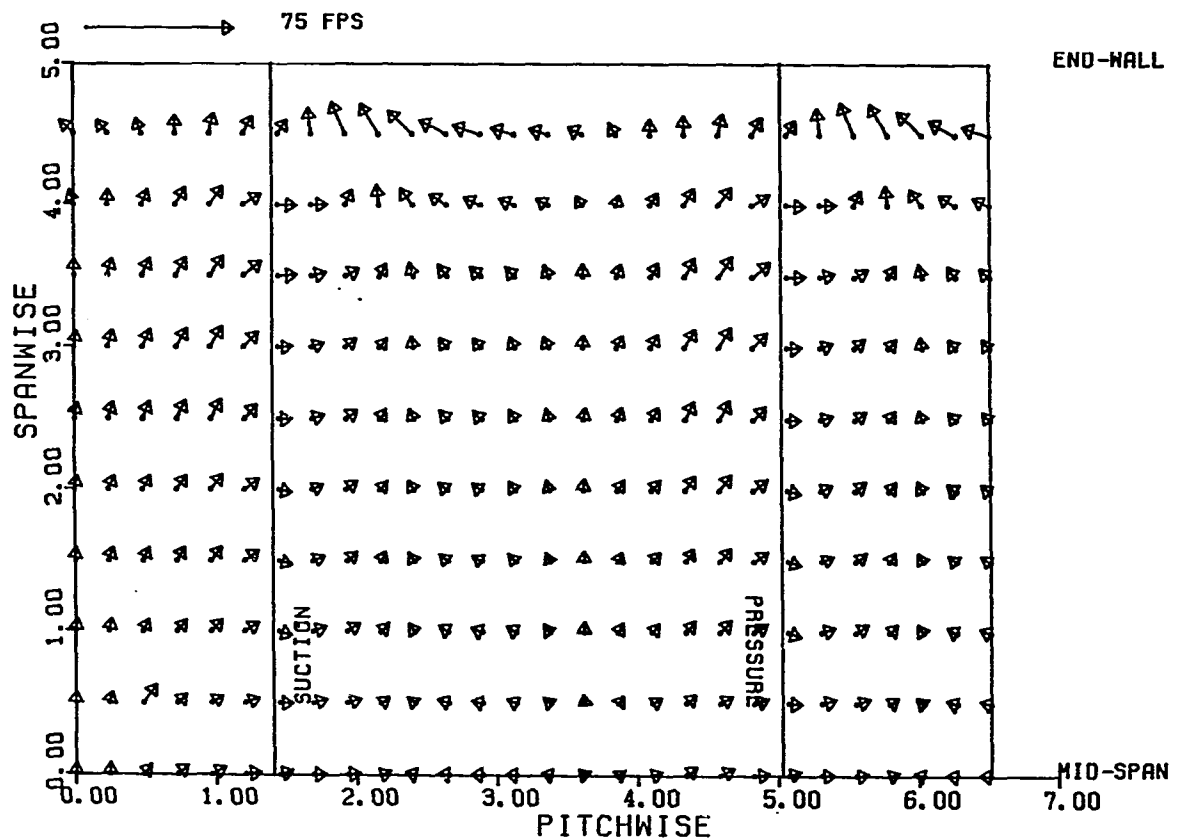


FIGURE 56. Secondary velocity vectors, $\beta_1 = 45^\circ$, NGRID, RE2

NO-GRID

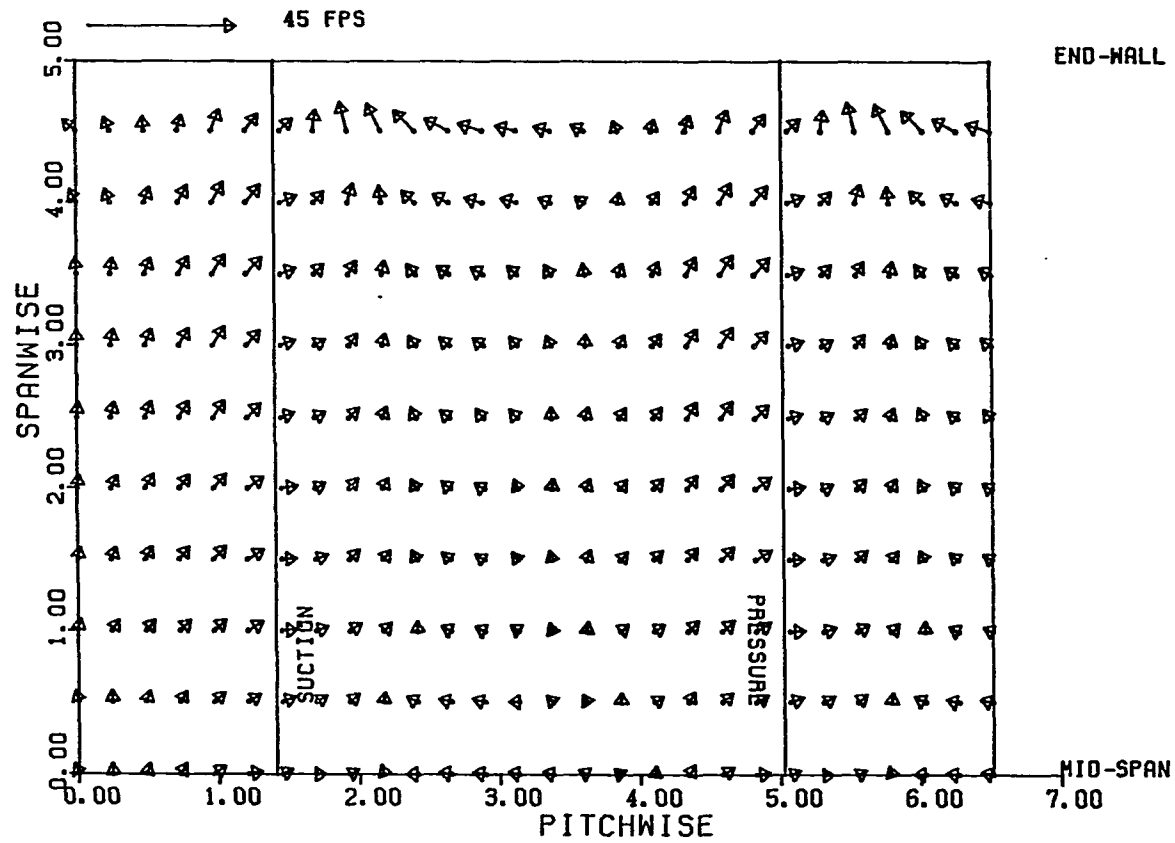


FIGURE 57. Secondary velocity vectors, $\beta_1 = 45^\circ$, NGRID, RE3

GRID1

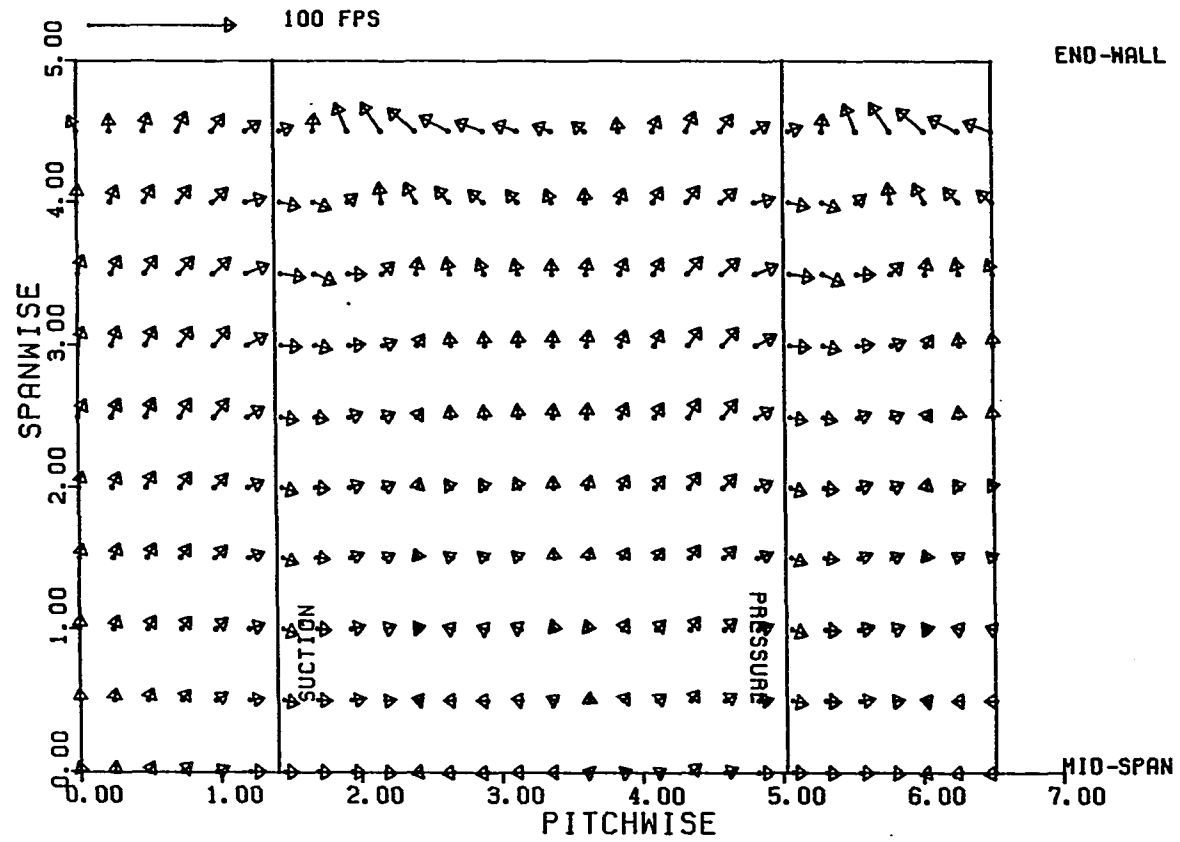


FIGURE 58. Secondary velocity vectors, $\beta_1 = 45^\circ$, GRID1, RE1

GRID2

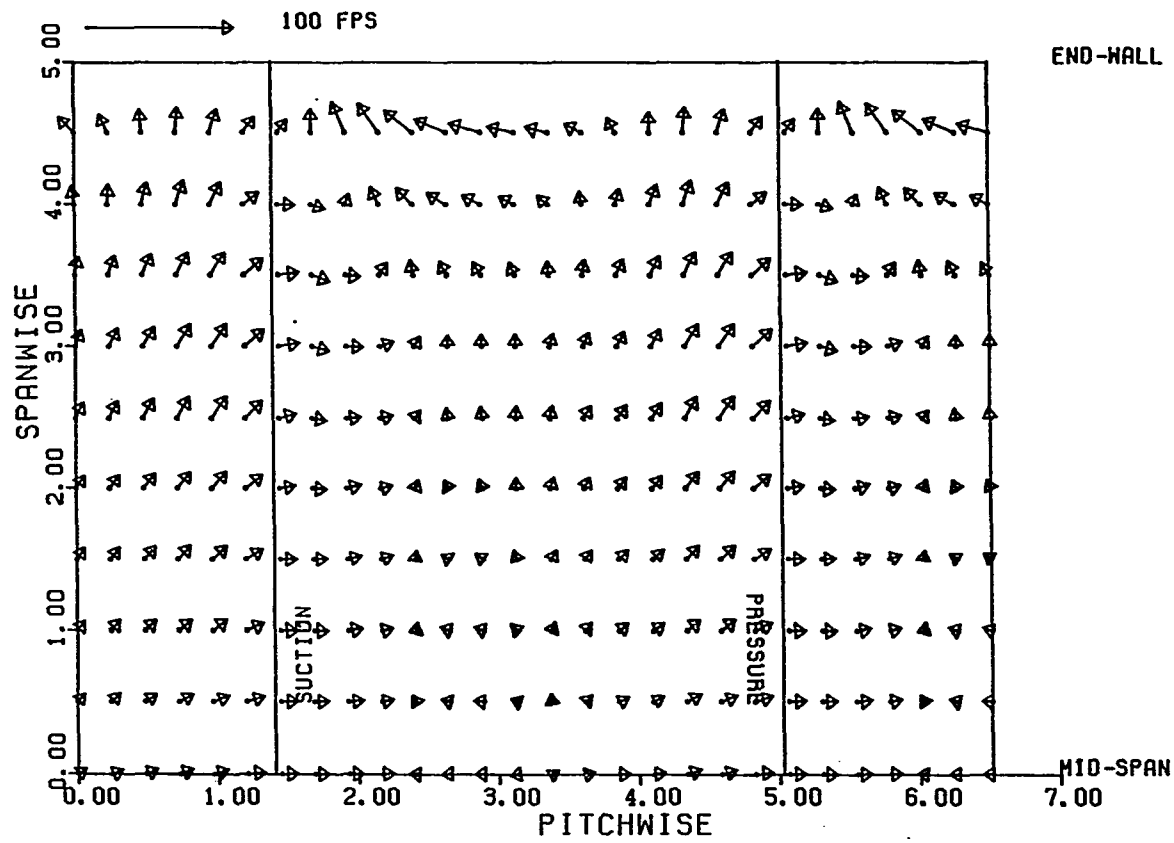


FIGURE 59. Secondary velocity vectors, $\beta_1 = 45^\circ$, GRID2, RE1

GRID3

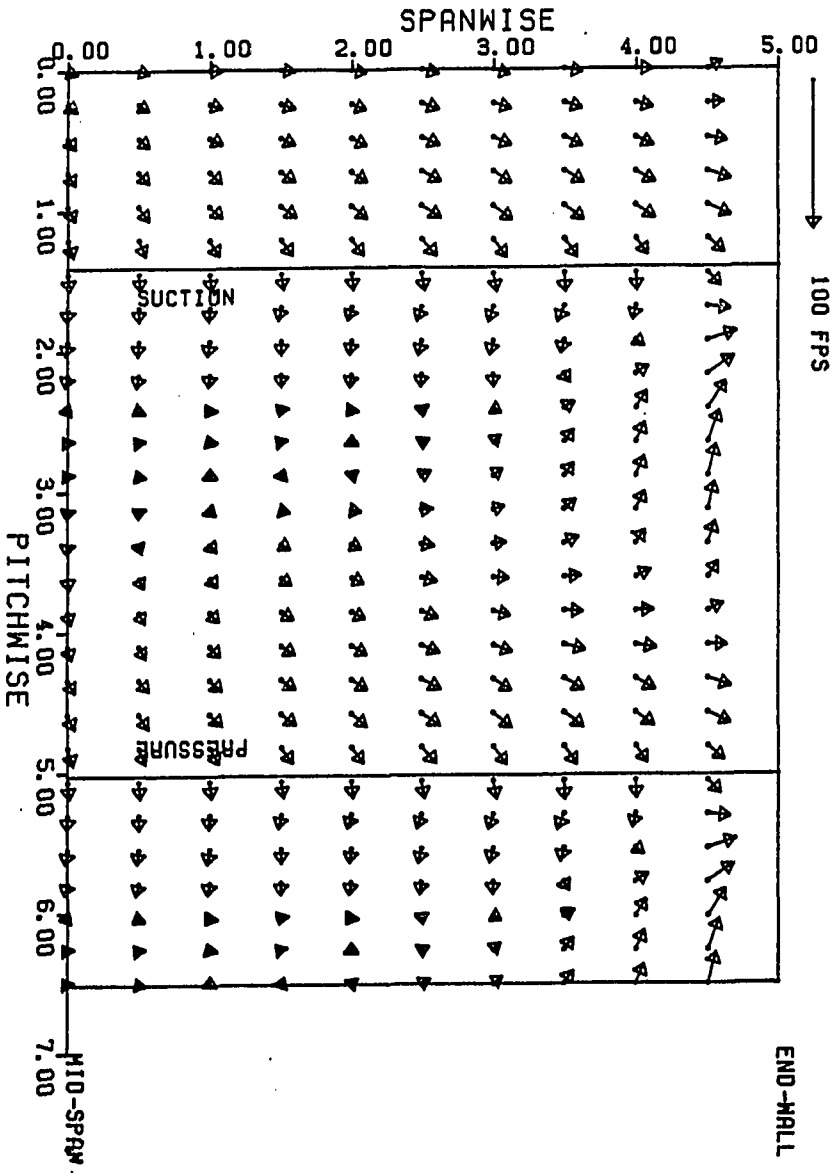


FIGURE 60. Secondary velocity vectors, $\beta_1 = 45^\circ$, GRID3, RE1

the entire passage flow is dominated by 3-D effects, with very little 2-D flow existing along the airfoil span. High loss levels are observed near the endwall boundary layer region and in the passage vortex.

Figure 65 shows the pitch-averaged values of the losses just discussed in Figures 61 through 64, with the pitch-averaged loss coefficient plotted against spanwise location. Loss levels are seen to increase slightly with turbulence level at midspan, but to decrease slightly in the region of the passage vortex. This decrease in loss levels in the vortex core can be attributed to the larger diffusion at high turbulence levels. The variation of the pitch-averaged loss coefficient over the blade span in Figure 65 is similar to the results of Langston et al. [51]. In general, the variation depends on the position of the passage vortex, which in turn depends on inlet endwall boundary layer thickness, aspect ratio and blade loading. More details on the variation of spanwise loss distribution with inlet endwall boundary layer and blade loading can be found in Sieverding [52], and in Gregory-Smith and Graves [53].

The total pressure loss coefficient contours are plotted again in Figures 66 through 71, but for the conditions of endwall suction applied. Figures 66 through 68 are for flow conditions NGRID and Reynolds numbers RE1, RE2, and RE3. The presence of the passage vortex can still be seen at the higher Reynolds numbers, although the associated loss levels are lower than in the case without endwall

suction (Figure 61). The contour lines are also parallel for at least half the span, indicating 2-D flow over the airfoil in that region. Figures 69 through 71 show the contour plot of loss coefficient for flow conditions GRID1, GRID2, GRID3, and Reynolds number RE1. Again, the plots indicate 2-D flow over a large portion of the span and lower loss levels as compared to those for no endwall suction.

Figure 72 is a composite plot of pitch-averaged loss coefficient with endwall suction for all the tested turbulence levels and Reynolds numbers. When compared to Figure 65 (without endwall suction), it can be seen that the loss levels are lower. Also, the characteristic hump in the curves representing the passage vortex is much closer to the endwall, if indeed not completely absent. The increase in loss levels as the endwall is approached is due both to endwall boundary layer and passage vortex effects. Near midspan, a constant loss coefficient representing the 2-D profile loss is observed over a large portion of the span.

It is seen from Figure 72 that the profile losses for a given turbulence level does not change with Reynolds number. This may be explained by the relatively narrow range of Reynolds numbers investigated (7.1×10^5 to 3.3×10^5). Within this range, the flow is largely transitional, and trends in losses are generally unpredictable. Denton [54] discusses the effects of Reynolds number on cascade losses and summarizes that, for Reynolds numbers less than 10^5 , the flow is predominantly laminar and losses vary as $Re^{-0.5}$, while for Reynolds

numbers greater than 10^6 , the flow is predominantly turbulent and losses vary as $Re^{-0.2}$. However, in the Reynolds number range of 10^5 to 10^6 , Denton indicates that losses may either increase, decrease or remain constant, depending upon other factors such as surface roughness, surface velocity distribution and turbulence level.

Finally it is observed in Figure 72 that losses do not change appreciably with turbulence level. This behavior in the losses is due to compensating effects. At low turbulence levels, where one would expect losses to be lower, separation bubbles appear on the airfoil to again increase the losses to levels comparable to those at higher turbulence levels. More discussion on the effects of turbulence level on losses is presented following the results of glue-on hot-film gage measurements.

4. Hot-wire traverse results

Results from hot-wire traverses conducted in the cascade exit plane are presented as turbulence level contour plots for the four tested inlet turbulence levels. Endwall suction was applied for all the cases.

Figure 73 shows the turbulence level contours for flow conditions NGRID and Reynolds number $RE1$. The upper half-span of the passage for one blade pitch is shown, with the endwall at the top of the plot. As seen in Figure 73, turbulence level varies from less than 1% in the main flow to over 15% in the core of the passage vortex. In the wake region, the turbulence level is as high as 9%. When compared to Figure

CURVE LABEL	CURVE VALUE	8	0.80000E 00
1	0.10000E 00	9	0.90000E 00
2	0.20000E 00	10	0.10000E 01
3	0.30000E 00	11	0.11000E 01
4	0.40000E 00	12	0.12000E 01
5	0.50000E 00	13	0.13000E 01
6	0.60000E 00	14	0.14000E 01
7	0.70000E 00	15	0.15000E 01

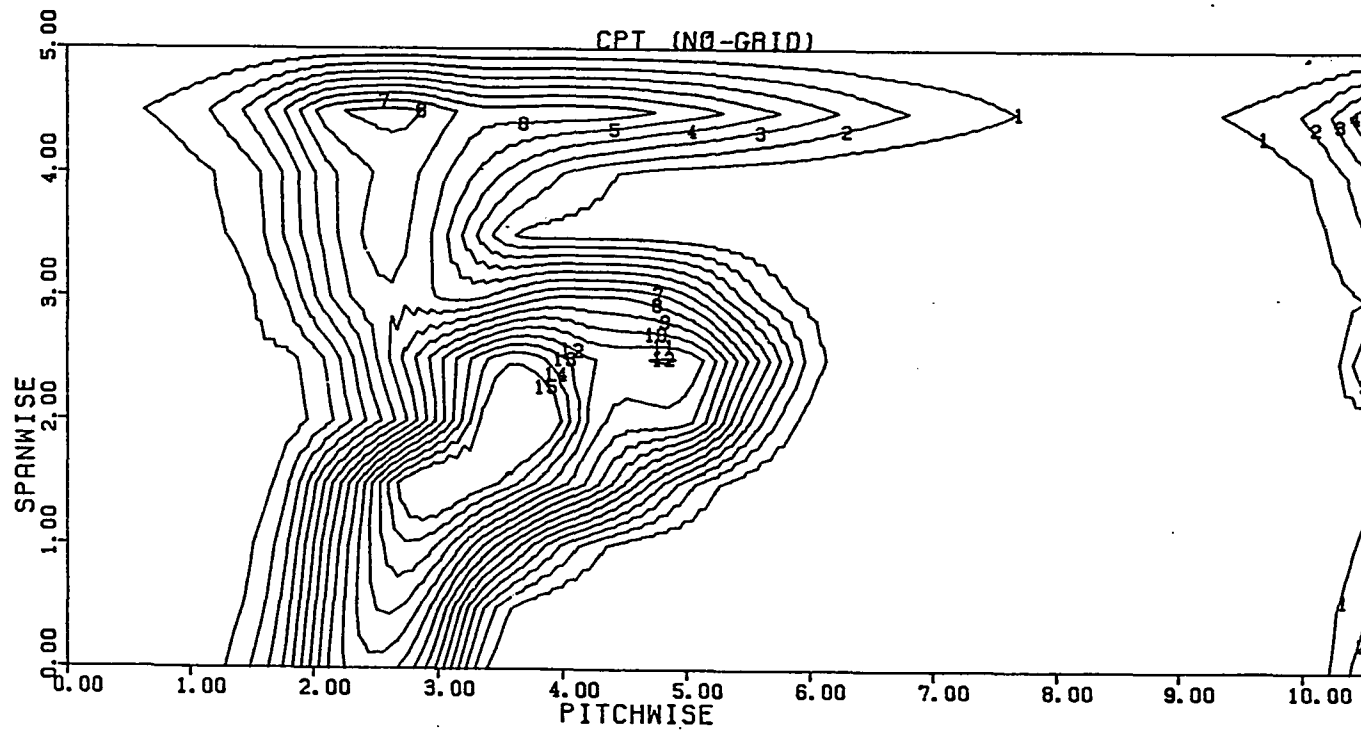


FIGURE 61. Total pressure loss contours, $\beta_1 = 45^\circ$, NGRID, RE1 (No endwall suction)

CURVE LABEL	CURVE VALUE
8	0.800000E 00
1	0.100000E 00
2	0.200000E 00
3	0.300000E 00
4	0.400000E 00
5	0.500000E 00
6	0.600000E 00
7	0.700000E 00
9	0.900000E 00
10	0.100000E 01
11	0.110000E 01
12	0.120000E 01
13	0.130000E 01
14	0.140000E 01
15	0.150000E 01

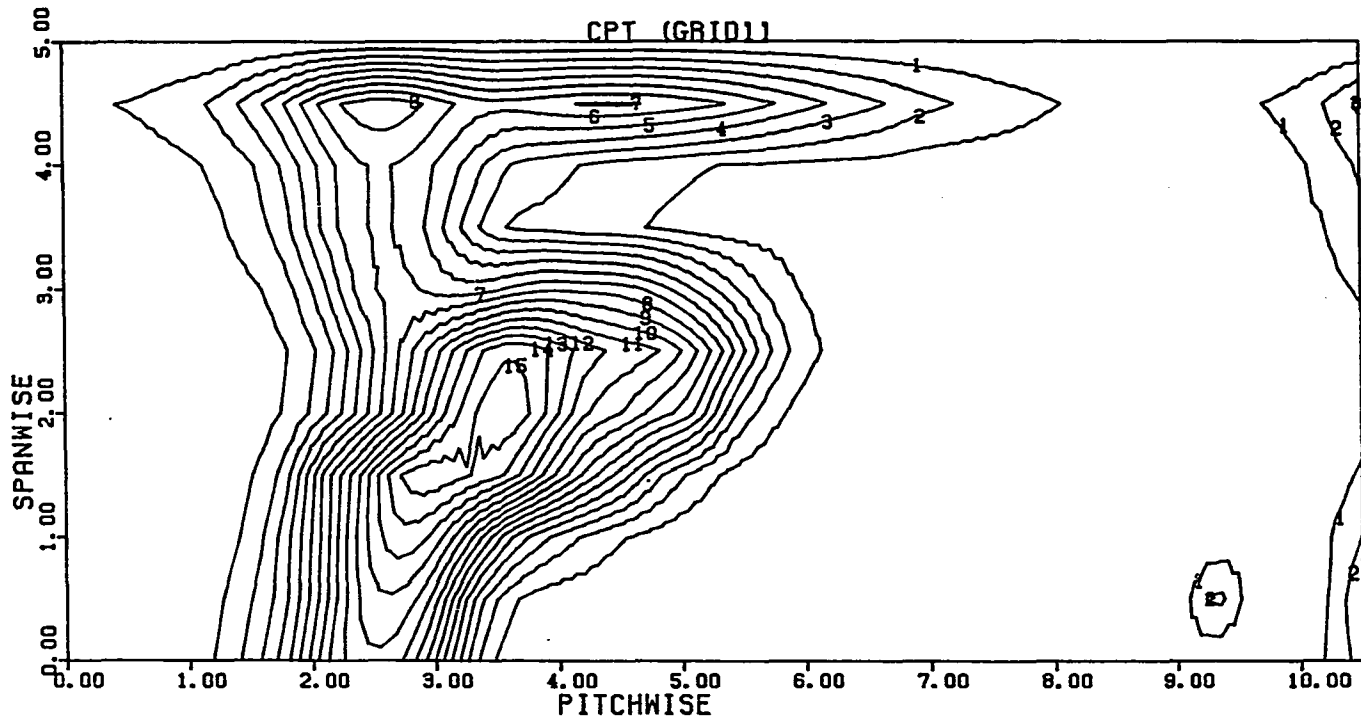


FIGURE 62. Total pressure loss contours, $\beta_1 = 45^\circ$, GRID1, RE1 (No endwall suction)

CURVE LABEL	CURVE VALUE	CURVE LABEL	CURVE VALUE
1	0.100000E 00	8	0.800000E 00
2	0.200000E 00	9	0.900000E 00
3	0.300000E 00	10	0.100000E 01
4	0.400000E 00	11	0.110000E 01
5	0.500000E 00	12	0.120000E 01
6	0.600000E 00	13	0.130000E 01
7	0.700000E 00	14	0.140000E 01

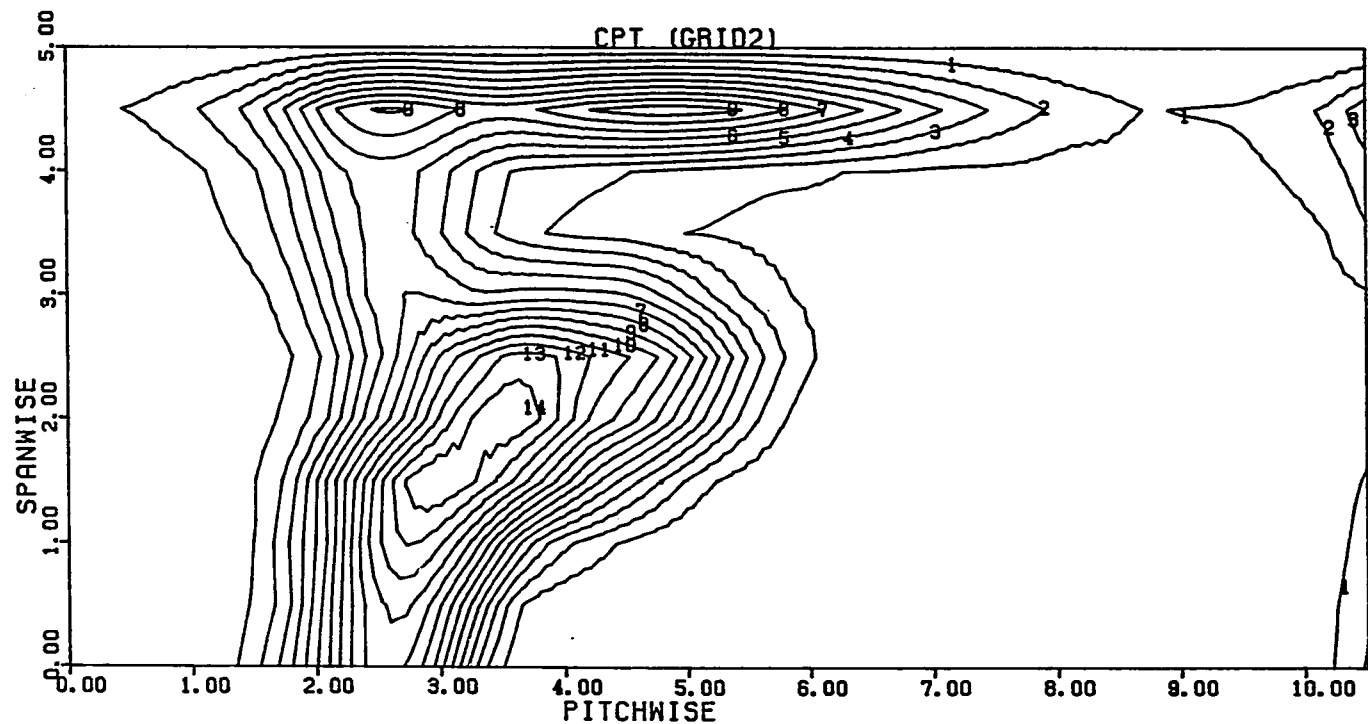


FIGURE 63. Total pressure loss contours, $\beta_1 = 45^\circ$, GRID2, RE1 (No endwall suction).

CURVE LABEL	CURVE VALUE	CURVE LABEL	CURVE VALUE
1	0.100000E 00	8	0.800000E 00
2	0.200000E 00	9	0.900000E 00
3	0.300000E 00	10	0.100000E 01
4	0.400000E 00	11	0.110000E 01
5	0.500000E 00	12	0.120000E 01
6	0.600000E 00	13	0.130000E 01
7	0.700000E 00	14	0.140000E 01

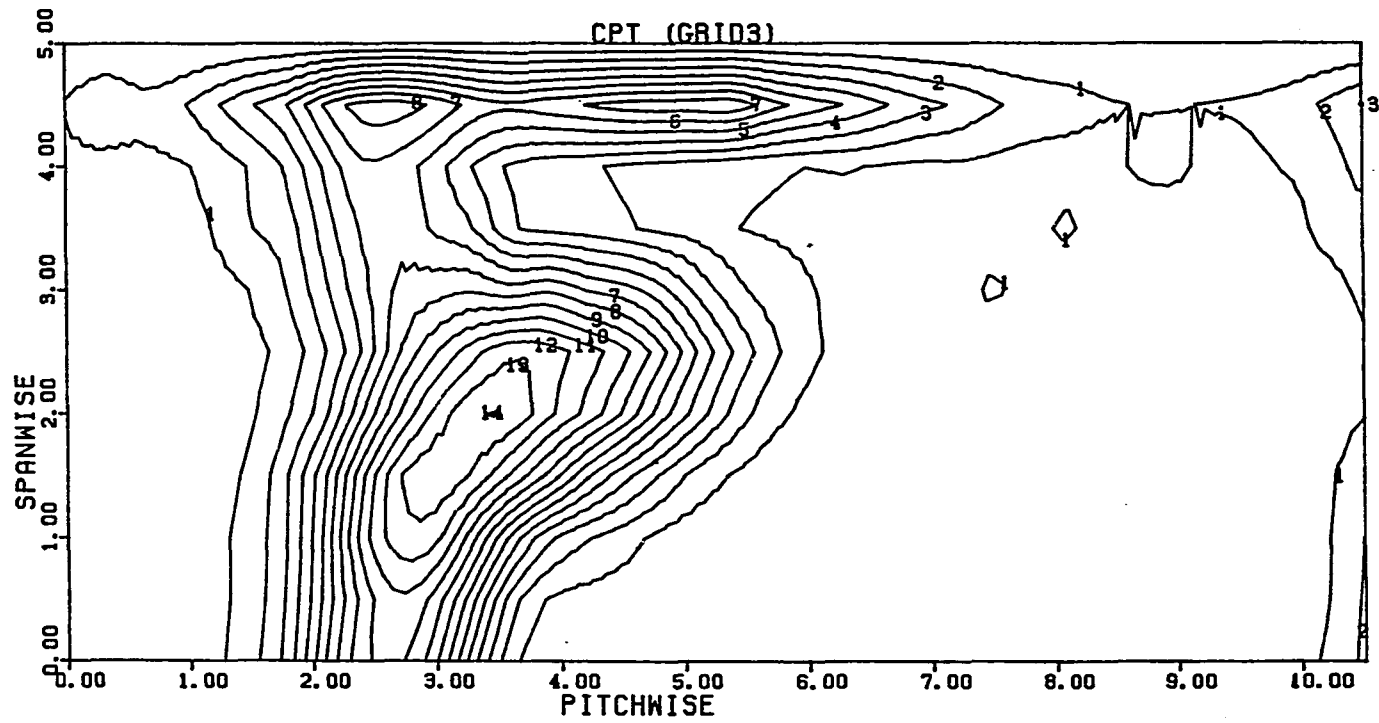


FIGURE 64. Total pressure loss contours, $\beta_1 = 45^\circ$, GRID3, RE1 (No endwall suction)

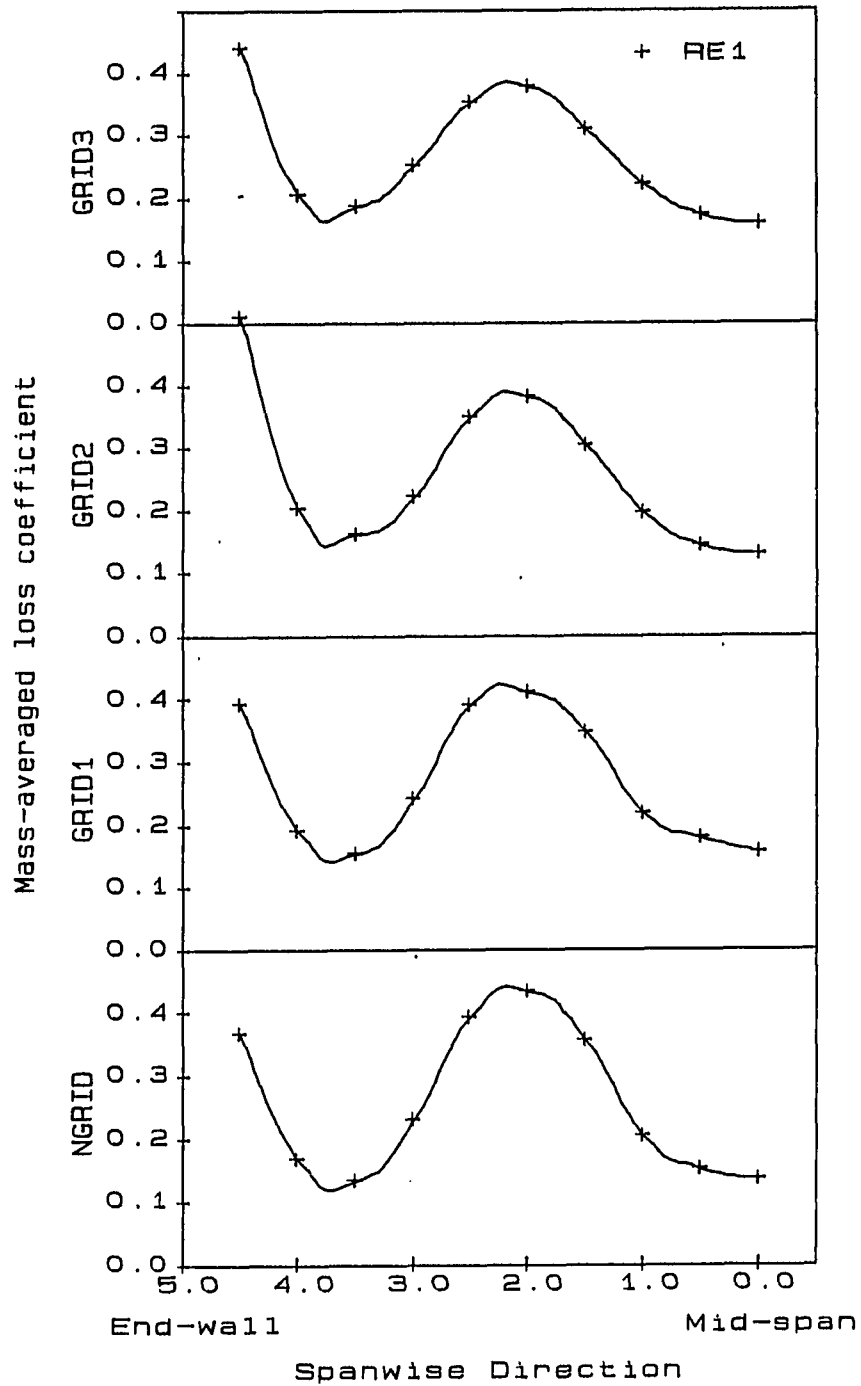


FIGURE 65. Pitch-averaged loss coefficient, $\beta_1 = 45^\circ$ (No endwall suction)

CURVE LABEL	CURVE VALUE
1	0.100000E 00
2	0.200000E 00
3	0.300000E 00
4	0.400000E 00
5	0.500000E 00
6	0.600000E 00
7	0.700000E 00
8	0.800000E 00
9	0.900000E 00
10	0.100000E 01
11	0.110000E 01

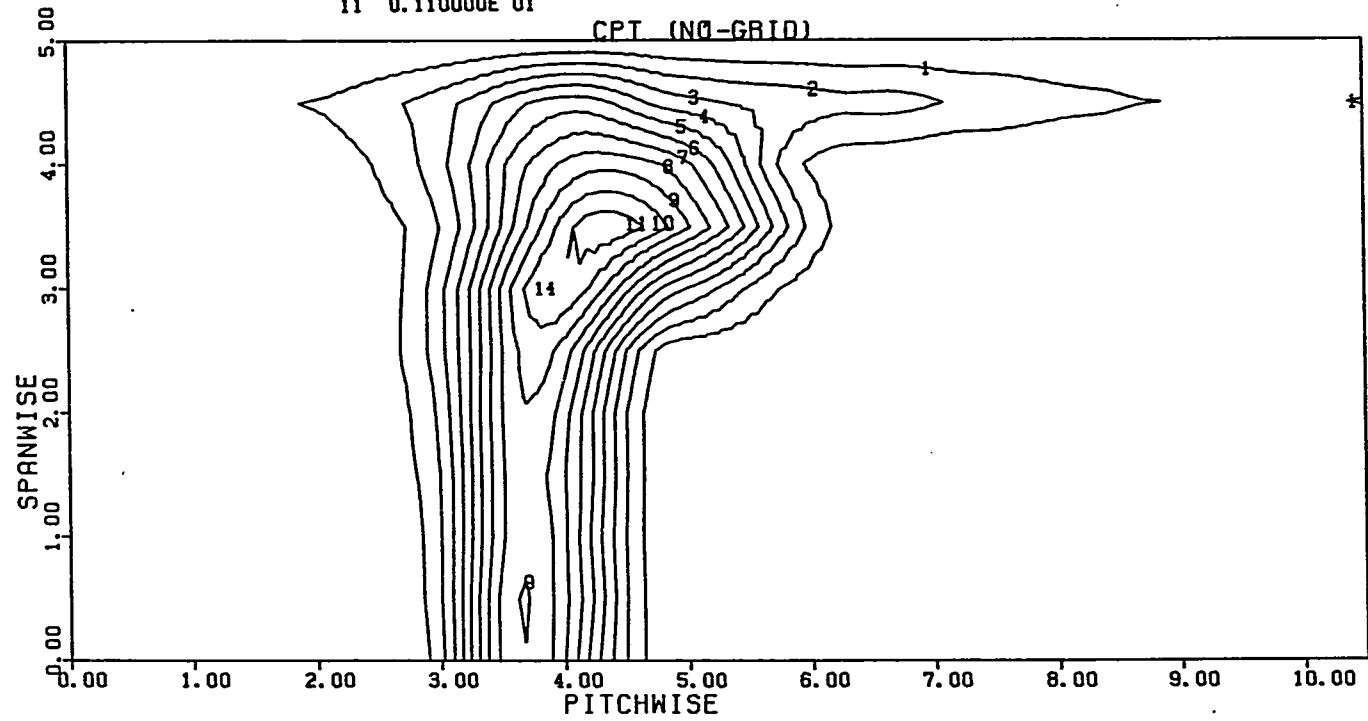


FIGURE 66. Total pressure loss contours, $\beta_1 = 45^\circ$, NGRID, RE1

CURVE LABEL	CURVE VALUE
1	0.100000E 00
2	0.200000E 00
3	0.300000E 00
4	0.400000E 00
5	0.500000E 00
6	0.600000E 00
7	0.700000E 00
8	0.800000E 00
9	0.900000E 00
10	0.100000E 01

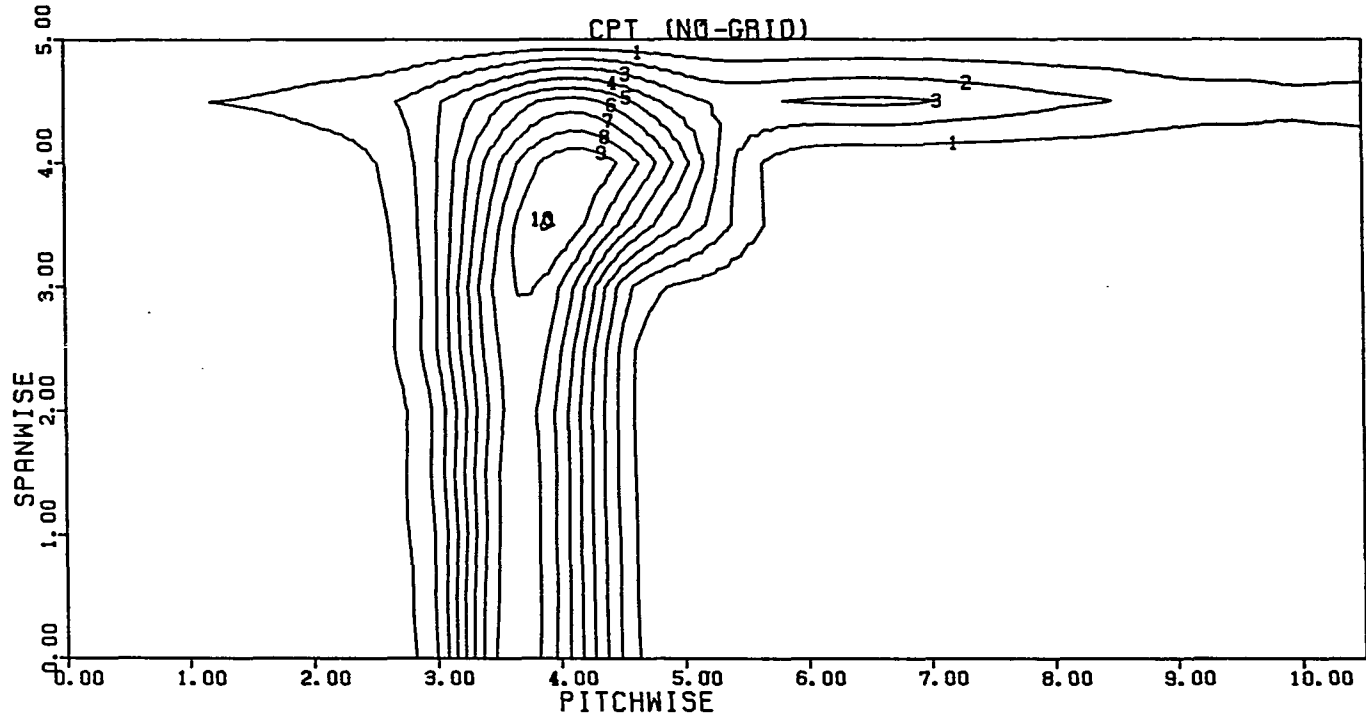


FIGURE 67. Total pressure loss contours, $\beta_1 = 45^\circ$, NGRID, RE2

CURVE LABEL	CURVE VALUE
1	0.100000E 00
2	0.200000E 00
3	0.300000E 00
4	0.400000E 00
5	0.500000E 00
6	0.600000E 00
7	0.700000E 00
8	0.800000E 00
9	0.900000E 00

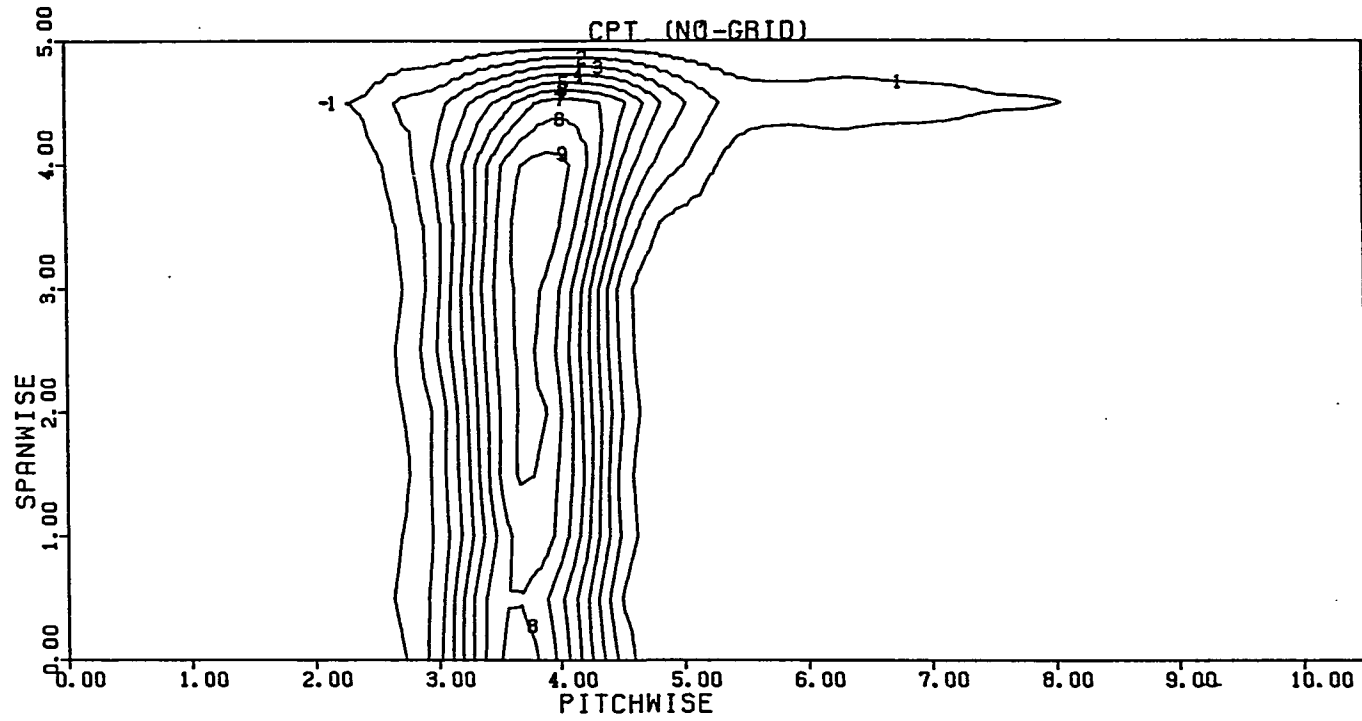


FIGURE 68. Total pressure loss contours, $\beta_1 = 45^\circ$, NGRID, RE3

CURVE LABEL	CURVE VALUE
1	0.100000E 00
2	0.200000E 00
3	0.300000E 00
4	0.400000E 00
5	0.500000E 00
6	0.600000E 00
7	0.700000E 00
8	0.800000E 00
9	0.900000E 00
10	0.100000E 01

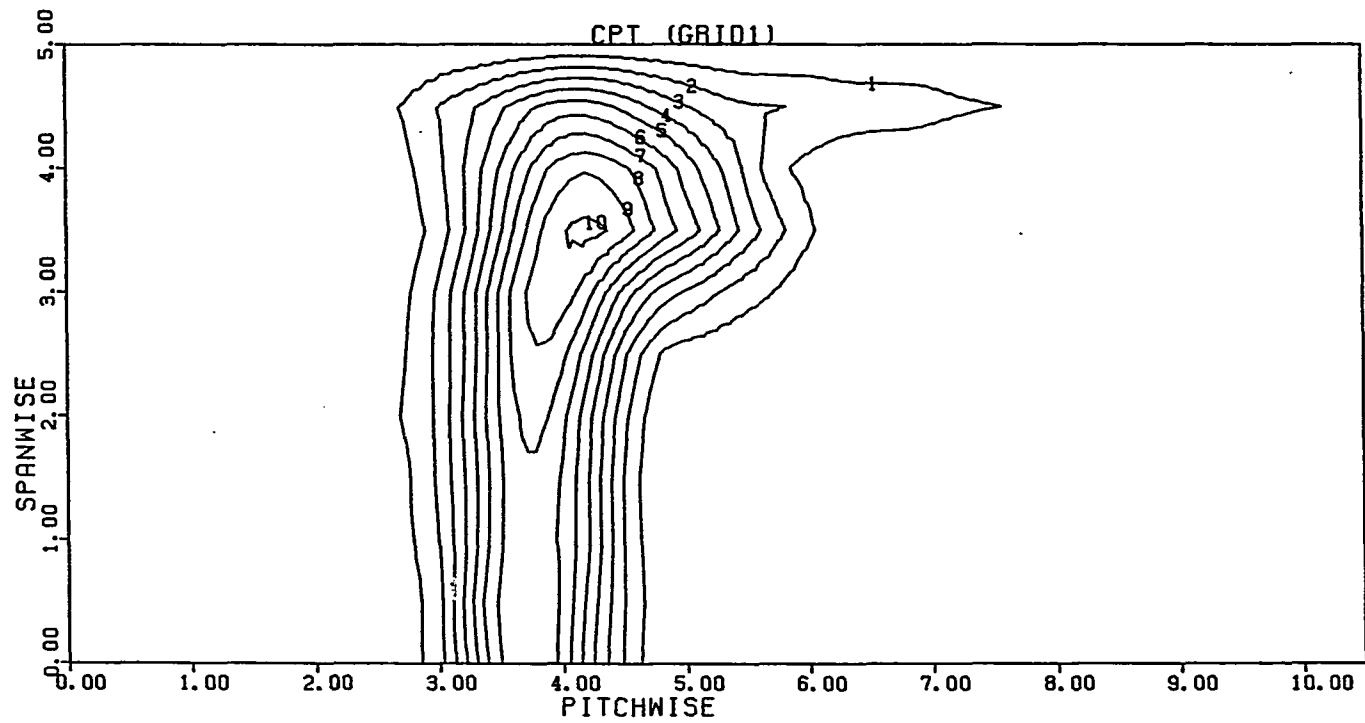


FIGURE 69. Total pressure loss contours, $\beta_1 = 45^\circ$, GRID1, RE1

CURVE LABEL	CURVE VALUE
1	0.100000E 00
2	0.200000E 00
3	0.300000E 00
4	0.400000E 00
5	0.500000E 00
6	0.600000E 00
7	0.700000E 00
8	0.800000E 00
9	0.900000E 00

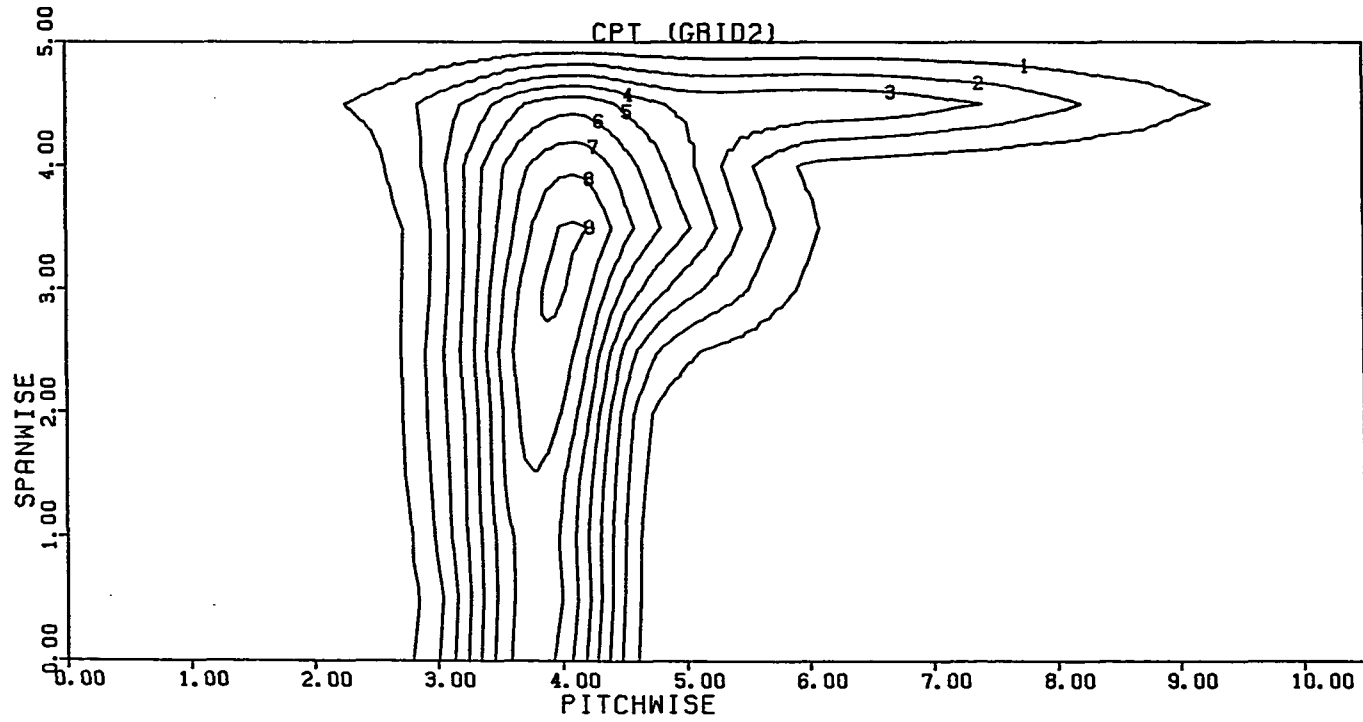


FIGURE 70. Total pressure loss contours, $\beta_1 = 45^\circ$, GRID2, RE1

CURVE LABEL	CURVE VALUE
1	0.100000E 00
2	0.200000E 00
3	0.300000E 00
4	0.400000E 00
5	0.500000E 00
6	0.600000E 00
7	0.700000E 00
8	0.800000E 00

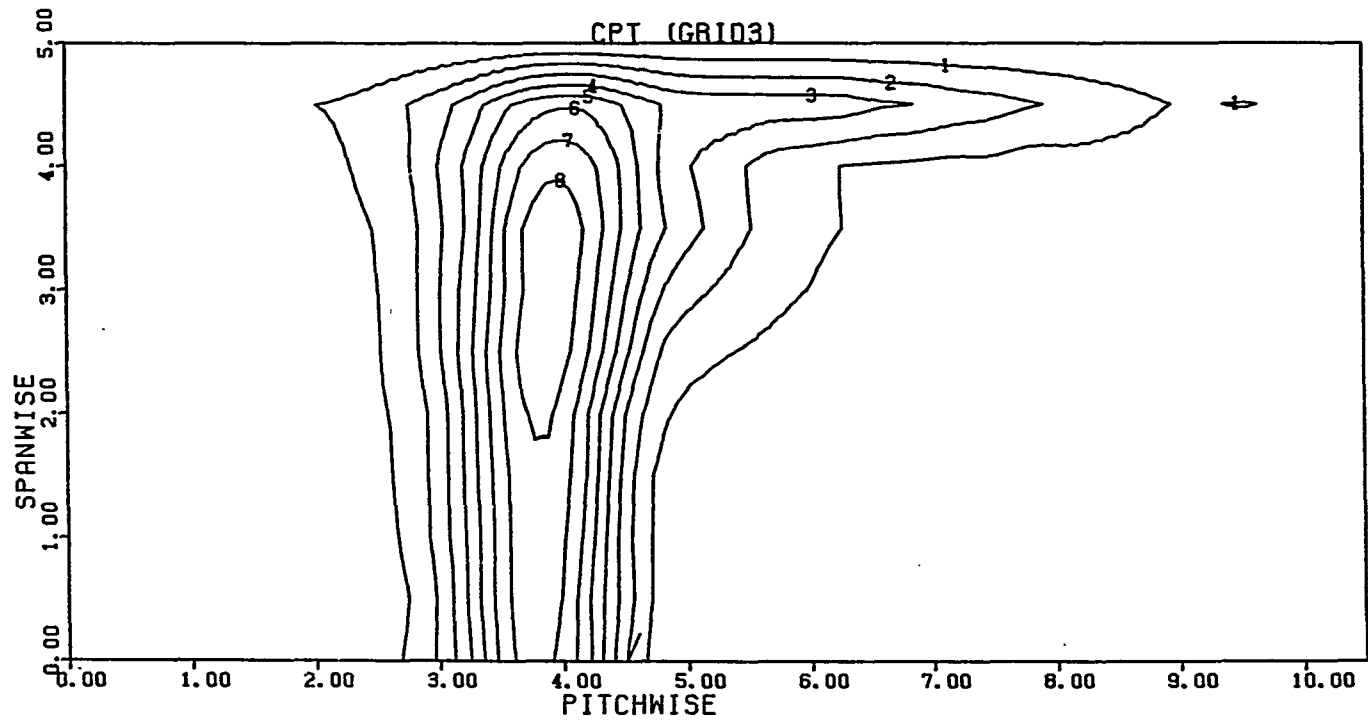


FIGURE 71. Total pressure loss contours, $\beta_1 = 45^\circ$, GRID3, RE1

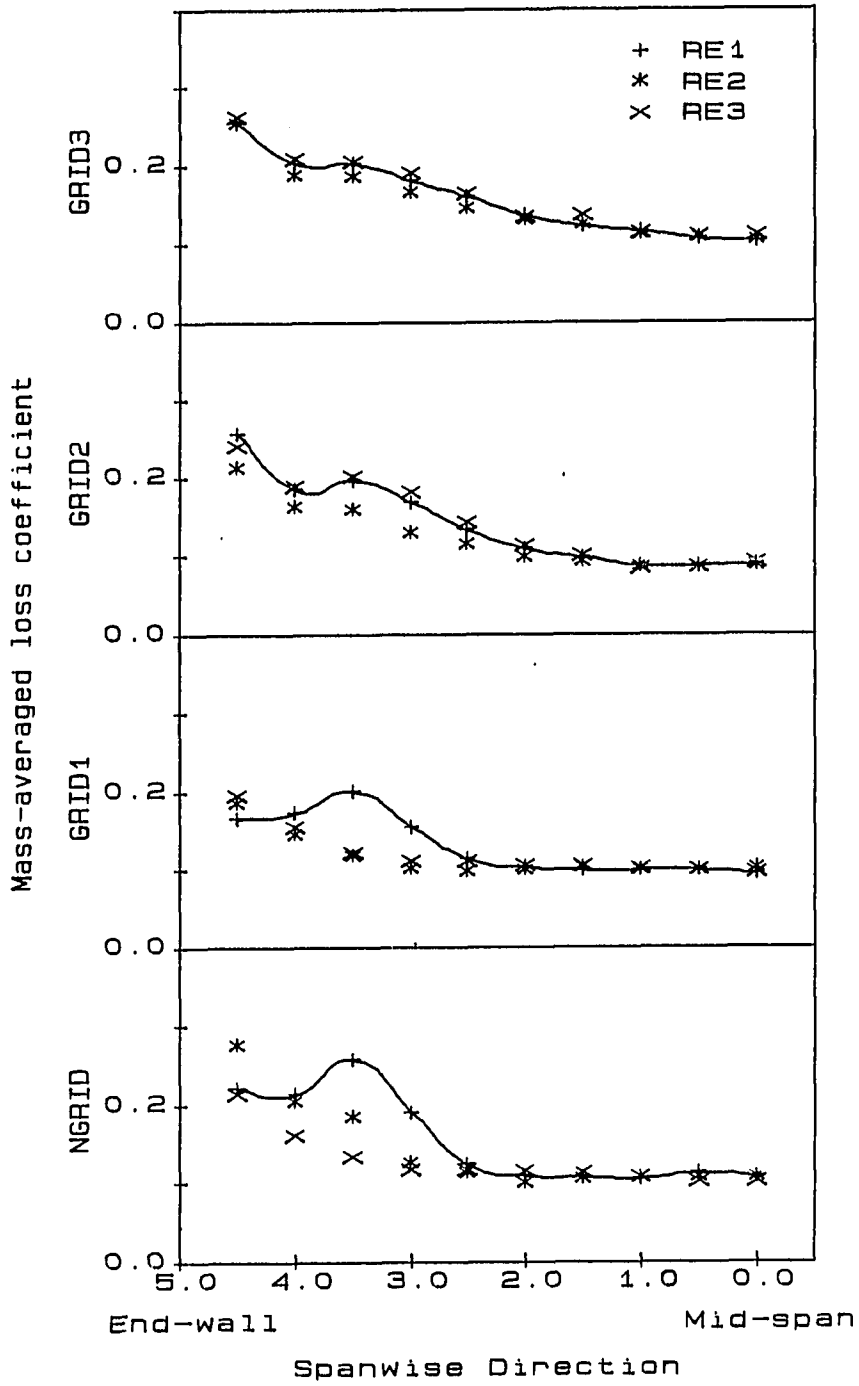


FIGURE 72. Pitch-averaged loss coefficient, $\beta_1 = 45^\circ$ (With endwall suction)

66, which is a plot of loss coefficient contours for this case, it can be seen that the high turbulence levels in the passage vortex coincide with high losses. In general, the loss and turbulence level contours are similar, confirming the location of the passage vortex.

Figures 74, 75, and 76 show the turbulence level contours for flow conditions GRID1, GRID2, and GRID3 and Reynolds number RE1. In these Figures, turbulence level in the main flow is about 1.5% for GRID1, 2.8% for GRID2, and 3.4% for GRID3. In the vortex core, the turbulence level is about 16% for GRID1, and about 15% for GRID2 and GRID3. The general features observed in Figure 73 are also observed in Figures 74, 75, and 76. The locations of the vortex core in these three Figures coincide with those determined by the loss coefficient contours in the corresponding cases in Figures 69, 70, and 71. Also, the shape of the loss and turbulence level contours are similar.

The following general features are observed from the turbulence level contour plots. The highest measured turbulence level is in the core of the passage vortex and is independent of the inlet turbulence level. The wake region as indicated by the turbulence level contours appears to be wider than that indicated by the loss contours. However, the apparently narrower wake regions indicated by the loss contours may be explained by considering that the lowest contour levels of loss coefficient start at 0.1. Actual measured loss coefficient at midspan for NGRID and RE1 was 0.02 at a pitch location of 2.4 in, and 0.03 at a pitch location 4.8 in. If contours for these loss coefficient values

CURVE LABEL	CURVE VALUE
1	0.100000E 01
2	0.300000E 01
3	0.500000E 01
4	0.700000E 01
5	0.900000E 01
6	0.110000E 02
7	0.130000E 02
8	0.150000E 02

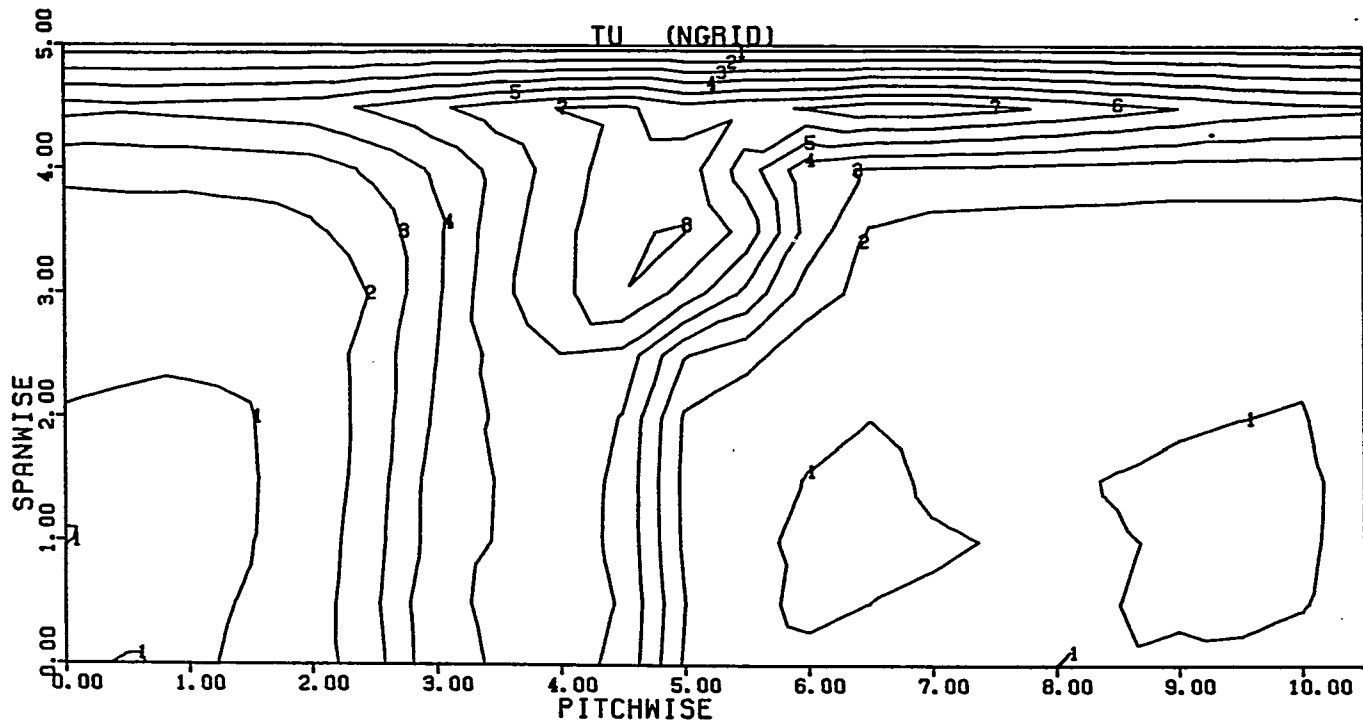


FIGURE 73. Turbulence level contours, $\beta_1 = 45^\circ$, NGRID, RE1

CURVE LABEL	CURVE VALUE
1	0.20000E 01
2	0.40000E 01
3	0.60000E 01
4	0.80000E 01
5	0.10000E 02
6	0.12000E 02
7	0.14000E 02
8	0.16000E 02

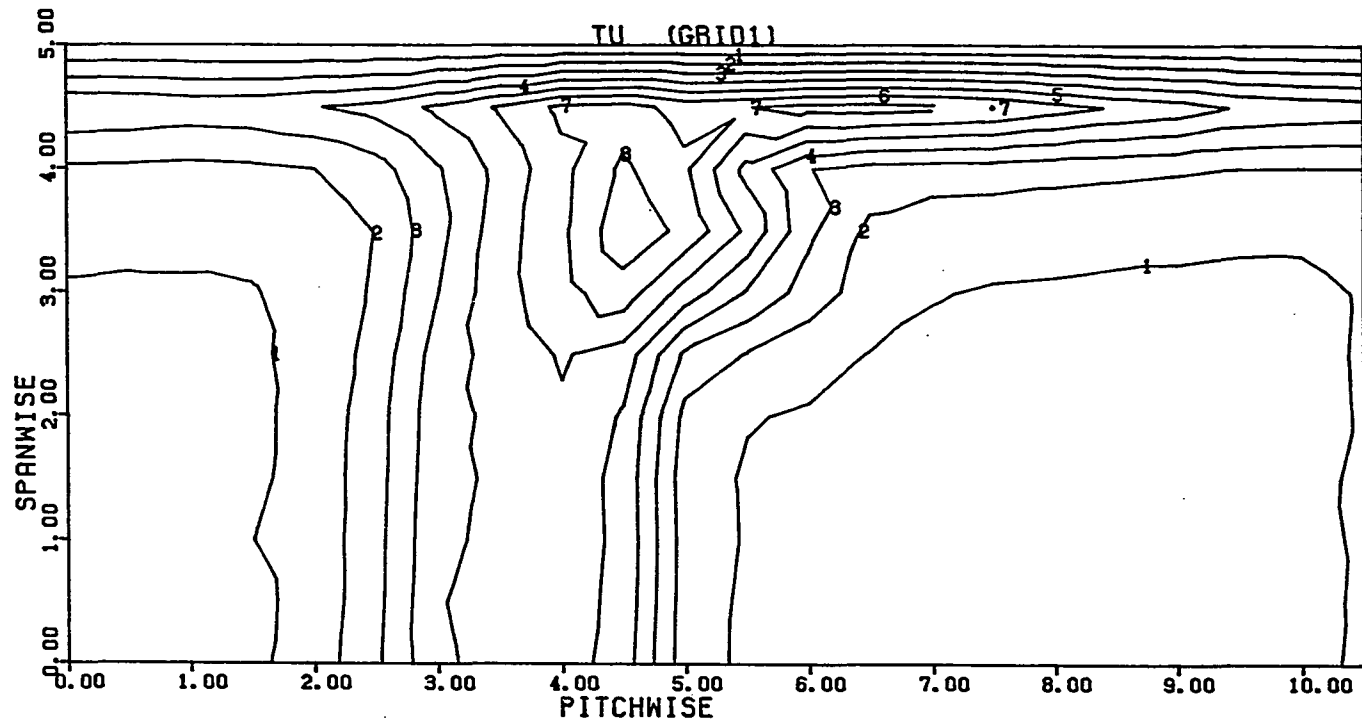


FIGURE 74. Turbulence level contours, $\beta_1 = 45^\circ$, GRID1, RE1

CURVE LABEL	CURVE VALUE
1	0.30000E 01
2	0.50000E 01
3	0.70000E 01
4	0.90000E 01
5	0.11000E 02
6	0.13000E 02
7	0.15000E 02

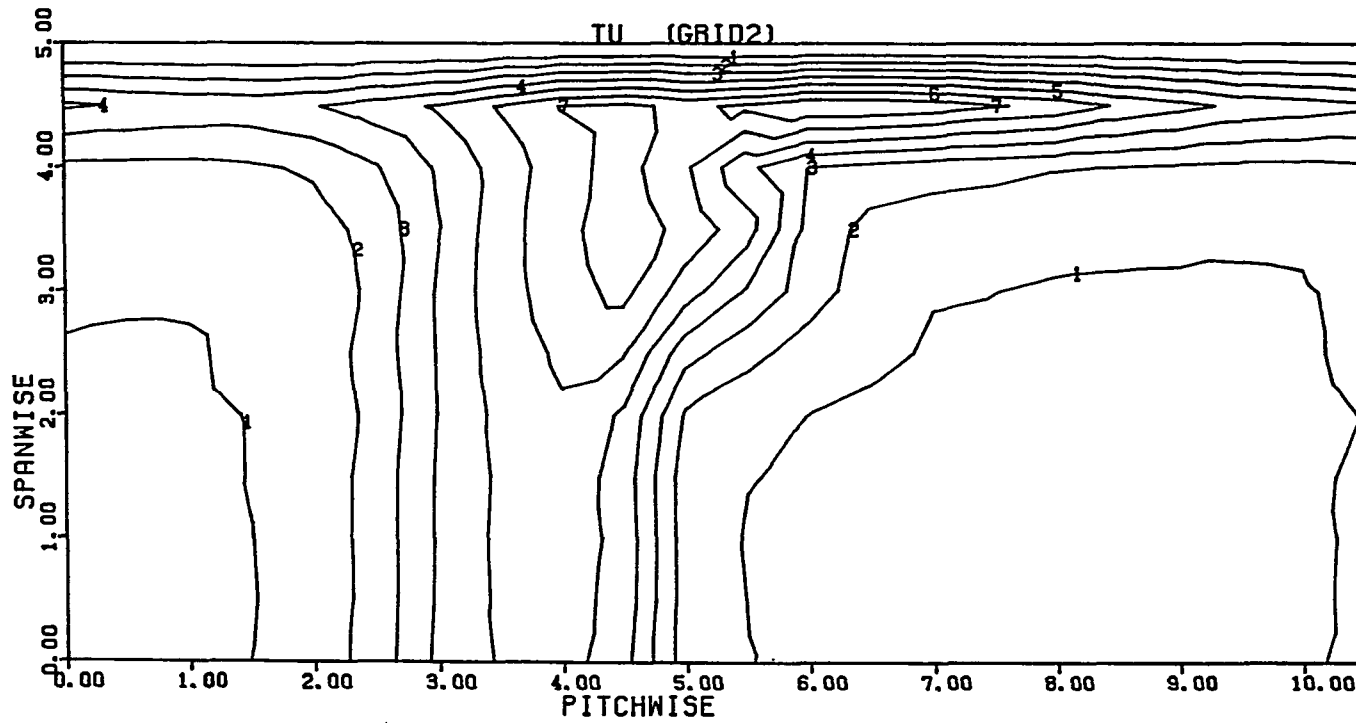


FIGURE 75. Turbulence level contours, $\beta_1 = 45^\circ$, GRID2, RE1

CURVE LABEL	CURVE VALUE
1	0.40000E 01
2	0.60000E 01
3	0.80000E 01
4	0.10000E 02
5	0.12000E 02
6	0.14000E 02
7	0.15000E 02

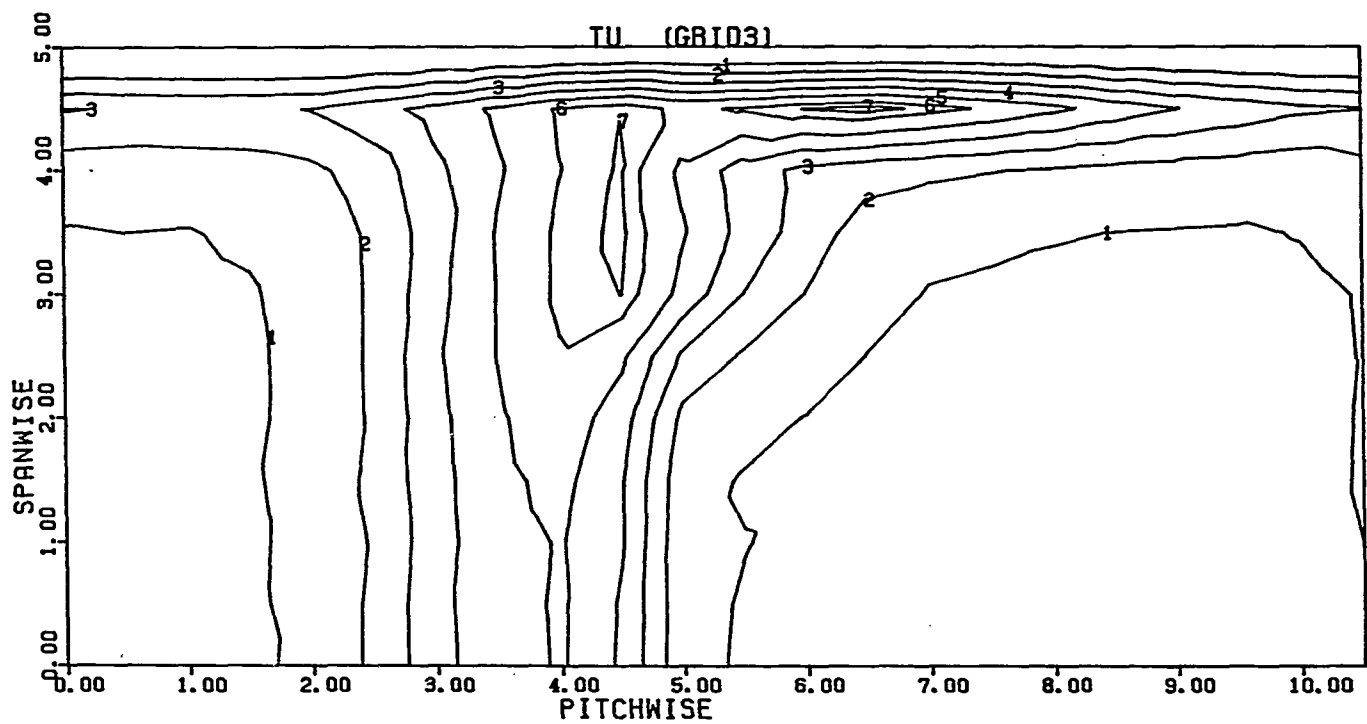


FIGURE 76. Turbulence level contours, $\beta_1 = 45^\circ$, GRID3, RE1

were also considered in the loss contour plot in Figure 66, a wider wake region similar to the one in the turbulence level contours would be seen.

With regard to measured turbulence levels for the main flow in the exit plane, it was found that in the NGRID case the turbulence level increased from an inlet turbulence level of 0.8% to about 1.0%. For the GRID1, GRID2, and GRID3 cases, however, the turbulence level in the exit plane decreased from inlet levels of 2.0%, 4.5%, and 6.4% to about 1.5%, 2.8%, and 3.4%, respectively. These reductions indicate reduction ratios of 0.75, 0.62, and 0.54. For the design area contraction ratio of 1.76 ($\sin\beta_1/\sin\beta_2$) for the cascade, Batchelor's [55] linear analysis of decay of local turbulence level predicts a turbulence level reduction ratio of 0.6. This predicted ratio agrees closely with the measured ratio for GRID2, while for NGRID and GRID1 the measured ratio is higher, and for GRID3 the measured ratio is lower. These differences in the measured and predicted ratios may be explained by considering the two opposing effects acting on the local turbulence level. First there is an amplifying effect due to the contribution of the passage vortex and endwall bleeds; secondly, there is a decaying effect due to the flow acceleration in the blade passage. At low inlet turbulence levels, the amplifying effect is dominant and, as a result, the exit turbulence level is higher than predicted. However, at high inlet turbulence levels, while the amplifying effect remains the same, the decaying effect dominates.

5. Hot-film gage results

Results obtained from the glue-on hot-film gages on the suction surface of the airfoil are presented for the four turbulence levels and three Reynolds numbers tested. As described previously, fourteen gages were used, positioned at 1.0 in intervals along the suction surface. The gages were numbered #1 through #14, starting with the one near the leading edge. Noting the location of the gages against the static pressure distribution for this inlet angle case (see Figure 77) it is seen that gages #1 through #4 are located in a favorable pressure gradient, gages #6 through #14 are located in an adverse pressure gradient, and gage #5 is located close to the minimum pressure point.

a. Time-domain analysis The time-domain analysis results are shown in Figures 78 through 89. Each Figure is composed of a part (a) which is a plot of the mean and RMS voltage for each gage, and a part (b) which presents sample 0.1 second traces of the A.C. signal recorded for each gage. The mean and RMS voltages are plotted as normalized values $(E-E_0)/E_0$ and e/E_0 , respectively, where E_0 is the gage zero-flow condition voltage. Since the mean and the RMS voltage signals can be interpreted as the time-averaged and fluctuating wall shear stresses, the state of the profile boundary layer and its development along the suction surface can be determined from the hot-film gage results.

Figure 78 shows the gage results for flow conditions NGRID and Reynolds number RE1. As seen in part (a) of Figure 78, the mean signal initially increases for gages #1 through #4 due to the strong

acceleration of the flow over the forward portion of the airfoil, which in turn leads to increased shear stress (see Schlichting [3]). Just beyond gage #4, the mean signal reduces again, since the shear stress decreases as the flow approaches an adverse pressure gradient region, and a laminar separation bubble is formed between gages #6 and #8. The formation of the bubble is also confirmed in the flow visualizations. Within the separated region, the mean signal reduces dramatically and then increases again to a maximum when the boundary layer reattaches. Beyond gage #8, the boundary layer is completely turbulent, and the mean signal reduces again with the boundary layer developing in an adverse pressure gradient. The associated RMS signal in part (a) of Figure 78 is seen to remain constant in the laminar region, and then increase sharply to a maximum at gage #6 where the laminar bubble has formed. After the boundary layer has reattached as a turbulent layer, the RMS signal remains nearly constant. The observed sudden increase in RMS signal is typical of boundary layer transition; however, for bubble-induced transition, as in this case, the RMS signal quickly reaches a constant value downstream of the bubble to indicate a relatively short transition length. As will be seen from the hot-film gage results at higher turbulence levels, natural transition shows longer transition lengths. Hence, a short transition length accompanied by distinct minimum and maximum mean heat transfer rates is characteristic of bubble-induced transition. These characteristics of minimum and maximum mean heat transfer rates corresponding to boundary

layer separation and reattachment have also been observed in hot-film gage measurements by Pucher and Göhl [56], and Bellhouse and Shultz [46].

In part (b) of Figure 78, gages #1 through #5 show quiet signals, representing a laminar boundary layer. Gage #6 shows large unsteady signals which, in this case, corresponds to the separation bubble. The signals quiet down again at gage #7, but increase from there on, indicating a fully turbulent boundary layer near gage #8. Beyond gage #8, there is little difference in the signals, all of which represent a fully turbulent boundary layer.

Figure 79 presents results for flow conditions NGRID and Reynolds number RE2. Here, there are distinct minimum and maximum mean signals corresponding to a laminar separation bubble. The RMS signal shows a sudden jump beyond gage #7, and then tends to a constant value beyond gage #9. In part (b) of Figure 79, the signal trace for gage #6 shows signs of turbulence, indicating that a laminar bubble is starting to form. Reattachment occurs at gage #8. Beyond gage #8, as in the preceding case, the signal is completely turbulent.

Figure 80 shows the results for flow conditions NGRID and Reynolds number RE3. The results are an extension of the RE1 and RE2 cases in Figures 78 and 79, with a laminar separation bubble beginning to form at gage #7 and the boundary layer reattaching as a turbulent boundary layer at gage #9. It is concluded from this discussion involving the three tested Reynolds numbers for NGRID, that at this low turbulence

level ($Tu = 0.8\%$) the boundary layer undergoes transition due to a separation bubble downstream of the minimum pressure point, and that, with decreasing Reynolds number, the separation point for the bubble moves further downstream.

Figures 81, 82, and 83 show results for flow conditions GRID1 and Reynolds numbers RE1, RE2, and RE3. For the case of RE1, no separation bubble is present, but natural transition occurs. According to part (a) of Figure 81, the mean signal shows a gradual increase in the accelerating region of the flow (gages #1 through #4), reaches a maximum at gage #6 in the transitional region, and then gradually decreases. However, little information regarding the state of the boundary layer is obtained from the mean signal. The RMS signal indicates transition starting between gages #4 and #5 and completing near gage #9. The laminar signals (gages #1 through #3) show higher values of the RMS signal as compared to the previous NGRID case due to the higher turbulence level. As will be seen from the results for GRID2 and GRID3, the RMS signal continues to increase as the turbulence level increases. The start of transition and development of a transitional boundary layer can also be clearly seen in the signal traces in part (b) of Figure 81. Turbulent spikes appear in traces for gages #4 and #5. For gage #6, the signal trace is predominantly turbulent, with laminar spikes in between. Fewer laminar spikes appear for gages #7 and #8, and by gage #9, the signal is completely turbulent.

Figure 82 shows the results for flow conditions GRID1 and Reynolds number RE2. For this case, the mean signals in part (a) shows distinct minimum and maximum values characteristic of separation. However, the RMS signals and the signal traces in part (b) of the Figure indicate that natural transition starts between gages #5 and #6. Hence, as inferred from the mean signals, the transitional flow extending into the adverse pressure gradient region tends to separate. The boundary layer becomes completely turbulent near gage #9. This conclusion is supported by the corresponding flow visualization, Figure 44, where no distinct separation bubble can be seen, but the flow pattern is not smooth to indicate a natural transition. For flow conditions GRID1 and Reynolds number RE3, as seen in part (a) of Figure 83, a separation bubble originates near gage #7 and reattaches near gage #9. The flow visualization in Figure 45 for this case also shows a separation bubble.

Hot-film gage results for GRID2 are shown in Figures 84, 85, and 86 for the three Reynolds numbers RE1, RE2, and RE3. For the Reynolds number RE1, the boundary layer undergoes natural transition. It can be seen from part (a) of Figure 84, that transition starts at gage #4 and is completed near gage #8. The signal traces in part (b) of Figure 84 show a transitional signal for gages #5, #6, and #7 with turbulent spikes for gage #5 and laminar spikes for gage #6 and #7. The situation is the same for the lower Reynolds number RE2. As seen in part (a) of Figure 85, transition starts at gage #5 and is completed by

gage #9. The signal traces in part (b) of Figure 85 show transition for gages #5 through #8. For Reynolds number RE3, as seen in part (a) of Figure 86, the transitional flow starting at gage #6 and extending into the adverse pressure gradient region tends to separate. The boundary layer is completely turbulent near gage #9. The mean signal, showing a clear minimum for gage #7 followed by a maximum for gage #9, confirms the separation tendency of the transitional boundary layer.

Figures 87, 88, and 89 show the hot-film gage results for GRID3. These results are similar to the one obtained for GRID2. Natural transition occurs for the first two Reynolds numbers, RE1 and RE2. For Reynolds number RE1, transition starts between gages #3 and #4 and is completed near gage #8. For the lower Reynolds number RE2, transition starts downstream of gage #4 and is completed near gage #9. For Reynolds number RE3, transition starts near gage #5, and the transitional flow extending into the adverse pressure gradient region tends to separate as indicated by the mean signal in part (a) of Figure 89. However, the boundary layer becomes completely turbulent near gage #9.

Summarising these results, the state of the profile boundary layer on the airfoil suction surface is seen to depend on the turbulence level and Reynolds number. At the minimum turbulence level of 0.8%, the flow undergoes transition by means of a separation bubble (bubble-induced transition). At the turbulence level of 2.0%, natural transition occurs at RE1, and a bubble-induced transition at RE3. At

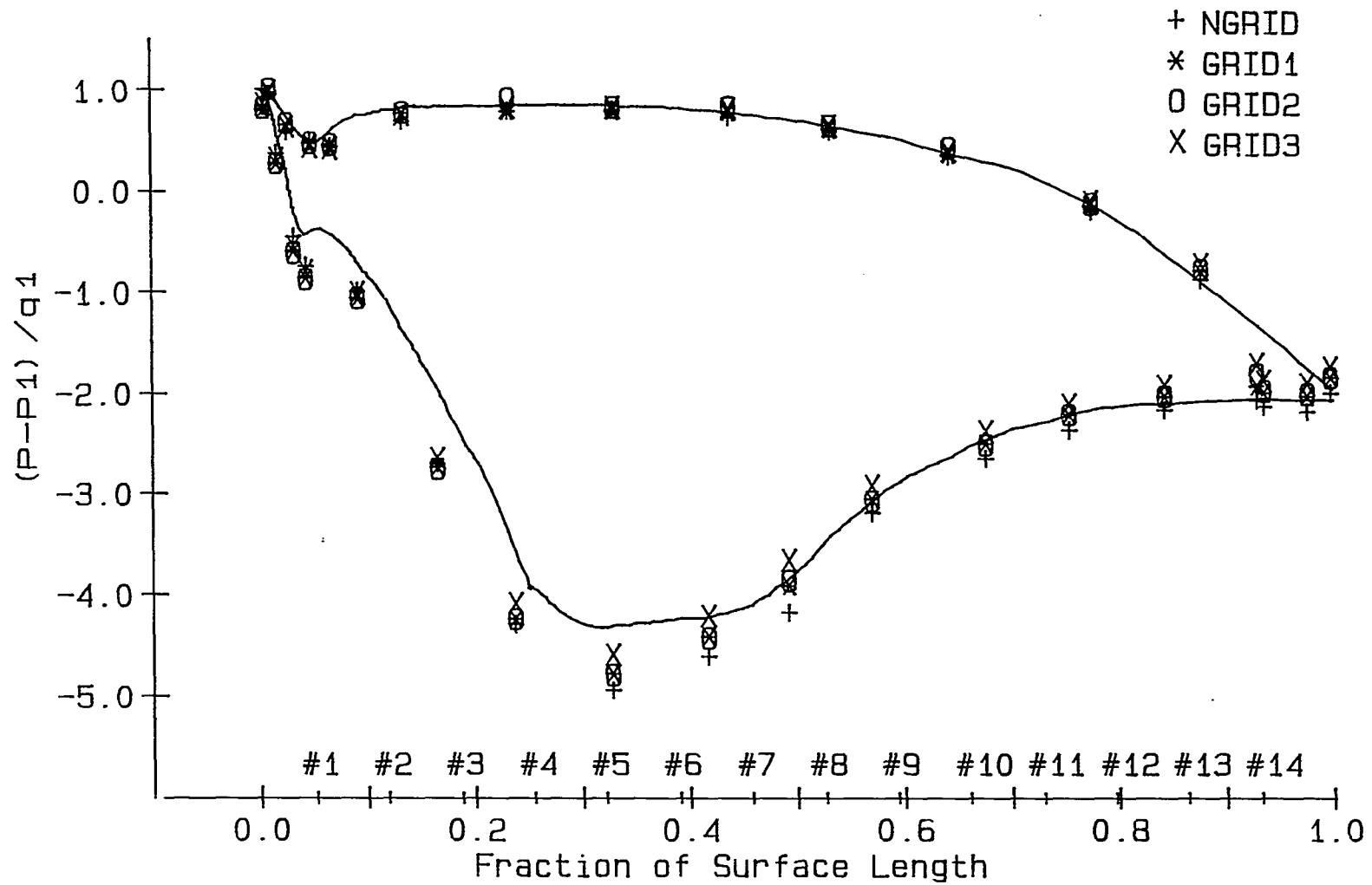


FIGURE 77. Hot-film gage locations plotted against the pressure distribution for $\beta_1 = 45^\circ$

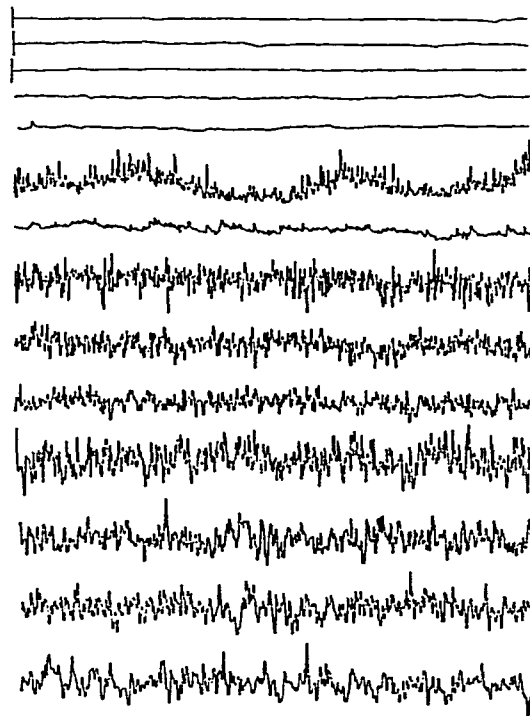
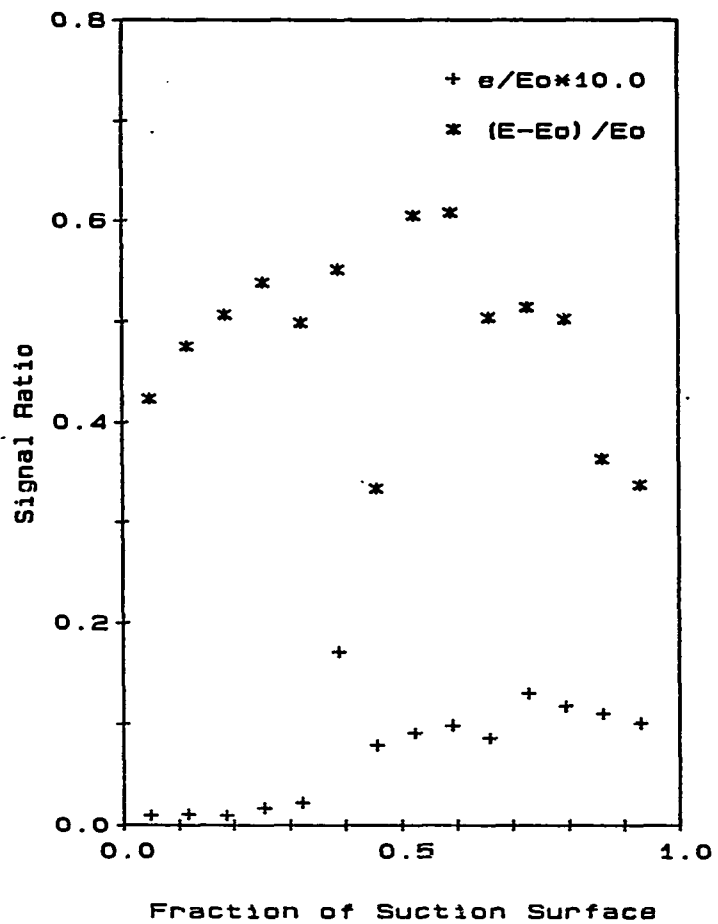


FIGURE 78. Hot-film gage results, $\beta_1 = 45^\circ$, NGRID, RE1

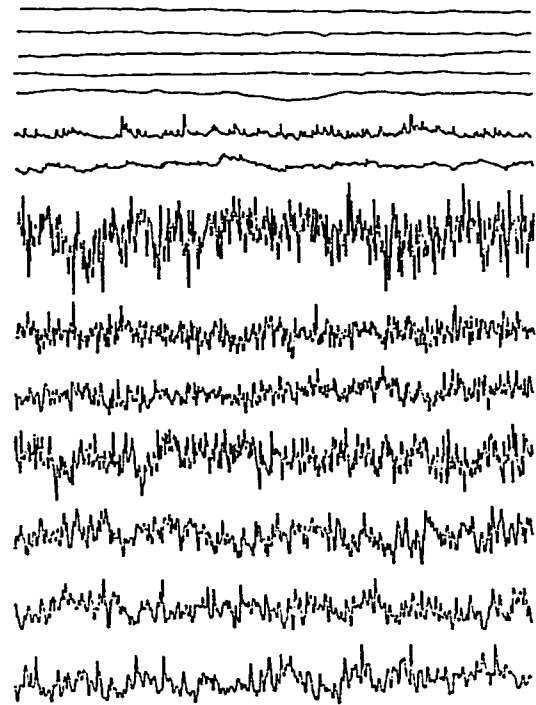
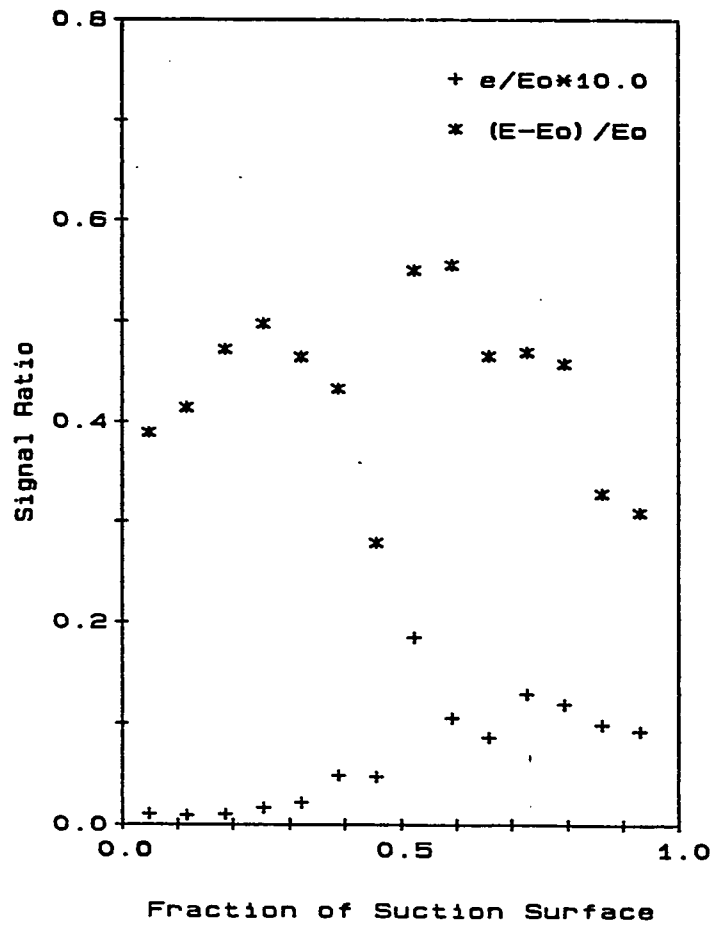


FIGURE 79. Hot-film gage results, $\beta_1 = 45^\circ$, NGRID, RE2

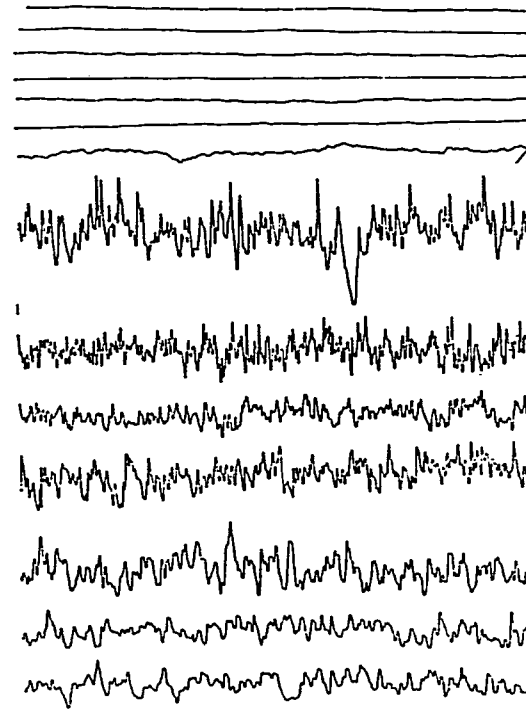
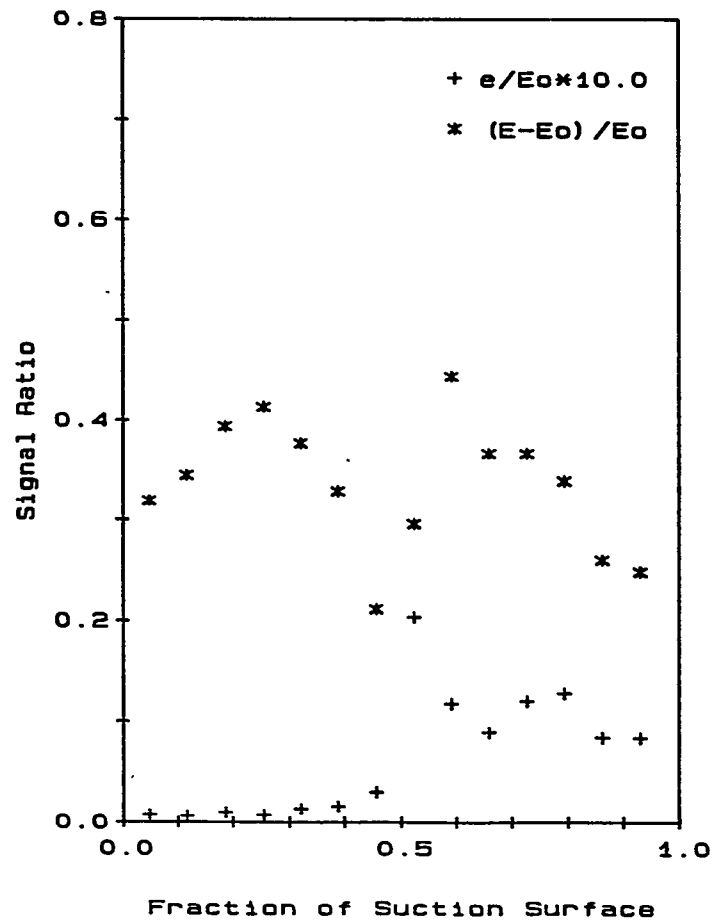


FIGURE 80. Hot-film gage results, $\beta_1 = 45^\circ$, NGRID, RE3

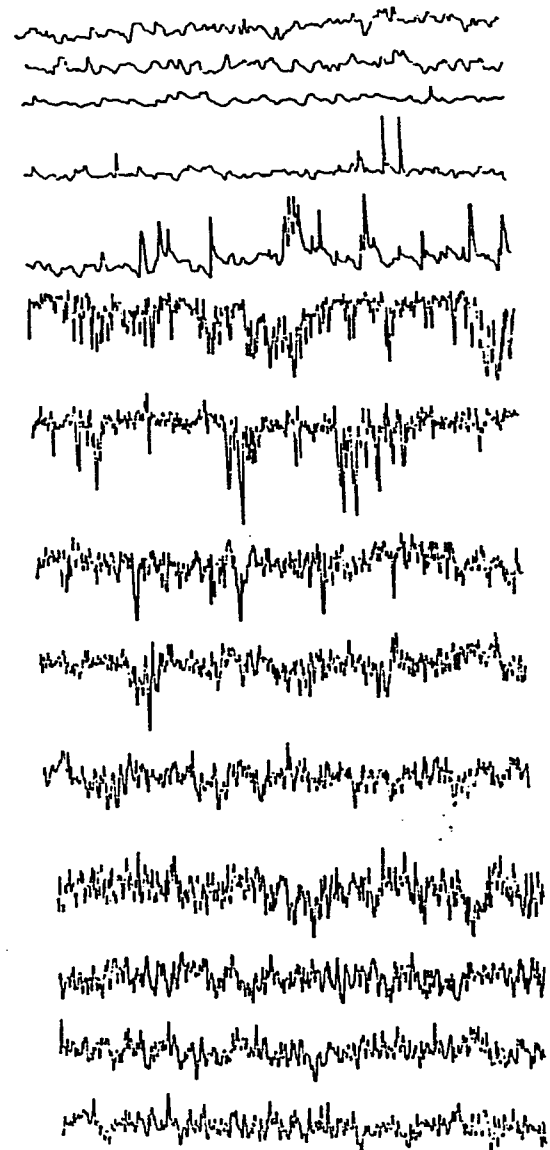
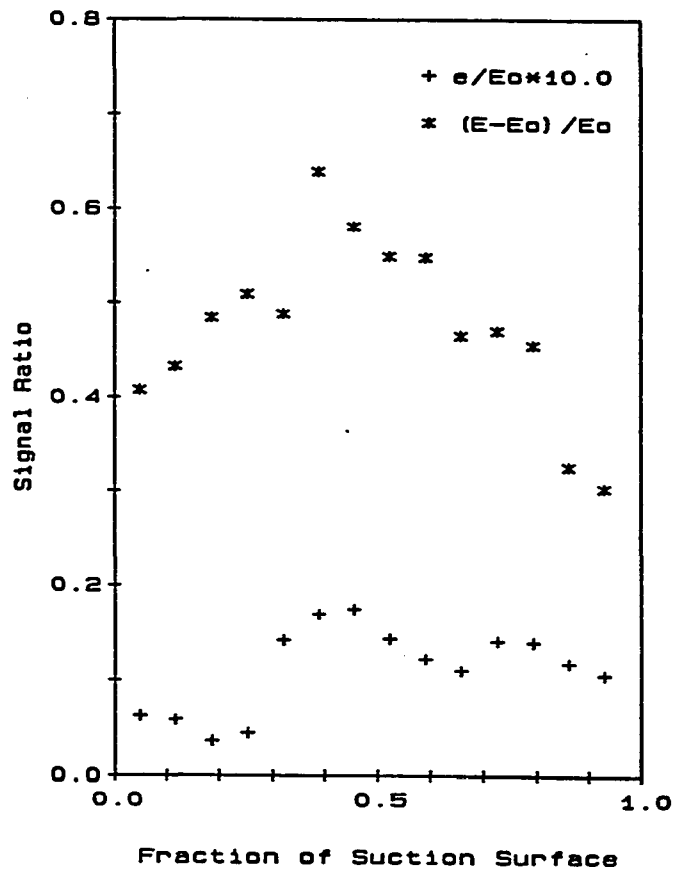


FIGURE 81. Hot-film gage results, $\beta_1 = 45^\circ$, GRID1, RE1

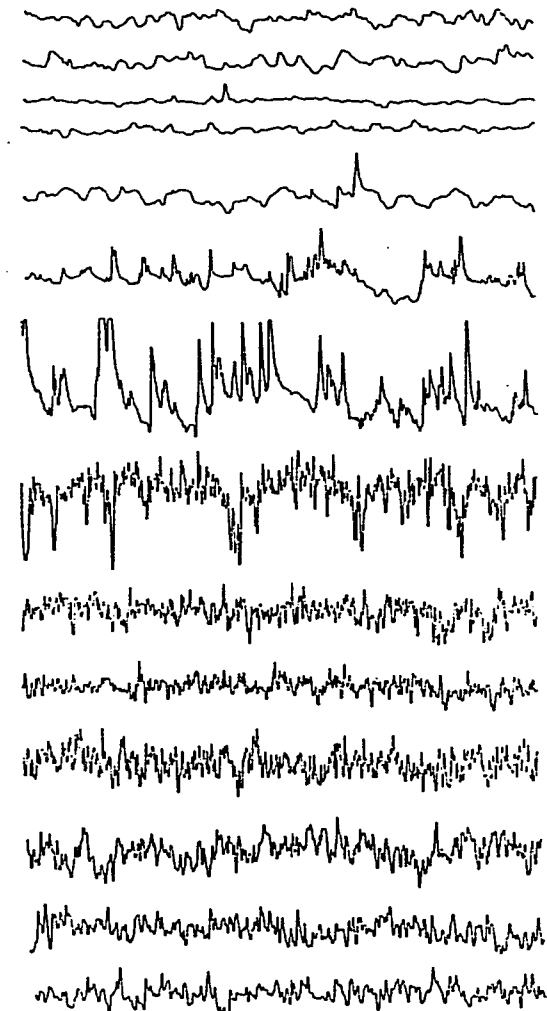
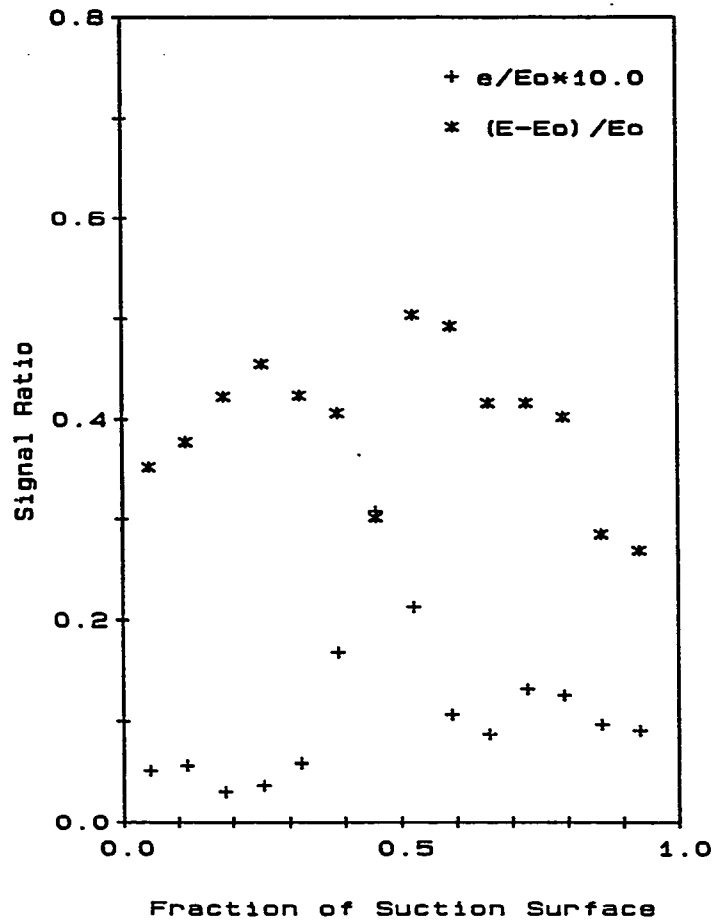


FIGURE 82. Hot-film gage results, $\beta_1 = 45^\circ$, GRID1, RE2

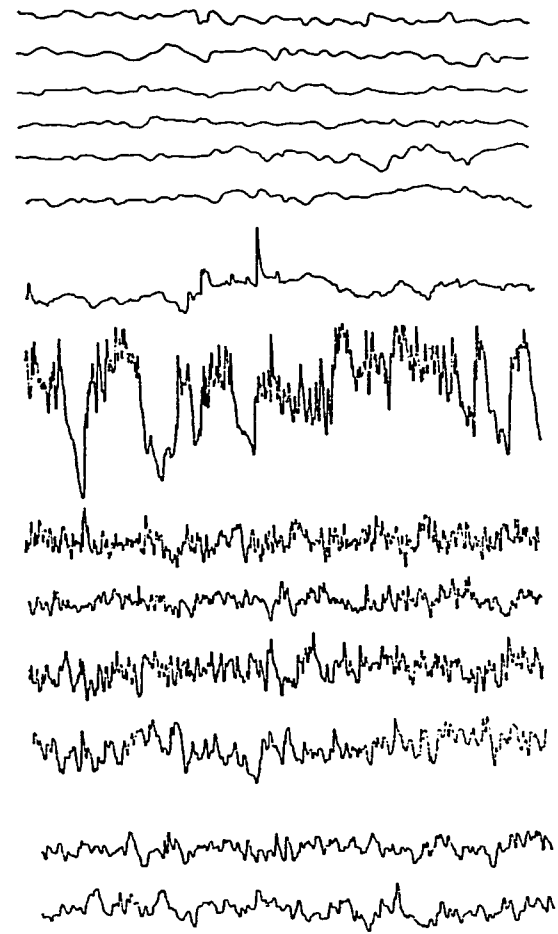
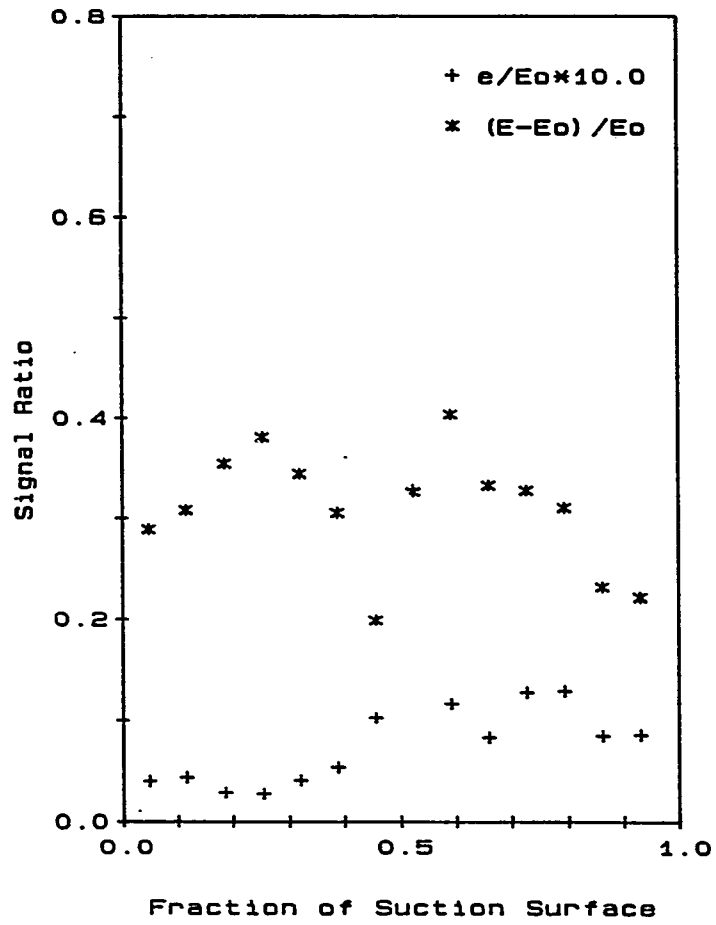


FIGURE 83. Hot-film gage results, $\beta_1 = 45^\circ$, GRID1, RE3

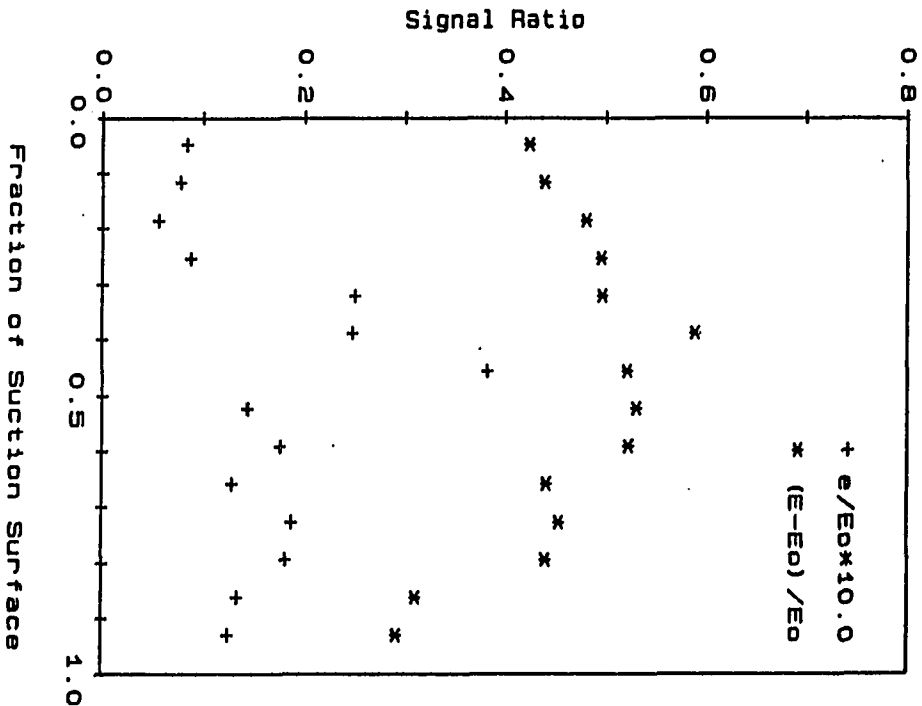
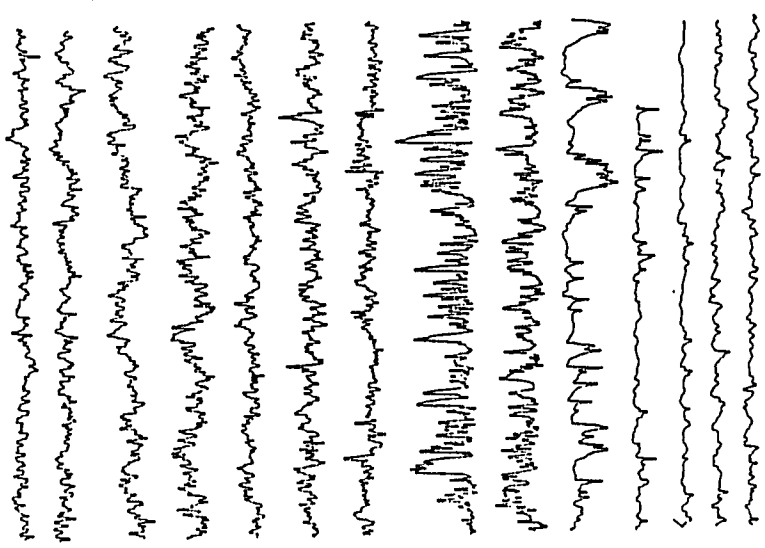


FIGURE 84. Hot-film gage results, $\beta_1 = 45^\circ$, GRID2, RE1



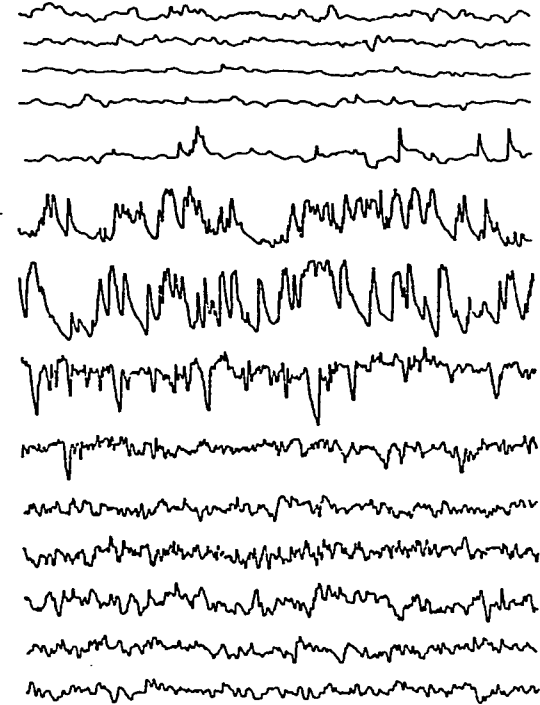
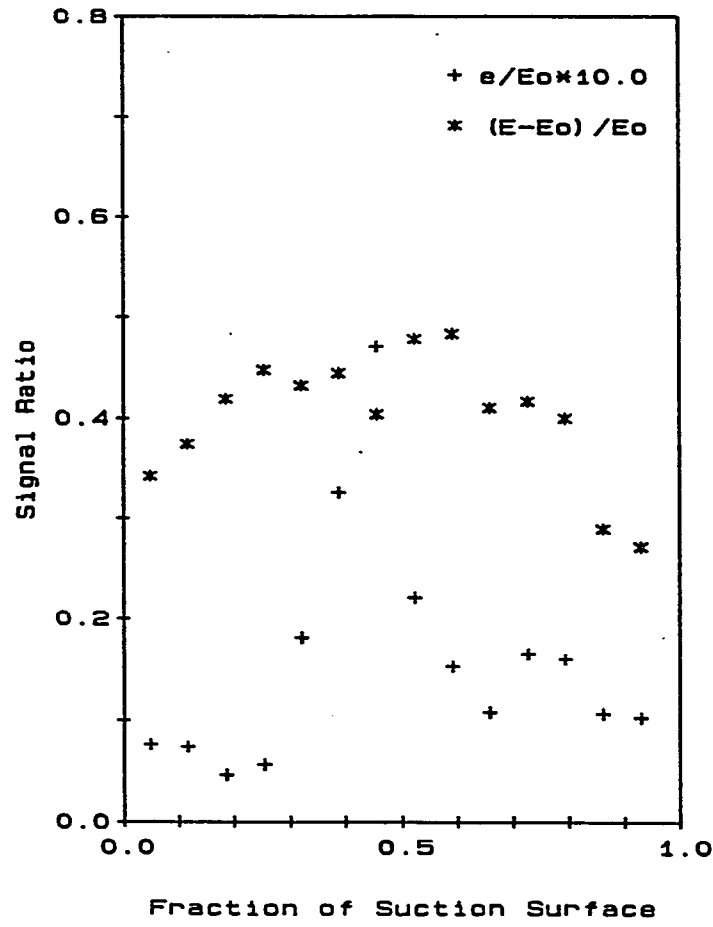


FIGURE 85. Hot-film gage results, $\beta_1 = 45^\circ$, GRID2, RE2

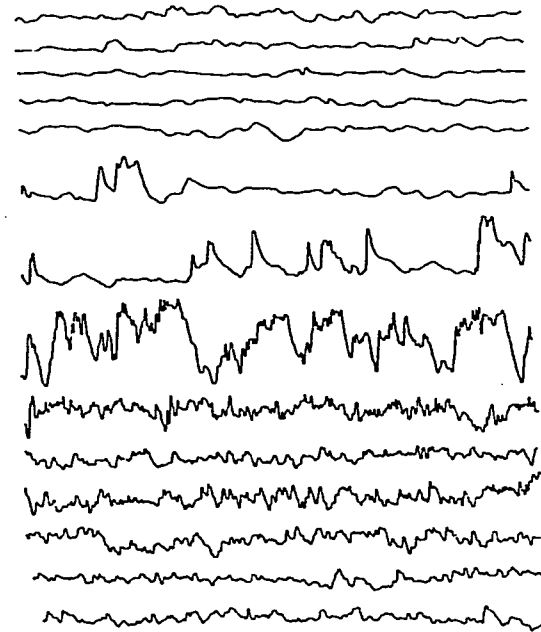
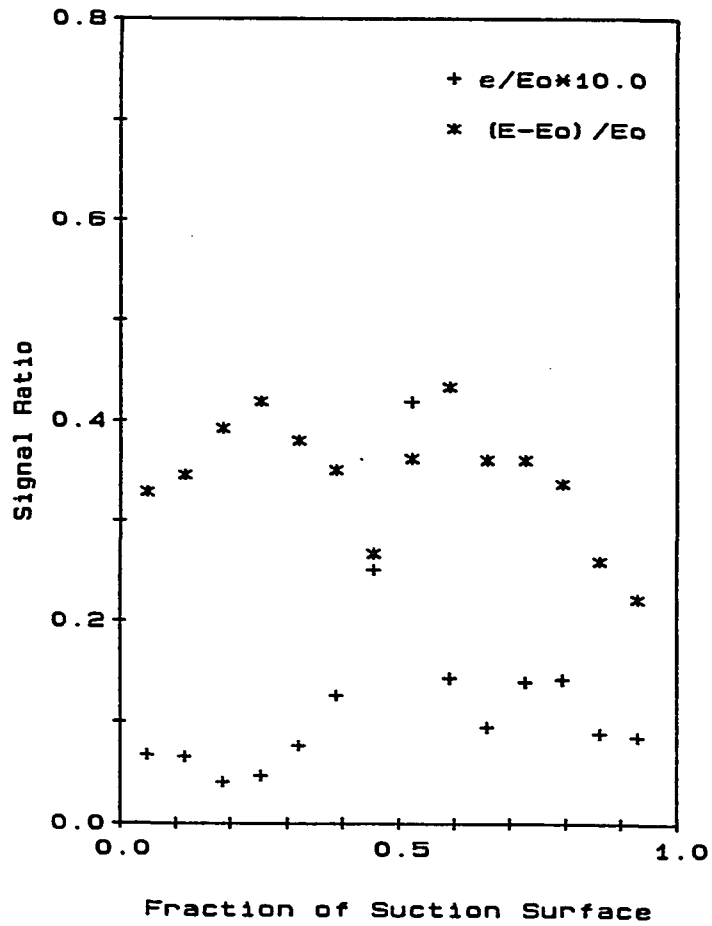


FIGURE 86. Hot-film gage results, $\beta_1 = 45^\circ$, GRID2, RE3

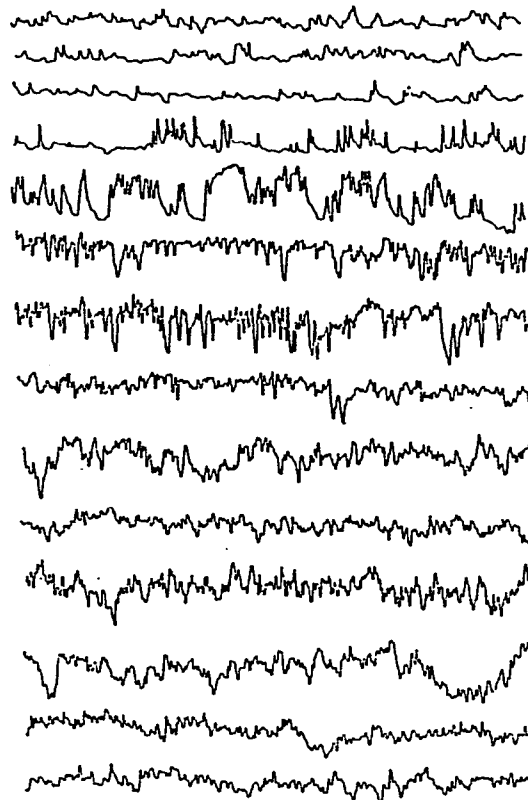
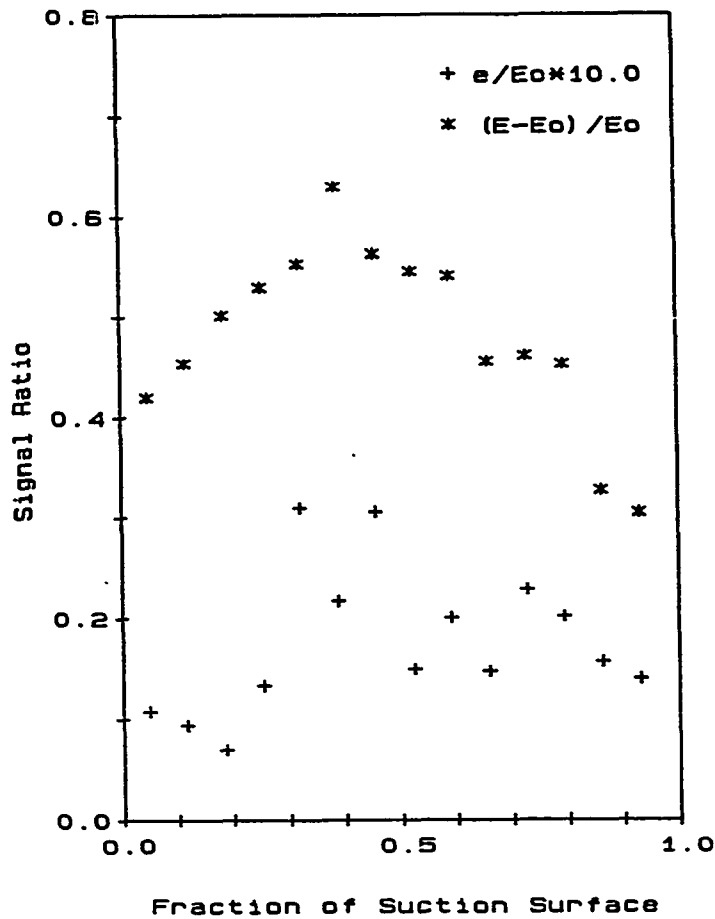


FIGURE 87. Hot-film gage results, $\beta_1 = 45^\circ$, GRID3, RE1

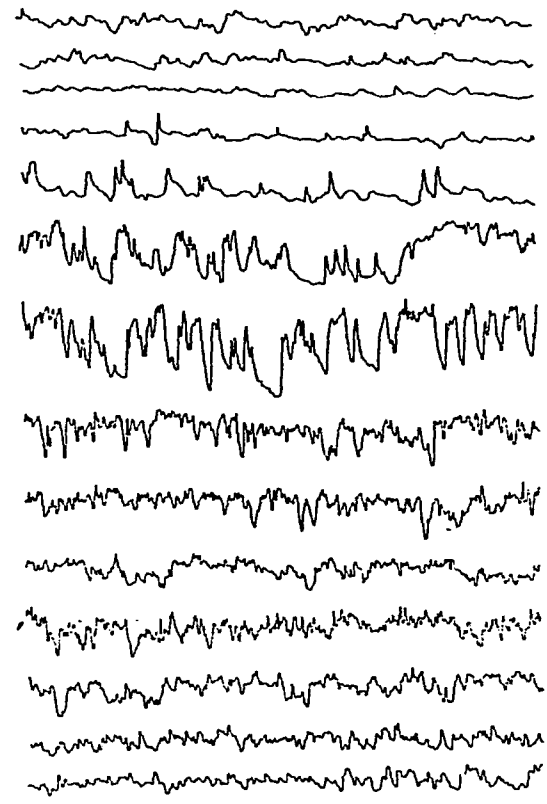
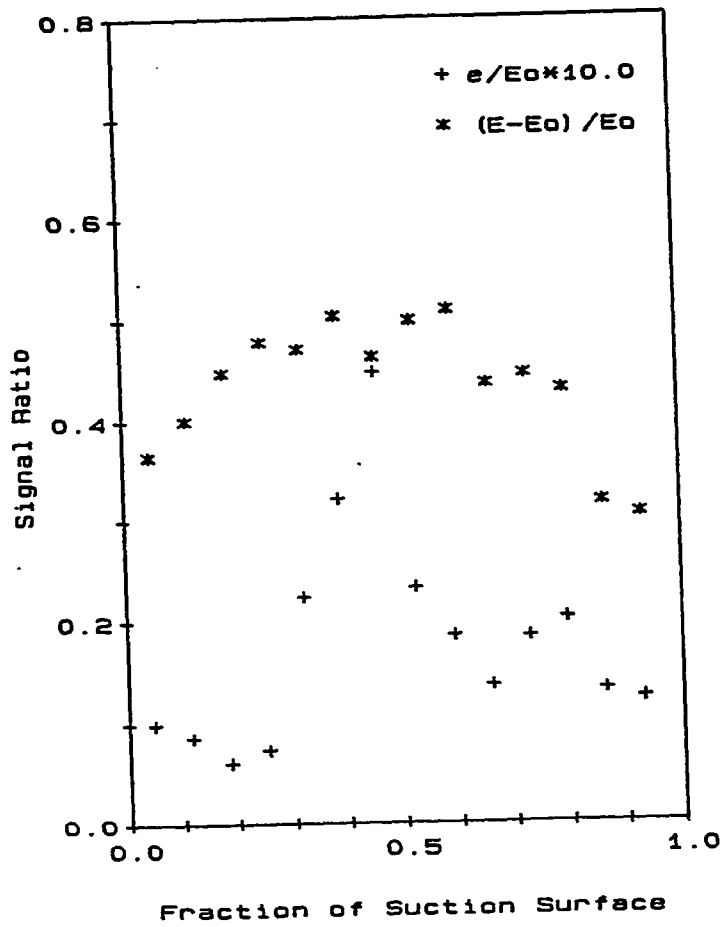


FIGURE 88. Hot-film gage results, $\beta_1 = 45^\circ$, GRID3, RE2

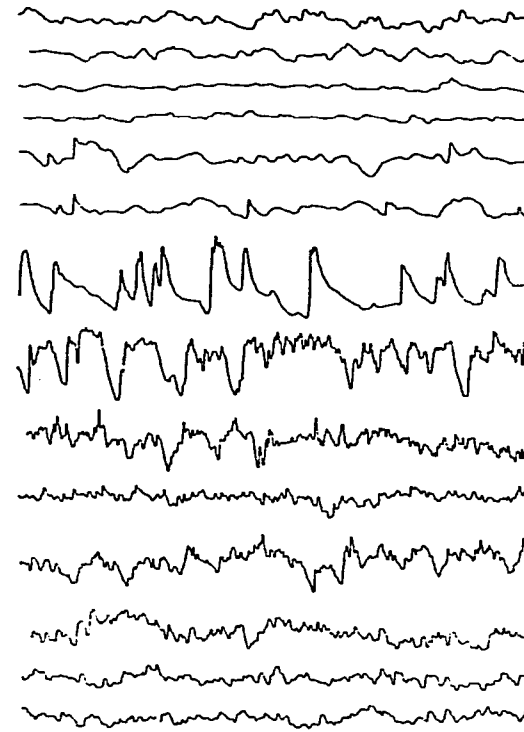
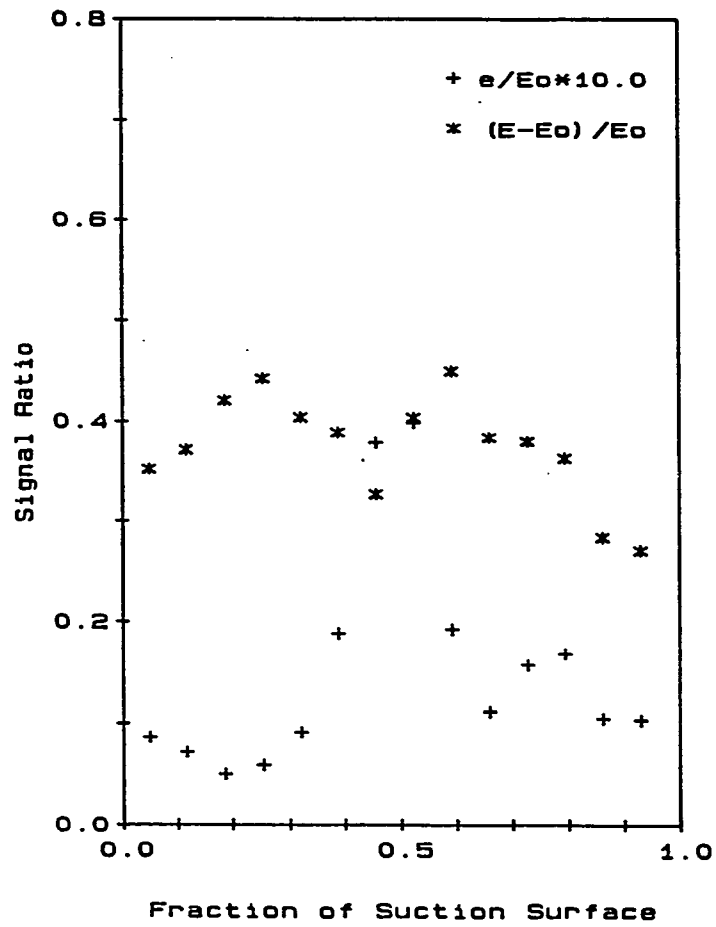


FIGURE 89. Hot-film gage results, $\beta_1 = 45^\circ$, GRID3, RE3

the intermediate Reynolds number RE_2 , transition starts naturally, but is completed by a bubble. At the high turbulence levels of 4.8% and 6.4%, natural transition occurs, except at the lowest Reynolds number tested where transition starts naturally, but is completed by a bubble. Furthermore, for the three cases where transition starts naturally, but is completed by a bubble, it is seen that transition starts close to the minimum pressure point. When the transitional flow encounters the adverse pressure gradient, it tends to separate due to the relatively low Reynolds number; however, the separation is not as distinct as for a laminar boundary layer and tends only to hasten the transition process. These cases appear then, to be marginal cases lying between natural transition and bubble-induced transition. The existence of a critical turbulence level for the formation of a laminar separation bubble has been observed also by Schlichting and Das [57]. They observed in tests on compressor cascades at a Reynolds number of 1.6×10^5 , that a laminar separation bubble disappeared above turbulence levels of 2.5%. When the Reynolds number was reduced to 0.9×10^5 , they found that the critical turbulence level increased to 4.5% .

Other features observed in the results are that transition starts either naturally or by means of a separation bubble close to the minimum pressure point for all the test cases, and that the flow is fully turbulent by gage #8 or #9. These conclusions indicate the strong influence of pressure distribution on the boundary layer development. In the forward portion of the airfoil, due to the strong

favorable pressure gradient, the flow remains laminar in all cases. In fact, over this region, the pressure gradient parameter $((\nu/U^2)(dU/dx))$ is close to a value of 3×10^{-6} , which is a lower limit for relaminarization as given by Kline [58]. For this inlet angle case of $\beta_1 = 45^\circ$, values of the pressure gradient parameter close to the relaminarization limit exist along the first 20% of the suction surface. Beyond the minimum pressure point, the adverse pressure gradient causes either natural transition, or a bubble-induced transition, or a combination of both, with the flow becoming completely turbulent at approximately the same streamwise location at all inlet flow conditions tested.

b. Frequency-domain analysis The power spectra of the hot-film gage outputs were examined in an attempt to determine the transition location at the various flow conditions. Results showed that transition or separation bubbles could not be easily identified from the power spectra. While some distinction was possible in the NGRID cases, at the high turbulence levels (GRID1 through GRID3) no distinction could be made between the power spectra of laminar, transitional, and turbulent boundary layers. Similar observations on the power spectra were also made by Pucher and Göhl [56] in their boundary layer studies on airfoil with hot-film gages.

Since no decisive information regarding the state of the boundary layer could be obtained from the power spectra, results for only two cases are presented in Figures 90 and 91 to show that this technique

was not reliable in transition measurements. The power spectra of the voltage output from gage #1 through gage #14 are arranged in order from top to bottom in the Figures. The abscissa of the spectra denotes frequency ranging from 0 to 5 kHz, and the ordinate denotes the amplitude ranging from -100 dB to 0 dB.

Figure 90 shows the results for flow conditions NGRID and Reynolds number RE1. As previously determined from the time-domain analysis for this flow condition, output for gages #1 through #5 represent a laminar flow, and for gages #6 and #7 a laminar separation bubble. However, as seen in Figure 90, there is little to distinguish between the power spectra for these seven gages. They all show a higher power spectral density at lower frequencies. Spectra for gages #8 and #9, which are located where the separated boundary layer reattaches, indicate nearly flat or white noise spectra. Spectra for gages #10 through #14, representing a fully turbulent boundary layer, are similar to those for a laminar boundary layer, although the difference in the power spectral density between the higher and lower frequencies for the two spectra is smaller for the case of the turbulent boundary layer.

Figure 91 shows the results for GRID2 and Reynolds number RE1. For this case, the boundary layer undergoes a natural transition. As seen in the Figure, there is no distinction between the power spectra for the laminar, transitional and turbulent states. All the spectra have a higher power spectral density at the lower frequencies which decreases with increasing frequency.

The results obtained from the power spectrum measurements are in line with those of Klebanoff [59] who obtained power spectra of turbulence velocities and turbulent shear stresses in a boundary layer along a smooth flat plate with zero pressure gradient. Klebanoff has shown that the highest value of power spectral density occurs at the lowest measured frequency, and that, as the frequency is increased, the power spectral density decreases as (frequency)^{-5/3}. As the frequency is increased further, power spectral density decreases at a still faster rate and ultimately at very high frequencies, according to Heisenberg's theory (cited in Schlichting [3]), decreases as (frequency)⁻⁷. Figure 92 is a log-log plot of the power spectrum of the output of gage #14 with fully turbulent flow for the flow condition GRID2 and RE1. As seen in the Figure, the power spectrum follows the (-5/3) slope line closely indicating that the measured spectrum agrees with Klebanoff's theory.

B. Inlet Angle, $\beta_1 = 52^\circ$ (-14° incidence)

1. Static pressure measurements

Static pressure measurements were made for all the test conditions (four turbulence levels and three Reynolds numbers) for this inlet angle. Figures 93 and 94 show the pressure distribution on the airfoil for the four turbulence levels at Reynolds number RE1. In Figure 94, the pressure distribution is plotted against axial chord, and, in Figure 93, it is plotted against the fraction of pressure or suction

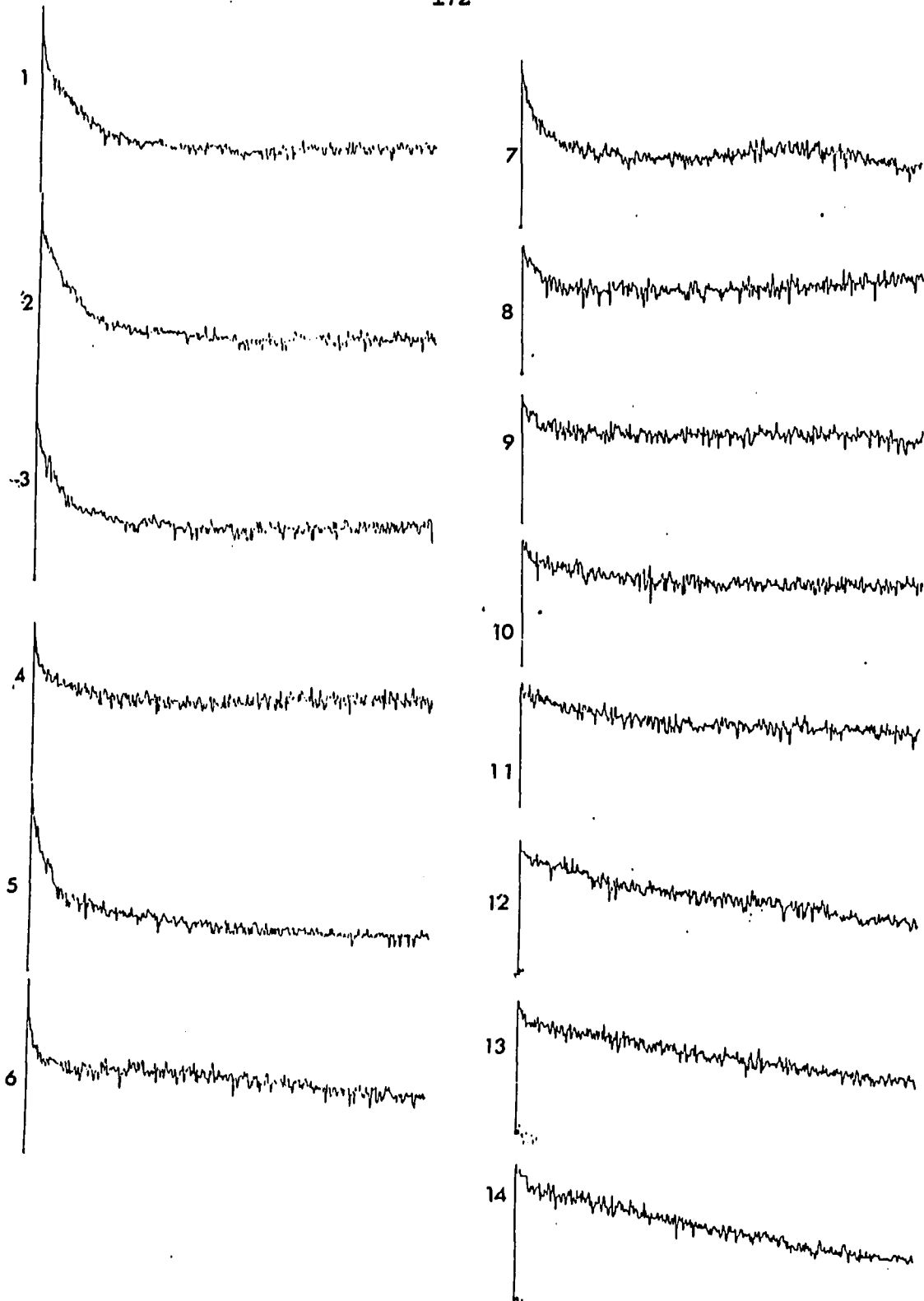


FIGURE 90. Power spectrum results, $\beta_1 = 45^\circ$, NGRID, RE1

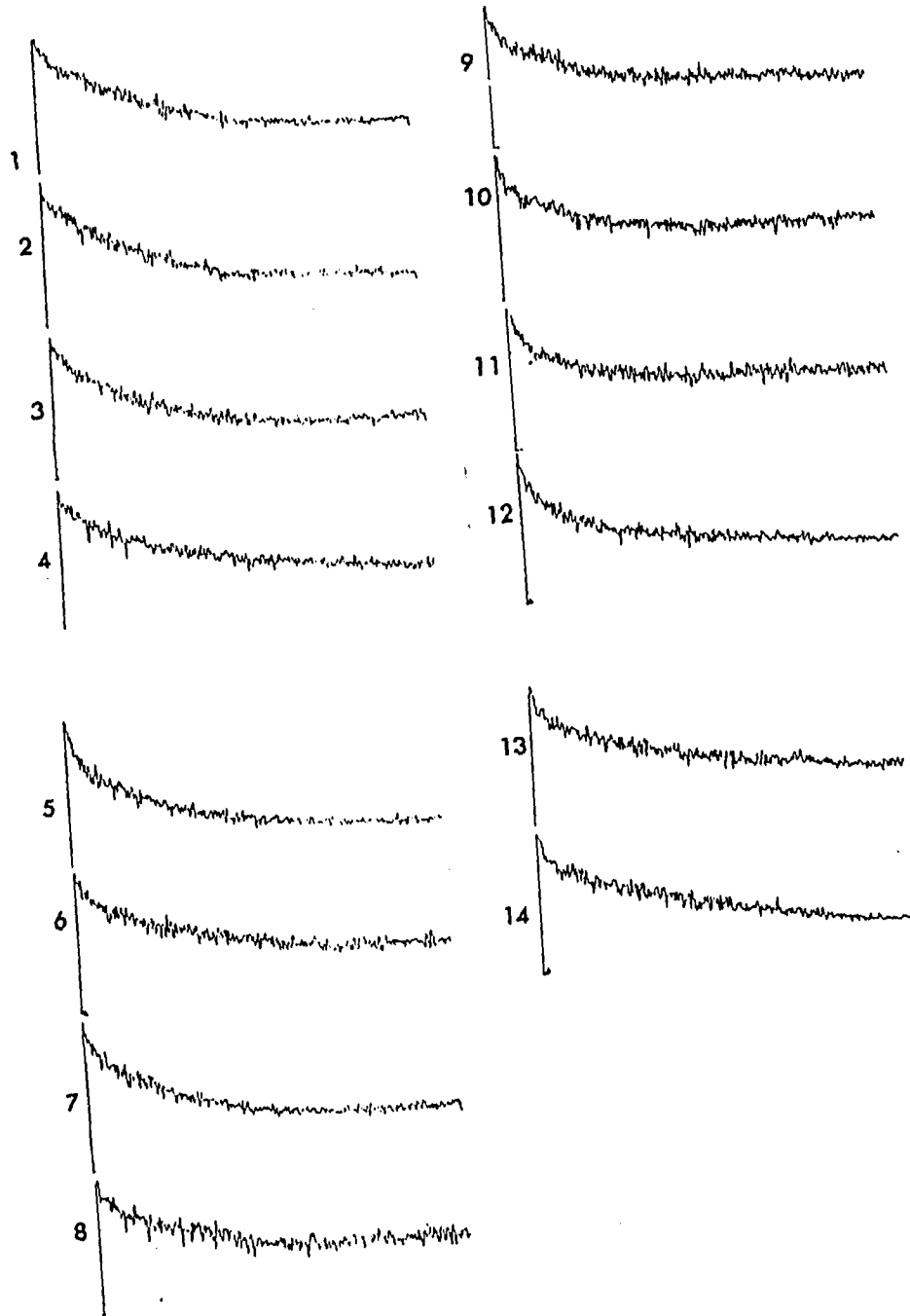


FIGURE 91. Power spectrum results, $\beta_1 = 45^\circ$, GRID2, REL

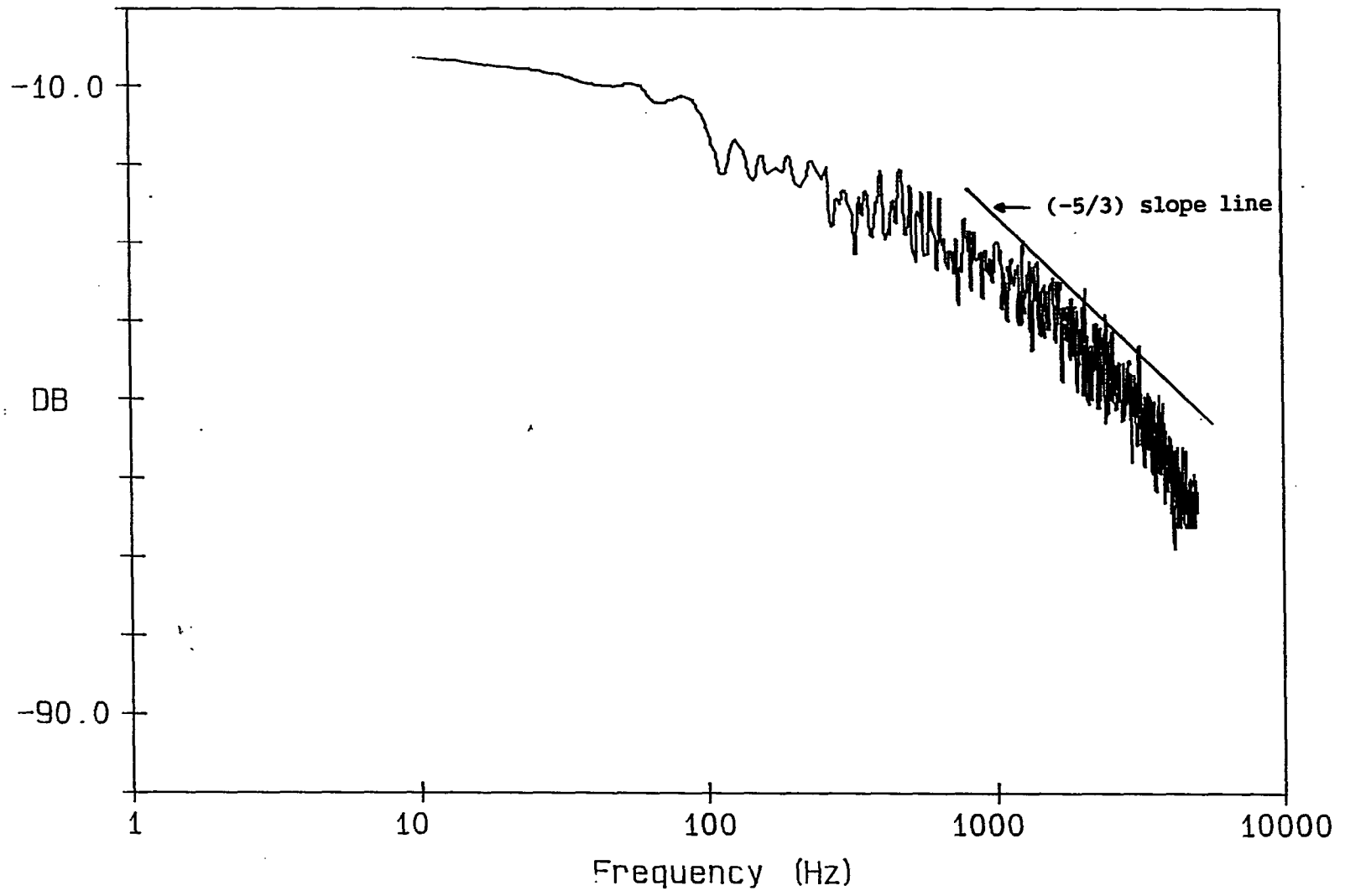


FIGURE 92. Power spectrum of hot-film gage#14, $\beta_1 = 45^\circ$, GRID2, RE1

surface length from the stagnation point. Also shown for comparison is the predicted 2-D distribution (the solid line). Similar to the results at the design inlet angle $\beta_1 = 45^\circ$, Figures 93 and 94, show that, as the turbulence level increases, loading tends to decrease on the suction surface. The measured pressure distribution follows the predicted distribution closely on the suction side, except near the trailing edge where there is a slight unloading. On the pressure side, the measured distribution follows the leading edge overspeeding, but does not follow the predicted deceleration after the overspeeding for the two flow conditions NGRID and GRID1. Instead, at these low turbulence levels, a flatter pressure distribution is seen, indicating a separation zone. For flow conditions GRID2 and GRID3 however, the measured distribution on the pressure surface follows the predicted pattern closely.

Figures 95 through 98 show the pressure distributions at the four turbulence levels plotted for the three Reynolds numbers. Similar to the case of $\beta_1 = 45^\circ$, the measured pressure distribution is seen to be independent of Reynolds number. Also the leading edge overspeeding on the pressure surface for this inlet angle has increased over that for $\beta_1 = 45^\circ$, while the underspeeding on the suction surface has almost disappeared (see Figure 33).

2. Flow visualizations

Figures 99, 100, and 101 show the flow visualization patterns on the suction surface for flow conditions NGRID, GRID1, and GRID3 and Reynolds number RE1. Endwall suction was applied for all cases. The

flow proceeds from right to left, with gravity acting from top to bottom. Figure 99 for NGRID shows a laminar separation bubble at near the 50% point along the suction surface. Figure 100 for GRID1 shows signs of separation with streaks of pigment deposits, but no clear separation line is seen. Figure 101 for GRID3 indicates no separation and that natural transition has occurred. In all three Figures, the limiting streamlines from the endwall flow are barely observable, and a much wider 2-D flow over the span is seen compared to $\beta_1 = 45^\circ$ case.

Figure 102 (the right-hand portion) shows the flow pattern on the pressure surface for flow conditions GRID3 and Reynolds number RE1. The stagnation point can be seen just to the left of center of the Figure, and a distinct separation bubble is present downstream of the stagnation point. The low flow velocities on the pressure surface downstream of the bubble are unable to create a flow pattern, and only close to the trailing edge can a flow pattern be observed.

Finally, Figure 103 shows the endwall flow pattern for this inlet angle. Similar to the $\beta_1 = 45^\circ$ case, saddle points of separation and separation lines created by the horseshoe vortex are clearly seen. The distance between the saddle points is one blade pitch, and the measured flow angle from the flow pattern ahead of the saddle points agrees with the inlet angle setting for the cascade.

Summarizing the flow visualization results for this case, $\beta_1 = 52^\circ$, it is seen that a large region of 2-D flow exists over the airfoil span. Also, a separation bubble is present on the suction

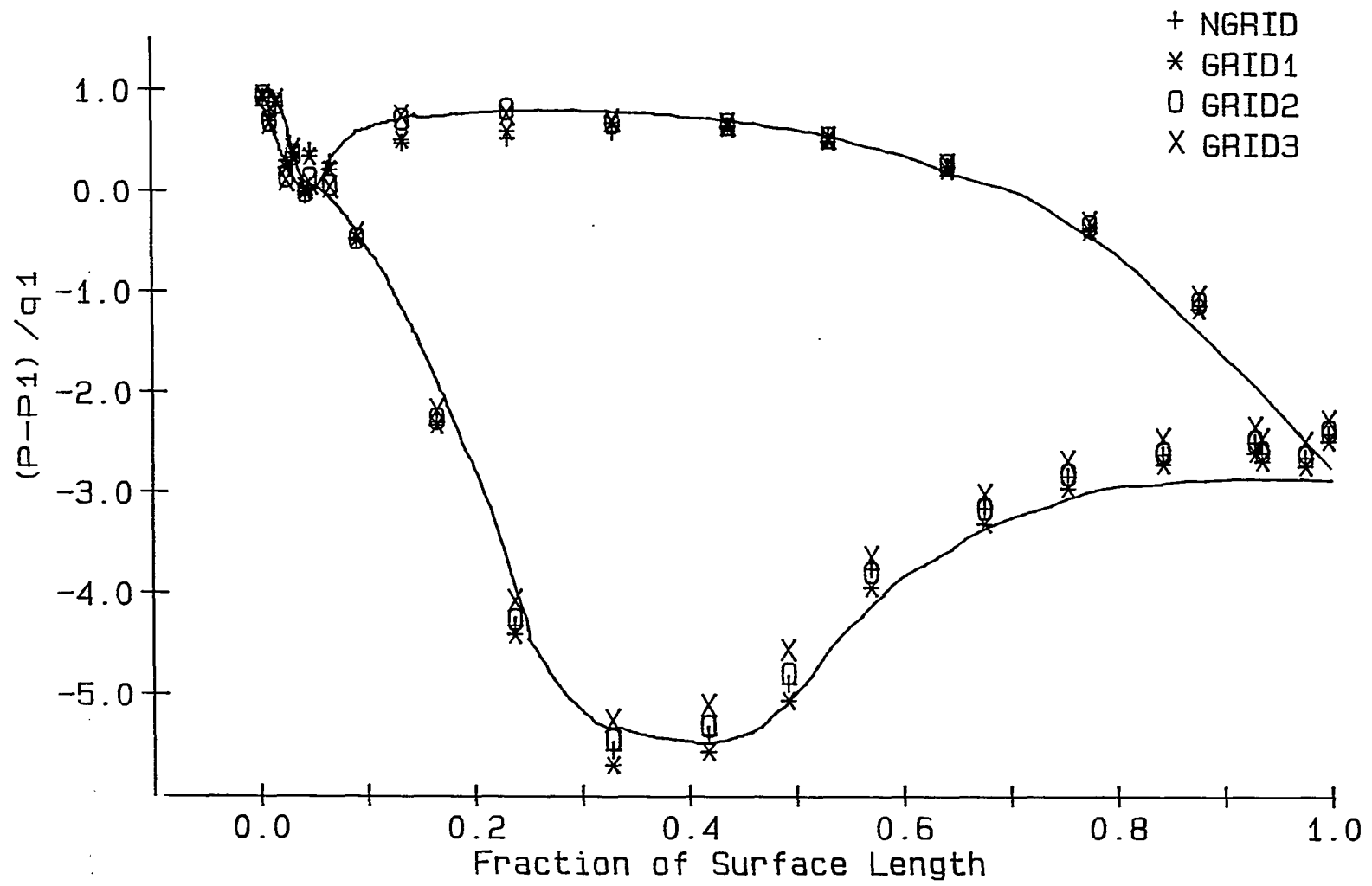


FIGURE 93. Static pressure distribution, $\beta_1 = 52^\circ$, RE1

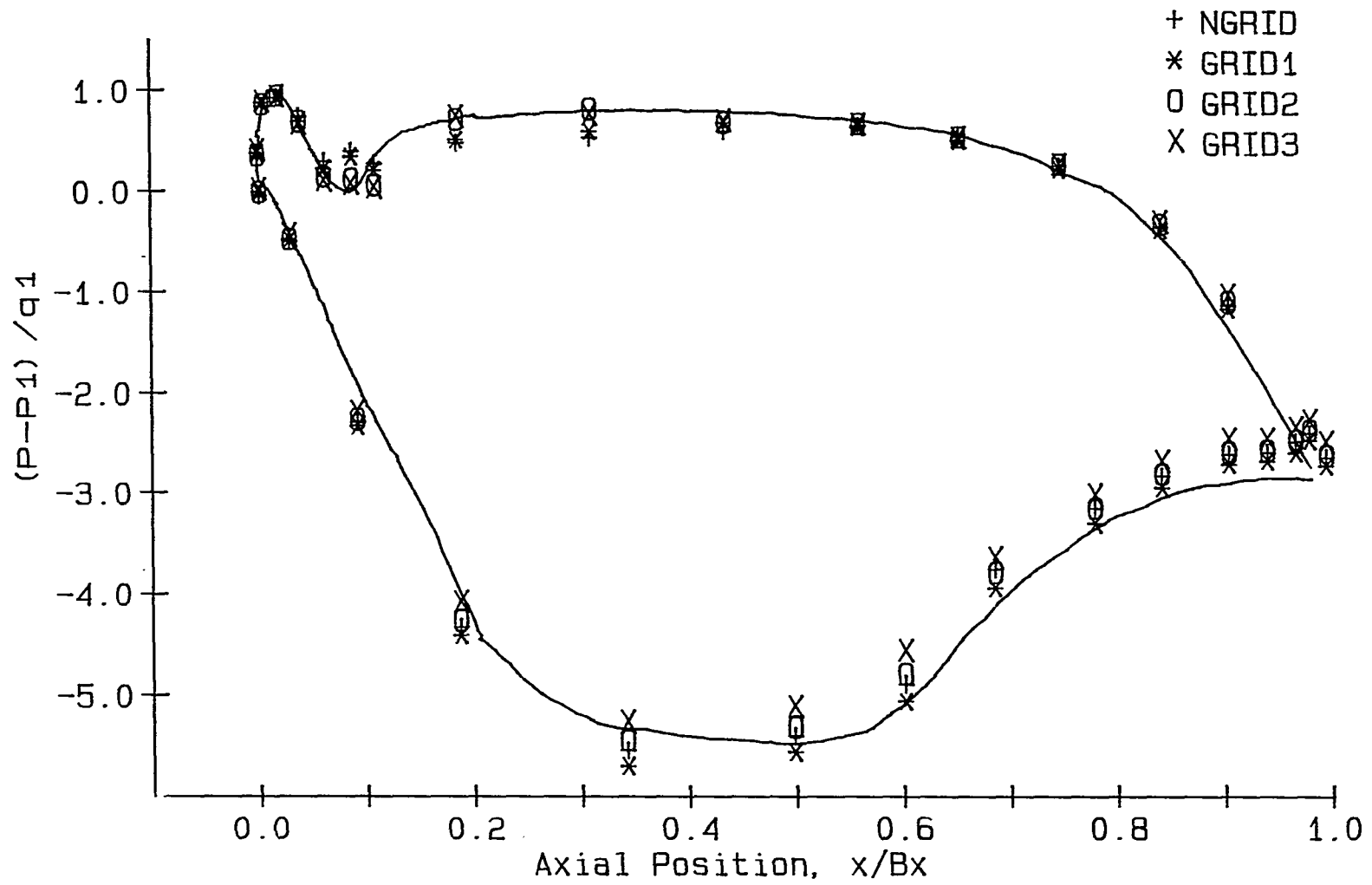


FIGURE 94. Static pressure distribution, $\beta_1 = 52^\circ$, RE1

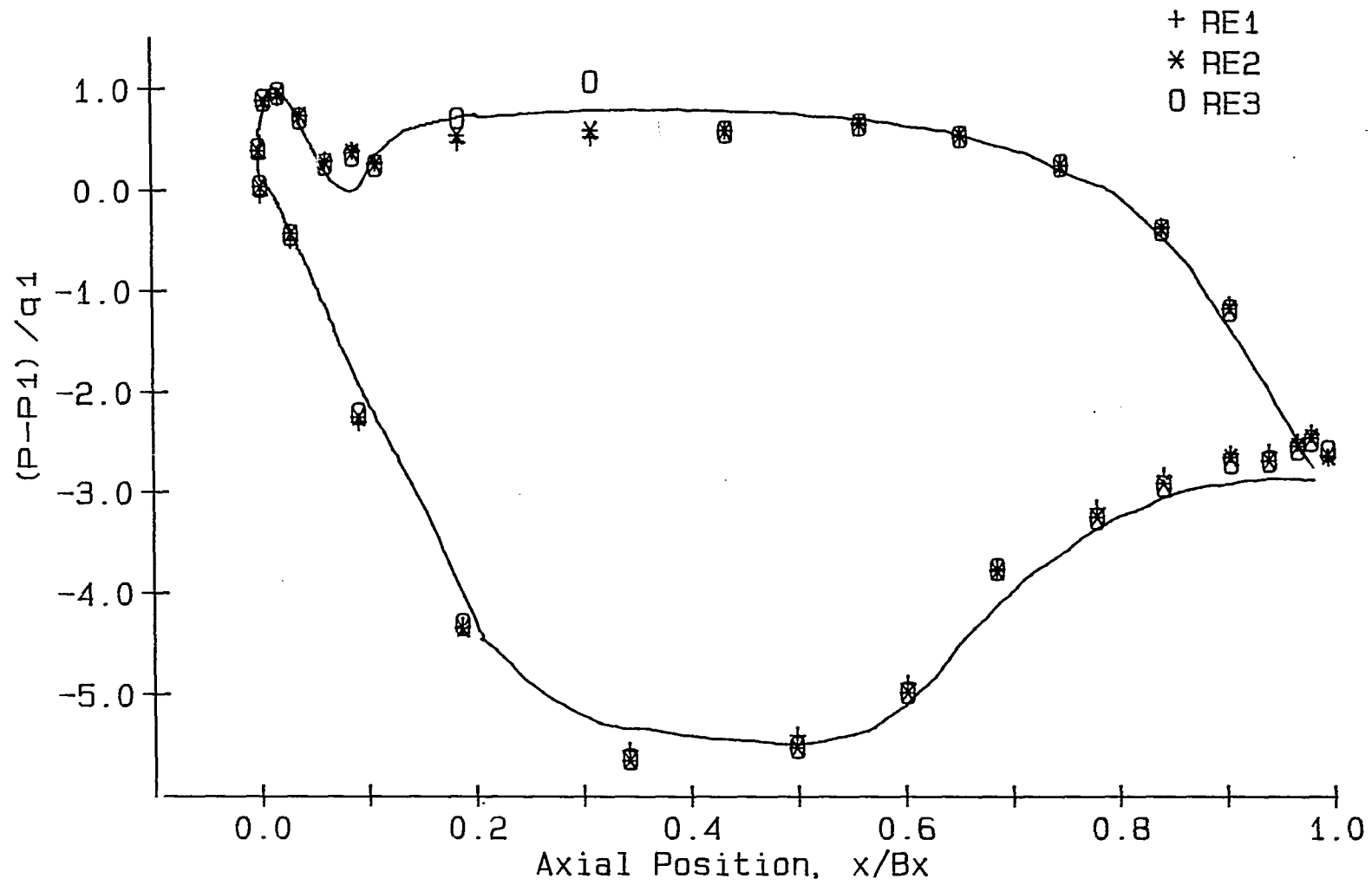


FIGURE 95. Static pressure distribution, $\beta_1 = 52^\circ$, NGRID

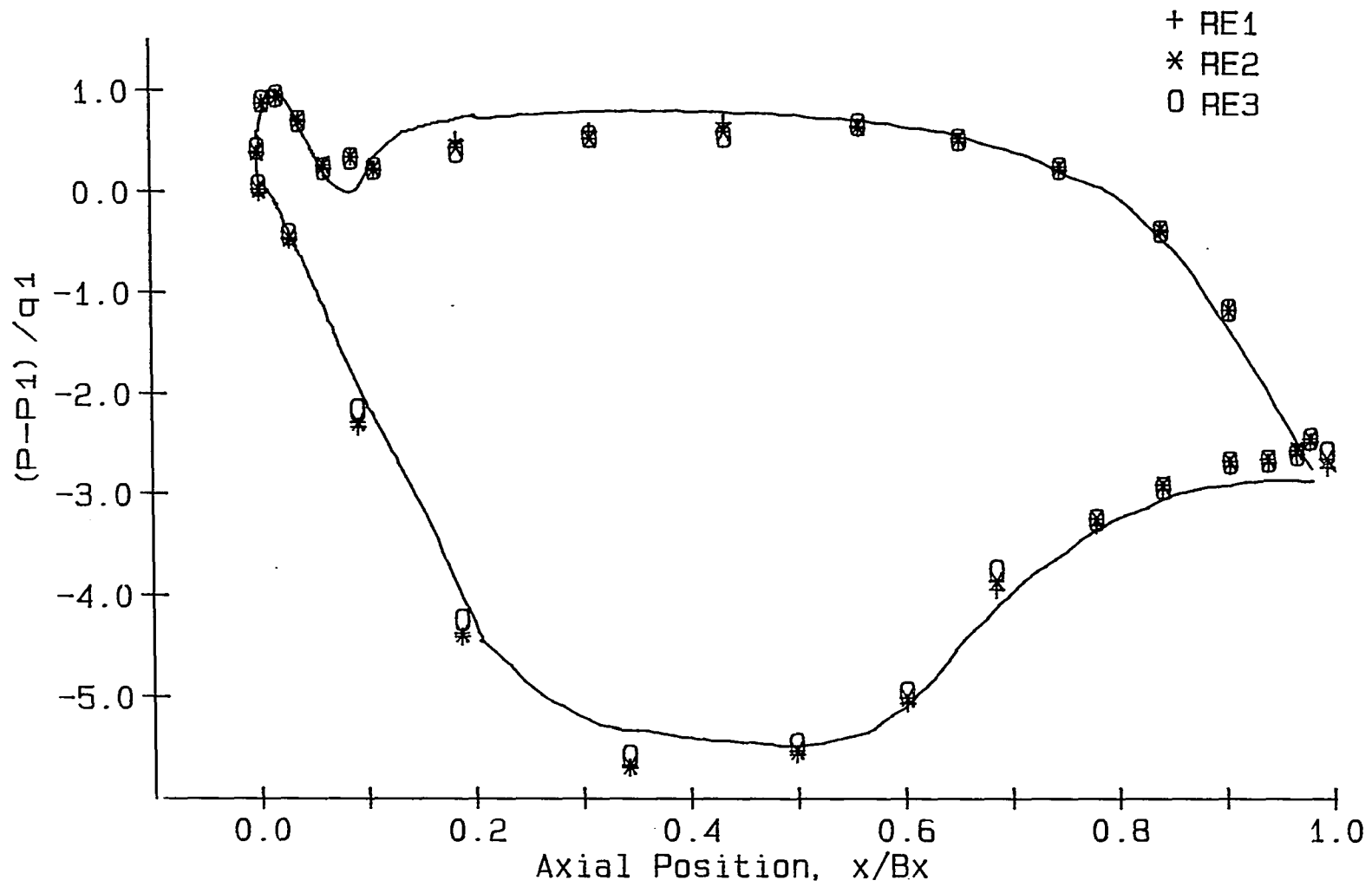


FIGURE 96. Static pressure distribution, $\beta_1 = 52^\circ$, GRID1

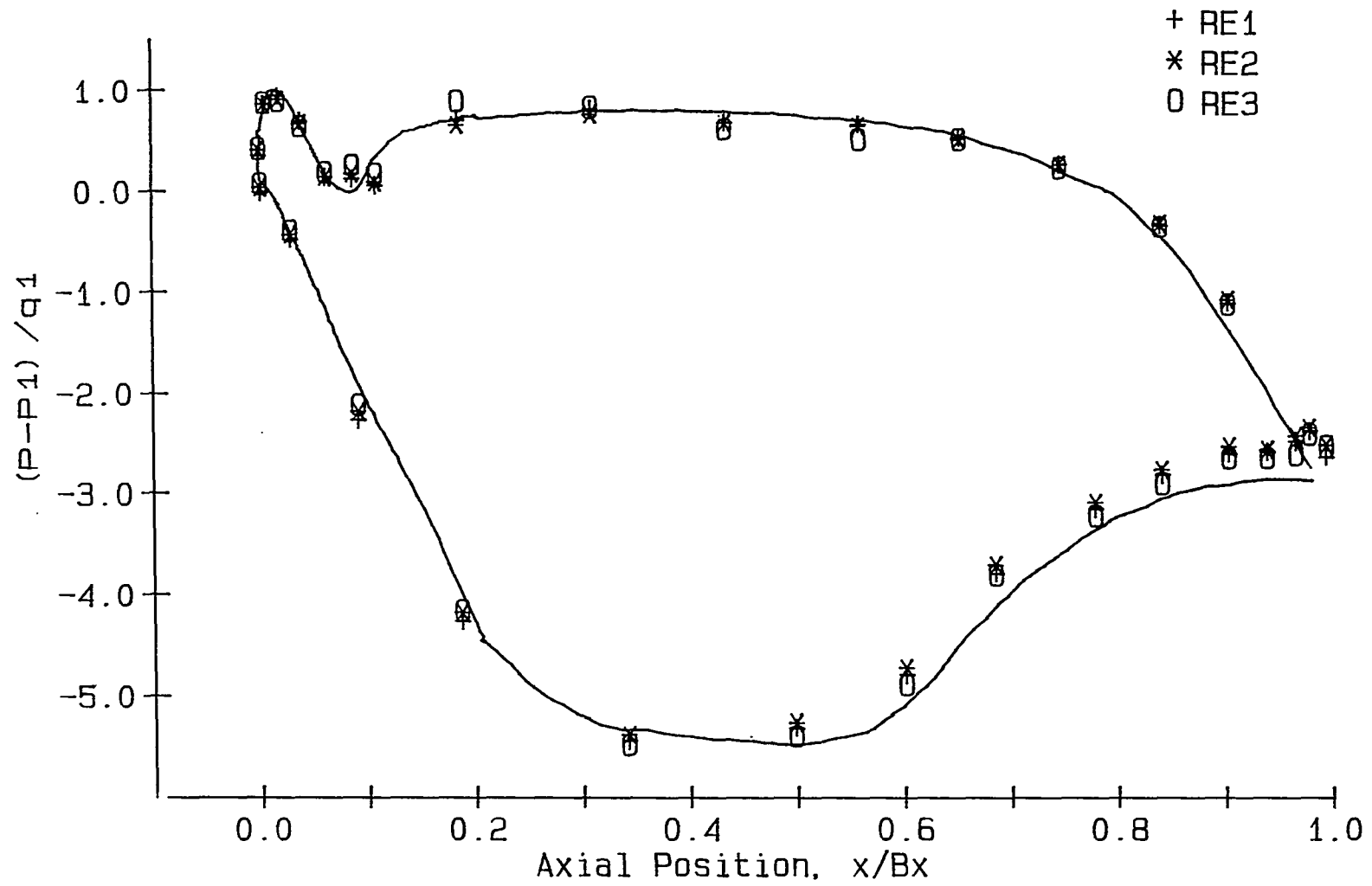


FIGURE 97. Static pressure distribution, $\beta_1 = 52^\circ$, GRID2

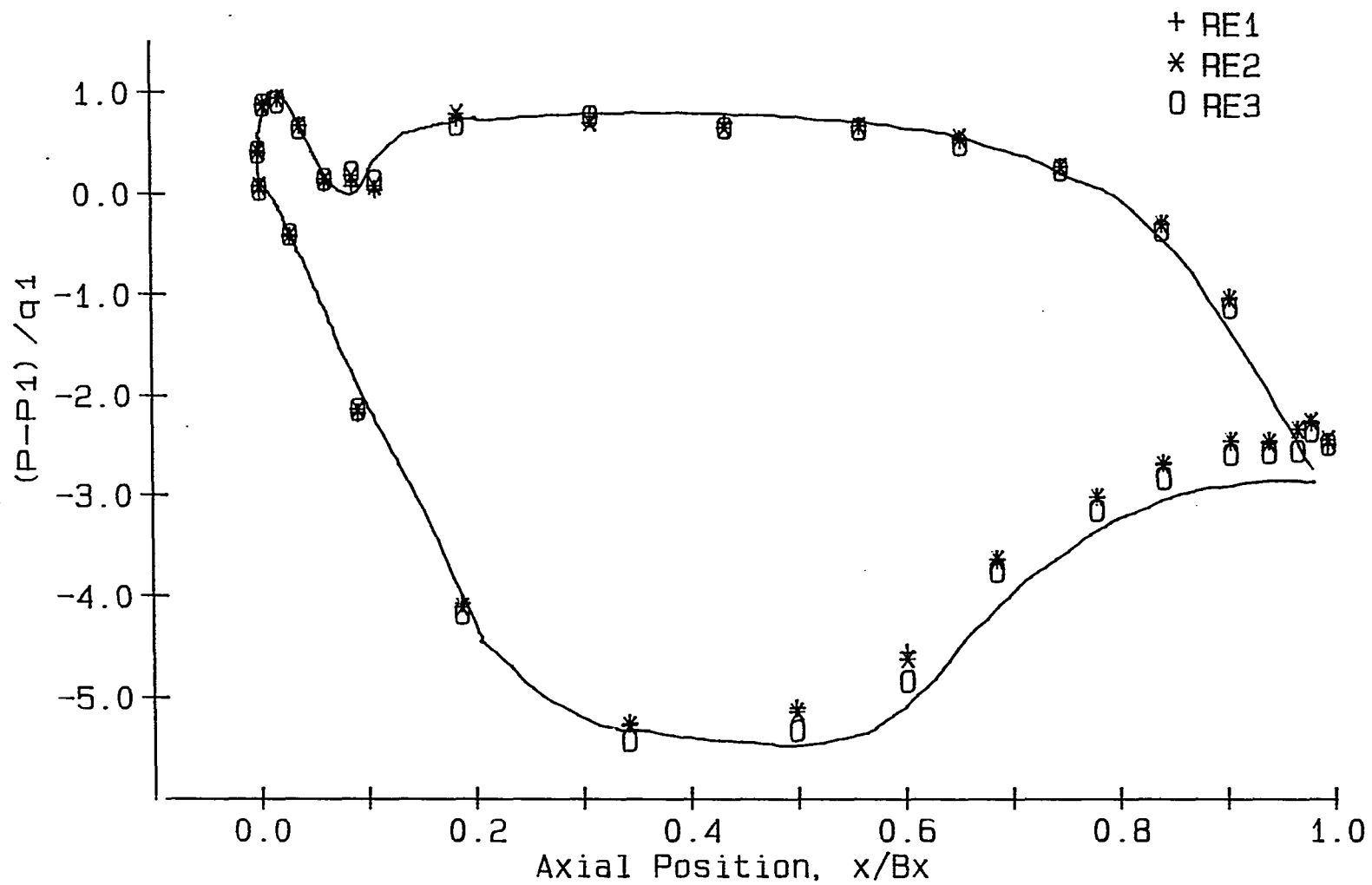


FIGURE 98. Static pressure distribution, $\beta_1 = 52^\circ$, GRID3

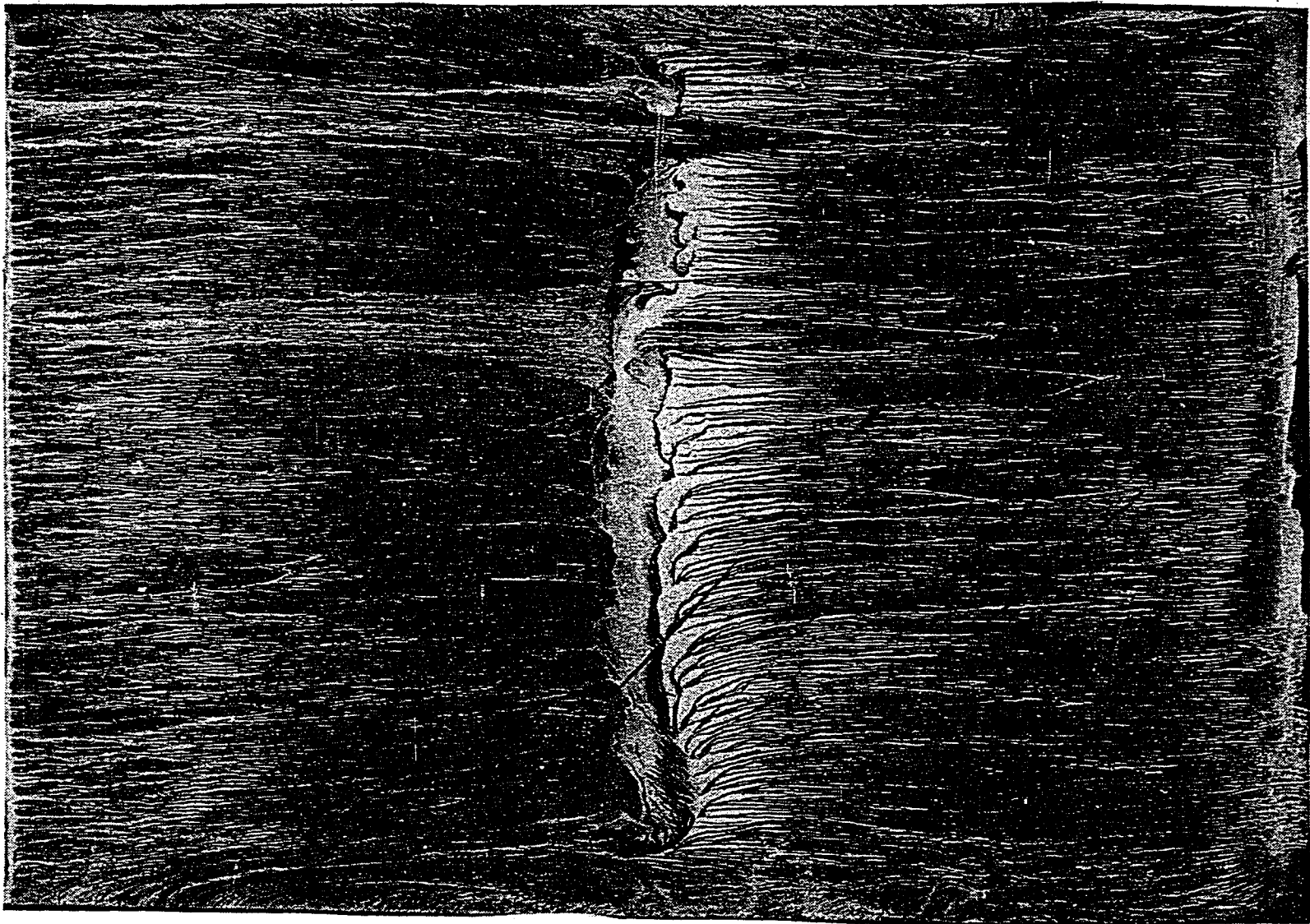


FIGURE 99. Flow pattern, Suction surface, $\beta_1 = 52^\circ$, NGRID, REL

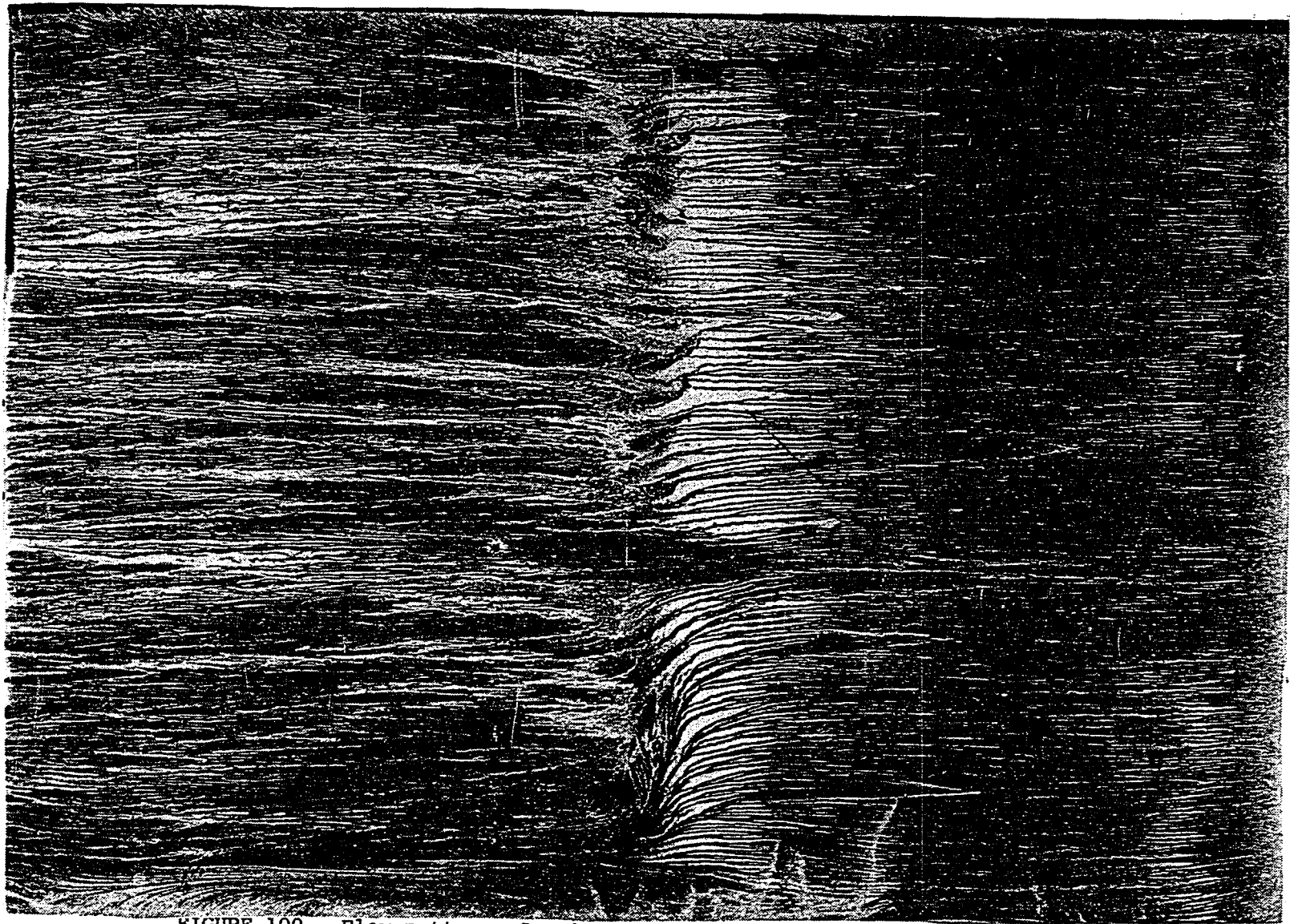


FIGURE 100. Flow pattern, Suction surface, $\beta_1 = 52^\circ$, GRID1, REL

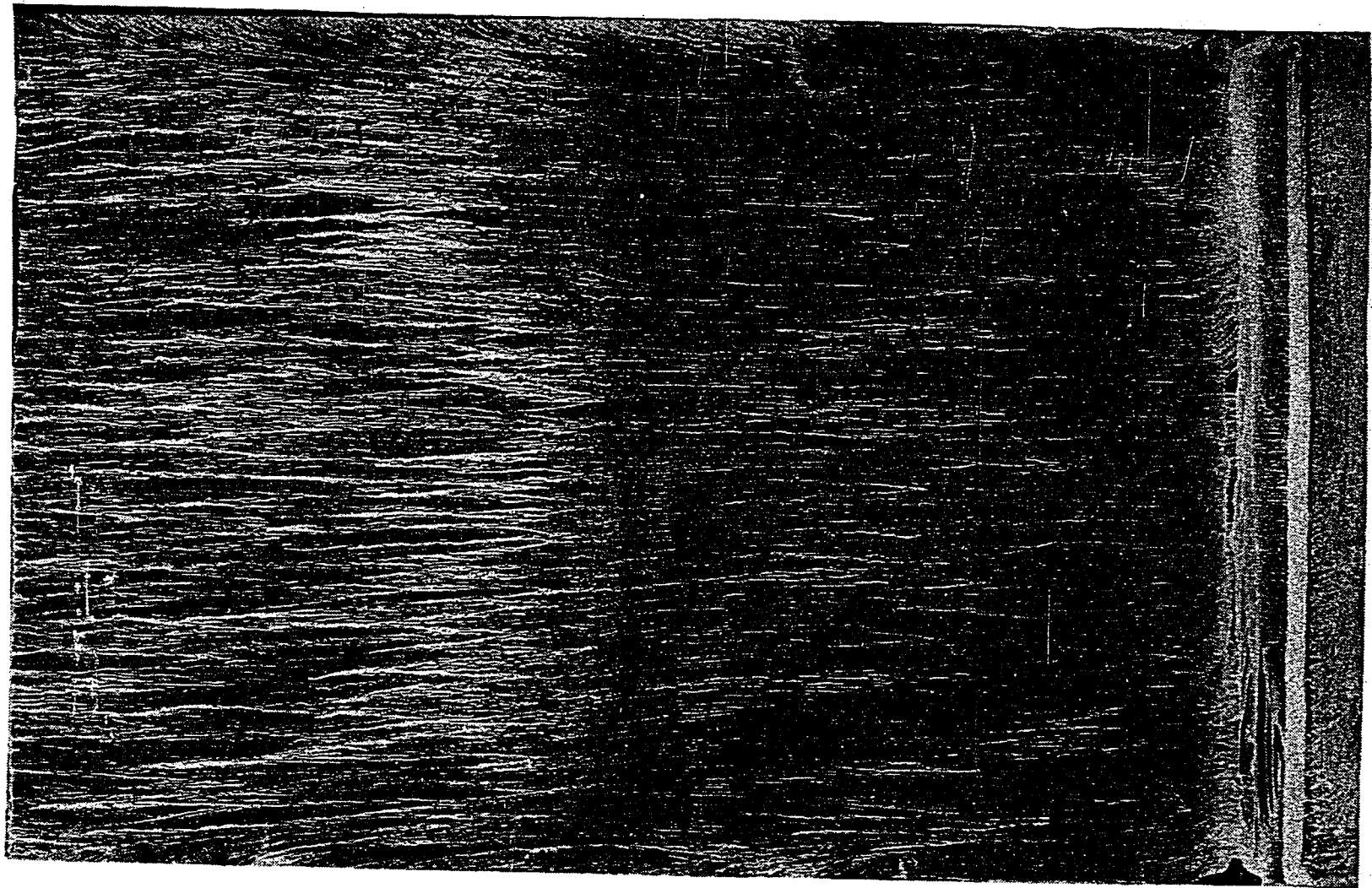


FIGURE 101. Flow pattern, Suction surface, $\beta_1 = 52^\circ$, GRID3, RE1

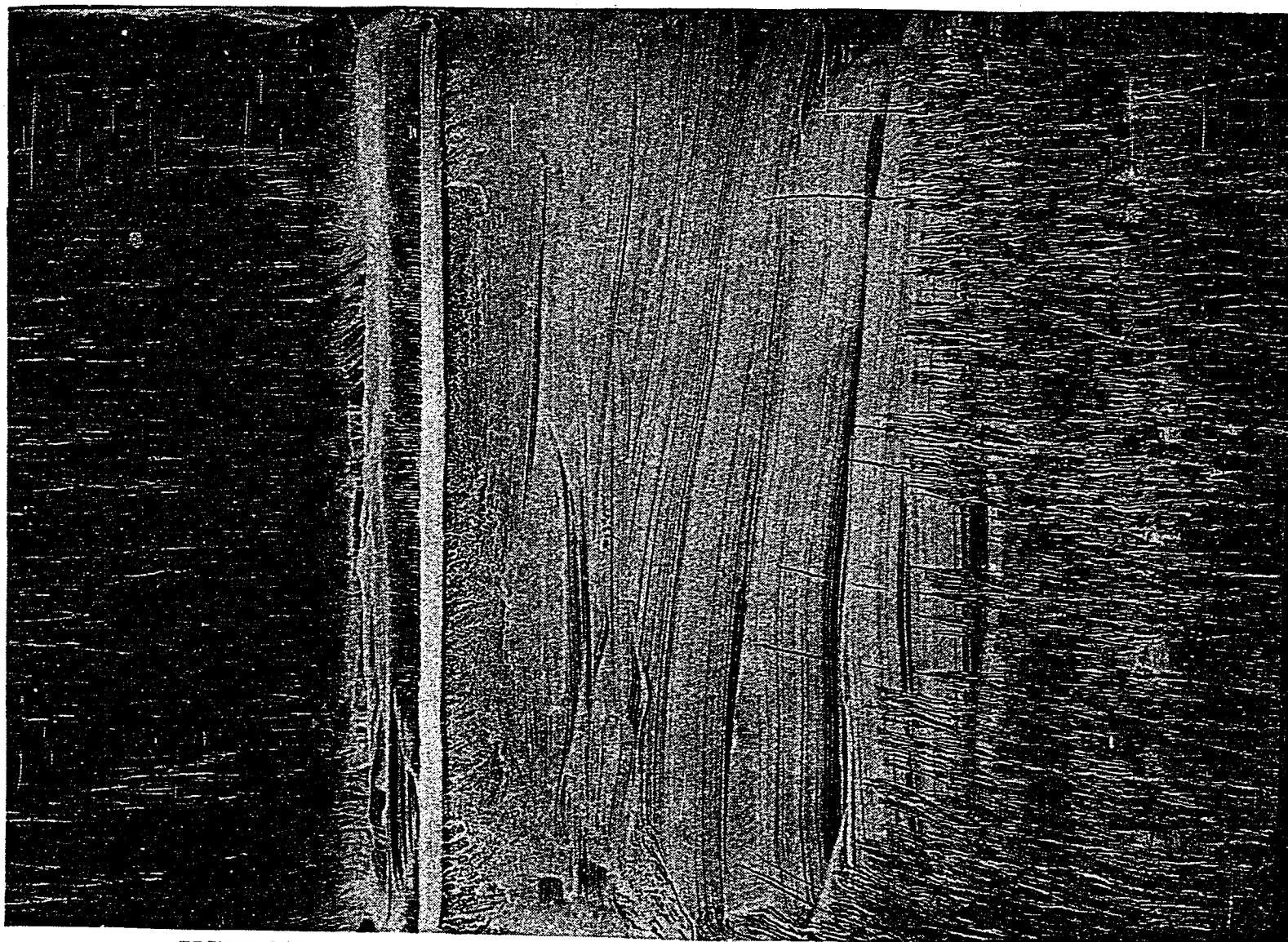


FIGURE 102. Flow pattern, Pressure surface, $\beta_1 = 52^\circ$, GRID3, RE1

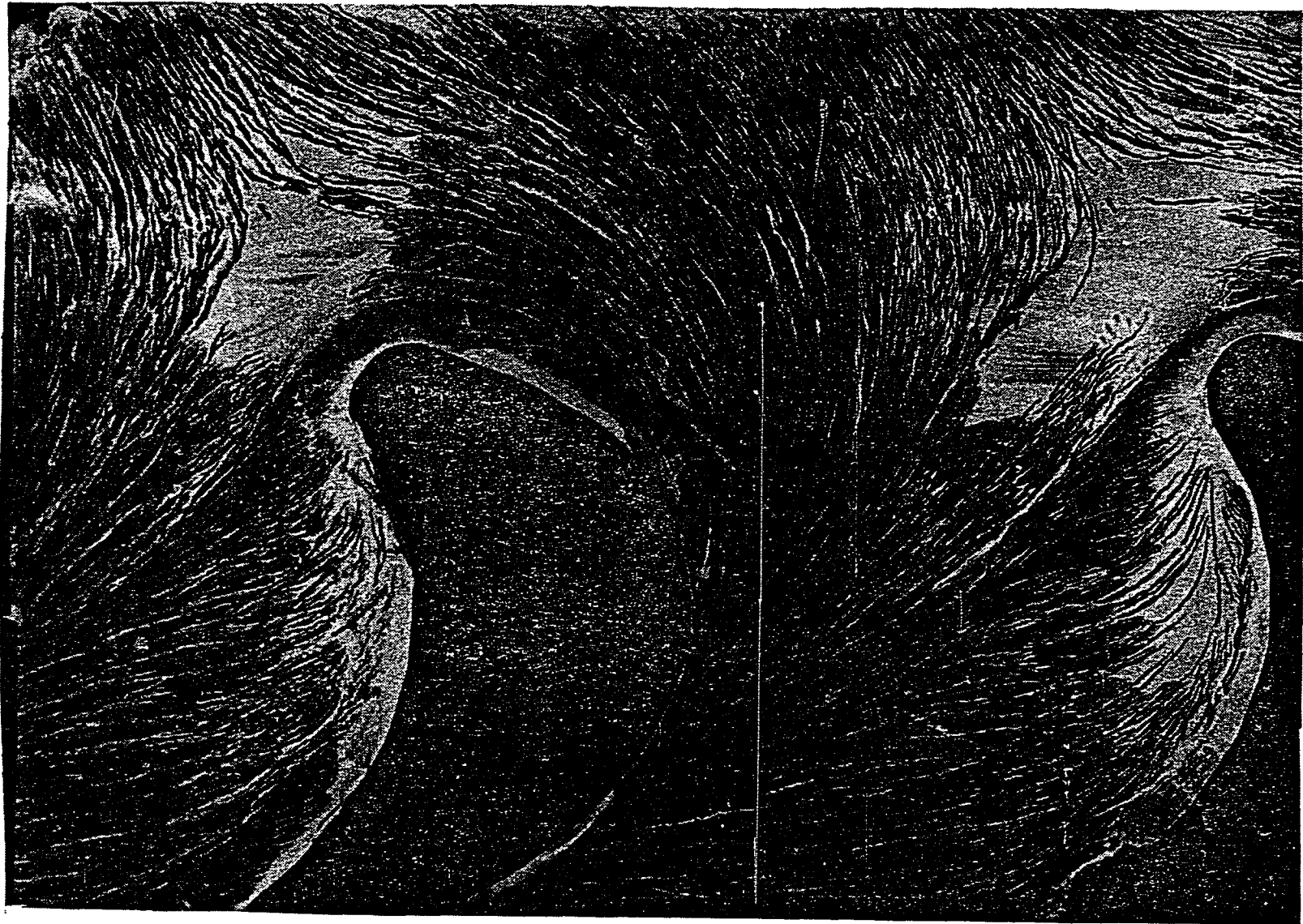


FIGURE 103. Flow pattern, Endwall, $\beta_1 = 52^\circ$

surface at low turbulence levels, but is absent at high turbulence levels. On the pressure surface, a separation bubble is observed near the leading edge for all turbulence levels. These observations were also made for the $\beta_1 = 45^\circ$ case.

3. Five-hole probe traverse results

At inlet angle $\beta_1 = 52^\circ$, five-hole probe traverses were conducted in the cascade exit plane at midspan for all test Reynolds numbers and turbulence levels. However, complete traverses of the upper-half of exit plane were conducted at flow condition NGRID. For all the test conditions, endwall suction was applied.

a. Secondary velocity vector plots Figure 104 shows the secondary velocity vector plot for flow conditions NGRID and Reynolds number RE1 in a plane normal to the mean camberline at the trailing edge of the airfoil. There is no sign of the passage vortex. The vectors indicate a spanwise flow towards the upper endwall due to the endwall suction, and overturning is again observed near the upper endwall. Secondary velocity vector patterns observed at Reynolds numbers RE2 and RE3 (but not shown here) were similar to the RE1 case.

b. Total pressure loss coefficient Contour plots of total pressure loss coefficient are shown in Figures 105, 106, and 107 for flow conditions NGRID and Reynolds numbers RE1, RE2, and RE3. The contours are seen to be straight and parallel for over 80% of the span, indicating a 2-D flow over that region. The highest loss levels are seen only in the wake, and appear to increase with decreasing Reynolds

numbers from a value of 0.9 for RE1, to 1.0 for RE2, and 1.1 for RE3. Close to the endwall, the higher loss levels are due to the endwall boundary layer.

Figure 108 is a plot of the pitch-averaged loss coefficient obtained from the five-hole probe traverses. For flow condition NGRID the loss levels remain constant for 80% of the span, and unlike the $\beta_1 = 45^\circ$ case, no hump due to a passage vortex is present in the distribution. Also, the loss levels are seen to increase slightly with decrease in Reynolds number. The results at midspan for flow condition GRID1 show that the loss level remains nearly constant for all three Reynolds numbers, while for GRID2 and GRID3 they increase slightly with a decrease in Reynolds number.

4. Hot-film gage results

Hot-film gage measurements were made for all the test turbulence levels and Reynolds numbers. Similar to the $\beta_1 = 45^\circ$ case, results are presented in the form of mean and RMS signals, along with the AC signal traces of the hot-film gage output. For this inlet angle, gages #1 through #5 were located in a favorable pressure gradient while gages #6 through #14 were located in an adverse pressure gradient region (see Figure 109).

Figures 110, 111, and 112 show the results for flow conditions NGRID and Reynolds numbers RE1, RE2, and RE3. For all three Reynolds numbers, it can be seen that a laminar separation bubble is formed and the boundary layer reattaches as a turbulent layer. For Reynolds

BETA1=52

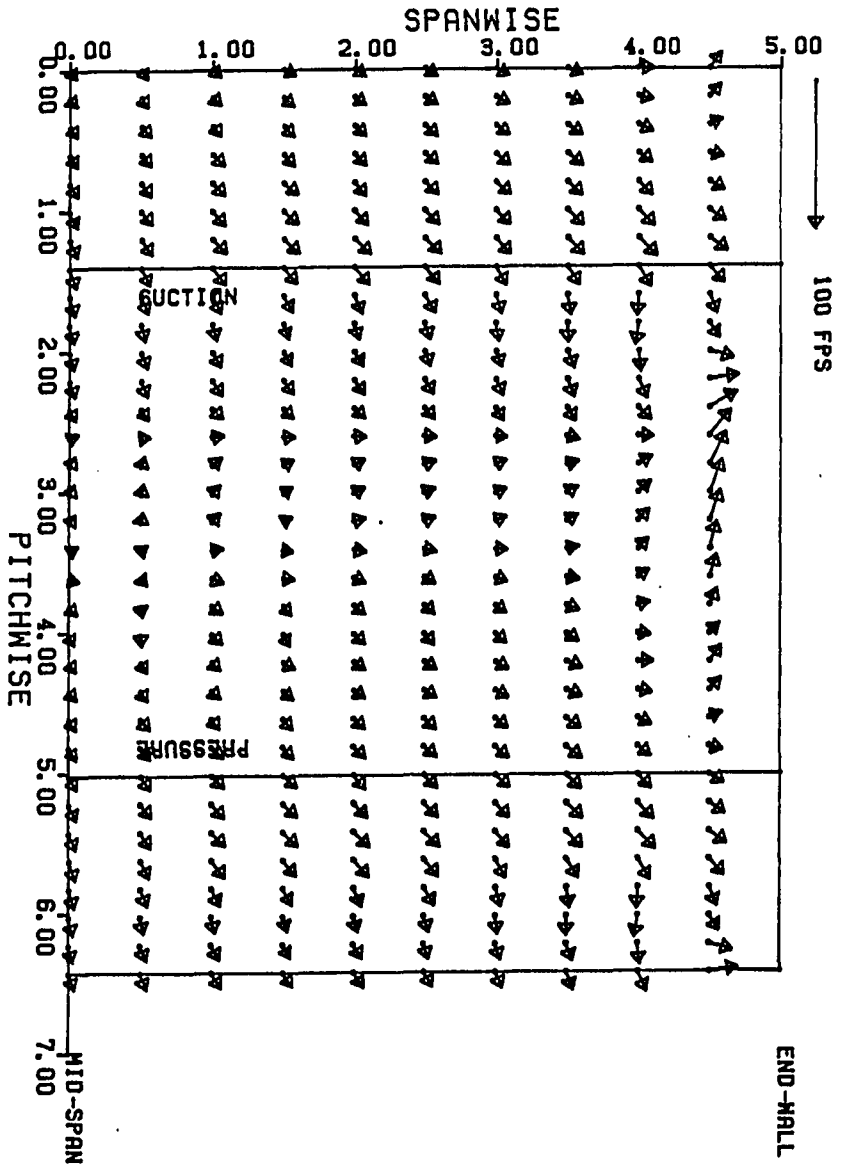


FIGURE 104. Secondary velocity vectors, $\beta_1 = 52^\circ$, NGRID, REL

CURVE LABEL	CURVE VALUE
1	0.100000E 00
2	0.200000E 00
3	0.300000E 00
4	0.400000E 00
5	0.500000E 00
6	0.600000E 00
7	0.700000E 00
8	0.800000E 00
9	0.900000E 00

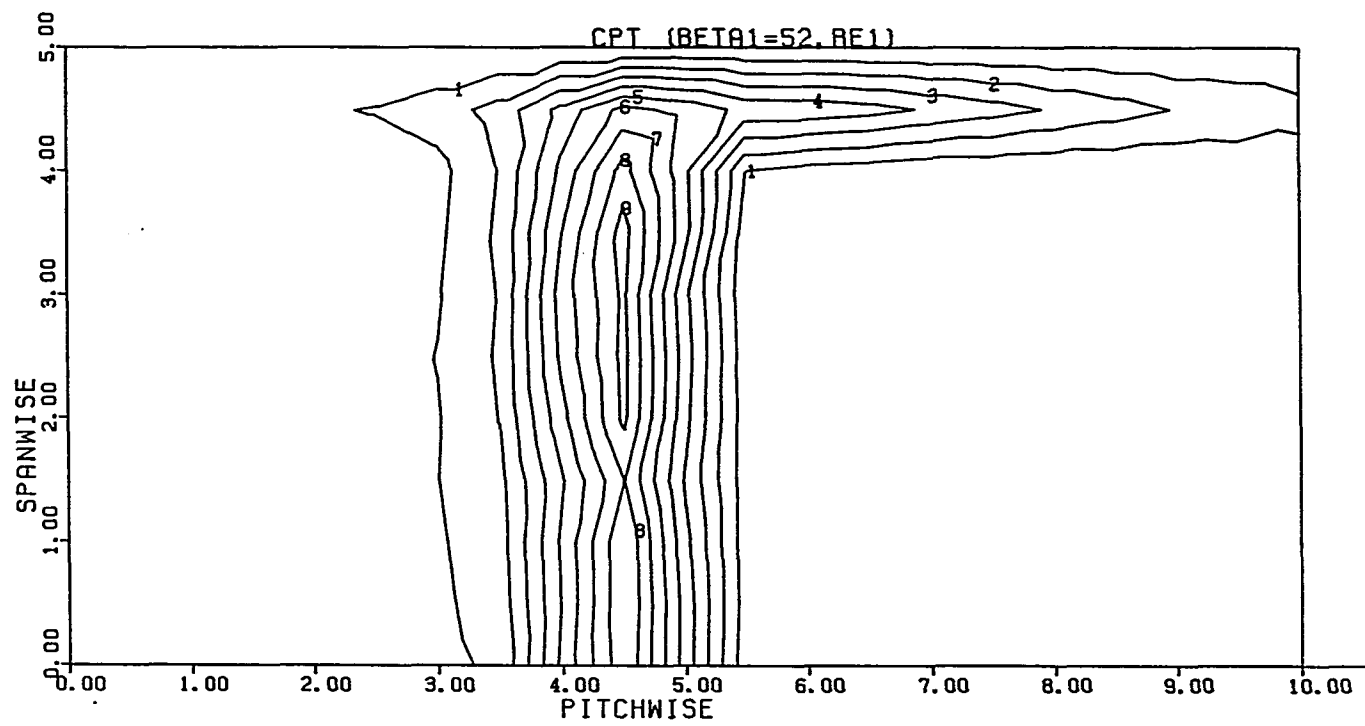


FIGURE 105. Total pressure loss contours, $\beta_1 = 52^\circ$, NGRID, RE1

CURVE LABEL	CURVE VALUE
1	0.100000E 00
2	0.200000E 00
3	0.300000E 00
4	0.400000E 00
5	0.500000E 00
6	0.600000E 00
7	0.700000E 00
8	0.800000E 00
9	0.900000E 00
10	0.100000E 01

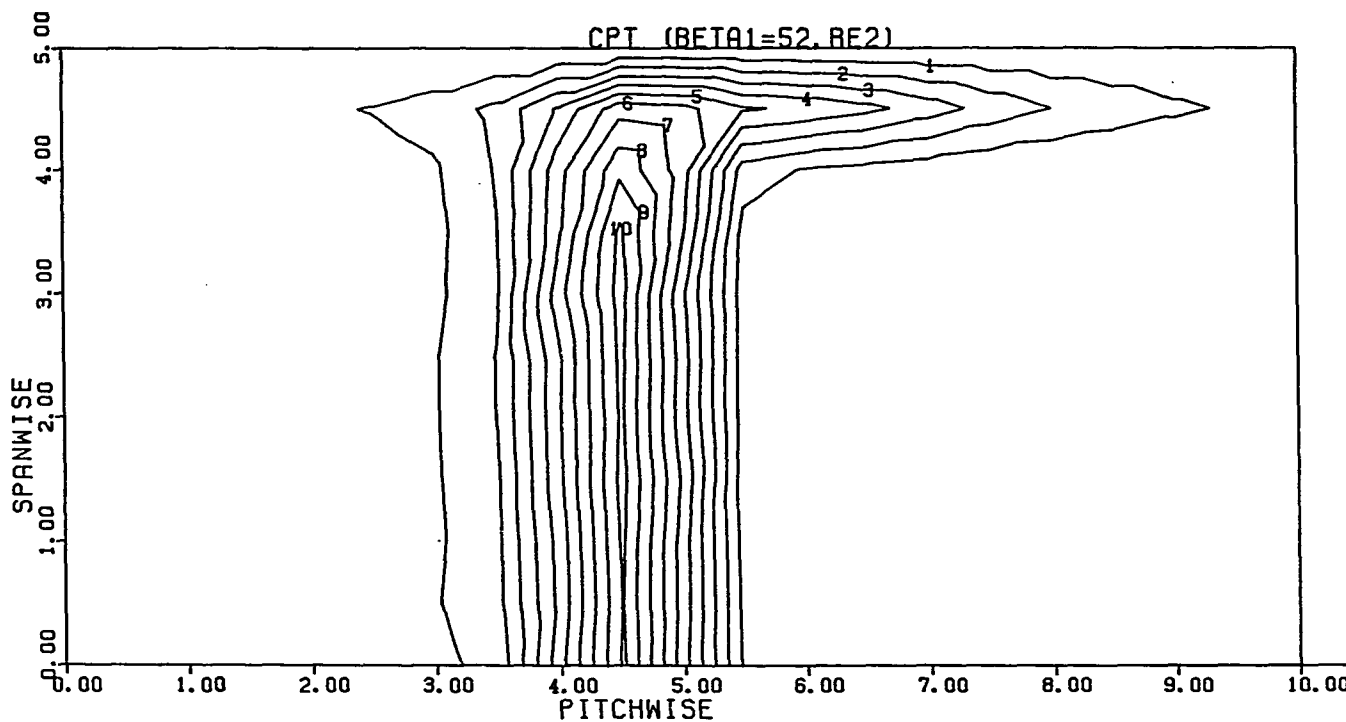


FIGURE 106. Total pressure loss contours, $\beta_1 = 52^\circ$, NGRID, RE2

CURVE LABEL	CURVE VALUE
1	0.100000E 00
2	0.200000E 00
3	0.300000E 00
4	0.400000E 00
5	0.500000E 00
6	0.600000E 00
7	0.700000E 00
8	0.800000E 00
9	0.900000E 00
10	0.100000E 01
11	0.110000E 01

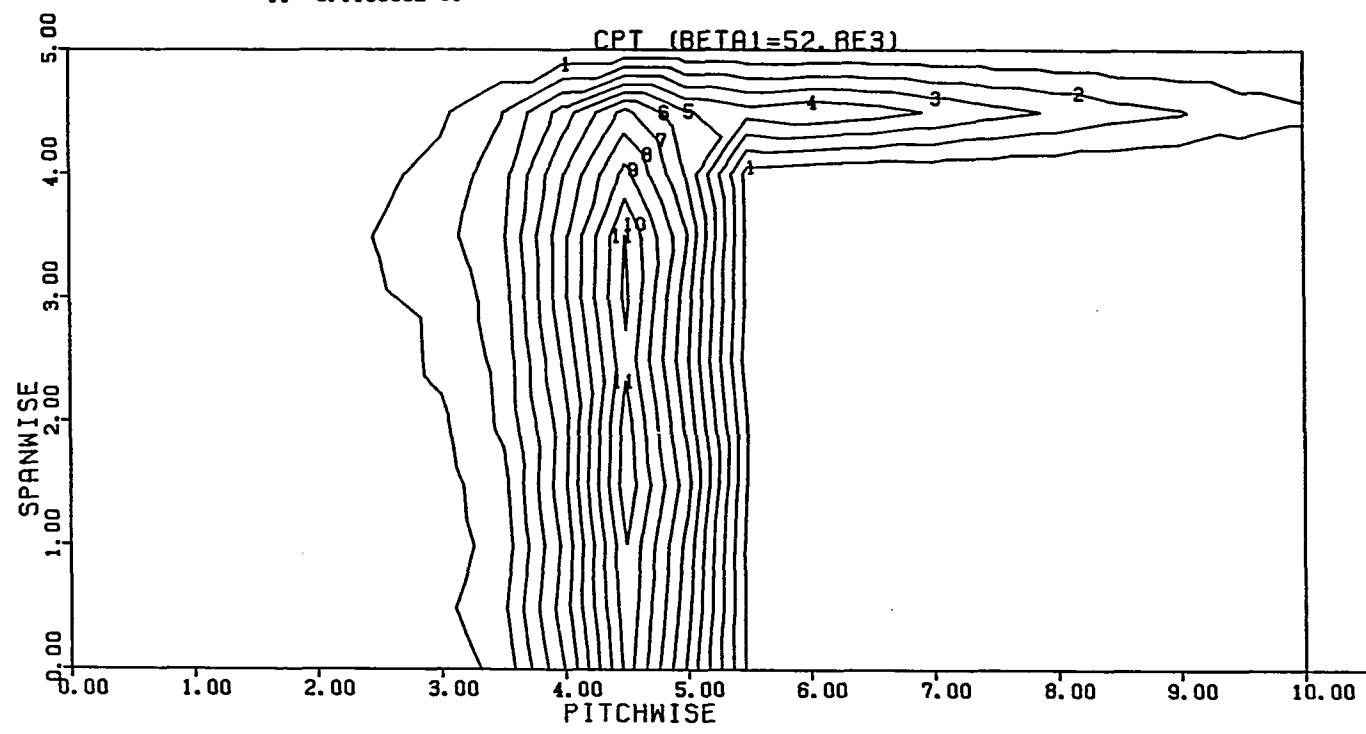


FIGURE 107. Total pressure loss contours, $\beta_1 = 52^\circ$, NGRID, RE3

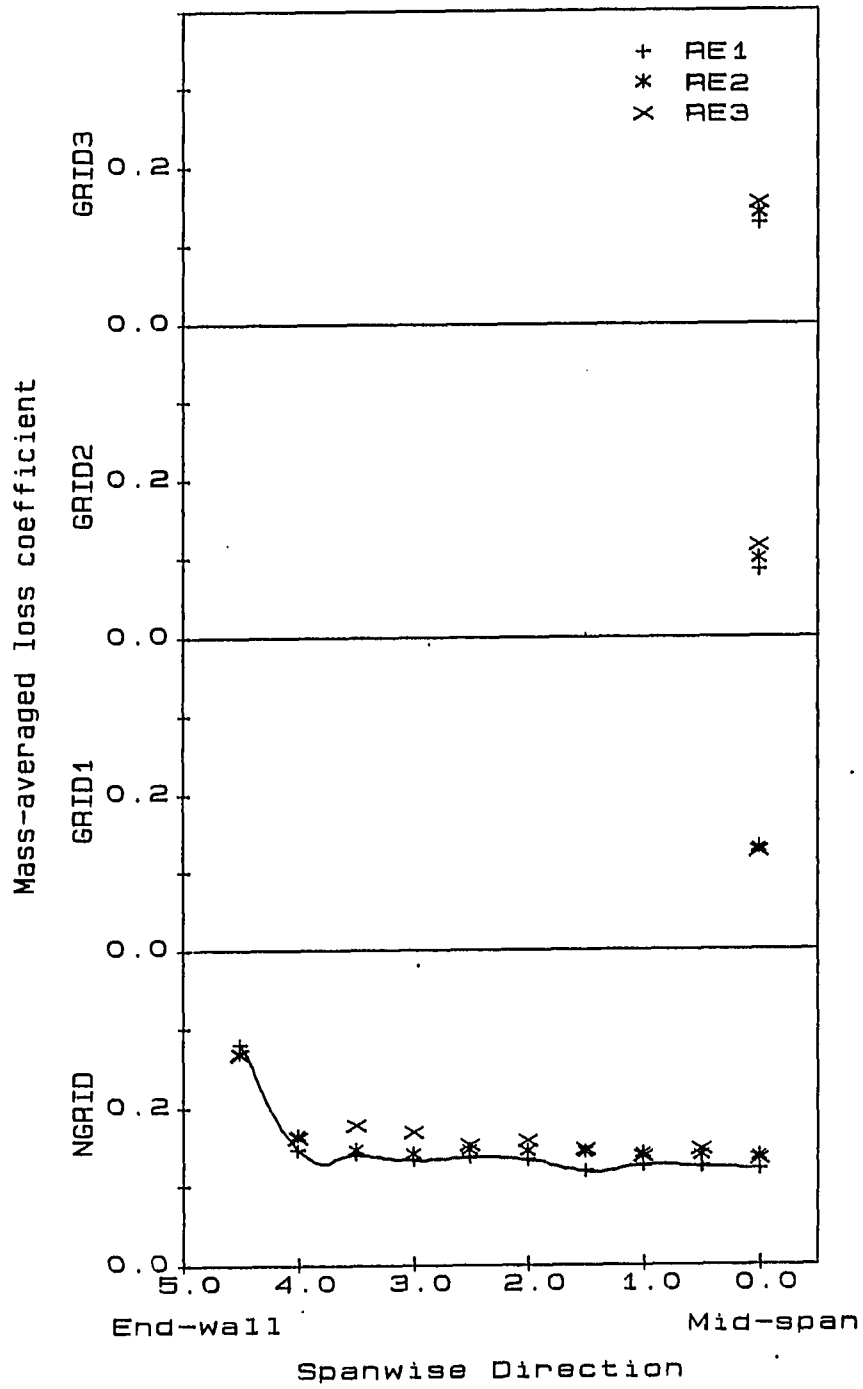


FIGURE 108. Pitch-averaged loss coefficient, $\beta_1 = 52^\circ$

number RE1, as seen in Figure 110, the separation bubble is formed downstream of gage #7, near the 50% point along the suction surface. Gage #8, located in the separated region, shows large fluctuations. The boundary layer reattaches at a point between gages #8 and #9. The flow visualization in Figure 99 also shows the separation bubble at the same streamwise location. Figure 111 for Reynolds number RE2 shows the laminar separation bubble and reattachment at the same locations as for RE1. However, for Reynolds number RE3, Figure 112 shows the separation bubble further downstream, near gage #8.

Figures 113, 114, and 115 show hot-film gage results for flow conditions GRID1 and Reynolds numbers RE1, RE2, and RE3. Figure 113 for RE1 indicates a start of natural rather than bubble-induced transition downstream of gage #5, and the end of transition at gage #9. However, the mean signal has minimum and maximum values, indicating separation, so that transition appears to be completed with a bubble. Also, flow visualization for this case (Figure 100) shows separation. In Figures 114 and 115 for RE2 and RE3, a separation bubble is indicated at gage #8, with reattachment of a fully turbulent boundary layer near gage #9.

Results for flow conditions GRID2 indicate a natural transition at Reynolds number RE1, a bubble-induced transition at RE3, and a combination of natural and bubble-induced transition at RE2. Figure 116 for RE1 shows the start of transition downstream of gage #5, and the end of transition downstream of gage #9. Turbulent spikes are

observed in signal traces for gages #6 and #7, while laminar spikes are observed in gages #8 and #9. For RE2, Figure 117 shows transition to start near gage #6 and to end abruptly near gage #9. For RE3, as seen in Figure 118, a separation bubble is formed at gage #7 and a fully turbulent boundary layer reattaches at gage #9.

The situation for flow condition GRID3 is the same as that for GRID2. Figure 119 for Reynolds number RE1 shows transition beginning at gage #5 and ending at gage #9. For RE2, as seen in Figure 120, transition starts naturally between gages #5 and #6, but ends abruptly near gage #9. For RE3, as seen in Figure 121, a separation bubble is formed at gage #7, and a turbulent boundary layer reattaches at gage #9.

The general features observed in the hot-film gage results for the inlet angle $\beta_1 = 52^\circ$, case are similar to those observed in the $\beta_1 = 45^\circ$ case. The laminar boundary layer on the airfoil suction surface undergoes natural transition at high turbulence levels and Reynolds numbers, a bubble-induced transition at low turbulence levels and Reynolds numbers, and a natural transition which is completed by a bubble at intermediate turbulence levels and Reynolds numbers. However, unlike the $\beta_1 = 45^\circ$ case, where natural transition was observed to start upstream of the minimum pressure point for the flow conditions GRID2 and GRID3 and Reynolds number RE1, transition for the $\beta_1 = 52^\circ$ case always started at the minimum pressure point or downstream of it. These results are probably due to the stronger

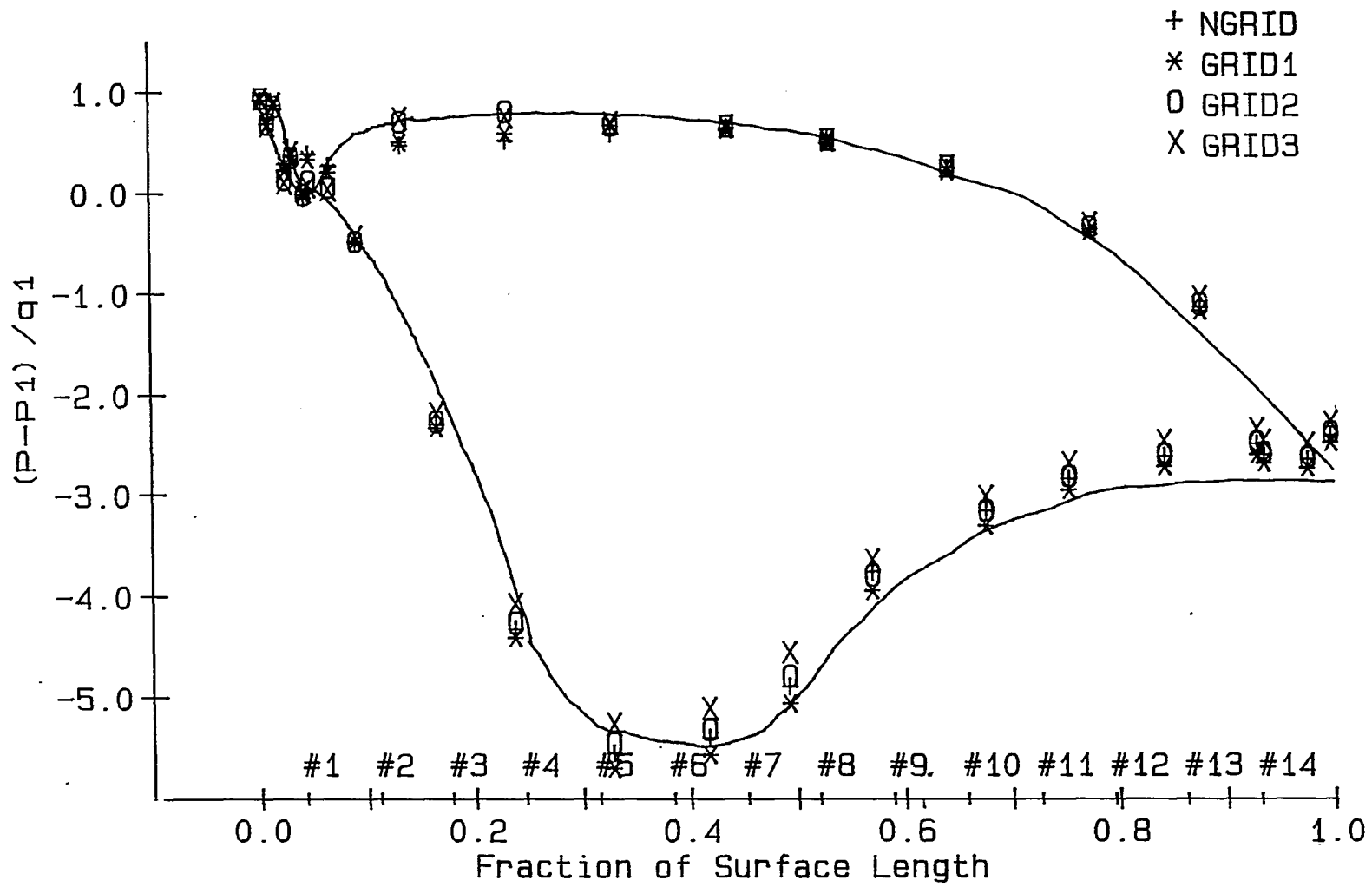


FIGURE 109. Hot-film gage locations plotted against the pressure distribution for $\beta_1 = 52^\circ$

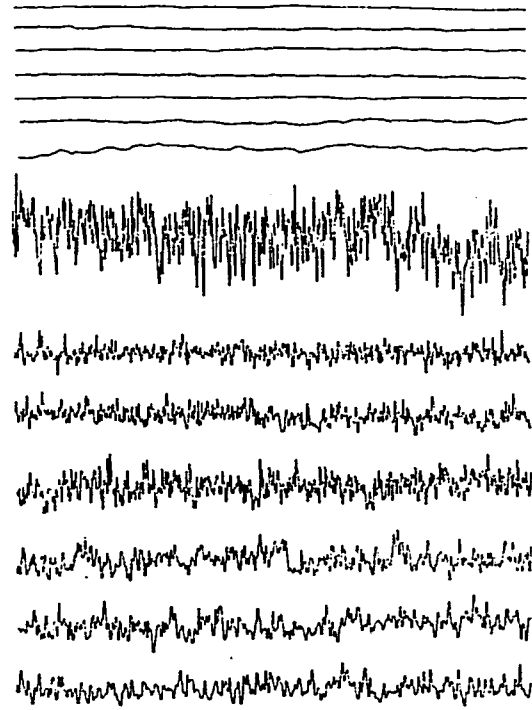
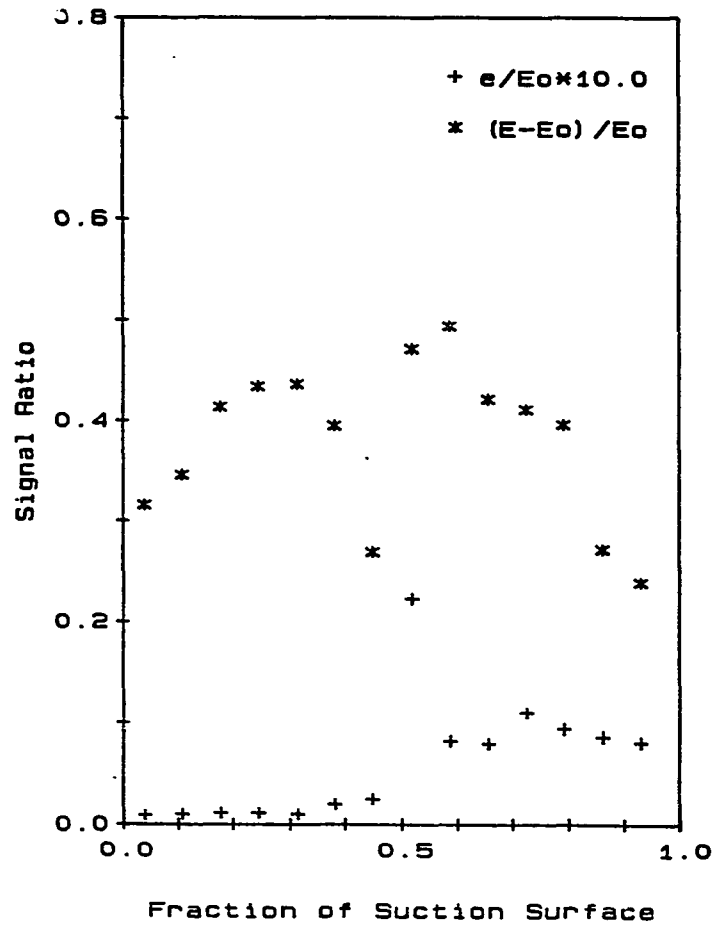


FIGURE 110. Hot-film gage results, $\beta_1 = 52^\circ$, NGRID, RE1

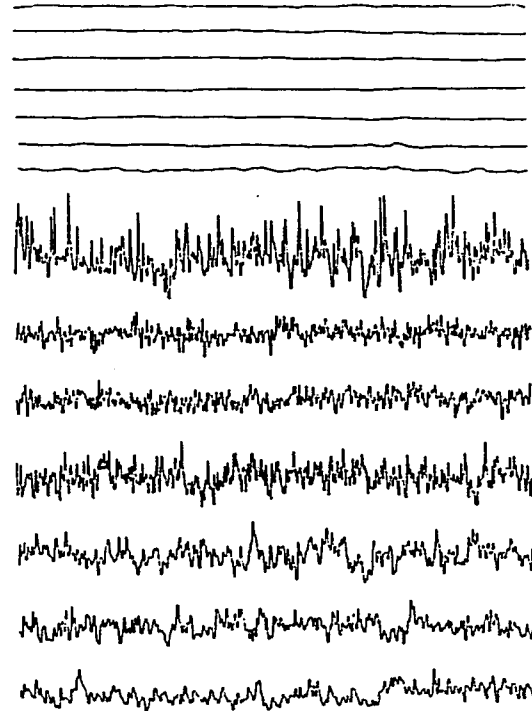
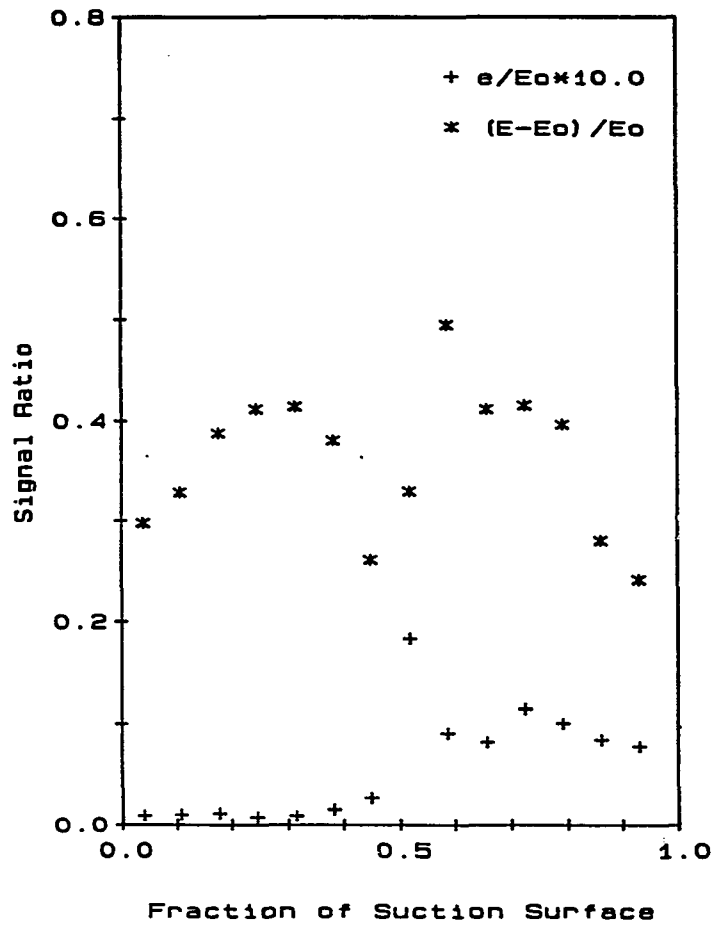


FIGURE 111. Hot-film gage results, $\beta_1 = 52^\circ$, NGRID, RE2

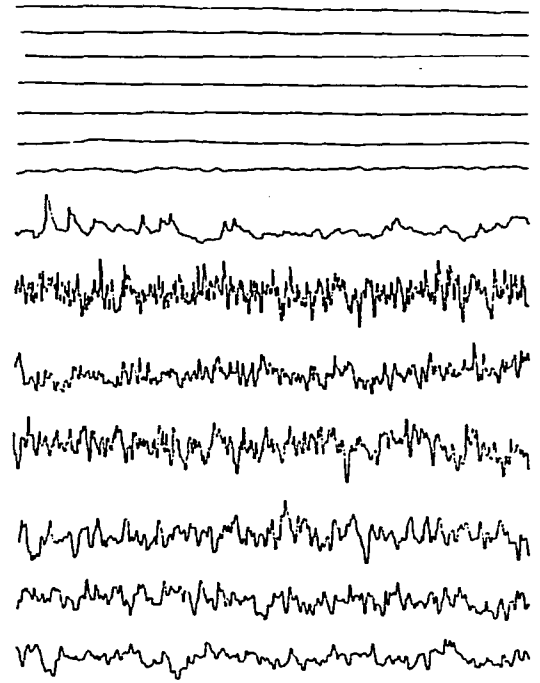
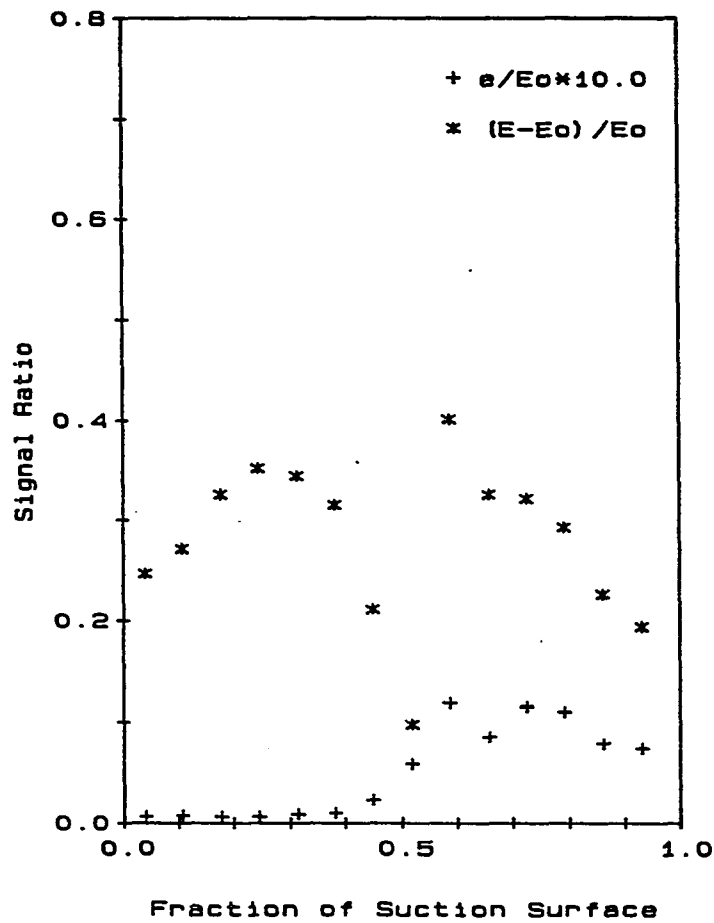


FIGURE 112. Hot-film gage results, $\beta_1 = 52^\circ$, NGRID, RE3

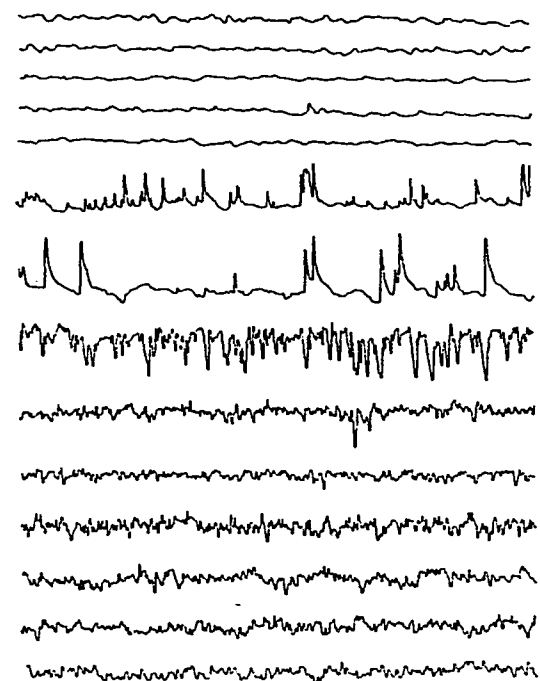
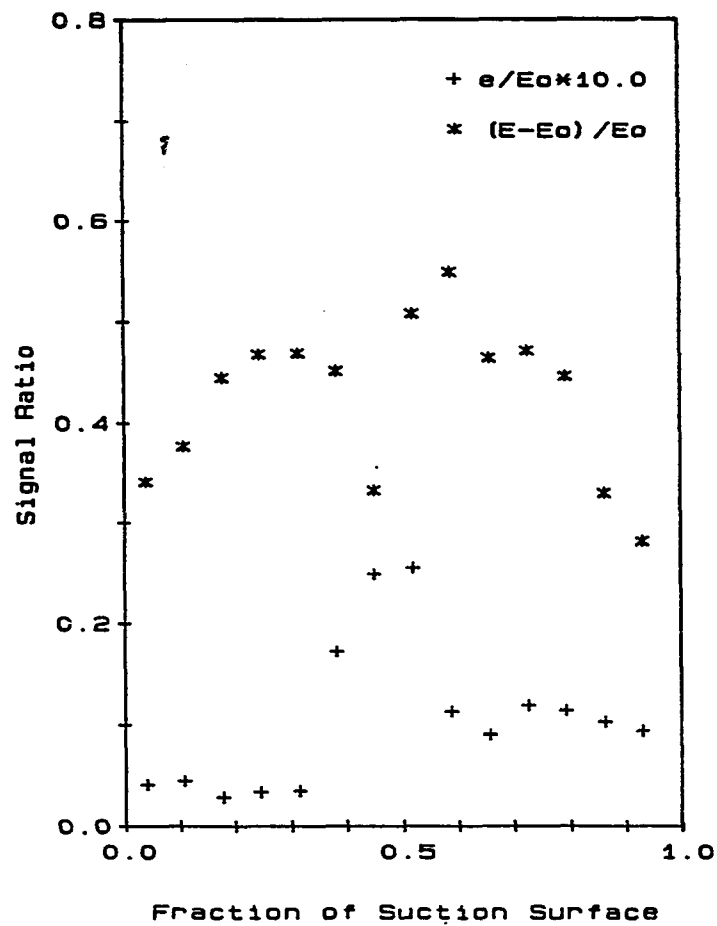


FIGURE 113. Hot-film gage results, $\beta_1 = 52^\circ$, GRID1, RE1

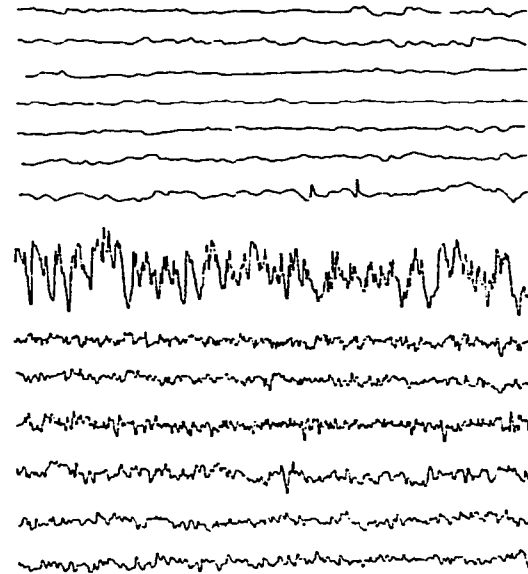
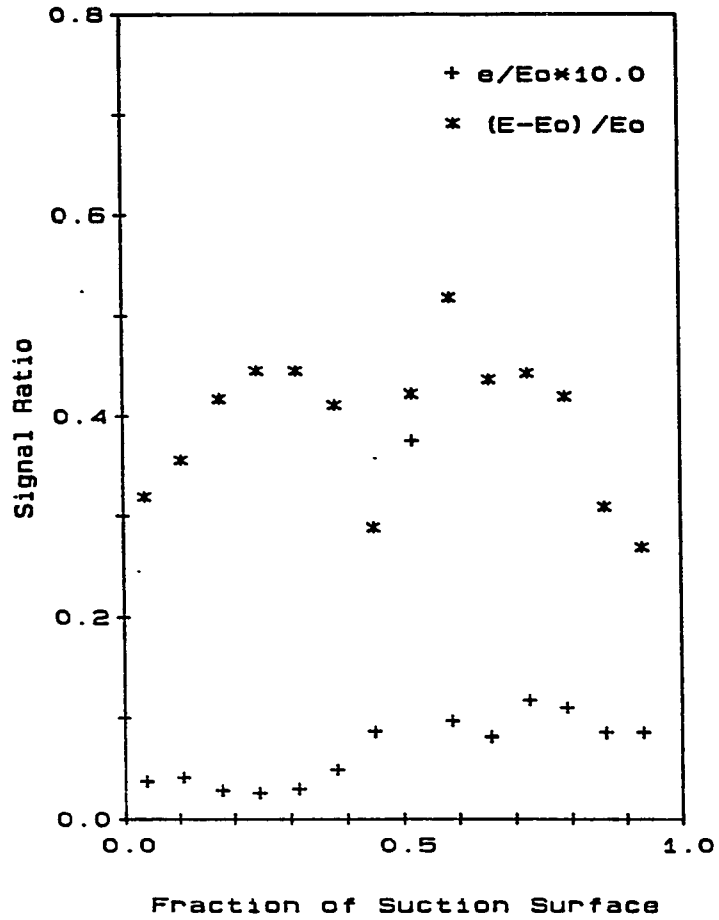


FIGURE 114. Hot-film gage results, $\beta_1 = 52^\circ$, GRID1, RE2

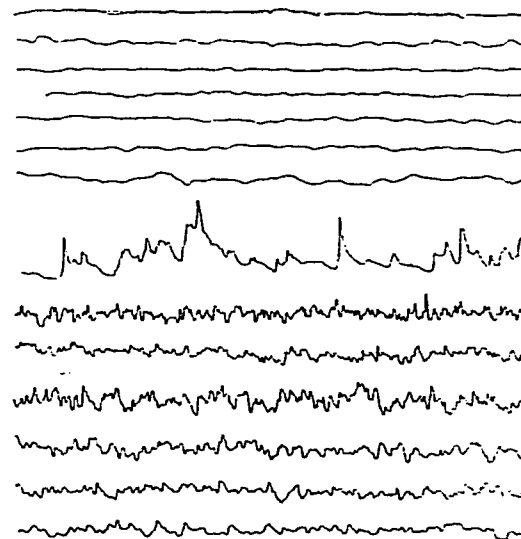
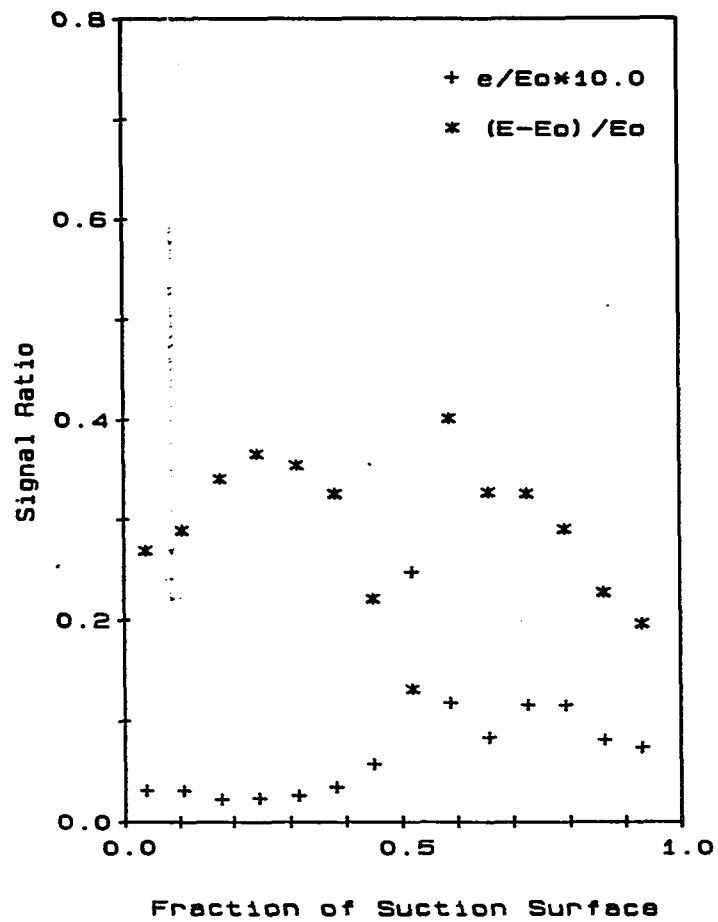


FIGURE 115. Hot-film gage results, $\beta_1 = 52^\circ$, GRID1, RE3

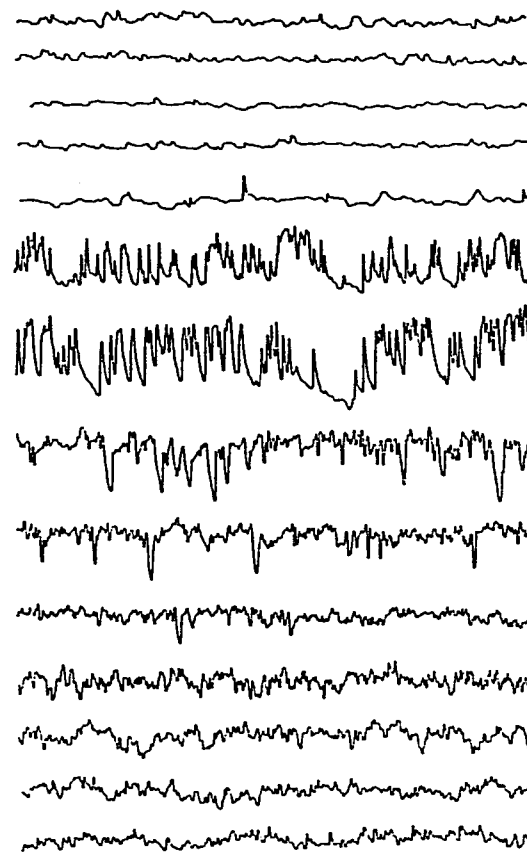
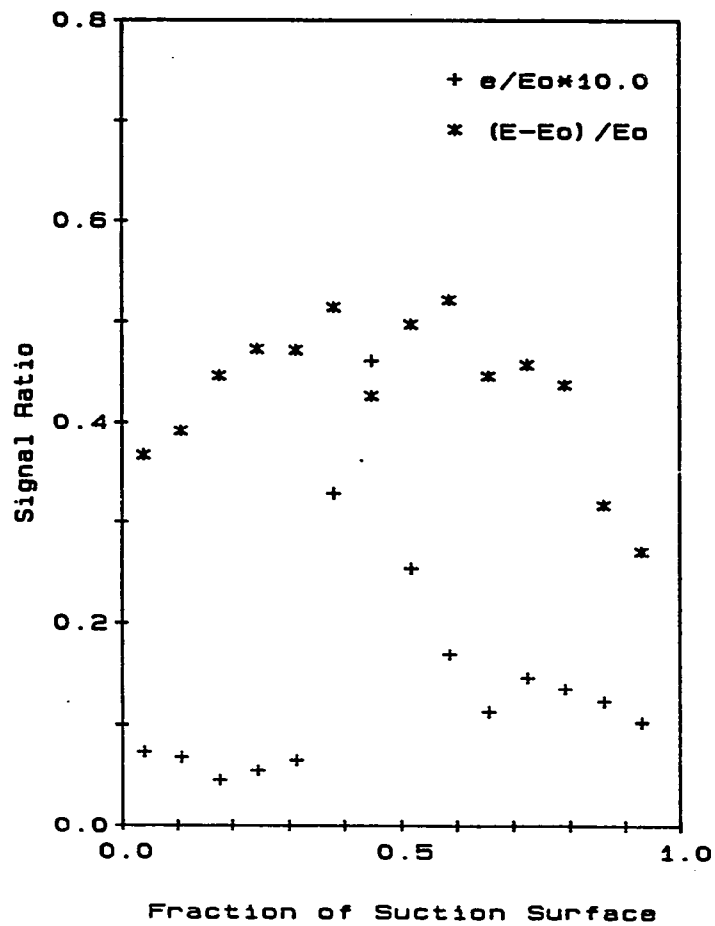


FIGURE 116. Hot-film gage results, $\beta_1 = 52^\circ$, GRID2, RE1

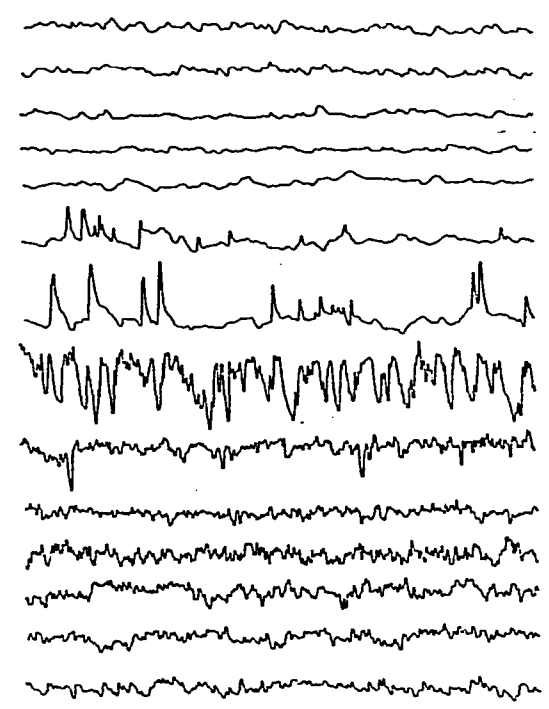
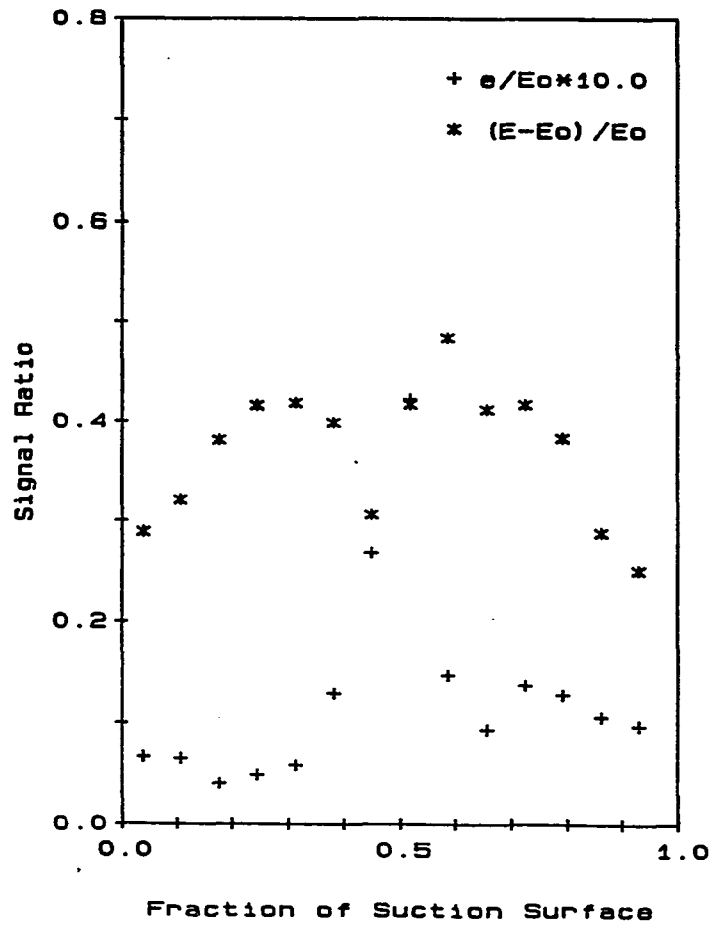


FIGURE 117. Hot-film gage results, $\beta_1 = 52^\circ$, GRID2, RE2

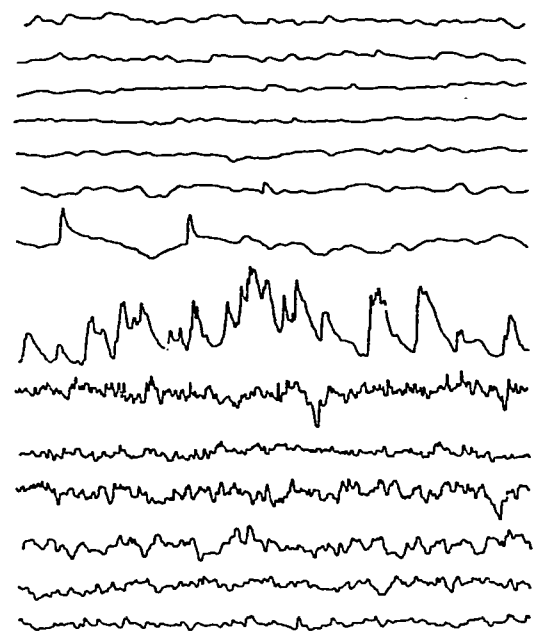
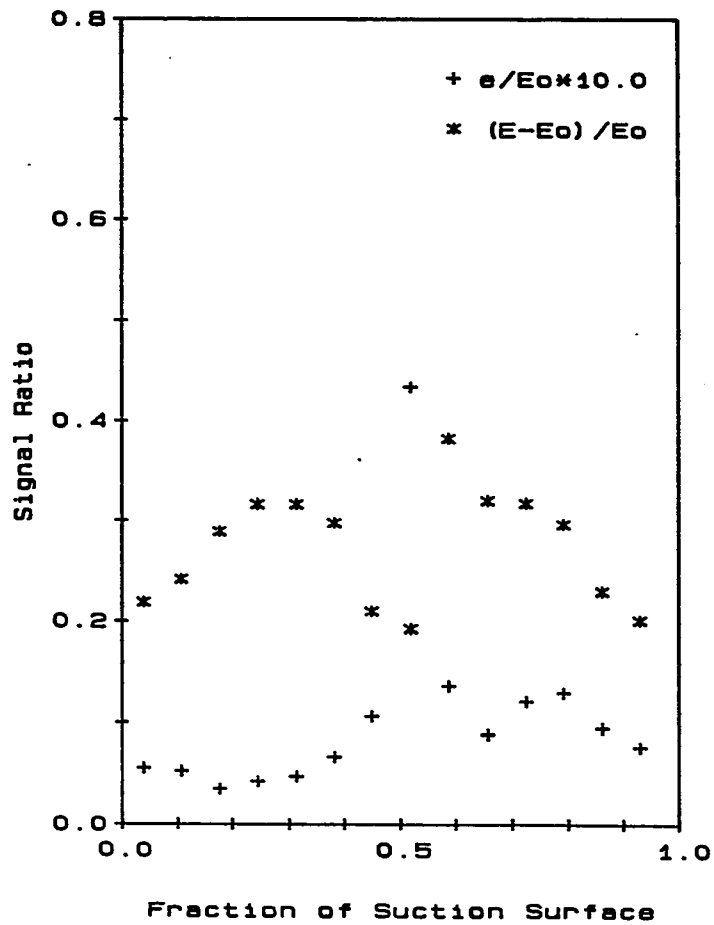


FIGURE 118. Hot-film gage results, $\beta_1 = 52^\circ$, GRID2, RE3

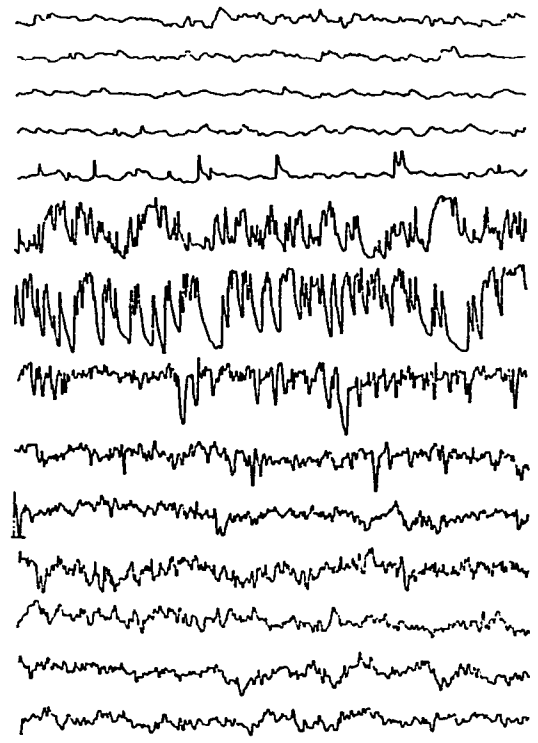
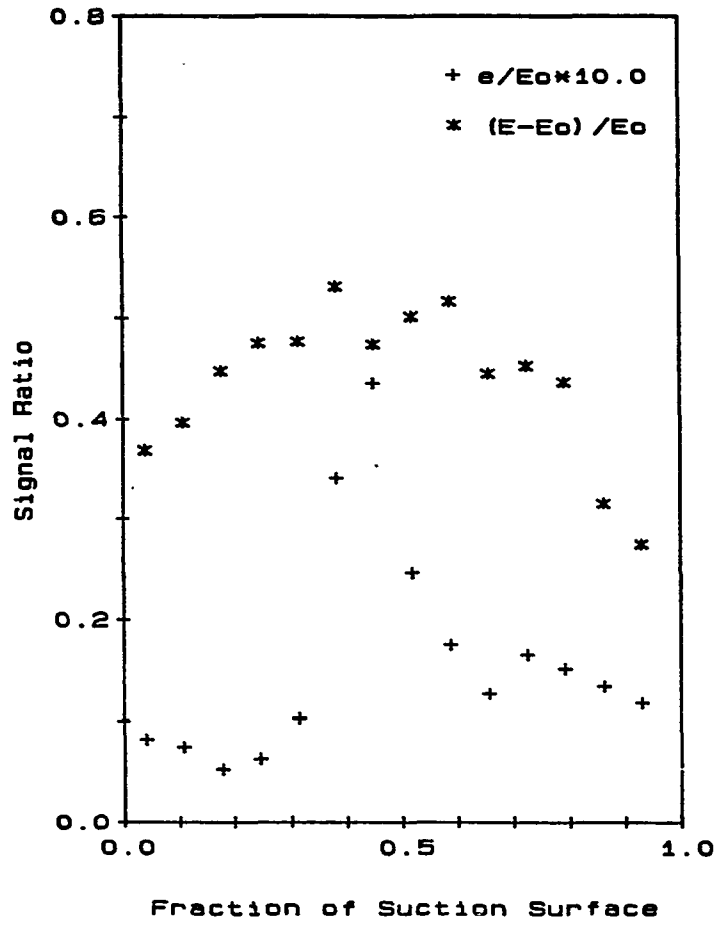


FIGURE 119. Hot-film gage results, $\beta_1 = 52^\circ$, GRID3, RE1

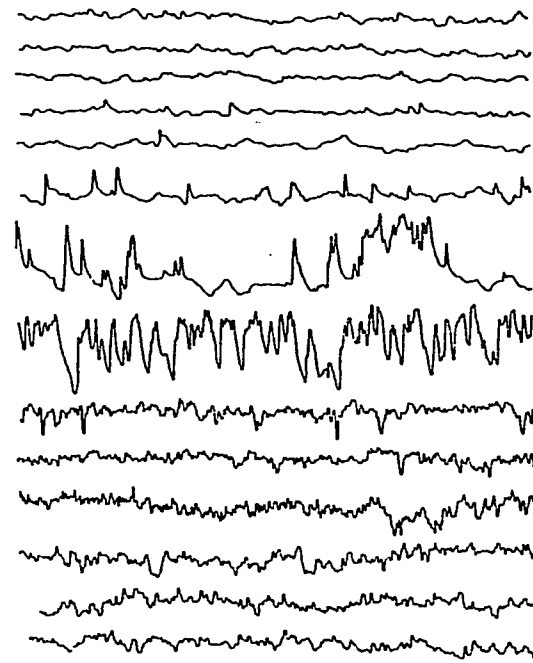
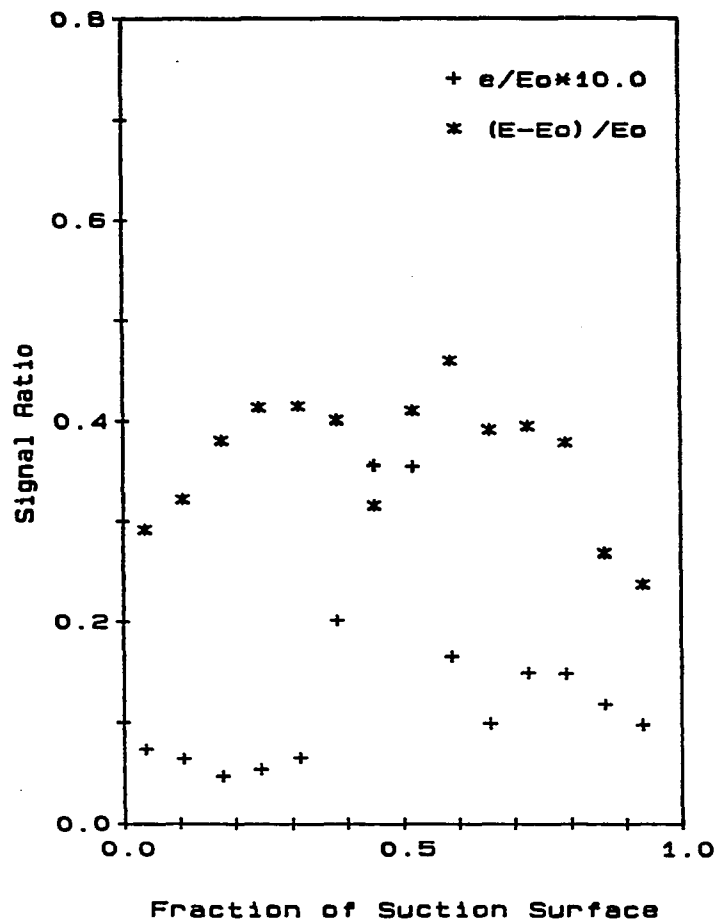


FIGURE 120. Hot-film gage results, $\beta_1 = 52^\circ$, GRID3, RE2

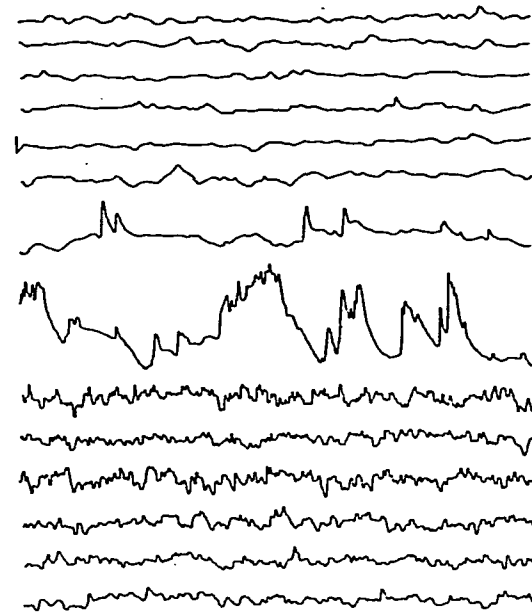
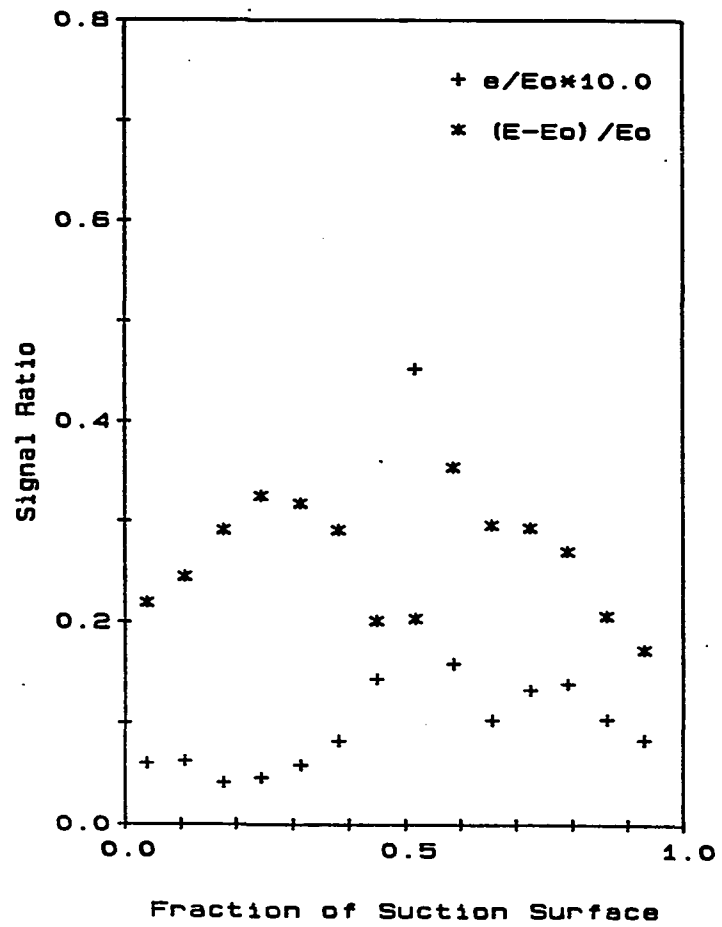


FIGURE 121. Hot-film gage results, $\beta_1 = 52^\circ$, GRID3, RE3

favorable pressure gradient in the forward portion of the suction surface for $\beta_1 = 52^\circ$.

C. Inlet Angle, $\beta_1 = 38^\circ$ (0° incidence)

1. Static pressure measurements

Static pressure measurements were made for all the test conditions, as in the $\beta_1 = 45^\circ$ and $\beta_1 = 52^\circ$ cases. Figure 122 shows the measured static pressure distribution for the four turbulence levels at Reynolds number RE1 plotted against the fraction of suction or pressure surface length from the stagnation point. Also shown for comparison is the predicted 2-D distribution (the solid line). As seen in Figure 122, similar to the previous results, there is a reduction in loading on the suction surface with an increase in turbulence level. Also on the suction surface the measured distribution fails to follow the underspeeding predicted near the leading edge. On the pressure surface, the measured distribution agrees well with the predicted distribution and closely follows the leading edge overspeeding. Figures 123 through 126 show the pressure distribution at the four turbulence levels plotted for the three Reynolds numbers. As seen, the measured distribution is independent of Reynolds number for the range tested.

2. Flow visualizations

Figures 127, 128, and 129 show the flow pattern on the suction surface of the airfoil for flow conditions NGRID, GRID1, and GRID3, and

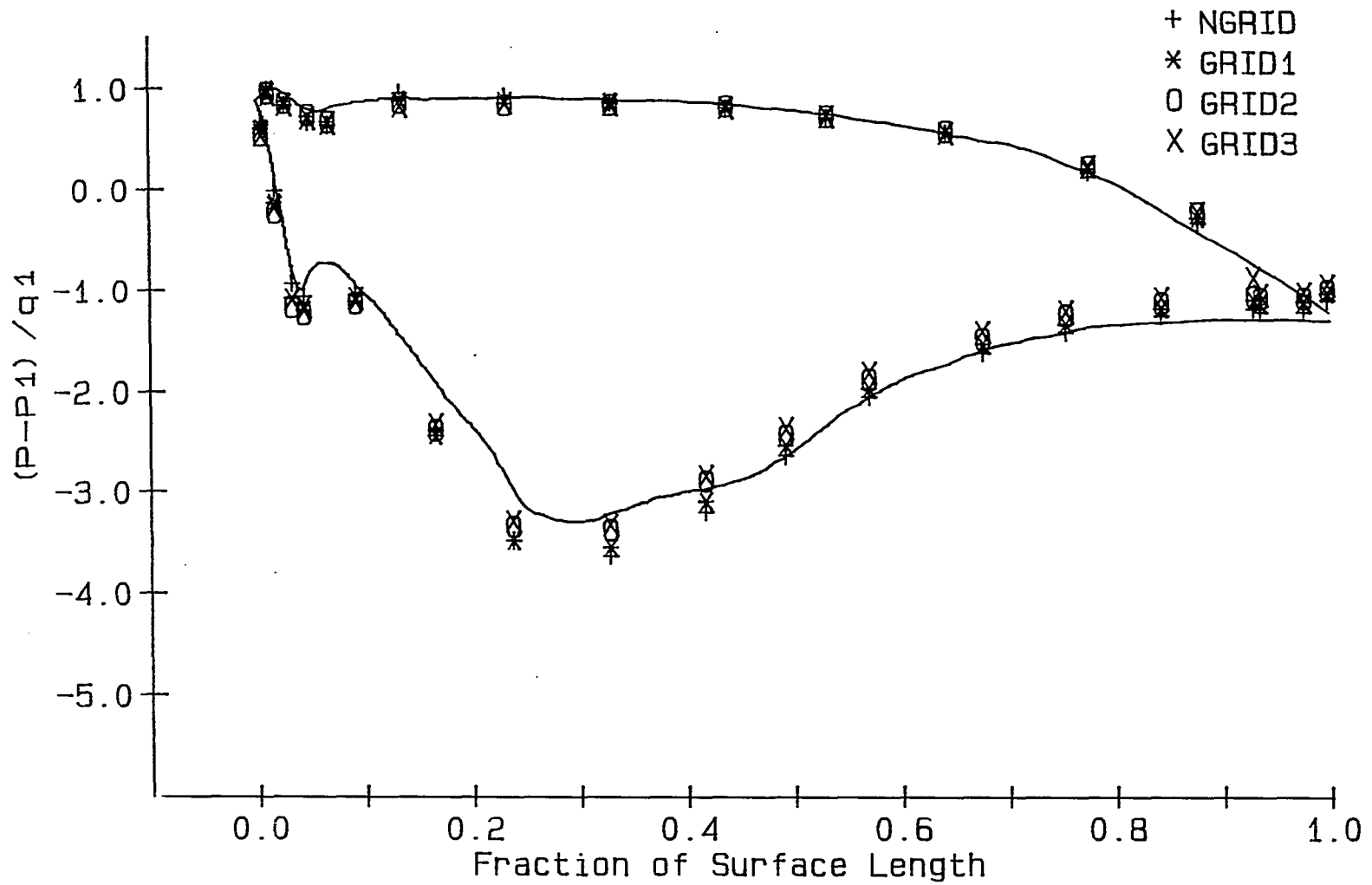


FIGURE 122. Static pressure distribution, $\beta_1 = 38^\circ$, RE1

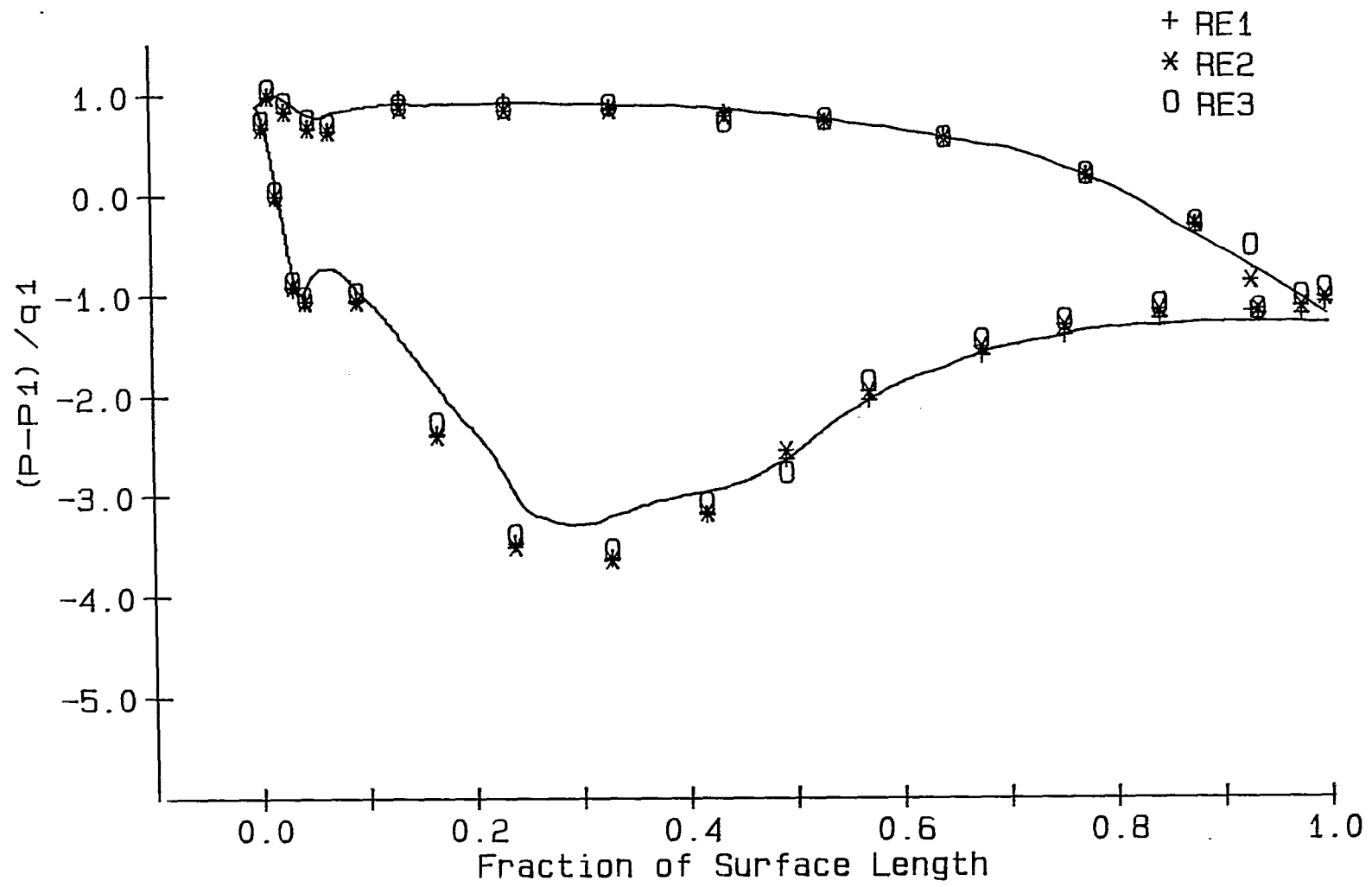


FIGURE 123. Static pressure distribution, $\beta_1 = 38^\circ$, NGRID

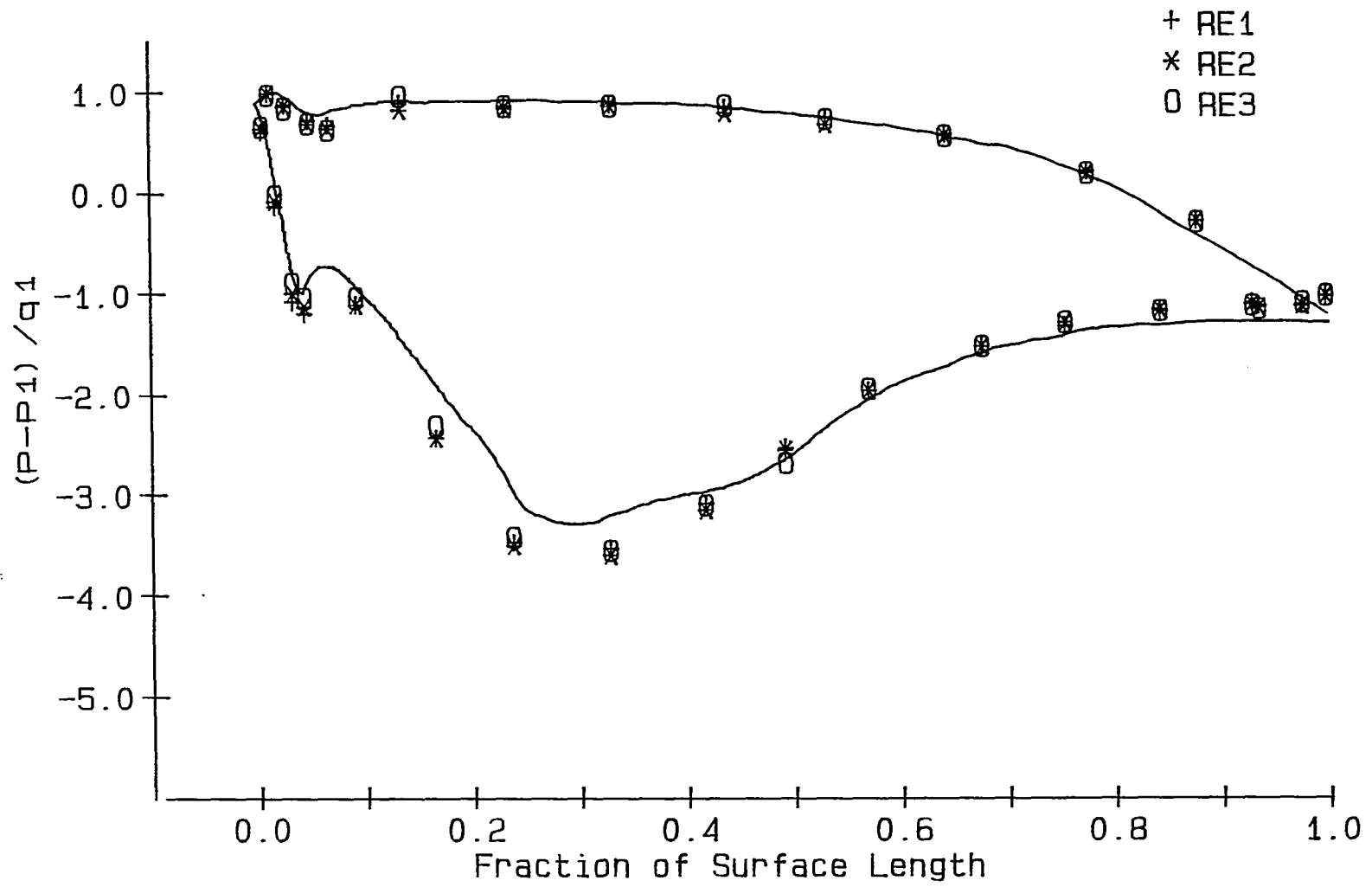


FIGURE 124. Static pressure distribution, $\beta_1 = 38^\circ$, GRID1

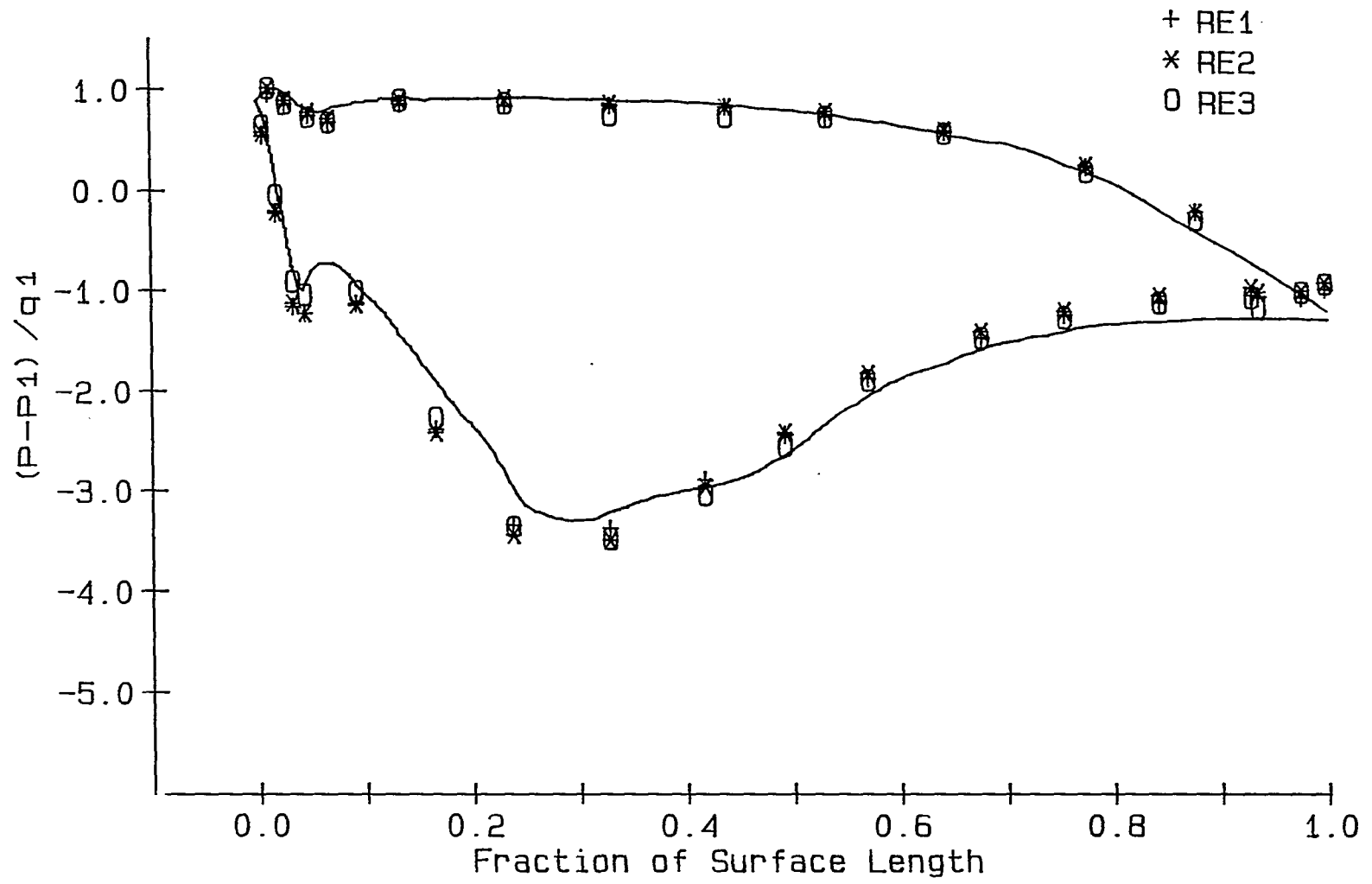


FIGURE 125. Static pressure distribution, $\beta_1 = 38^\circ$, GRID2

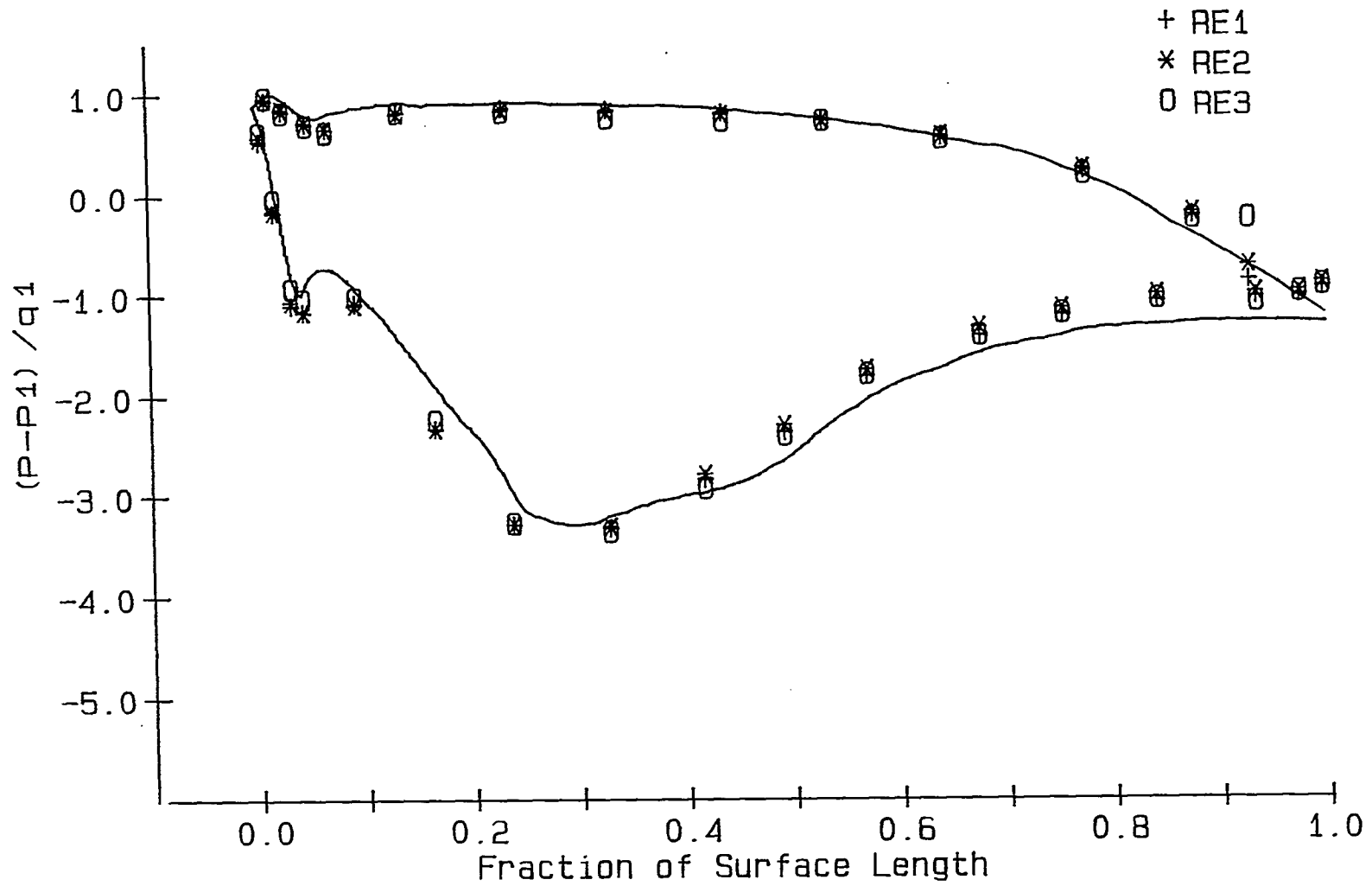


FIGURE 126. Static pressure distribution, $\beta_1 = 38^\circ$, GRID3

Reynolds number RE1. Endwall suction was applied for all the cases. The flow is from right to left and gravity acts from top to bottom. Figure 127 for NGRID shows a laminar separation bubble at near the 40% point along the surface length. Figure 128 for GRID1 shows streaks of pigment deposits, indicating separation patterns similar to the $\beta_1 = 45^\circ$ and $\beta_1 = 52^\circ$ cases. Figure 129 for GRID3 indicates no separation and that natural transition has occurred. In all three figures, migration of the limiting streamlines towards midspan can be seen. This effect is more pronounced for this inlet angle than in the $\beta_1 = 45^\circ$ case.

The flow pattern for the pressure surface in Figure 130 is very similar to that for the $\beta_1 = 45^\circ$ case. A separation bubble is present downstream of the stagnation point. Figure 131, showing the endwall flow pattern, is similar to the $\beta_1 = 45^\circ$ and $\beta_1 = 52^\circ$ cases, with the saddle points of separation and the separation lines caused by the suction and pressure side legs of the horseshoe vortex clearly seen. The distance between the saddle points is one blade pitch, and the measured flow angle from the flow pattern ahead of the saddle points agrees with the inlet angle setting of the cascade.

Summarizing the flow visualization results for this inlet angle, it is seen that a separation bubble is formed on the suction surface at a low turbulence level. At the higher turbulence levels, this bubble disappears, indicating natural transition occurs upstream of where the laminar separation bubble had formed. On the pressure surface, a

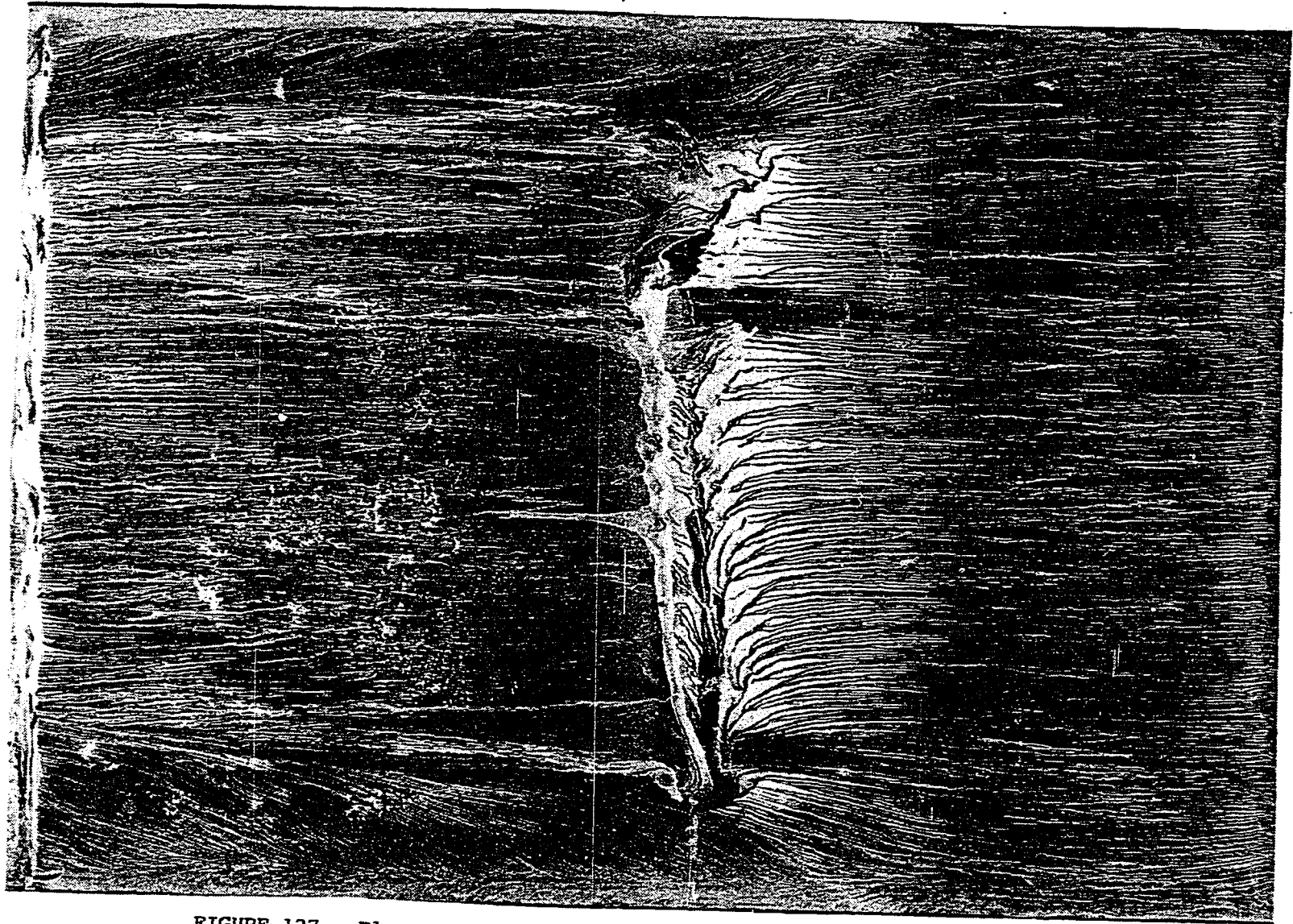


FIGURE 127. Flow pattern, Suction surface, $\beta_1 = 38^\circ$, NGRID, RE1

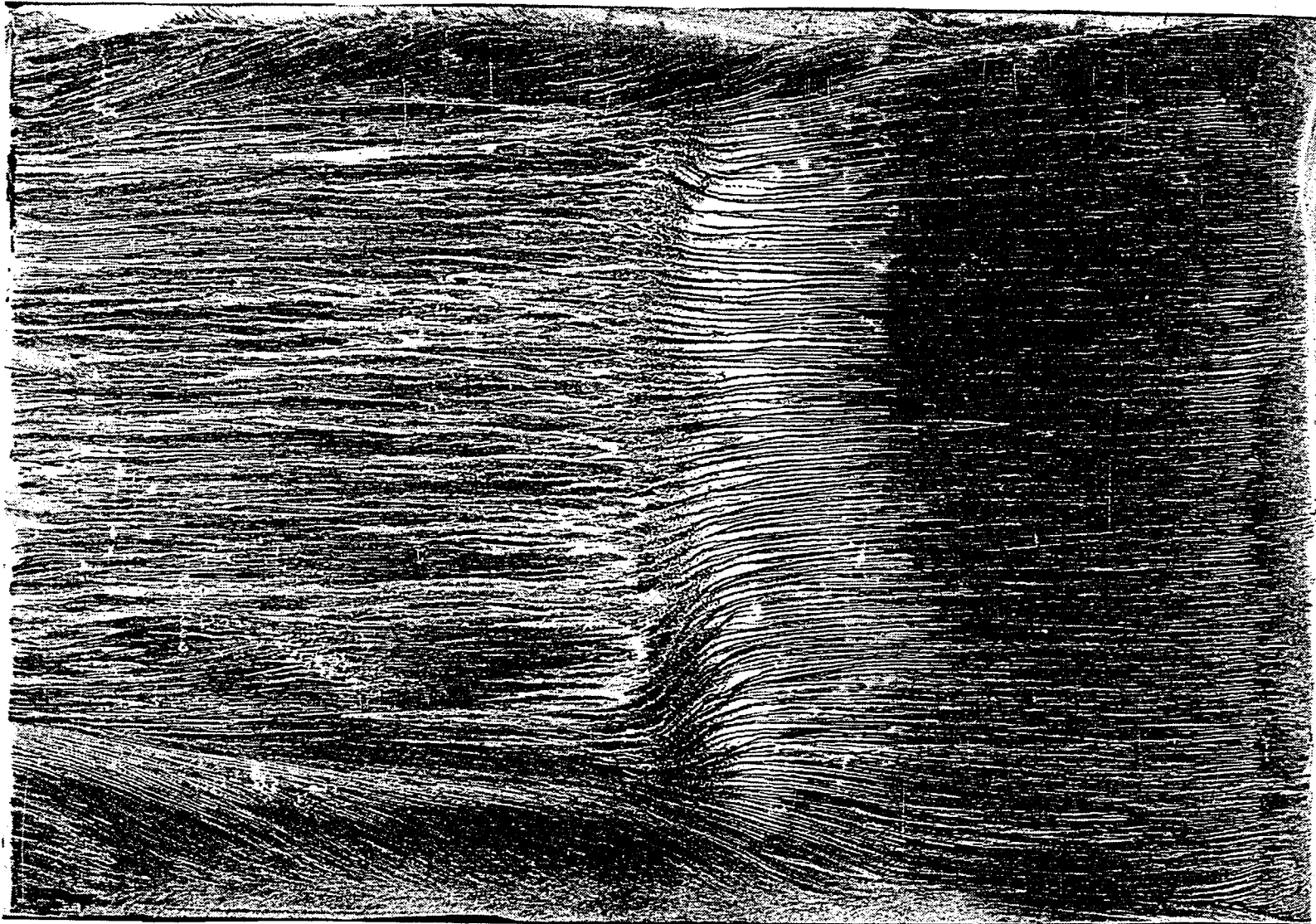


FIGURE 128. Flow pattern, Suction surface, $\beta_1 = 38^\circ$, GRID1, RE1

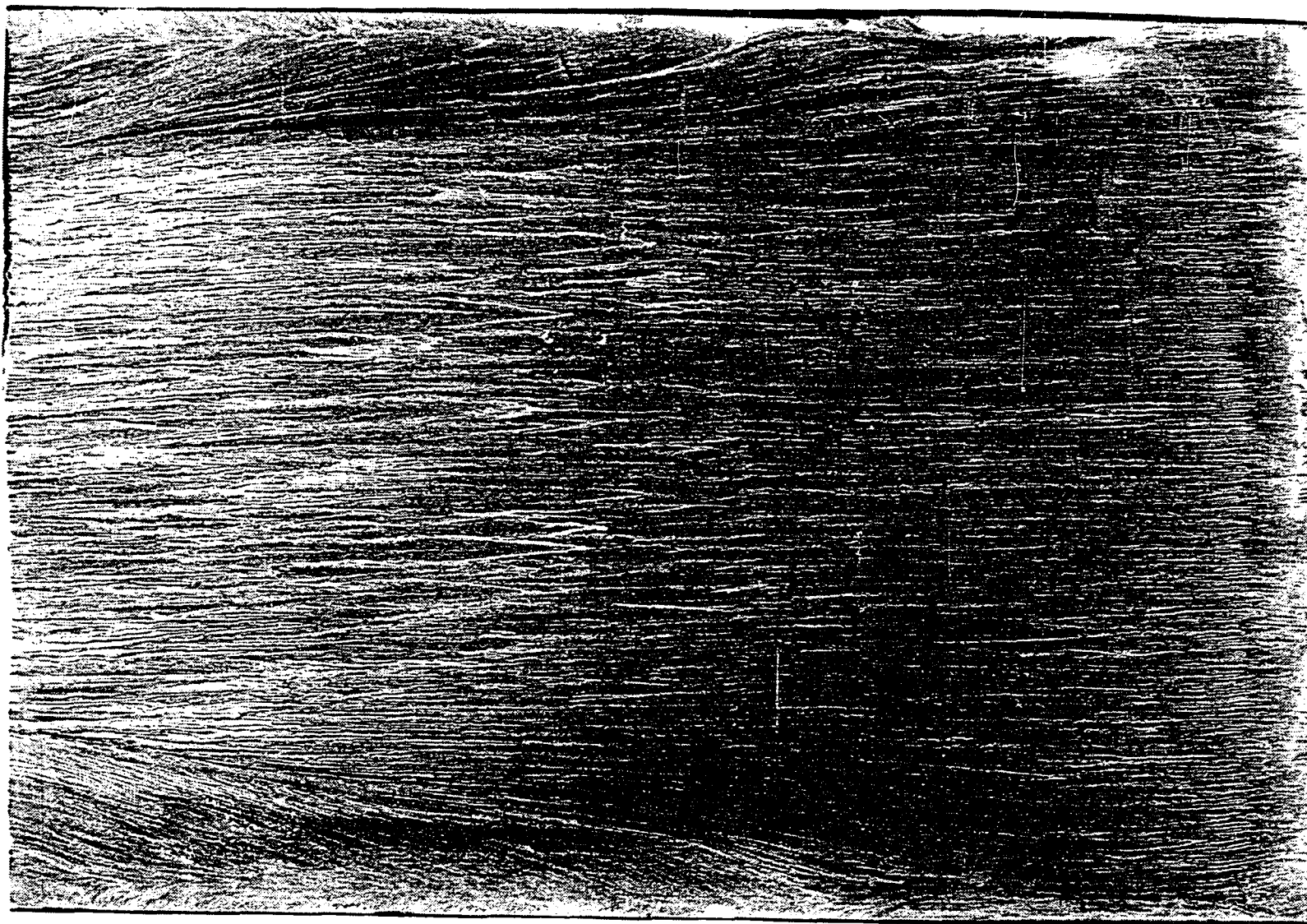


FIGURE 129. Flow pattern, Suction surface, $\beta_1 = 38^\circ$, GRID3, RE1

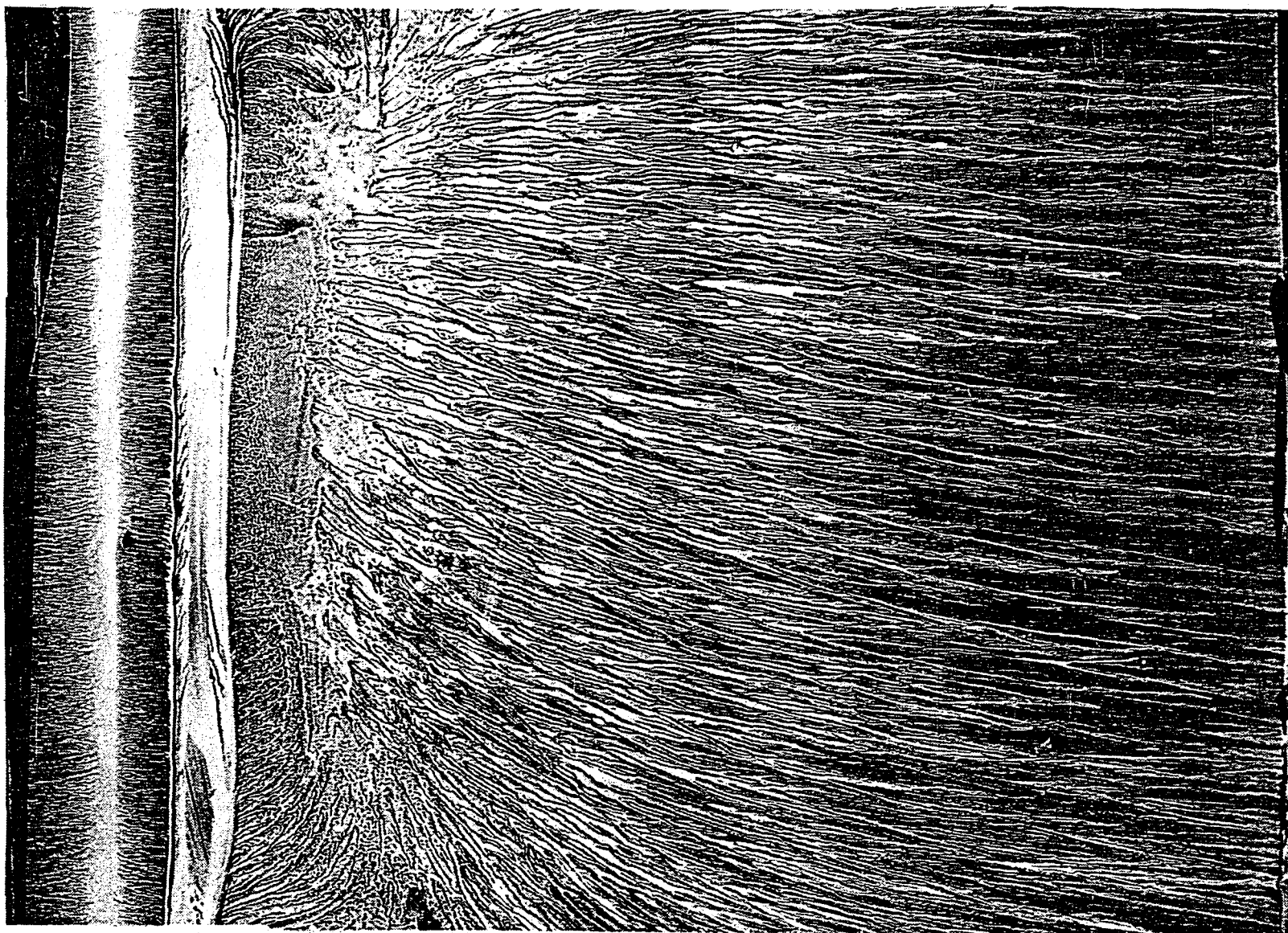


FIGURE 130. Flow pattern, Pressure surface, $\beta_1 = 38^\circ$, NGRID, RE1

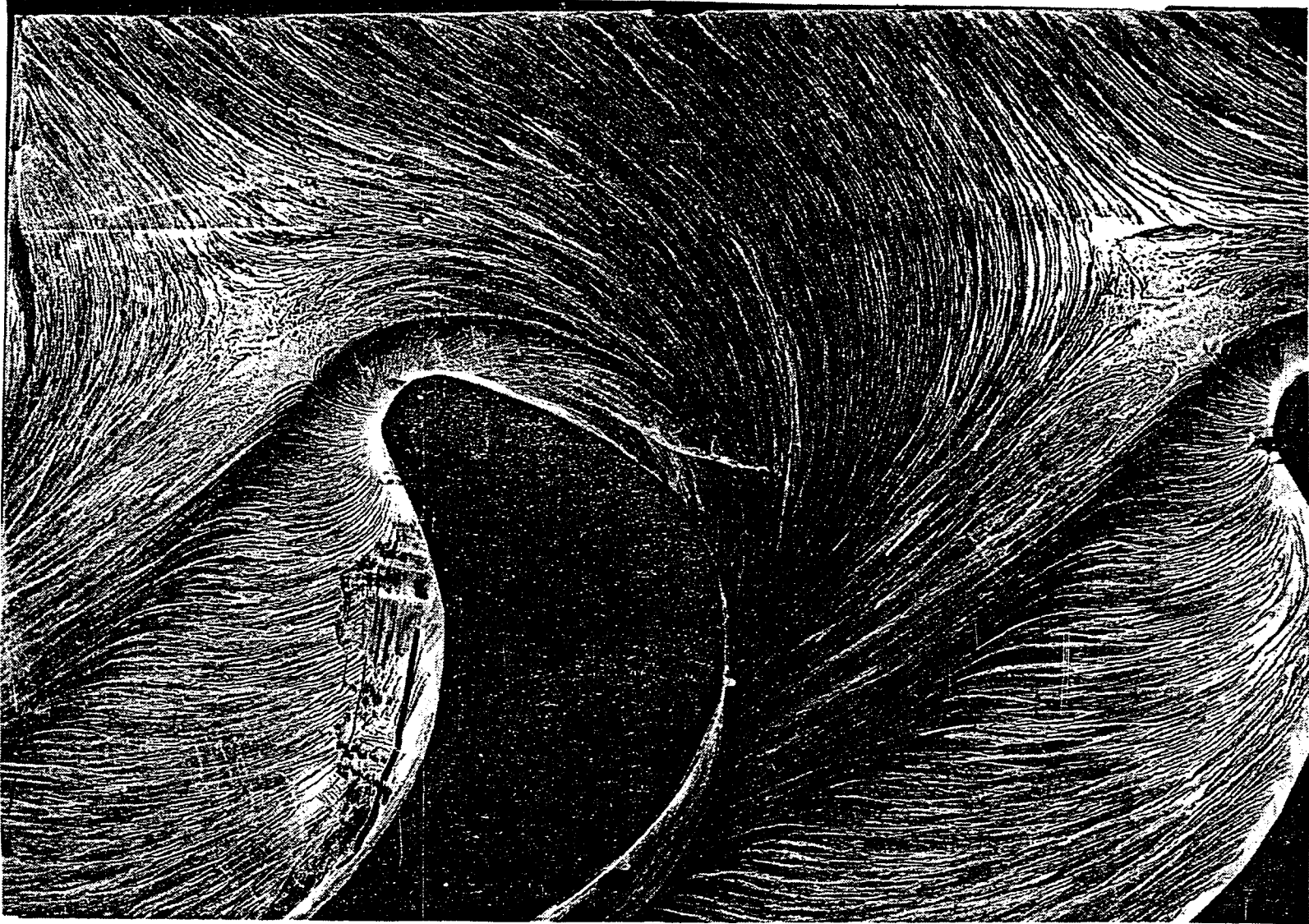


FIGURE 131. Flow pattern, Endwall, $\beta_1 = 38^\circ$

separation bubble occurs close to the leading edge as in $\beta_1 = 45^\circ$ and $\beta_1 = 52^\circ$ cases. Also, for this inlet angle, the limiting streamlines on the suction surface move towards the midspan from either endwalls to produce a narrower region of 2-D flow than in the $\beta_1 = 45^\circ$ case. This is due to the fact that, with increased turning through the cascade, the passage vortex was stronger and the endwall suction was less effective in removing the endwall flow.

3. Five-hole probe traverses

a. Secondary velocity vector plots Similar to the $\beta_1 = 52^\circ$ case, five-hole probe traverses were conducted in the cascade exit plane at midspan for all the test conditions, and in the upper half of the exit plane for flow condition NGRID. Endwall suction was applied for all cases. Figure 132 shows the secondary velocity vector plot in the plane normal to the mean camberline at the trailing edge of the airfoil for flow conditions NGRID and Reynolds number RE1. The passage vortex is seen centered approximately 2.0 inches from the upper endwall, and the vectors located away from the vortex indicate a spanwise flow due to the endwall suction. Overturning is also observed near the upper endwall, similar to the other inlet angle cases.

b. Total pressure loss coefficient Contour plots of total pressure loss coefficient for flow conditions NGRID and Reynolds numbers RE1, RE2, and RE3 are shown in Figures 133, 134, and 135. Endwall suction was applied for all the cases. As seen in Figure 133, the presence of the passage vortex is most prominent for Reynolds

number RE1; in Figures 134 and 135, for RE2 and RE3, the passage vortex is considerably smaller. This feature is also observed in the distribution of the pitch-averaged loss coefficient in Figure 136. Here, for flow condition NGRID, the hump in loss levels indicating the presence of a passage vortex is seen clearly only for RE1. For RE2 and RE3, there is barely a hump in the loss distribution. Also in these two cases, the hump is closer to the endwall indicating that most of the passage vortex has been sucked away. At midspan for RE1, the loss coefficient values increase slightly with turbulence level, while for RE2 and RE3, no such trend is observed.

4. Hot-film gage results

Results from hot-film gage measurements are presented in the same form as for the $\beta_1 = 45^\circ$ and $\beta_1 = 52^\circ$ cases. At this inlet angle, gages #1 through #4 are located in the favorable pressure gradient region, and gages #6 through #14 are located in the adverse pressure gradient region similar to $\beta_1 = 45^\circ$ case. Gage #5 is located close to the minimum pressure point (see Figure 137).

Figures 138, 139, and 140 show the results for flow conditions NGRID and Reynolds numbers RE1, RE2, and RE3. Figure 138 for RE1 indicates a laminar separation bubble beginning to form at gage #5 and the boundary layer reattaching as a turbulent layer near gage #8. Figures 139 and 140 for RE2 and RE3 indicate the laminar bubble forming further downstream at gages #6 and #7. However, the boundary layer for all three Reynolds numbers reattaches as a turbulent layer at the same location, gage #8.

BETA1=38

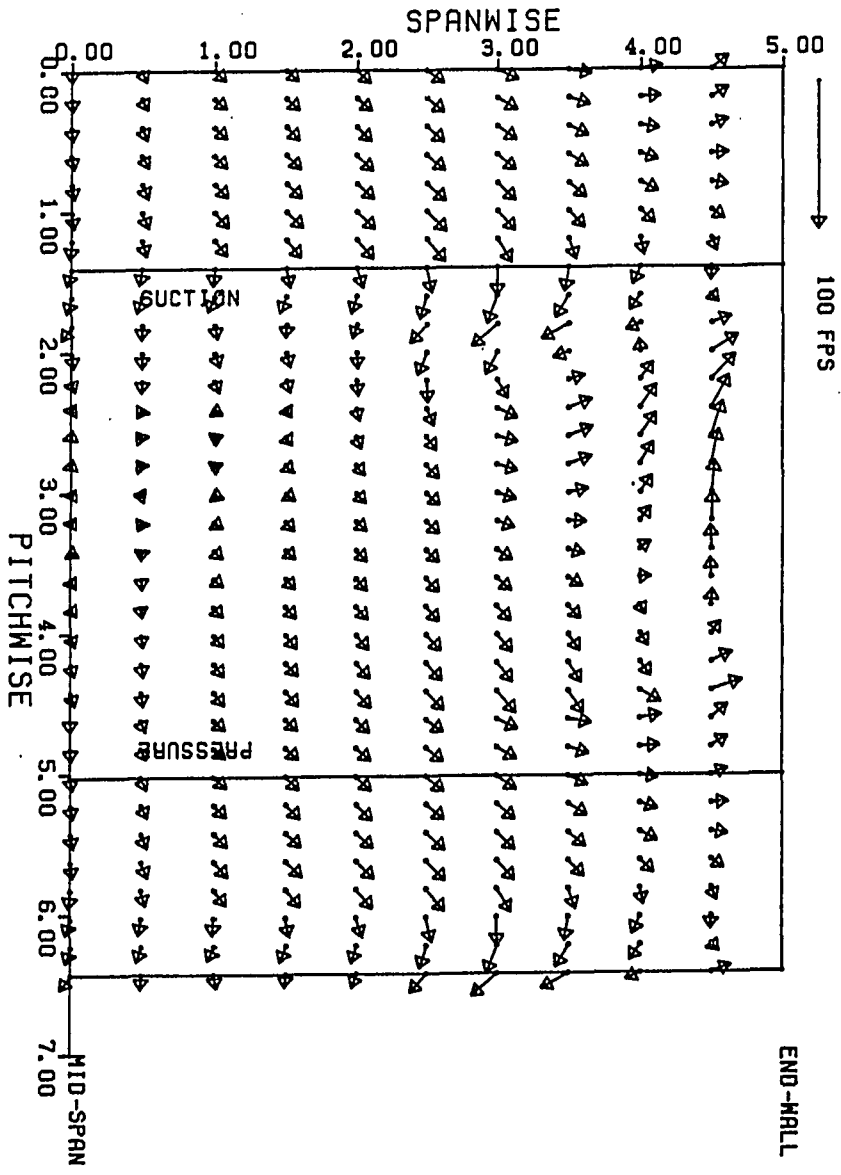


FIGURE 132. Secondary velocity vectors, $\beta_1 = 38^\circ$, NGRID, RE1

CURVE LABEL	CURVE VALUE
1	0.100000E 00
2	0.200000E 00
3	0.300000E 00
4	0.400000E 00
5	0.500000E 00
6	0.600000E 00
7	0.700000E 00
8	0.800000E 00
9	0.900000E 00
10	0.100000E 01

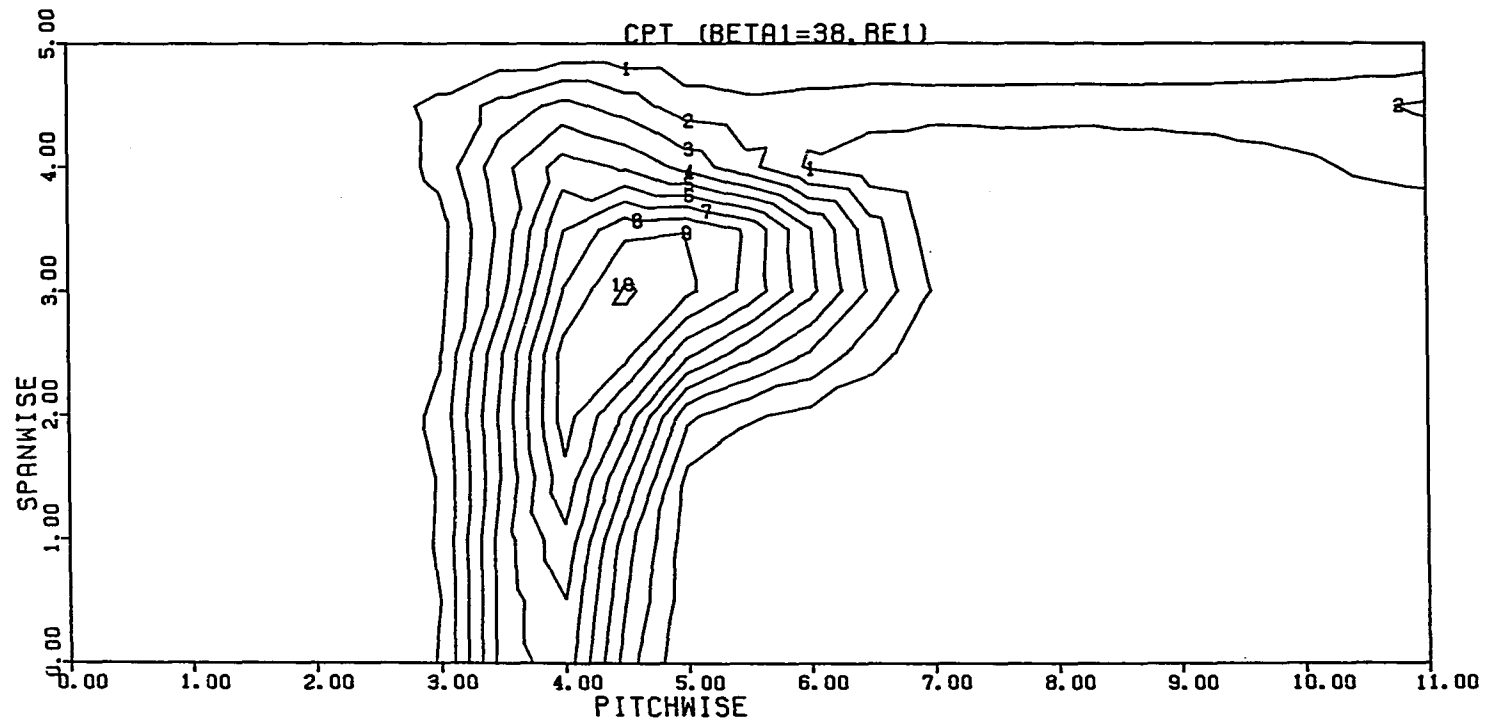


FIGURE 133. Total pressure loss contours, $\beta_1 = 38^\circ$, NGRID, RE1

CURVE LABEL	CURVE VALUE
1	0.100000E 00
2	0.200000E 00
3	0.300000E 00
4	0.400000E 00
5	0.500000E 00
6	0.600000E 00
7	0.700000E 00
8	0.800000E 00

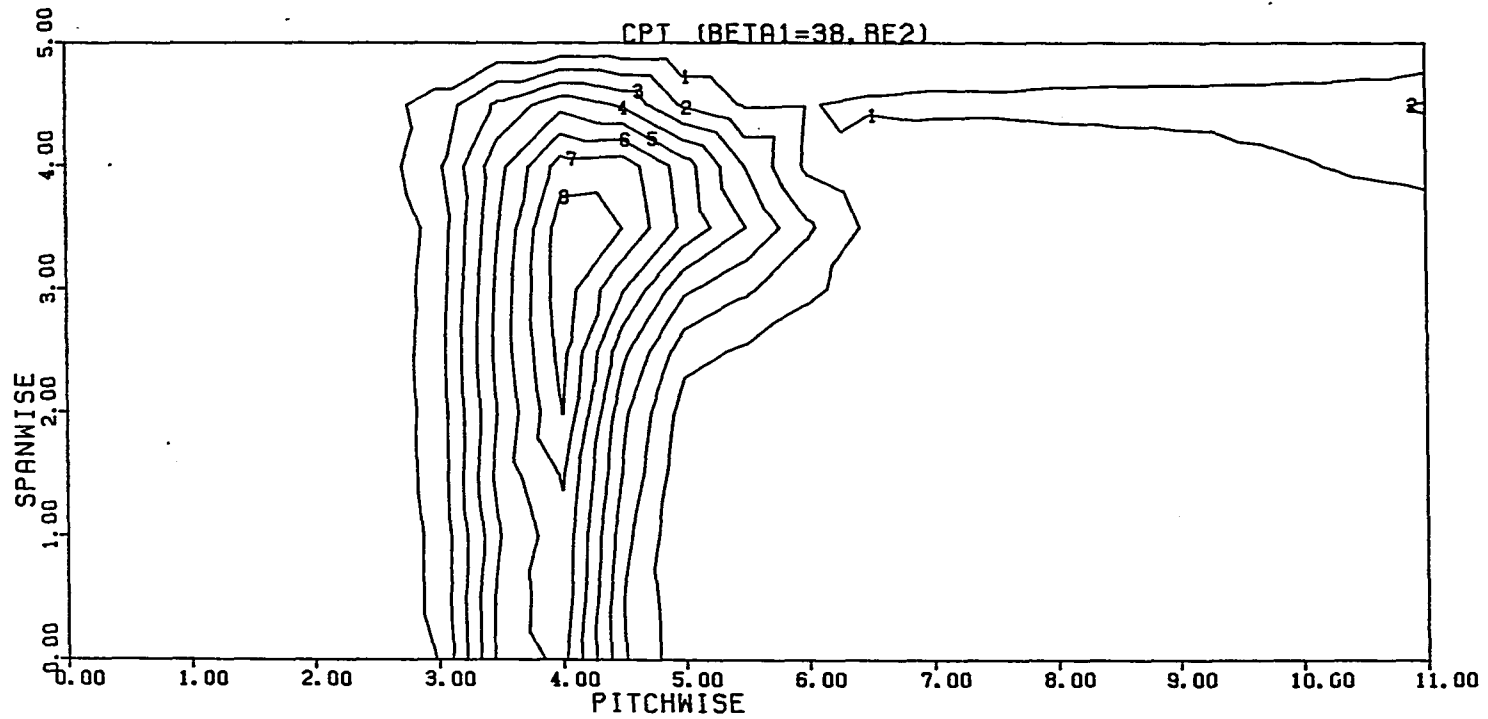


FIGURE 134. Total pressure loss contours, $\beta_1 = 38^\circ$, NGRID, RE2

CURVE LABEL	CURVE VALUE
1	0.100000E 00
2	0.200000E 00
3	0.300000E 00
4	0.400000E 00
5	0.500000E 00
6	0.600000E 00
7	0.700000E 00
8	0.800000E 00
9	0.900000E 00

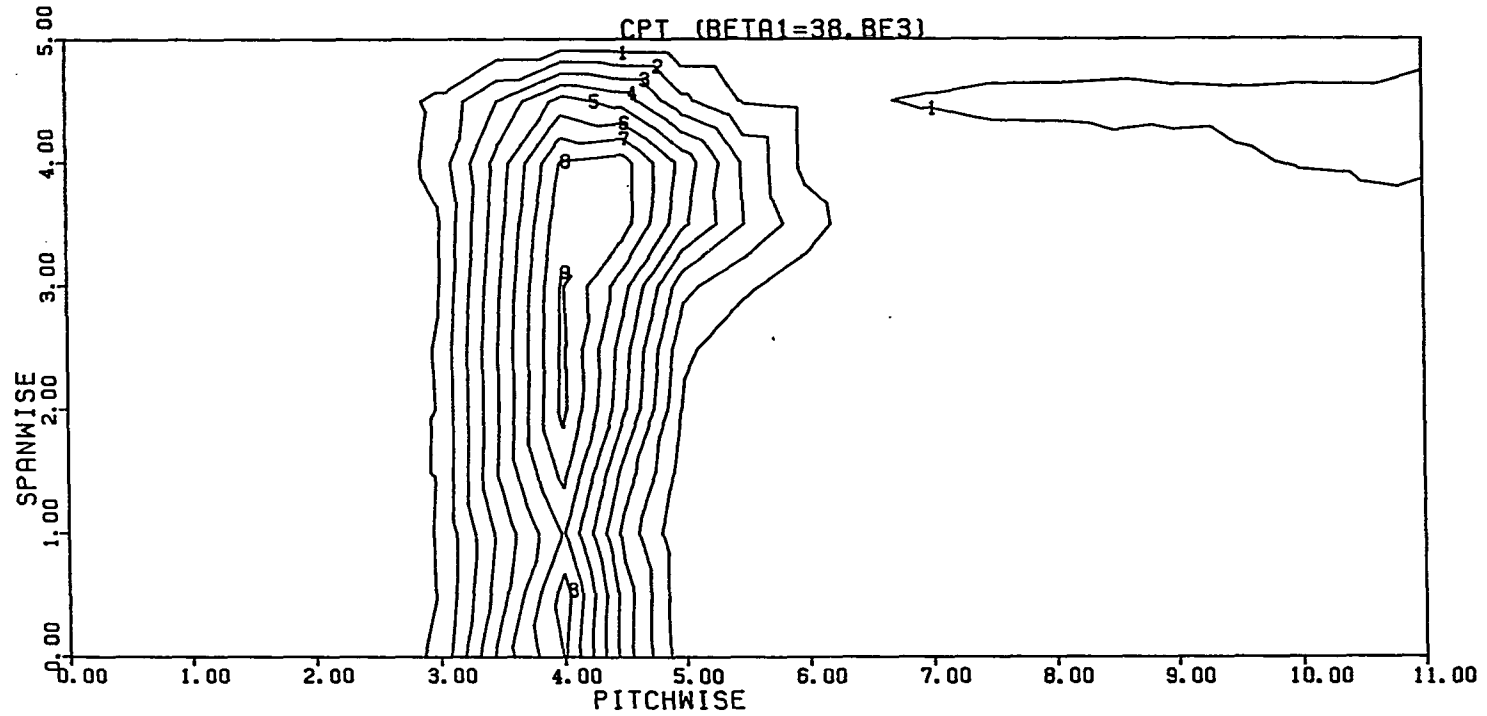


FIGURE 135. Total pressure loss contours, $\beta_1 = 38^\circ$, NGRID, RE3

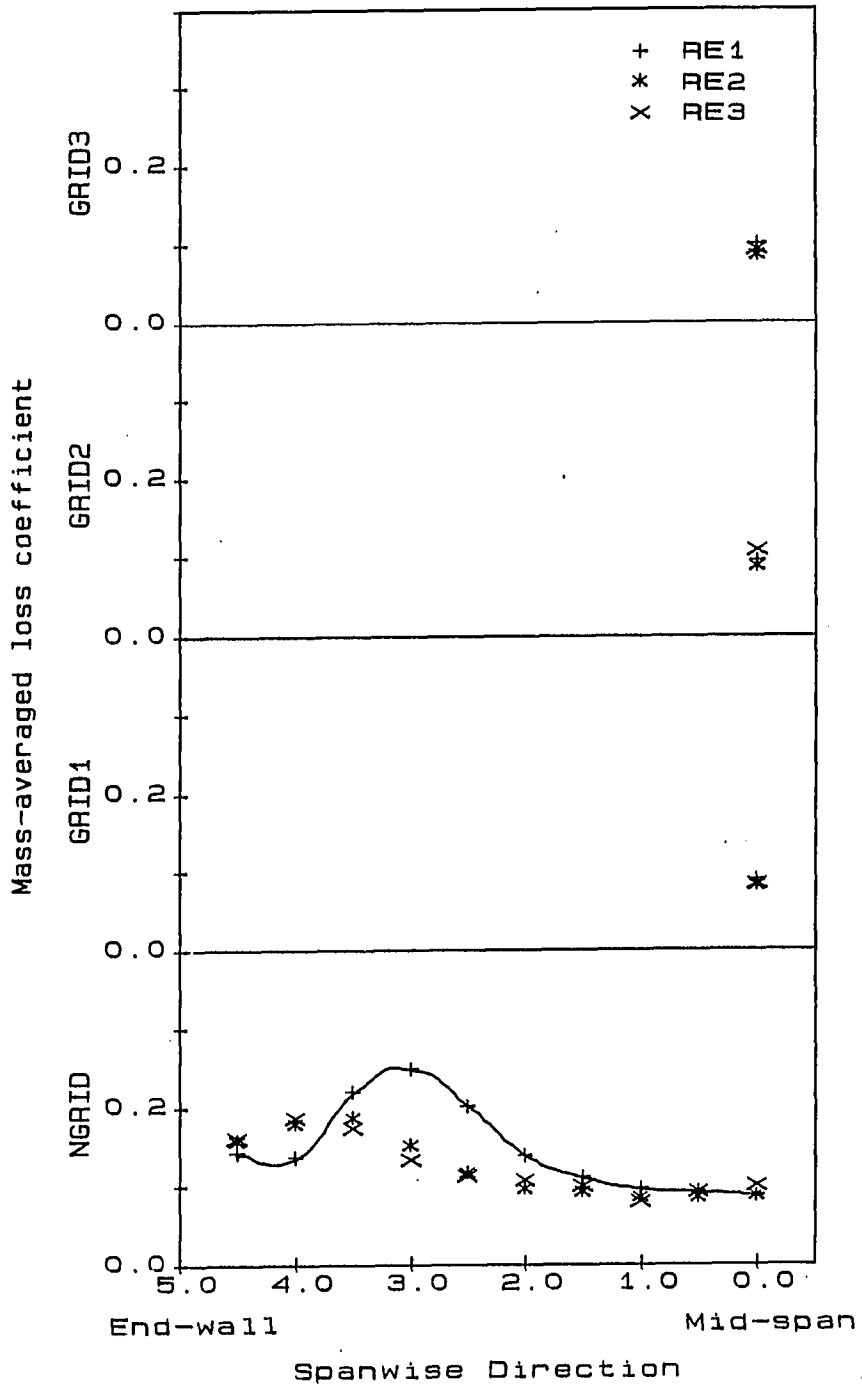


FIGURE 136. Pitch-averaged loss coefficient, $\beta_1 = 38^\circ$

Results for GRID1 are shown in Figures 141, 142 and 143 for the three Reynolds numbers. Figure 141 for Reynolds number RE1 indicates that transition starts naturally at gage #4 and ends at gage #8. Figure 142 for Reynolds number RE2 indicates that transition starts further downstream at gage #5, but still ends at gage #8. However, for Reynolds number RE3, as seen in Figure 143, a laminar bubble starts at gage #6 and the boundary layer reattaches as a turbulent layer near gage #9.

Results for GRID2 are shown in Figures 144, 145, and 146 for the three Reynolds numbers. Figure 144 for RE1 indicates that transition starts naturally downstream of gage #3 and ends near gage #6. For RE2, as seen in Figure 145, transition starts naturally downstream of gage #4 and ends near gage #6. However, for RE3, as seen in Figure 146, a laminar bubble forms downstream of gage #5 and the boundary layer reattaches as a turbulent layer downstream of gage #8.

Results for GRID3 presented in Figures 147, 148, and 149 indicate that for each Reynolds number, same results are obtained as for GRID2. For Reynolds numbers RE1 and RE2 natural transition occurs and for Reynolds number RE3, a bubble-induced transition occurs. For RE1, as seen in Figure 147, transition starts downstream of gage #3 and ends near gage #6. For RE2, as seen in Figure 148, transition starts downstream of gage #4 and ends near gage #6. For RE3, as seen in Figure 149, a laminar bubble forms downstream of gage #5 and the boundary layer reattaches as a turbulent layer downstream of gage #8.

In general, for this inlet angle considerable scatter in the RMS signal is observed for GRID2 and GRID3.

D. Comparison of measured and predicted results

The measured profile losses for the cascade (mass-averaged loss coefficient at midspan) were compared against the results predicted by STAN5 boundary layer calculations for the three inlet angles and four turbulence levels at Reynolds number RE1 (see Chapter III for a brief description of STAN5 code and its use to predict the profile losses). Also, the start and end of transition points on the suction surface determined from the glue-on hot-film gages were compared against the predicted results from the Abu-Ghanaam and Shaw transition model [22], and the Dhawan and Narasimha transition length model [16] described in Chapter II. Similar comparisons made for Reynolds numbers RE2 and RE3 yielded results similar to those obtained for Reynolds number RE1, and, hence, are not discussed.

Airfoil static pressures measured from surface pressure taps were used to calculate the velocity distribution required for the STAN5 code input data. On the suction surface, boundary layer calculations were started in the laminar mode and then switched to turbulent mode by two different methods. In the first method, the Abu-Ghanaam and Shaw and Dhawan and Narasimha models, herein referred to as AGS and DN respectively, were used. In the second method, the actual transition points and transition lengths obtained from hot-film gage results were

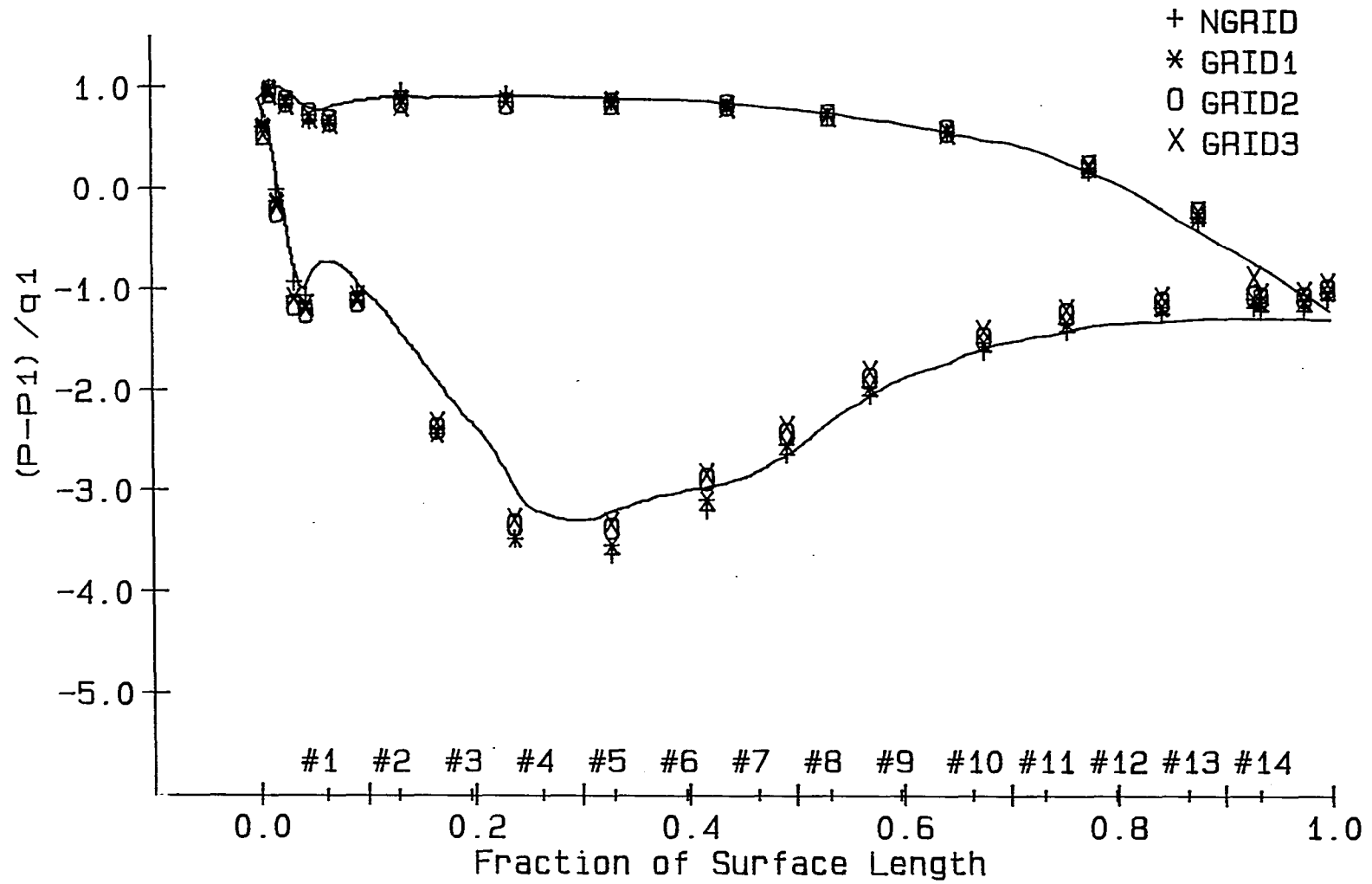


FIGURE 137. Hot-film gage locations plotted against the pressure distribution for $\beta_1 = 38^\circ$

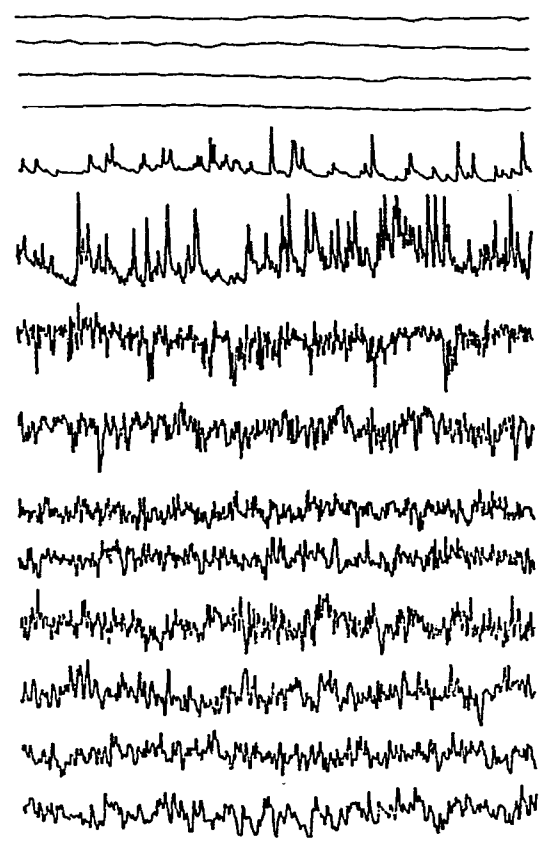
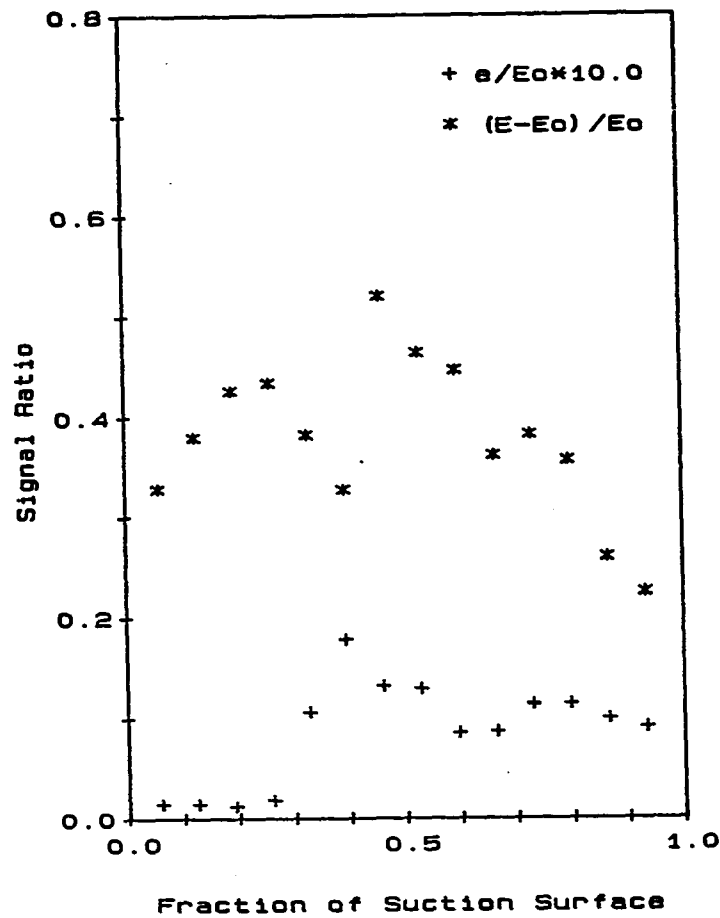


FIGURE 138. Hot-film gage results, $\beta_1 = 38^\circ$, NGRID, RE1

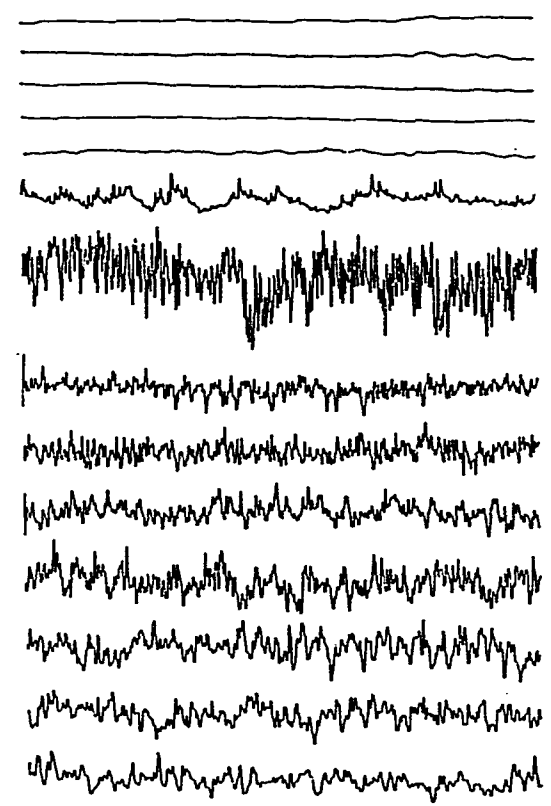
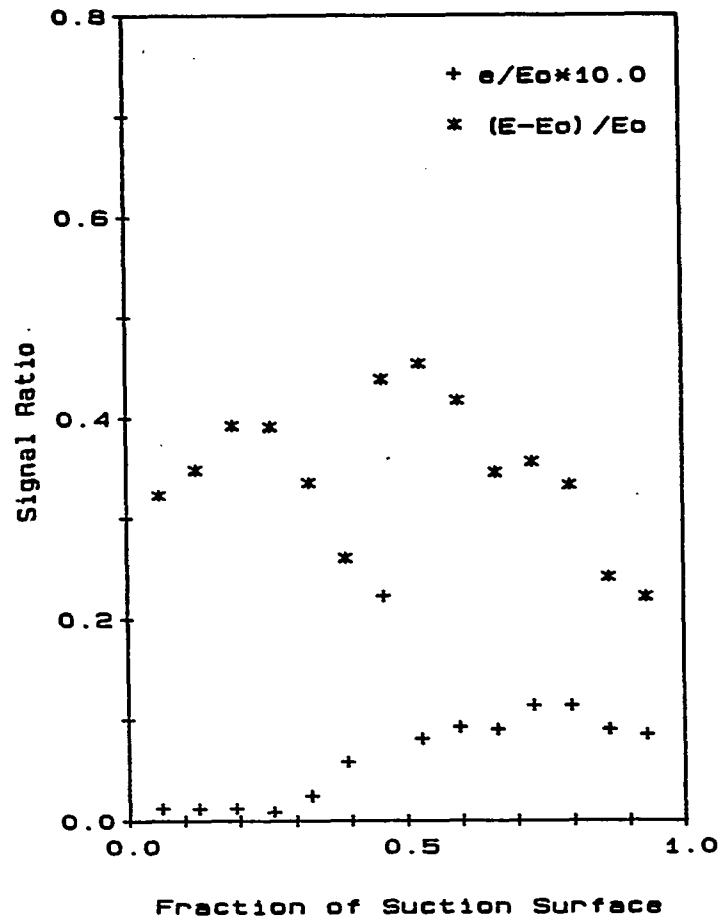


FIGURE 139. Hot-film gage results, $\beta_1 = 38^\circ$, NGRID, RE2

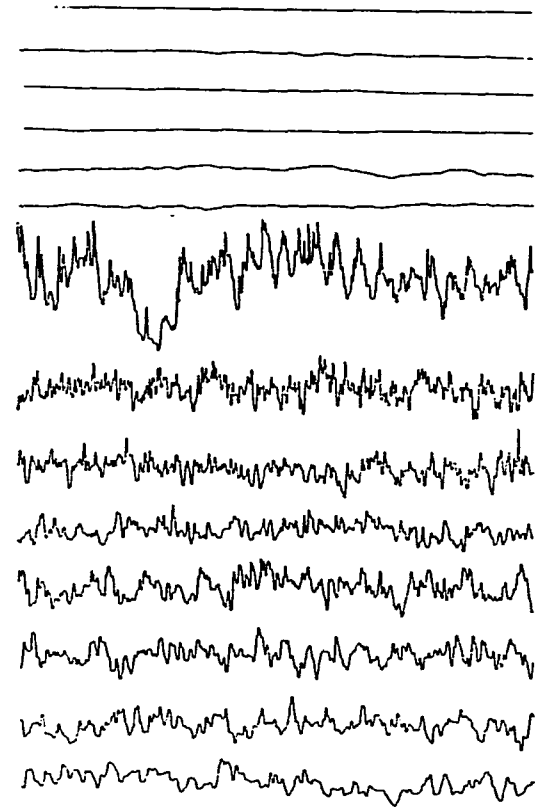
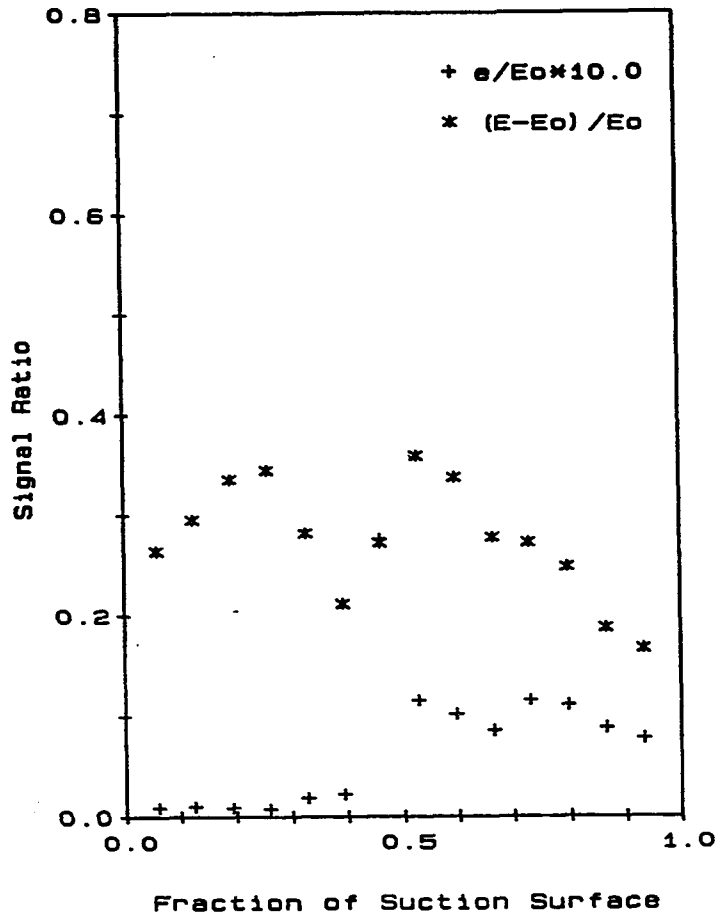


FIGURE 140. Hot-film gage results, $\beta_1 = 38^\circ$, NGRID, RE3

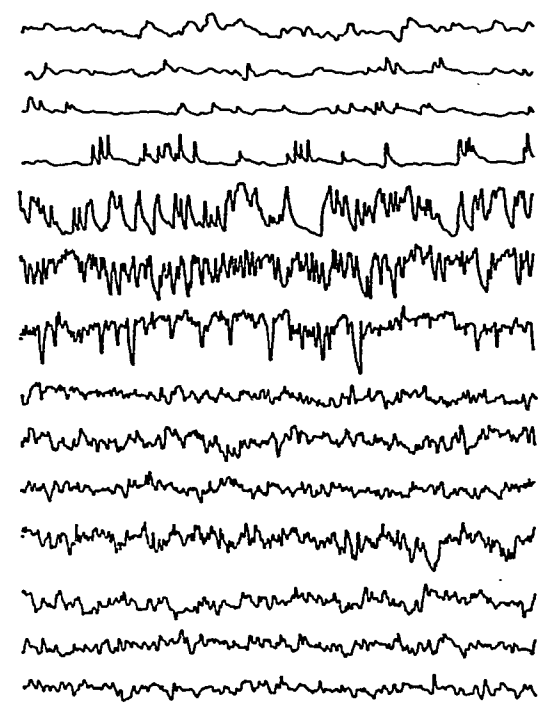
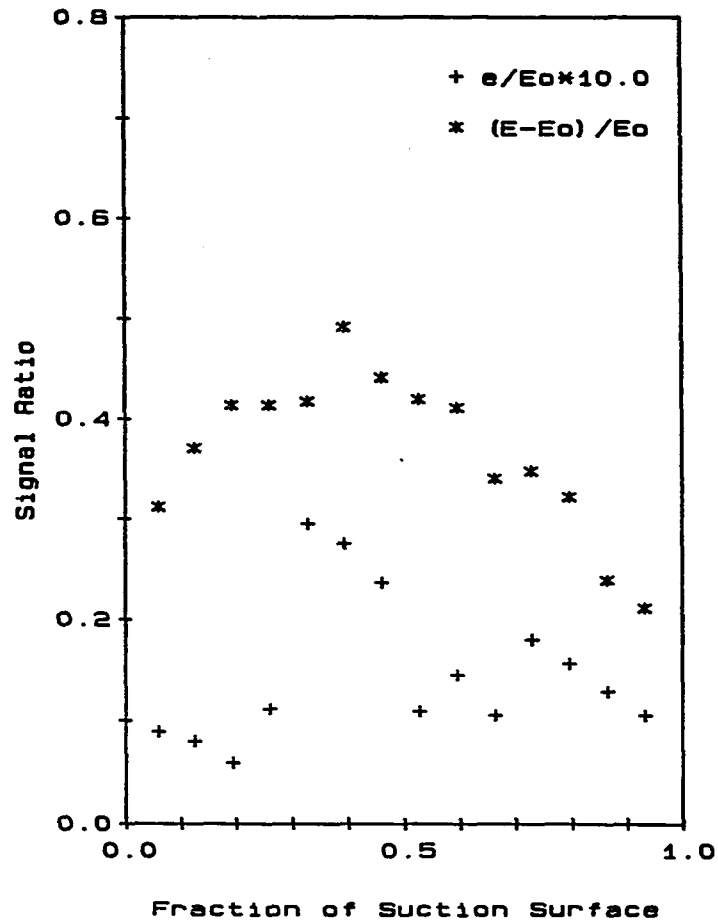


FIGURE 141. Hot-film gage results, $\beta_1 = 38^\circ$, GRID1, RE1

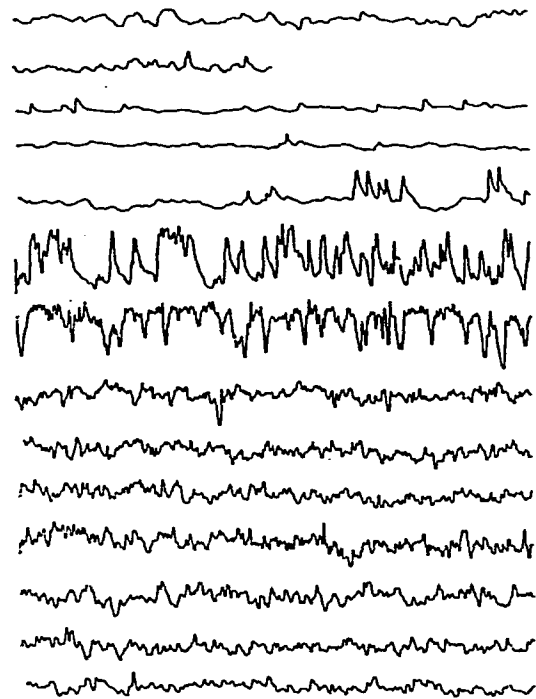
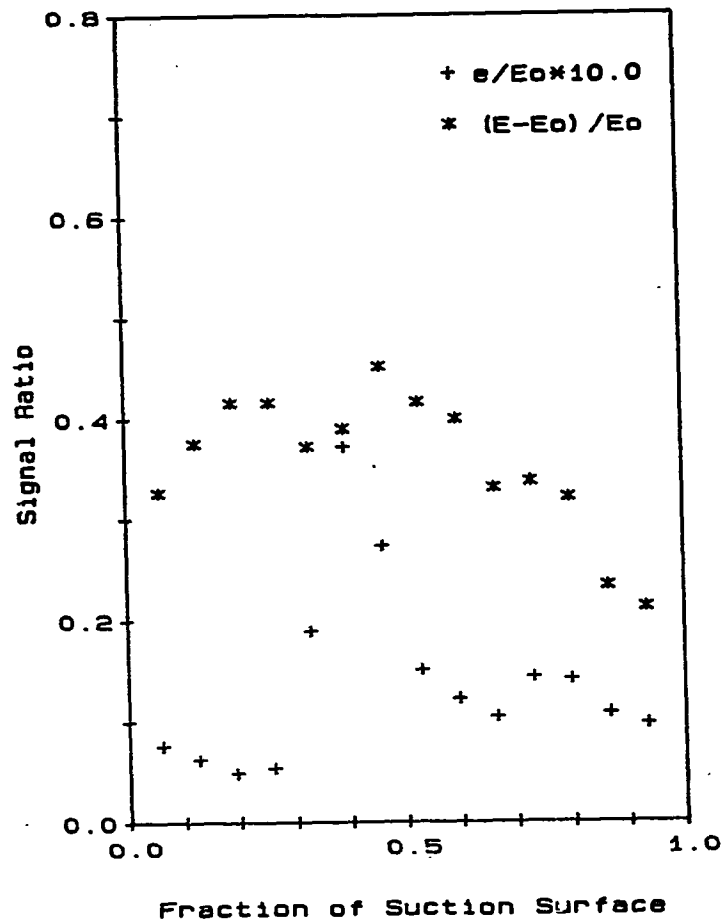


FIGURE 142. Hot-film gage results, $\beta_1 = 38^\circ$, GRID1, RE2

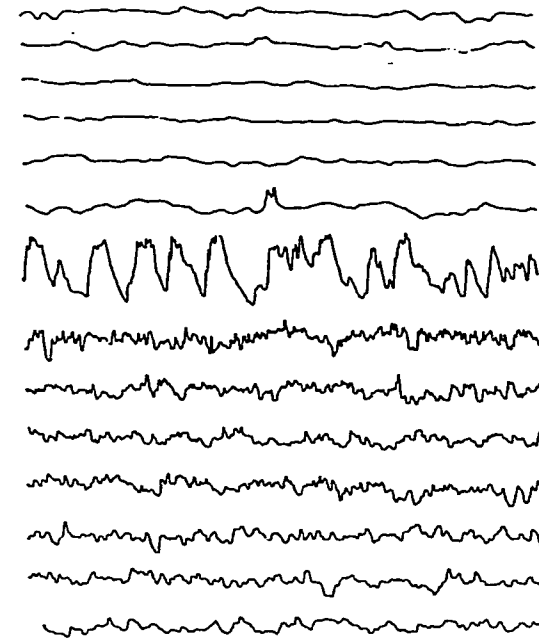
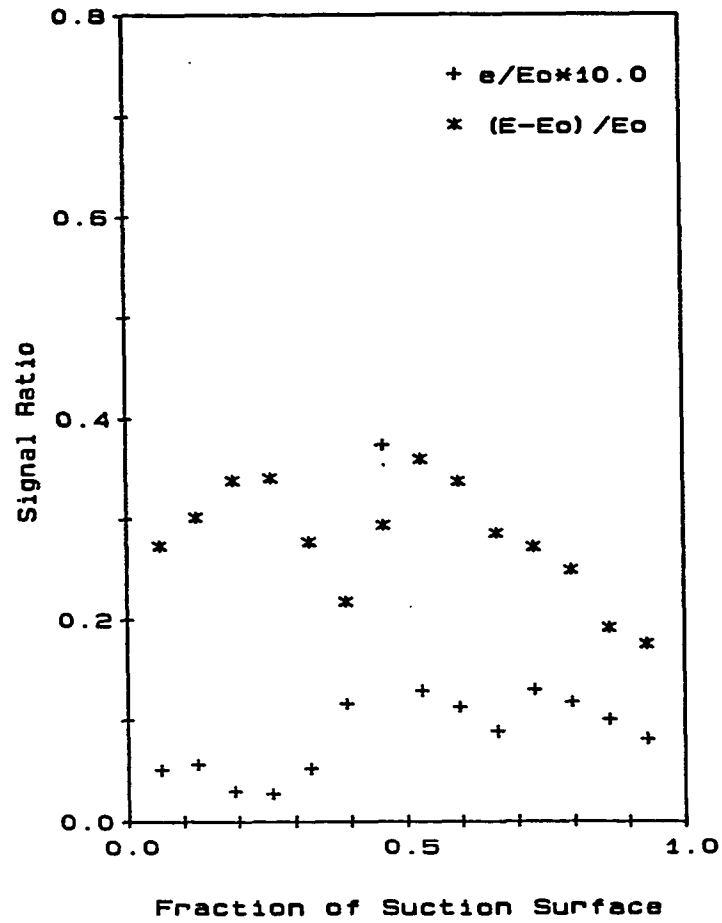


FIGURE 143. Hot-film gage results, $\beta_1 = 38^\circ$, GRID1, RE3

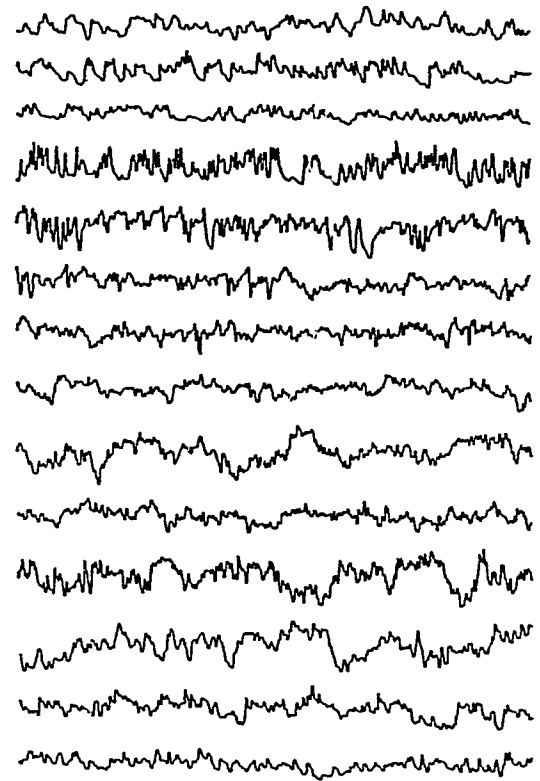
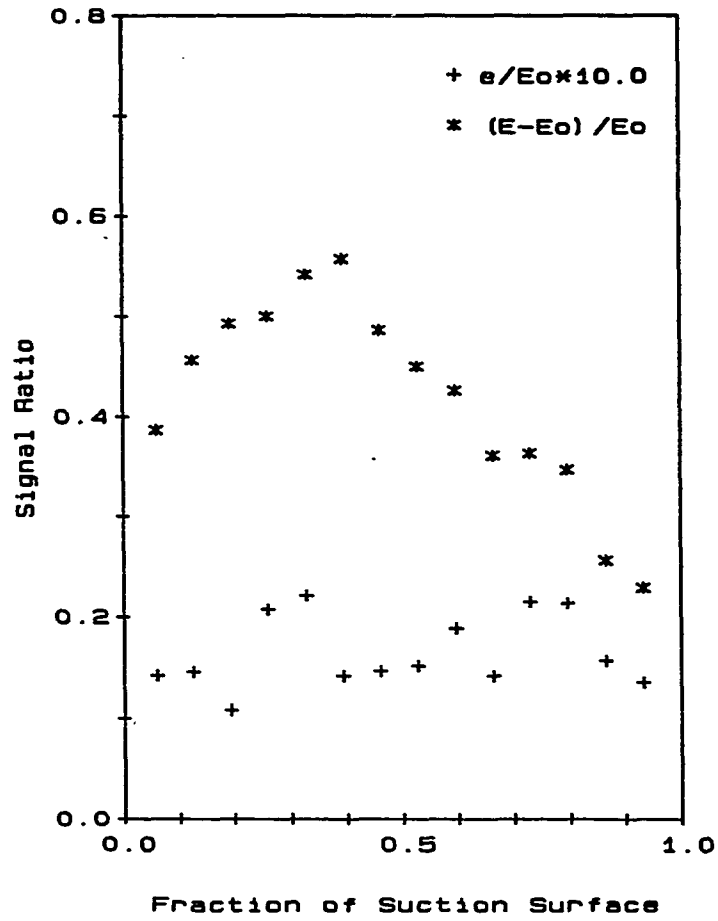


FIGURE 144. Hot-film gage results, $\beta_1 = 38^\circ$, GRID2, RE1

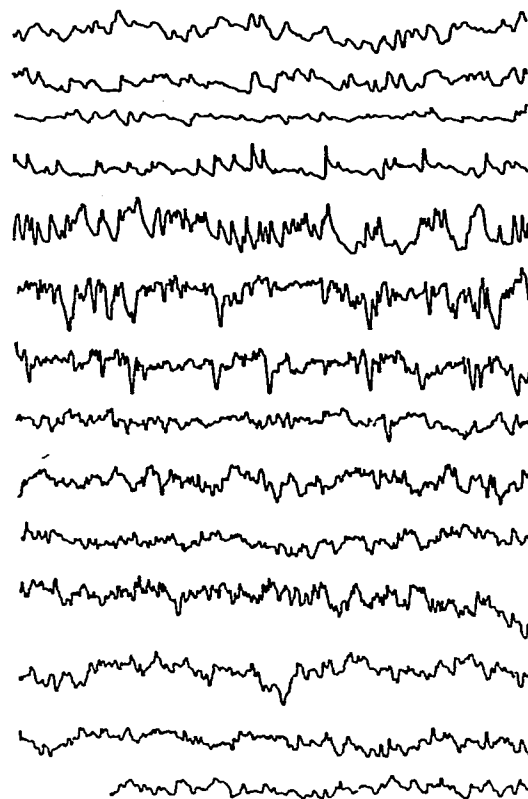
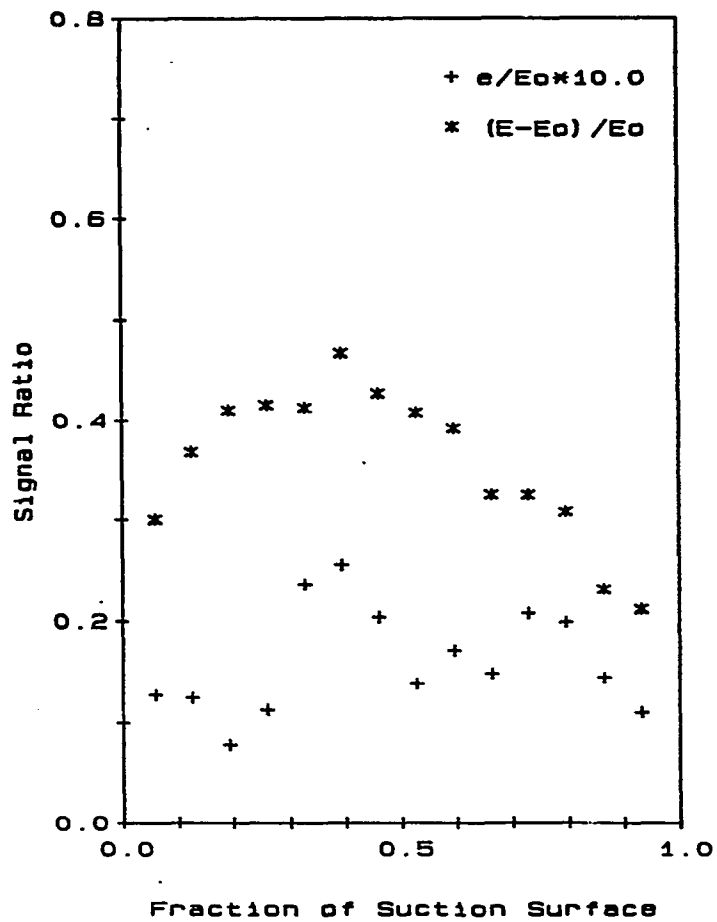


FIGURE 145. Hot-film gage results, $\beta_1 = 38^\circ$, GRID2, RE2

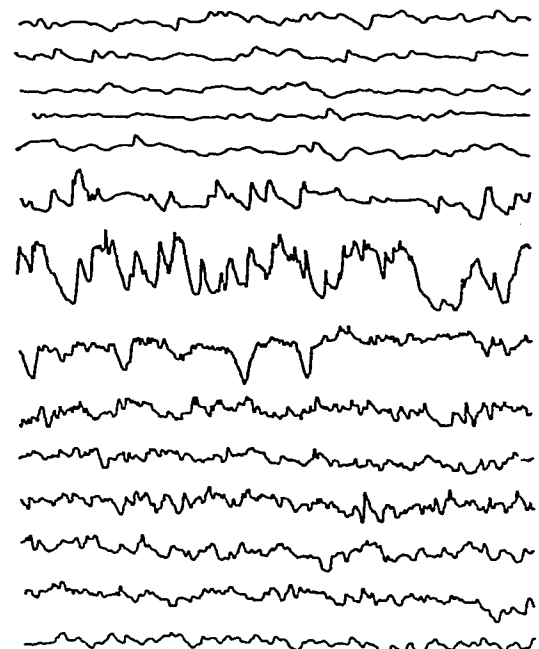
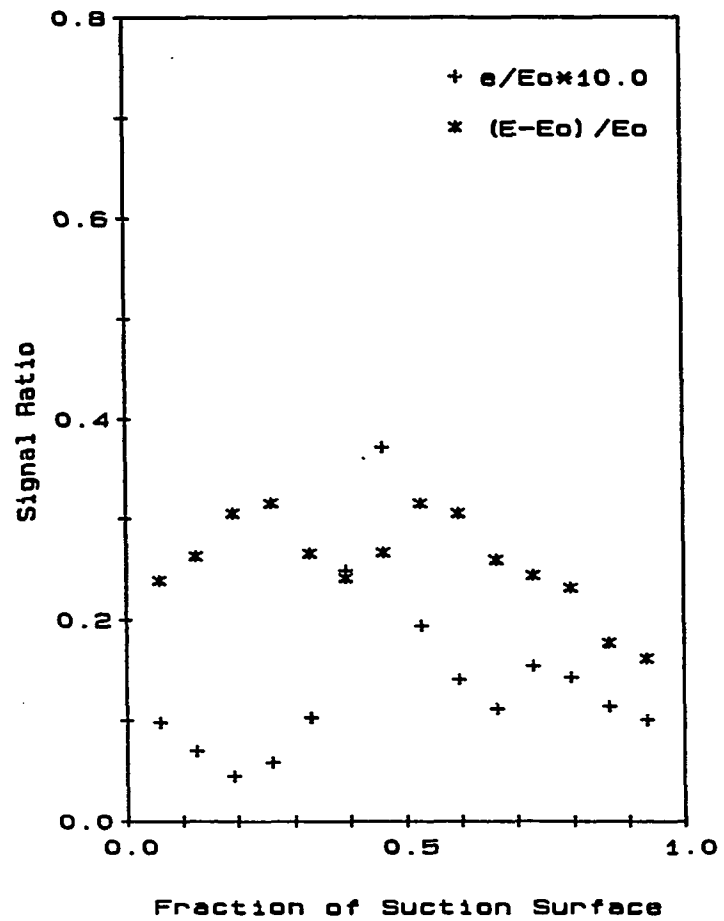


FIGURE 146. Hot-film gage results, $\beta_1 = 38^\circ$, GRID2, RE3

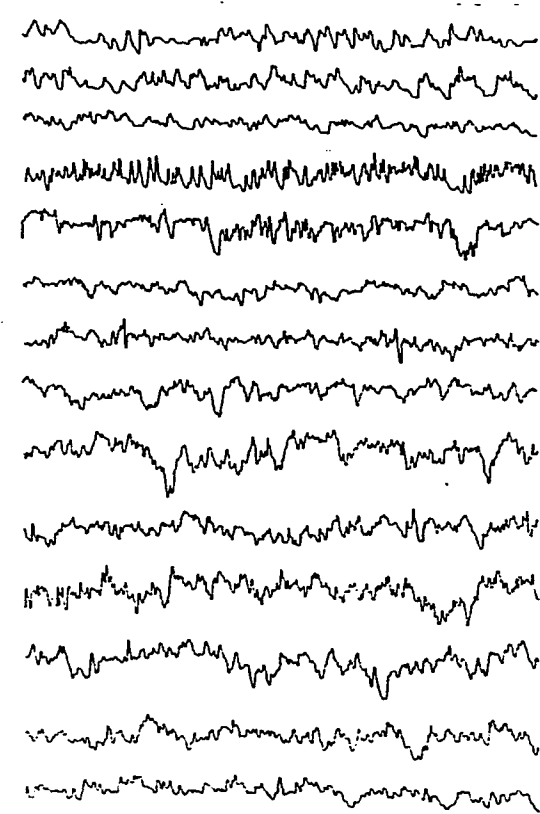
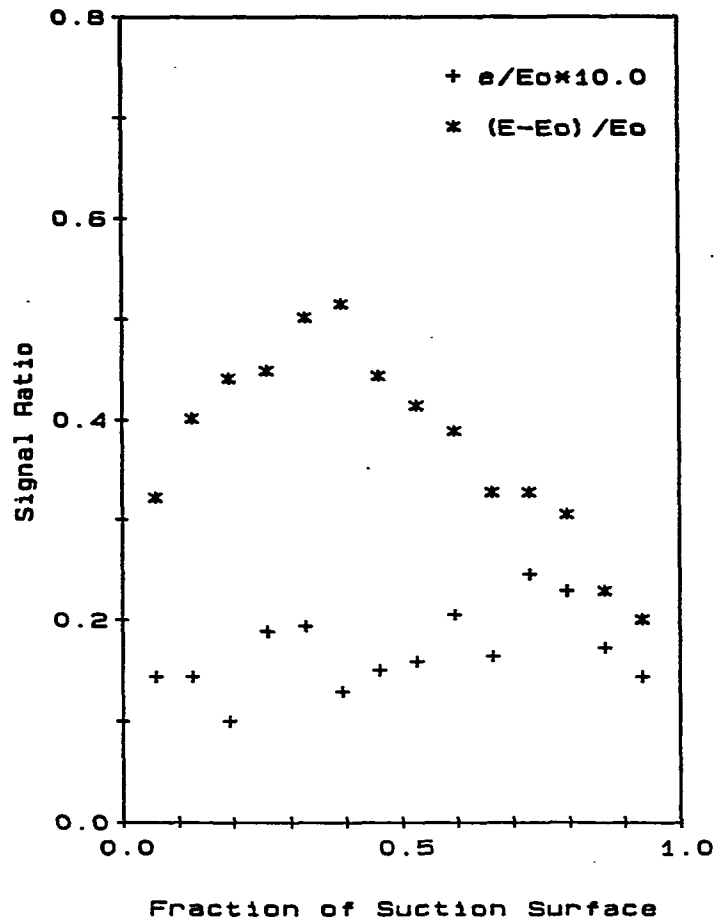


FIGURE 147. Hot-film gage results, $\beta_1 = 38^\circ$, GRID3, RE1

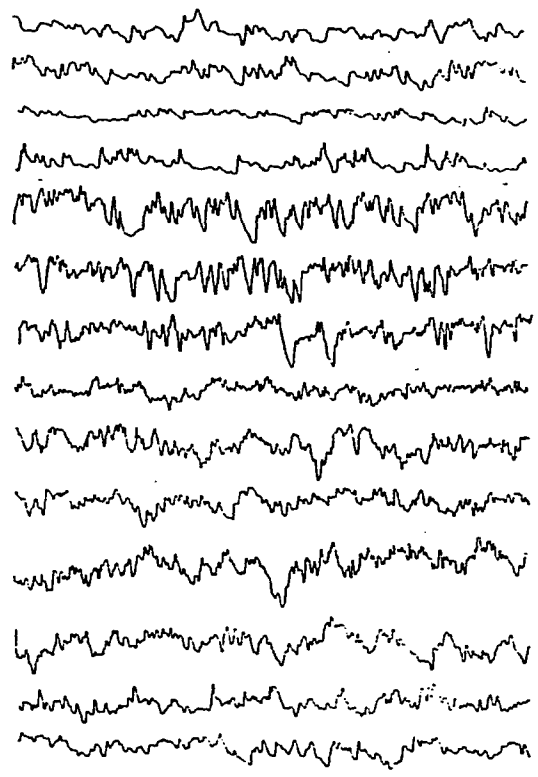
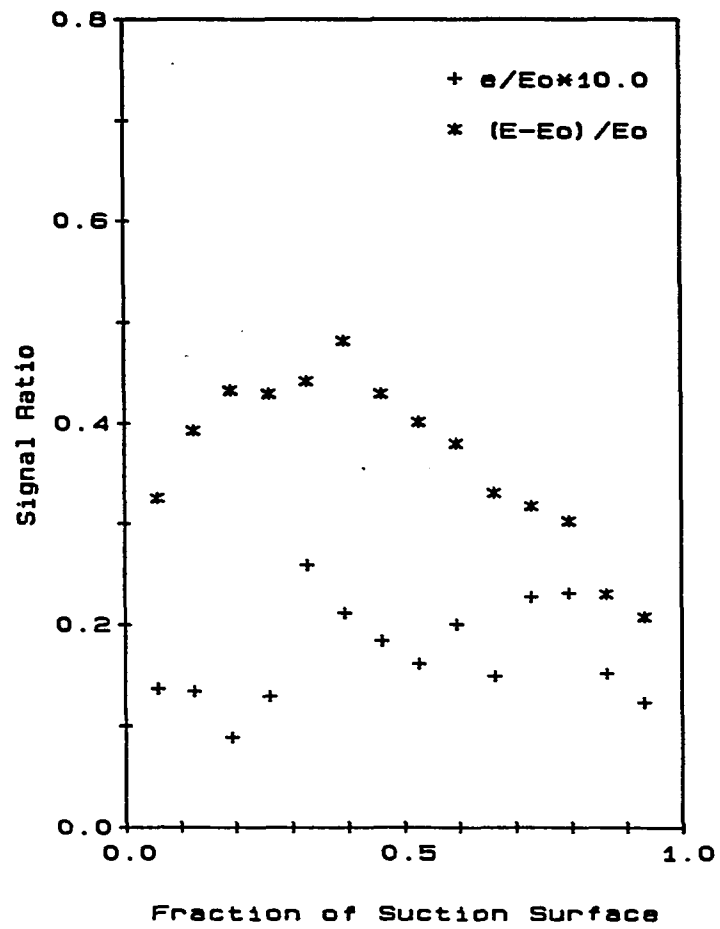


FIGURE 148. Hot-film gage results, $\beta_1 = 38^\circ$, GRID3, RE2

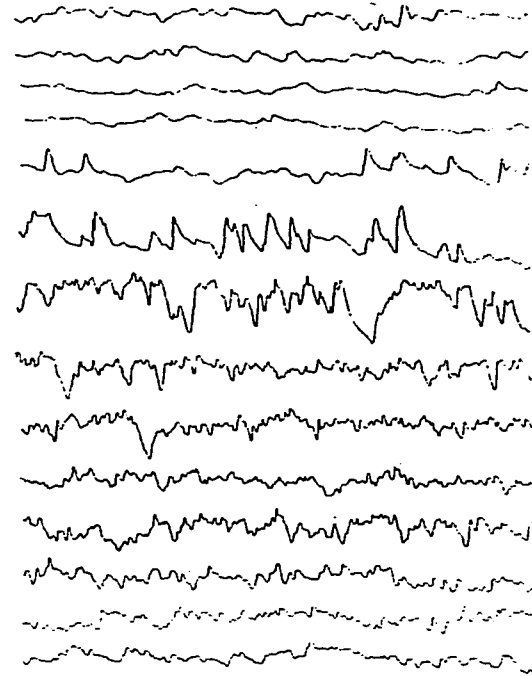
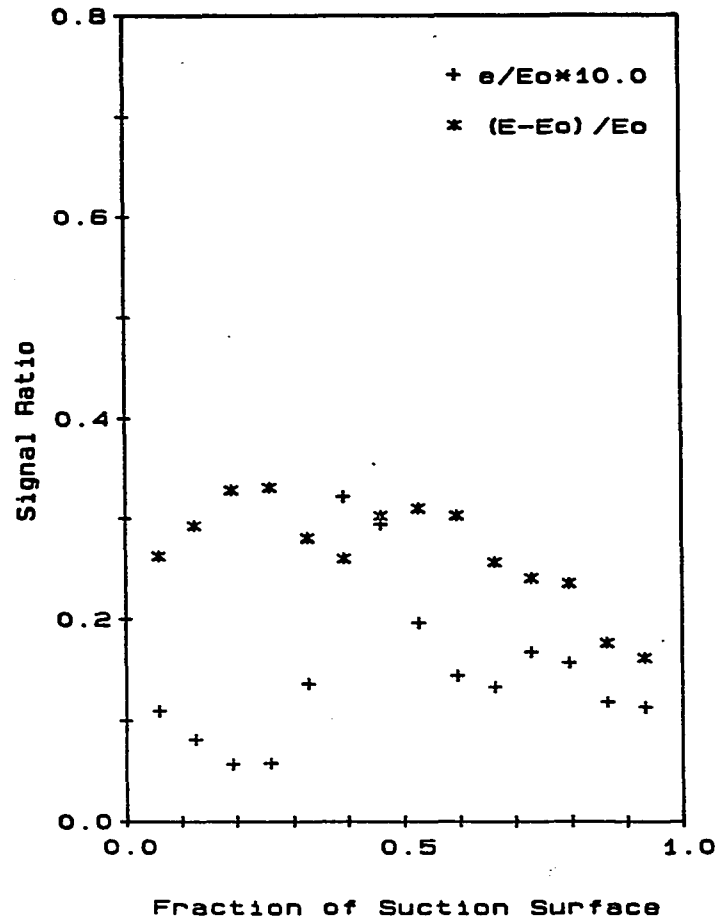


FIGURE 149. Hot-film gage results, $\beta_1 = 38^\circ$, GRID3, RE3

used. On the pressure surface, due to the presence of a laminar separation bubble close to the leading edge for all three inlet angles, no laminar-turbulent calculations were possible; hence, a fully turbulent calculation from the stagnation point onwards was made. In all the calculations, the eddy viscosity for the turbulent boundary layer was calculated using Prandtl's mixing length hypothesis. Also, the Stanford curvature model to include surface curvature effects of the airfoil on the turbulent boundary layer was used.

Table 4, summarizing the STAN5 results, shows the measured total pressure loss coefficients, the predicted and observed transition start and end points on the suction surface, and the loss coefficient results obtained in the two different boundary layer calculations described above. As seen from Table 4, at turbulence level of 0.8% (NGRID), the AGS and DN models predicted start of transition near the 45% point along the suction surface, and the end of transition near the trailing edge for all three inlet angles. In checking the pressure distributions for the three inlet angles (see Figures 137, 77, 109), it is concluded that start of transition was predicted in an adverse pressure gradient shortly downstream of the minimum pressure point in each case. However, the transitional calculations also predicted separation soon after the transition starting point. These predicted separation locations corresponded to the laminar separation bubble locations observed in the flow visualization and hot-film gage results. Since the boundary layer calculations could not be completed after

TABLE 4. Comparison of measured and predicted (STAN5) results at midspan for axial chord Reynolds number 700,000 (RE1)

	NGRID	GRID1	GRID2	GRID3
Start and end of transition on airfoil suction surface denoted as a percentage of surface length from stagnation point				
Inlet Tu level	0.8%	2.0%	4.8%	6.4%
<u>Inlet angle $\beta_1 = 38^\circ$ (0° inc)</u>				
Measured C_{PT2}	0.041	0.047	0.052	0.057
AGS & DN Trans. models				
Start of transition	41%	32%	9%	9%
End of transition	88%	71%	24%	23%
C_{PT2}	-	0.034	0.047	0.048
Trans. from HF gages				
Start of transition	29%	23%	23%	23%
End of transition	46%	50%	40%	40%
C_{PT2}	0.038	0.040	0.040	0.041
<u>Inlet angle $\beta_1 = 45^\circ$ (-7° inc)</u>				
Measured C_{PT2}	0.038	0.037	0.035	0.039
AGS & DN Trans. models				
Start of transition	45%	35%	17%	10%
End of transition	95%	75%	41%	25%
C_{PT2}	-	0.031	0.040	0.041
Trans. from HF gages				
Start of transition	32%	25%	22%	22%
End of transition	46%	52%	52%	46%
C_{PT2}	0.035	0.036	0.036	0.037
<u>Inlet angle $\beta_1 = 52^\circ$ (-14° inc)</u>				
Measured C_{PT2}	0.040	0.040	0.026	0.042
AGS & DN Trans. models				
Start of transition	46%	37%	20%	18%
End of transition	96%	80%	47%	43%
C_{PT2}	-	0.025	0.032	0.035
Trans. from HF gages				
Start of transition	45%	35%	31%	31%
End of transition	55%	59%	59%	59%
C_{PT2}	0.028	0.029	0.030	0.030

separation occurred, no predicted losses were obtained with the AGS and DN models for NGRID. In the hot-film gage results for the NGRID cases, transition was started in the calculations at the point where the RMS signal from the hot-film gages showed a sudden jump and was completed at the point where the signal became constant again. For these calculations, as seen in Table 4, the predicted loss agreed well with the measured loss for $\beta_1 = 38^\circ$ and $\beta_1 = 45^\circ$, while for $\beta_1 = 52^\circ$, the predicted loss was appreciably lower than the measured loss.

For the higher inlet turbulence level cases (GRID1, GRID2, GRID3), natural transition occurred at all three inlet angles for the Reynolds number RE1. For these cases, the AGS and DN models predicted transition without any separation, and a loss coefficient was calculated. As before, using the hot-film gage results, transition was started in the calculations at the point where the RMS signal showed a sudden jump and was completed where the signal became constant again. As seen in Table 4, at turbulence level of 2.0% (GRID1), the predicted start of transition points by the AGS and DN models were further downstream than the observed points from the hot-film gage results. The predicted losses by both the methods were lower than the measured loss for all three inlet angles, with the predicted loss using the hot-film gage results closer to the measured loss.

Results for turbulence level of 4.8% (GRID2) indicated that the AGS and DN models predicted start of transition upstream of the observed points. This was in contrast to the GRID1 case. For

$\beta_1 = 38^\circ$, the AGS and DN models predicted start of transition in a region where an adverse pressure gradient was observed due to the under speeding (see pressure distribution in Figure 137). The measured loss for $\beta_1 = 38^\circ$ was higher than the predicted loss, while for $\beta_1 = 45^\circ$ and $\beta_1 = 52^\circ$, the predicted losses were slightly higher. Also, for $\beta_1 = 38^\circ$, predicted loss using the AGS and DN models was closer to the measured loss, while for $\beta_1 = 45^\circ$ and $\beta_1 = 52^\circ$, predicted losses using the hot-film gage results were closer to the measured losses.

Results for turbulence level of 6.4% (GRID3) indicated that, similar to the GRID2 case, the AGS and DN models predicted start of transition upstream of the observed points for all three inlet angles. The measured losses were higher than the predicted losses for inlet angles $\beta_1 = 38^\circ$ and $\beta_1 = 52^\circ$, while for $\beta_1 = 45^\circ$ the measured loss was in between the two predicted losses. Also, for $\beta_1 = 38^\circ$ and $\beta_1 = 52^\circ$, losses predicted by the AGS and DN models were closer to the measured losses, while for $\beta_1 = 45^\circ$ the differences between the measured and the two predicted losses were the same.

Summarizing the results in Table 4, it is seen that at the design inlet angle of $\beta_1 = 45^\circ$, the predicted losses agreed well with the measured losses when transition points from hot-film gages were used. However, the agreement was poorer for the $\beta_1 = 38^\circ$ and $\beta_1 = 52^\circ$ cases, with the measured losses showing a higher value than the predicted losses. For $\beta_1 = 38^\circ$, this poor agreement was probably due to the influence of the endwall flow, since endwall suction was less effective

at this inlet angle. For $\beta_1 = 52^\circ$, the higher measured losses were possibly due to a turbulent separation on the pressure surface following the laminar separation bubble. The turbulent separation was also predicted in the integral boundary layer analysis (see Chapter III). In general, considering that the uncertainty in the measurement of C_{PT2} was 0.007 (see the section on Experimental accuracy in Chapter V), it can be seen that the predicted and measured loss coefficients for all the test cases were in reasonably good agreement.

Another feature observed in the measured losses for $\beta_1 = 45^\circ$ and $\beta_1 = 52^\circ$ was that the loss for GRID2 was lower than the loss for GRID1 and GRID3. Such a trend of lower losses at an intermediate turbulence level has also been observed by Schlichting and Das [57] in their compressor cascade tests (also referred to in the earlier section on hot-film gage results for $\beta_1 = 45^\circ$). Their results showed a critical turbulence level at which the losses were lowest. However, in their tests a laminar bubble-induced transition occurred near 50% chord of the airfoil at sub-critical turbulence levels, and the transition point shifted abruptly to the leading edge at turbulence levels above the critical value. Such a phenomenon was not observed in the present test results. Hence it is difficult to ascertain whether the GRID2 case results indicated a critical turbulence level or simply measurement error.

For each inlet angle, the start of transition locations predicted by the Abu-Ghanaam and Shaw transition model were seen to move closer

to the stagnation point as the turbulence level increased. Also, for each turbulence level, the start of transition point predicted by the model moved closer to the stagnation point as the incidence angle was increased. These two effects represented the turbulence level and pressure gradient effects on the model. With an increase in turbulence level, the model predicted transition at a smaller momentum thickness Reynolds number (Reynolds number based on the local velocity and momentum thickness). Similarly, with an increase in incidence and hence a smaller favorable pressure gradient in the forward region of the suction surface, the model predicted transition at a smaller momentum thickness Reynolds number. However, the observed start of transition locations from the hot-film gage results indicated that pressure gradient rather than turbulence level was the dominant factor in starting transition for the test cascade. It can be seen in Table 4, for each inlet angle, transition started at nearly the same location for each of the natural transition cases (turbulence levels of GRID1, GRID2, and GRID3). For these cases, for inlet angles $\beta_1 = 38^\circ$ and $\beta_1 = 45^\circ$, the observed start of transition point was between 22% to 25%, and for $\beta_1 = 52^\circ$, the point was between 31% and 35%. When the locations of these points are compared against the pressure distributions (see Figures 137, 77, 109), it can be seen that they lie close to the minimum pressure point. Hence, it can be said that for the three inlet angles tested, the strong favorable pressure gradients present on the forward region of the suction surface delayed transition

until the minimum pressure point was reached. The Abu-Ghanaam and Shaw transition model, with more emphasis on turbulence level, predicted transition ahead of the observed transition locations for the high turbulence levels of GRID2 and GRID3.

The transition length predicted by the Dhawan and Narasimha model depends upon the start of transition location. Using this model and the start of transition locations as determined from the hot-film gage results, transition lengths were predicted (not included in Table 4). For $\beta_1 = 38^\circ$, for the observed start of transition at 23%, (for GRID1, GRID2, and GRID3), the Dhawan and Narasimha transition length model predicted the end of transition at 52%. Similarly, for $\beta_1 = 45^\circ$ with the observed transition start points, the model predicted the end of transition at 57% for GRID1 and 50% for GRID2 and GRID3; for $\beta_1 = 52^\circ$, the model predicted end of transition at 75% for GRID1 and 60% for GRID2 and GRID3. If these predicted results are compared against the observed transition lengths from hot-film gages in Table 4, it can be seen that Dhawan and Narasimha model predicted transition lengths with reasonable accuracy for the test cascade. For $\beta_1 = 38^\circ$, the predicted transition end point agreed well with the observed end point of 50% for GRID1. For GRID2 and GRID3, the observed transition lengths were smaller, with transition being completed at 40%. The smaller transition length observed is in line with the concept of shorter transition lengths at higher turbulence levels. For $\beta_1 = 45^\circ$ and GRID1 the predicted transition end point at 57% agreed well with the observed

end point of 52%; for $\beta_1 = 45^\circ$ and GRID2 and GRID3, the predicted end point at 50% agreed well with the observed end points of 52% and 46%. Finally for $\beta_1 = 52^\circ$, the predicted end points at 75% for GRID1 and 68% for GRID2 and GRID3 were further downstream than the observed end point at 59% for all three turbulence levels. Since it is difficult in general to specify the exact end point of transition, and also since the precision of the hot-film gages in the transition measurements was limited, it can be said that Dhawan and Narasimha transition model was adequate in predicting the transition lengths for the test cascade.

In spite of the differences between the predicted and observed transition locations, it should be noted that the predicted loss coefficients with the two methods do not differ much. In fact, for some cases, loss coefficients predicted with the AGS and DN models were closer to the measured loss coefficients. This indicated that to obtain an overall loss coefficient value, the transition models were reliable and sufficient. However, to obtain the actual shear stress or heat transfer distribution on the airfoil surface, the models were inadequate and need to be improved.

VII. CONCLUSIONS

A large-scale, low-speed cascade was designed as a highly-loaded, high-turning angle turbine cascade using a fast interactive design code. The cascade was tested at three axial chord Reynolds numbers, four inlet turbulence levels, and three incidence angles for a total of 36 different test conditions. Endwall suction was applied to obtain a 2-D flow over a large spanwise region of the airfoils.

Glue-on hot-film gages were mounted on the suction surface, and transition was identified by examining the mean and RMS voltage output of these gages. Surface oil-flow visualizations using a fluorescing paint pigment as a tracer were also employed to assist with interpreting the output from the hot-film gages. In addition, static pressure distributions on the airfoil and detailed five-hole pressure probe and hot-wire probe traverses were made in an exit plane of the cascade. Results from these measurements were used to determine the state of the profile boundary layer and the overall cascade performance, including mass-averaged losses.

The overall conclusions drawn from this experimental study were as follows:

1. Information on the state of the profile boundary layer could only be obtained when the combined results of all the hot-film gages distributed over the airfoil suction surface from the leading edge to the trailing edge were studied. Results from the individual hot-film gages by themselves were insufficient to indicate the state of the

boundary layer. Also, both the mean and RMS signal of hot-film gages had to be studied to obtain a complete picture of the boundary layer. Power spectra results of the hot-film gage outputs were not helpful in identifying the state of the boundary layer, especially at the higher turbulence levels tested.

2. Transition occurred in the suction surface boundary layer by three different forms, depending on turbulence level and Reynolds number. The first was a bubble-induced transition, the second a natural transition, and the third a combination of natural and bubble induced transition; i.e., a natural transition concluded abruptly by a separation bubble. At the lowest turbulence level tested (0.8%), a bubble-induced transition occurred at all three Reynolds numbers. Also, at the lowest Reynolds number tested (330,000), a bubble-induced transition occurred at all four turbulence levels. At the higher turbulence levels (2.0%, 4.8%, 6.4%) and for the highest Reynolds number tested (700,000), natural transition occurred, while for the intermediate Reynolds number (540,000), transition started naturally, but was completed by a separation bubble. In general, the start of transition point moved slightly downstream along the airfoil suction surface as the turbulence level and/or the Reynolds number was decreased. This same trend in the start of transition was also observed with a decrease in incidence angle for otherwise similar flow conditions.

3. For each inlet angle tested, regardless of turbulence level or Reynolds number, transition in the suction surface boundary layer was completed at approximately the same streamwise location by one of the three different forms discussed above. This indicated that, for this cascade, transition was strongly dependent on the pressure distribution on the suction surface. On the other hand, for all test conditions, a separation bubble was formed on the pressure surface of the airfoil close to the leading edge. As a result, the lengths of the turbulent part of the profile boundary layers on both the suction and pressure surfaces remained nearly constant; hence, the overall performance of the cascade in terms of the measured loss coefficient was essentially independent of turbulence level or Reynolds number.

4. The measured transition locations on the suction surface were compared with those predicted by the Abu-Ghanaam and Shaw model. The general trends observed in the experimental results were predicted by the model. Transition was predicted closer to the stagnation point as the turbulence level was increased and/or as the pressure gradient was made less favorable. At low turbulence levels, the model predicted the start of transition close to those points where laminar separation bubbles were observed. At higher turbulence levels, the model predicted transition to occur upstream of that found in the testing. The predicted transitions occurred in a region of strongly favorable pressure gradient, indicating that the transition model was more influenced by the free-stream turbulence level than was justified. On

the pressure surface, since separation bubbles were always formed, transition models could not be used.

5. Transition lengths predicted for the suction surface by the Dhawan and Narasimha model when the observed start of transition points were used agreed well with the experimentally observed results.

6. For inlet angle $\beta_1 = 45^\circ$, (-7° design incidence), the overall loss coefficients determined from the STAN5 boundary layer calculations agreed well with the measured loss coefficients. The agreement was especially good when the measured transition locations were used in the calculations. For inlet angles $\beta_1 = 38^\circ$ (0° incidence) and $\beta_1 = 52^\circ$ (-14° incidence), the agreement was slightly poorer, with the measured losses showing higher values than predicted.

7. The STAN5 boundary layer code predicted results that were in better agreement with the measured results than did the integral analysis method. The major shortcoming of the STAN5 code was its inability to handle separation and reattachment.

8. The Abu-Ghanaam and Shaw transition model was sufficiently accurate to obtain overall loss coefficient values for the cascade. However, to obtain the actual shear stress or heat transfer distribution on the airfoil surface, the model was inadequate. One possible explanation for this inadequacy was that, for the test cascade, the transition model was extrapolated; i.e., no experimental data in the range of pressure gradients present on the airfoil surface had been used in deriving the model. By improving the model to include

more experimental data for the high pressure gradient and high turbulence level flow conditions, the model could be made more reliable.

9. For the test cascade, a major portion of the profile losses occurred due to the suction surface boundary layer (over 75%). By delaying transition on the suction surface, the length of the turbulent boundary layer, and, hence, the profile losses on the suction surface can be reduced. This can be achieved by designing the cascade such that a favorable pressure gradient exists over a large portion of the suction surface. On the pressure surface, the overspeeding near the leading edge which leads to a separation bubble should be prevented to reduce the losses. This could be achieved by modifying the shape of the leading edge.

VIII. REFERENCES

1. Gostelow, J. P. Cascade Aerodynamics. New York: Pergamon Press, 1983.
2. Stuart, J. T. "Hydrodynamic Stability." In Laminar Boundary Layers, pp. 482-579. Edited by L. Rosenhead. Oxford (Eng.): Clarendon Press, 1963.
3. Schlichting, H. Boundary Layer Theory. New York: McGraw-Hill Book Company, Inc., 1979.
4. Tollmien, W. "Über die Entstehung der Turbulenz." English translation. NACA TM 609, 1931.
5. Jordinson, R. "The Flat Plate Boundary Layer. Part 1, Numerical Integration of the Orr-Sommerfeld Equation." Journal of Fluid Mechanics 43 (1970): 801-811.
6. Ombrewski, H. G.; Morkovin, M. V.; and Landahl, M. "A Portfolio of Stability Characteristics of Incompressible Boundary Layers." AGARDograph No. 134, 1969.
7. Squire, H. B. "On the Stability of 3-D Disturbances of Viscous Fluid Flow Between Parallel Walls." Proceedings of the Royal Society of London A 142 (1933): 621-628.
8. Schubauer, G. B.; and Skramstaad, H. K. "Laminar Boundary Layer Oscillations and Stability of Laminar Flow." National Bureau of Standards Research Paper 1772, 1943.
9. Klebanoff, P. S.; Tidstorm, K. D.; and Sargent, L. M. "The Three Dimensional Nature of the Boundary Layer Instability." Journal of Fluid Mechanics 12 (1962): 1-34.
10. Hinze, J. O. Turbulence. New York: Mc-Graw Hill Book Company, Inc., 1975.
11. Emmons, H. W. "The Laminar Turbulent Transition in a Boundary Layer Part I." Journal of the Aeronautical Sciences 18 (1951): 490-498.
12. Michener, M. "Propagation of Turbulence from an Instantaneous Point of Disturbance." Journal of the Aeronautical Sciences 21 (1954): 350-351.
13. Schubauer, G. B.; and Klebanoff, P. S. "Contributions on the Mechanics of Boundary Layer Transition." NACA TN 3489, 1955.

14. Criminale Jr., W. O.; and Kovaszany, L. S. G. "The Growth of a Localized Disturbance in a Laminar Boundary Layer." Journal of Fluid Mechanics 14 (1962): 59-67.
15. Vasudeva, B. R. "Boundary Layer Instability Experiment With Localized Disturbance." Journal of Fluid Mechanics 29 (1967): 745-763.
16. Dhawan, S.; and Narasimha, N. R. "Some Properties of Boundary Layer Flow during Transition from Laminar to Turbulent Motion." Journal of Fluid Mechanics 3 (1958): 418-436.
17. Reshotko, Eli. "Boundary Layer Stability and Transition." In Annual Review of Fluid Mechanics, Vol. 8, pp. 311-349. Edited by M. Van Dyke. Palo Alto, CA: Annual Reviews Inc., 1976.
18. Morkovin, M. V. "On the Many Faces of Transition." In Viscous Drag Reduction, pp. 1-31. Edited by C. S. Wells Jr. New York: Plenum Press, 1969.
19. Taylor, G. I. "Statistical Theory of Turbulence--Effect of Turbulence on Boundary Layer." Proceedings of the Royal Society of London A 156 (1936): 307-317.
20. Van Driest, E. R.; and Blumer, C. B. "Boundary Layer Transition Free Stream Turbulence and Pressure Gradient Effects." AIAA Journal 1 (1963): 1303-1306.
21. White, F. Viscous Fluid Flow. New York: McGraw-Hill Book Company, Inc., 1974.
22. Abu-Ghanaam, B. J.; and Shaw, R. "Natural Transition of Boundary Layers--The Effects of Turbulence, Pressure Gradient and Flow History." Journal of Mechanical Engineering Science 22 (1980): 213-228.
23. Mack, L. M. "Boundary Layer Stability Theory." JPL Preprint 900-277, 1969.
24. Kendall, J. M. "Supersonic Boundary Layer Transition Studies." JPL Space Programme Summary 37-62 3 (1970): 43-47.
25. Fage, A.; and Preston, J. H. "On Transition from Laminar to Turbulent Flow in the Boundary Layer." Proceedings of the Royal Society of London A 178 (1941): 210-227.
26. Alarcon, G. "Design of Turbine Cascades with Transitional Profile Boundary Layers." Ph.D. Dissertation, Iowa State University, Ames, Iowa, 1980.

27. Ye, Z. -Q.; and Kavanagh, P. "Axial Flow Turbine Cascade Design Procedure and Sample Design Cases." Iowa State University Engineering Research Institute Technical Report TCRL-28, ISU-ERI-Ames-84159, January 1984.
28. Walz, A. Boundary Layers of Flow and Temperature. Cambridge, MA: MIT Press, 1969.
29. Crimi, P.; and Reeves, B. L. "A Method for Analysing Dynamic Stall of Helicopter Rotor Blades." NASA CR 2009, 1972.
30. Dunham, J. "Predictions of Bondary Layer Transition on Turbomachinery Blades." AGARDograph No. 164, 1972.
31. Roberts, W. B. "Effect of Reynolds Number and Laminar Separation on Axial Cascade Performance." Journal of Engineering for Power 97 (1975): 261-273.
32. Föttner, L. "Analytical Approach for the Loss and Deflection Behaviour of Cascades in Transonic Flow Including Axial Mass Flow Variation." AGARDograph No. 164, 1972.
33. Stewart, W. "Analysis of 2-D Compressible Flow Loss Characteristics Downstream of Turbomachinery Blade Rows in Terms of Basic Boundary Layer Characteristics." NACA TN 3515, 1955.
34. Gaugler, R. E. "Some Modifications to and Operational Experience with the 2-D, Finite-Difference, Boundary Layer Code STAN5." ASME Paper No. 81-GT-89, 1981.
35. Vijayaraghavan, S. B.; and Kroneman, M. "Automatic Profile Machining of Airfoils." Turbomachinery Laboratory, Department of Mechanical Engineering, Iowa State University, Ames, Iowa, 1985.
36. Blair, M. F.; and Werle, M. J. "The Influence of Free-Stream Turbulence on the Zero Pressure Gradient Fully Turbulent Boundary Layer." UTRC/R80-914338-12, 1980.
37. Mehta, R. D.; and Bradshaw, P. "Design Rules for Small Low Speed Wind Tunnels." Aeronautical Journal 83 (1979): 443-469.
38. Hottman, D. A. "Turbomachinery Laboratory Data Acquisition and Experiment Control System." Iowa State University Engineering Research Institute Tecnical Report TCRL-19, ISU-ERI-Ames-81113, November 1980.

39. Oberoi, M. S. "Effect of Wind Tunnel Contraction on the Free Stream Turbulence." Journal of Aeronautical Sciences 23 (1956): 754-764.
40. Vijayaraghavan, S. B.; and Kavanagh, P. "Data Acquisition and Reduction for the Large-Scale Low-Speed Cascade Test Facility." Turbomachinery Laboratory, Department of Mechanical Engineering, Iowa State University, Ames, Iowa, 1986.
41. Morgan, B. D. "A Water Column Balance Pressure Reference System." Turbomachinery Laboratory, Department of Mechanical Engineering, Iowa State University, Ames, Iowa, 1979.
42. Smith, P. G. "Calibration of Five-Hole Pressure Probes." Iowa State University Engineering Research Institute Technical Report TCRL-20, ISU-ERI-Ames-82188, November 1980.
43. Schimming, P.; and Starcken, H. "Data Reduction of Two-Dimensional Cascade Measurements." AGARDograph No. 207, 1975.
44. TSI Inc. Instruction Manual for the 1052 Linearizer. St. Paul, MN: TSI Inc., 1982.
45. Shyh, C. K. "Experimental Investigation of Endwall Crossflow in a Curved Rectangular Cross Section Duct." Master of Science Thesis, Iowa State University, Ames, Iowa, 1983.
46. Bellhouse, B. J.; and Shultz, D. L. "Determination of Mean and Dynamic Skin Friction, Separation and Transition in a Low-Speed Flow with a Thin-Film Heated Element." Journal of Fluid Mechanics 24 (1966): 379-400.
47. Hodson, H. D. "Boundary Layer Transition and Separation near the Leading Edge of a High-Speed Turbine Blade." ASME Paper No. 84-GT-179, 1984.
48. Wentz, W. H.; Ahmed, A.; and Nyenhuis, R. "Further Results of Natural Laminar Flow Flight Test Experiments." SAE Technical Paper Series, 850862, 1985.
49. Maltby, R. L. "Flow Visualization in Wind Tunnels Using Indicators." AGARDograph No. 70, 1962.
50. Kline, S. J.; and McClintock, F. A. "Describing Uncertainties in Single-Sample Experiments." Mechanical Engineering 75 (1953): 3-8.

51. Langston, L. S.; Nice, M. L.; and Cooper, R. M. "Three-Dimensional Flow within a Turbine Cascade Passage." Journal of Engineering for Power 99 (1977): 21-28.
52. Sieverding, C. H. "Recent Progress in the Understanding of the Basic Aspects of Secondary Flows in Turbine Blade Passages." Journal of Engineering for Power 107 (April 1985): 248-257.
53. Gregory-Smith, D. G.; and Graves, C. P. "Secondary Flows and Losses in a Turbine Cascade." Viscous Effects in Turbomachines. AGARD CP 351, 1983.
54. Denton, J. D. "A Survey of Comparison of Methods for Predicting the Profile Loss of Turbine Blades." In Heat and Fluid Flow in Steam and Gas Turbine Plant, pp. 204-212. Edited by J. C. Mundy. London: Institution of Mechanical Engineers, 1973.
55. Batchelor, G. K. Theory of Homogeneous Turbulence. Cambridge, MA: Cambridge University Press, 1953.
56. Pucher, P.; and Göhl, R. "Experimental Investigation of Boundary Layer Separation With Thin-Film Sensors." ASME Paper No. 86-GT-254, 1986.
57. Schlichting, H.; and Das, A. "On the Influence of turbulence level on the Aerodynamic Losses of Axial Turbomachines." In Flow Research on Blading, pp. 243-274. Edited by L. S. Dzung. Amsterdam, Netherlands: Elsevier Publishing Co., 1970.
58. Kline, S. J. "Turbulent Boundary Layer Prediction and Structure - The State of the Art." In Flow Research on Blading, pp. 372-396. Edited by L. S. Dzung. Amsterdam, Netherlands: Elsevier Publishing Co., 1970.
59. Klebanoff, P. S. "Characteristics of Turbulence in a Boundary Layer With Zero Pressure Gradient." NACA TR 124, 1955.
60. Graziani, R. A.; Blair, M. F.; Taylor, J. R.; and Mayle, R. E. "An Experimental Study of Endwall and Airfoil Surface Heat Transfer in a Large Scale Turbine Blade Cascade." Journal of Engineering for Power 102 (1980): 257-267.
61. Turner, A. B. "Local Heat Transfer Measurements on a Gas Turbine Blade." Journal of Mechanical Engineering Science 13 (1971): 21-46.

62. Hylton, L. D.; Mihelc, M. S.; Turner, E. R.; Nealy, D. A.; and York, R. E. "Analytical and Experimental Evaluation of the Heat Transfer Distribution Over the Surface of Turbine Vanes." NASA-CR-168015, 1983.

IX. ACKNOWLEDGMENTS

The author wishes to express his sincere thanks to Dr. P. Kavanagh for consenting to serve as his major professor and for his guidance during the course of this study. The author also wishes to thank the members of his dissertation committee, Dr. G. K. Serovy, Dr. R. H. Fletcher, Dr. J. C. Tannehill, and Dr. E. H. Johnston for their assistance. In addition, the author wishes to thank Dr. T. H. Okiishi.

The author is grateful to the sponsors of this study, Allison Gas turbines and would like to thank in particular Dr. R. A. Delaney and Dr. H. C. Mongia.

The author wishes to thank M. Kroneman, and technicians, R. D. Steed, G. N. Scandrett, and J. J. Dautremont who helped him complete his experimental work.

The author would like to dedicate this thesis to his parents Sidhappa and Neelaveni Balakrishnan and express his special thanks to his father for providing the motivation for this work. Finally, the author would like to thank his wife Saradha for her support and understanding.

X. APPENDIX A: COMPARISON OF STAN5 AND DISSIPATION INTEGRAL
ANALYSIS METHODS

To compare the dissipation integral analysis and the STAN5 analysis methods, the development of a boundary layer on a flat plate was studied using both methods for three different cases: a zero pressure gradient, a favorable pressure gradient, and an adverse pressure gradient. For all three cases, the boundary layer calculation was started at a distance of 0.05 ft from the leading edge; a free-stream velocity of 100 ft/sec and an inlet turbulence level of 1.5% were assumed. For the favorable and adverse pressure gradient cases, Falkner-Skan similarity flows of the type $U = Cx^m$ were assumed since the laminar velocity profile for these flows are available in tables (see White [21]) and can be directly substituted for the starting velocity profile required by the STAN5 program. For the starting conditions described, and for a Falkner-Skan parameter $\beta = 0.3$ ($\beta = (2m)/(m+1)$) describing the velocity profile, the streamwise velocity distribution for the favorable pressure gradient case reduces to $U = 169.64x^{0.1764}$. Likewise, with $\beta = -0.18$, the adverse pressure gradient case reduces to, $U = 78.09x^{-0.08257}$. As was stated above, the STAN5 analysis was started by direct substitution of the starting velocity profile. For the integral analysis, the calculations were started by entering a trial value of the shape factor at the starting location.

To handle transition, the Abu-Ghanaan and Shaw transition model combined with the Dhawan and Narasimha transition length model were used with the STAN5 analysis. For the dissipation integral analysis, the Abu-Ghanaam and Shaw transition and transition length model were used. Once transition was predicted and the transition length calculated, the STAN5 analysis marched through the transitional region using the intermittency factor of Abu-Ghanaam and Shaw to include the turbulent viscosity in the transitional calculations. On the other hand, the integral analysis stopped the calculations once transition was predicted and resumed the calculations at the fully turbulent point using empirical relations to relate the flow parameters at the start and end of transition. Hence, for the integral analysis, no flow parameters were calculated in the transitional region.

Results for the zero pressure gradient case are shown in Figure 150. In the laminar flow region, the two methods predict the same values of momentum thickness, skin friction coefficient, and shape factor. In the turbulent flow region, the rate of growth of momentum thickness is higher in the STAN5 method. To compare the predicted skin friction coefficients for turbulent flow, C_f as determined from an empirical correlation due to Schlichting [3] is also plotted. As seen in Figure 150, the C_f values predicted by the integral analysis are closer to the correlated values than are those predicted by the STAN5 method. Shape factor values predicted by the integral analysis are slightly lower than those predicted by the STAN5 method.

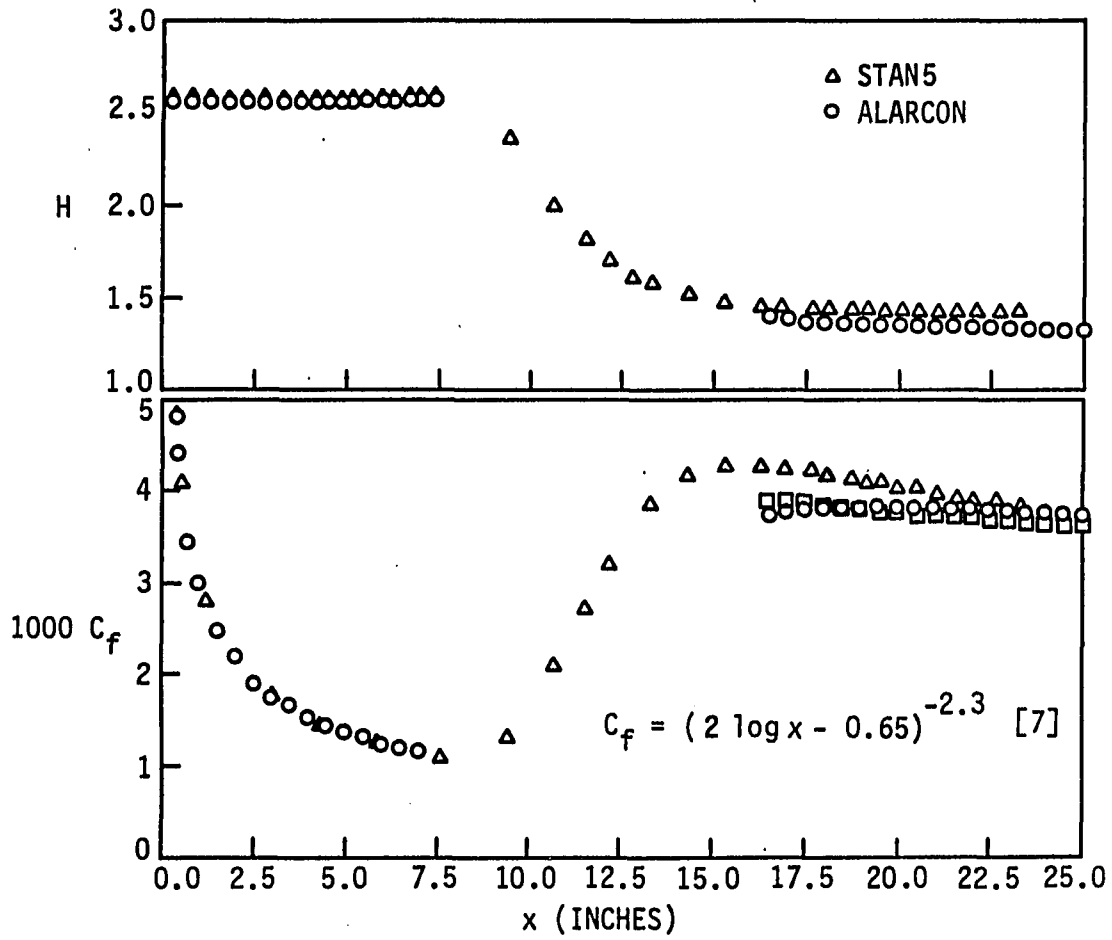


FIGURE 150. Comparison of STAN5 and dissipation integral analysis-- zero pressure gradient

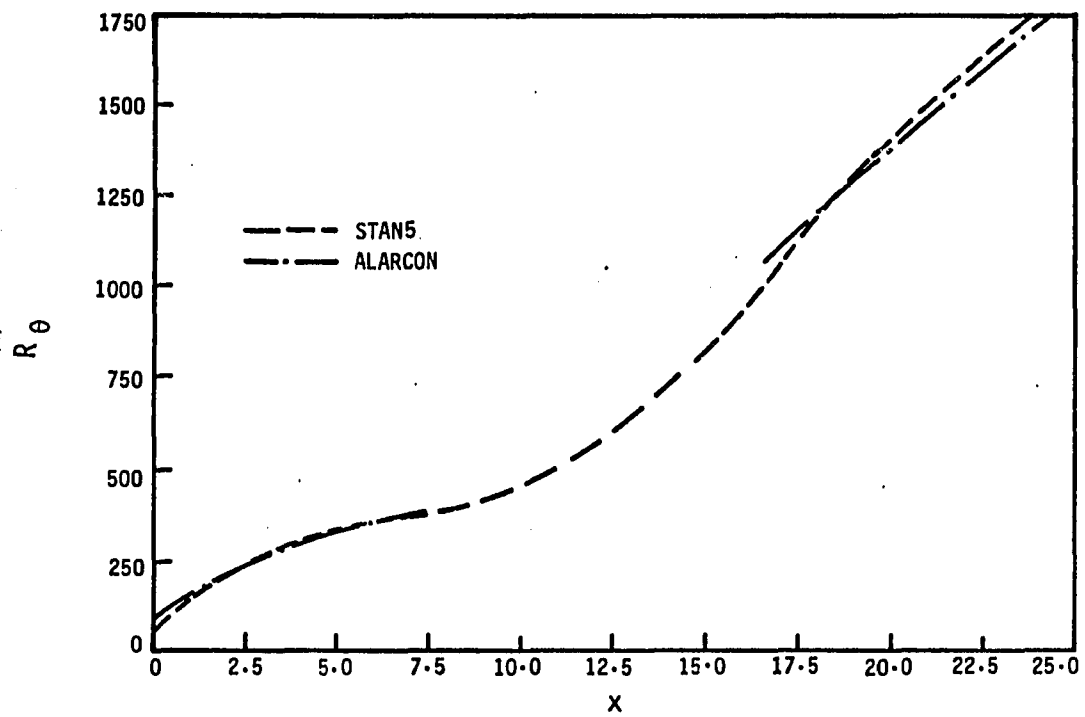


FIGURE 150 (continued)

Figure 151 shows the results for the favorable pressure gradient case. The trend in growth rate of momentum thickness is similar to that of the zero pressure gradient case with the STAN5 method predicting a higher growth rate of momentum thickness. Skin friction values fall off more rapidly for the STAN5 method as compared to the integral analysis method. Shape factor values show a similar trend to the zero pressure gradient case with the integral analysis method predicting slightly lower values.

Figure 152 shows the results for the adverse pressure gradient case. The agreement between the two methods is the poorest for this case. Momentum thickness predicted by the integral analysis is about 25% less than that predicted by STAN5 method for the turbulent region. Skin friction values in the laminar flow region are over 50% higher for the integral analysis compared to the STAN5 method, while for the turbulent region, the difference is considerably smaller. Shape factor values for the laminar region are higher for the STAN5 method. For the turbulent region, the shape factor shows a trend similar to that for the zero and favorable pressure gradient cases, with the integral analysis predicting slightly lower values.

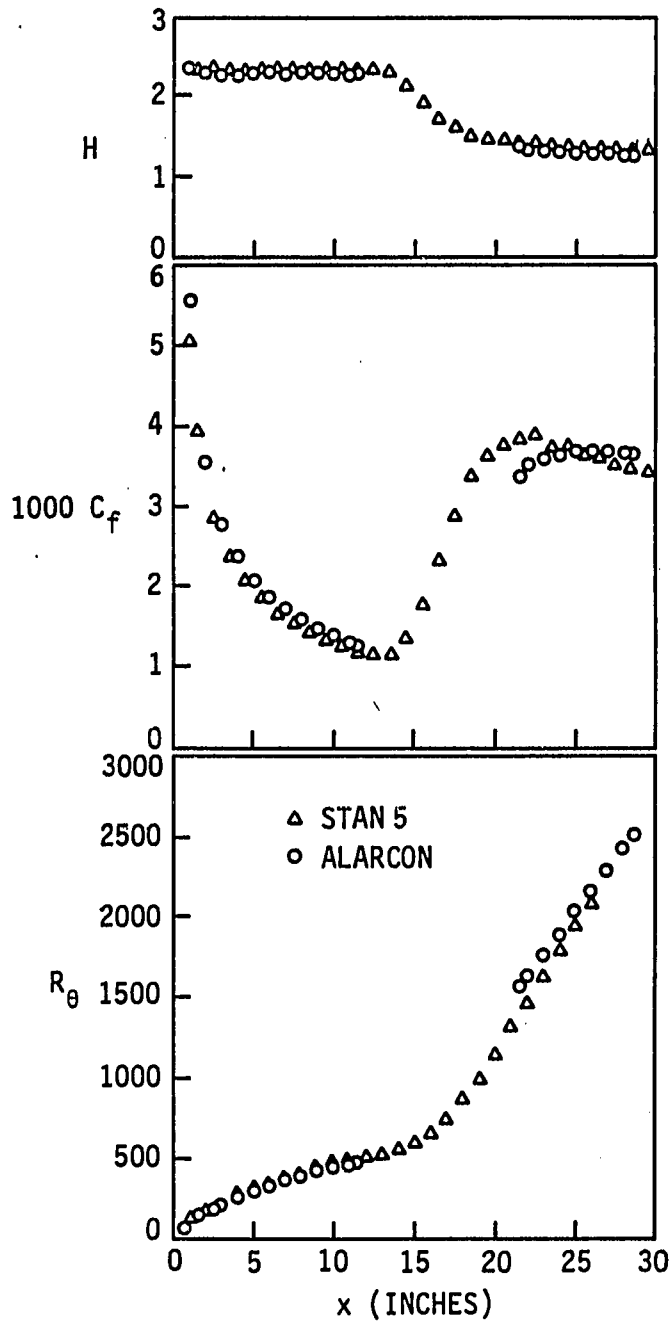


FIGURE 151. Comparison of STAN5 and dissipation integral analysis-- favorable pressure gradient

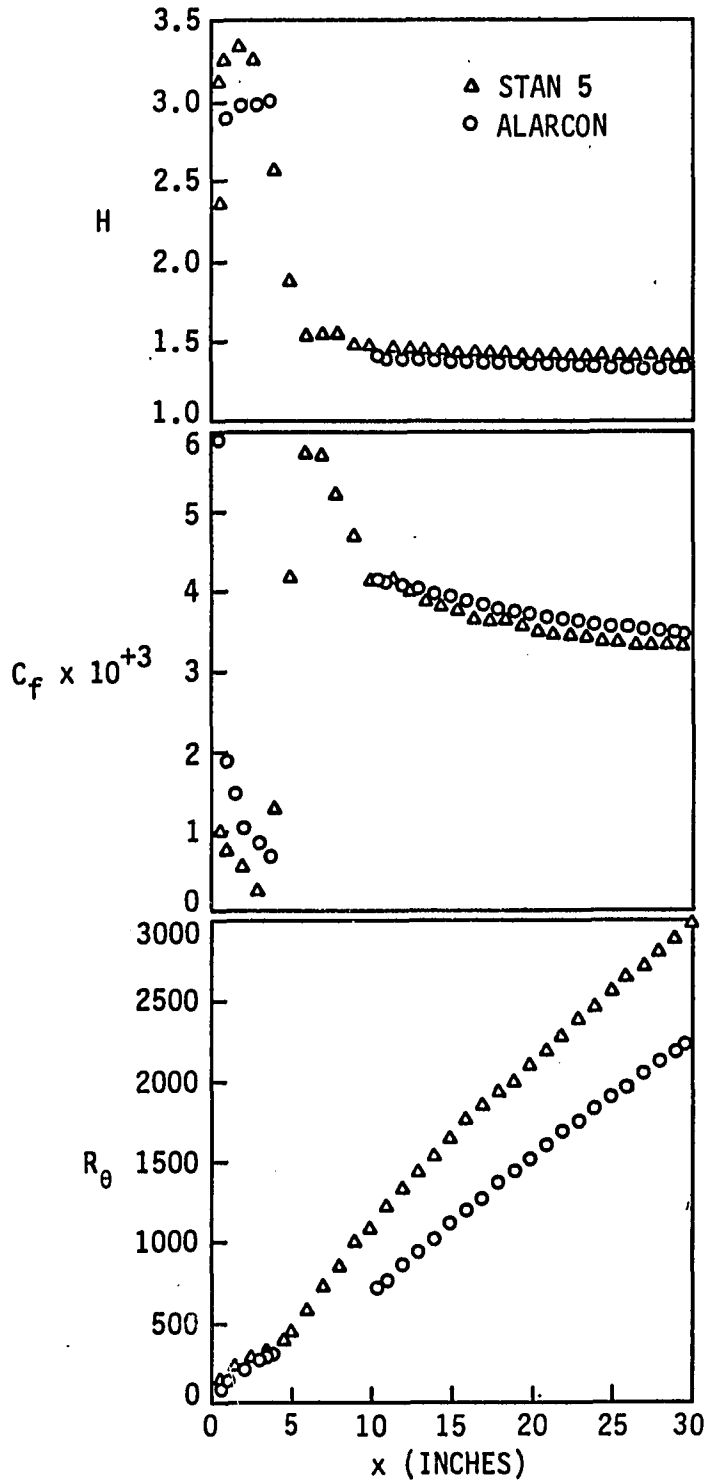


FIGURE 152. Comparison of STAN5 and dissipation integral analysis--adverse pressure gradient

XI. APPENDIX B: PRINCIPLE OF HOT-FILM GAGES FOR USE IN WALL SHEAR
STRESS MEASUREMENTS

The heat transfer rate from a hot-film gage to the fluid flowing over it is dependent upon the properties of the fluid, the local skin friction, and the gage dimensions. For a hot-film gage to be successfully used in wall shear stress measurements, the following conditions have to be met:

- The gage should be sufficiently thin in order to not disturb the velocity boundary layer.
- The thermal boundary layer developing over the gage should be much thinner than the velocity boundary layer to obtain a simple relationship between the wall shear stress and the heat transfer of the heated film. For turbulent flows, the thermal boundary layer should be thinner than the laminar sub-layer of the turbulent flow.
- The effective length of the film gage in the flow direction (length of the heating element) should be greater than the thickness of the thermal boundary layer for boundary layer treatment to be valid.

Under these conditions, the relationship between the wall shear stress and the heat transfer rate of the heated film reduces to (see Bellhouse and Shultz [46]):

$$\tau_w^{1/3} \propto (Q/\Delta T)$$

where, τ_w is the wall shear stress, Q is the heat transfer rate, and ΔT is the temperature difference of the gage and the free stream.

For a given film, the above result can be rewritten as:

$$(I^2R)/\Delta T = a(\tau_w)^{1/3+b}$$

in which I is the sensor current and R is the sensor operating resistance. The constants a and b indicated are functions of the fluid properties and the heat loss to the substrate, respectively. Tests by Bellhouse and Shultz [46] on hot-film gages have shown the above equation to be valid for a laminar boundary layer, thereby justifying the assumptions involved. However, the calibration constants a and b had to be modified for a turbulent boundary layer, indicating that a single calibration was not valid for both laminar and turbulent boundary layers.

From the cascade test results, a comparison of the shear stress distribution along the airfoil suction surface was made between the hot-film gage outputs and the shear stress predicted by the STAN5 code for two flow condition cases: 0.8% turbulence level (NGRID) and Reynolds number 700,000 (RE1) involving a laminar separation bubble, and 4.8% turbulence level (GRID2) and Reynolds number 700,000 (RE1) involving natural transition. The STAN5 code was started in the laminar mode and switched to turbulent mode at the transition points observed from hot-film gage results (see Chapter VI for details). Results of the comparisons are shown in Figures 153 and 154. Shown are the non-dimensional DC output of the gages $(E-E_0)/E_0$, which is

proportional to the square-root of the heat transfer Q ($Q = E^2/R$), compared against $(C_f U^2)^{1/6}$, where U is the velocity at the hot-film gage location and C_f is the skin friction coefficient predicted by the STAN5 code ($C_f = 2\tau_w / \rho U^2$).

Figure 153 shows the result for the NGRID and RE1 case, in which it is seen that the laminar shear stress distribution up to gage #5 and the turbulent shear stress distribution for gages #8 through #14 follow the same pattern for both the predicted and measured values (the gage # is determined by counting from the leading edge of the airfoil). Between gages #5 and #8, the hot-film signal shows a decrease, while the predicted shear stress distribution shows an increase. However, if the results from fully laminar calculations (indicated by the dark symbols) are considered instead of the transitional calculations in the region between gages #5 and #8, the predicted shear stress distribution agrees with the measured distribution. This indicates that the flow is laminar up to the separation point (near gage #7). Figure 154 shows the result for the GRID2 and RE1 case. Here the agreement between the predicted and measured shear stress distribution is good in both the laminar region (up to gage #4) and the turbulent region (beyond gage #8).

In both Figures 153 and 154, there is considerable scatter in the measured values, especially in the turbulent boundary layer region. However, the same general trend in shear stress distribution is observed both in the measured and predicted values, confirming the

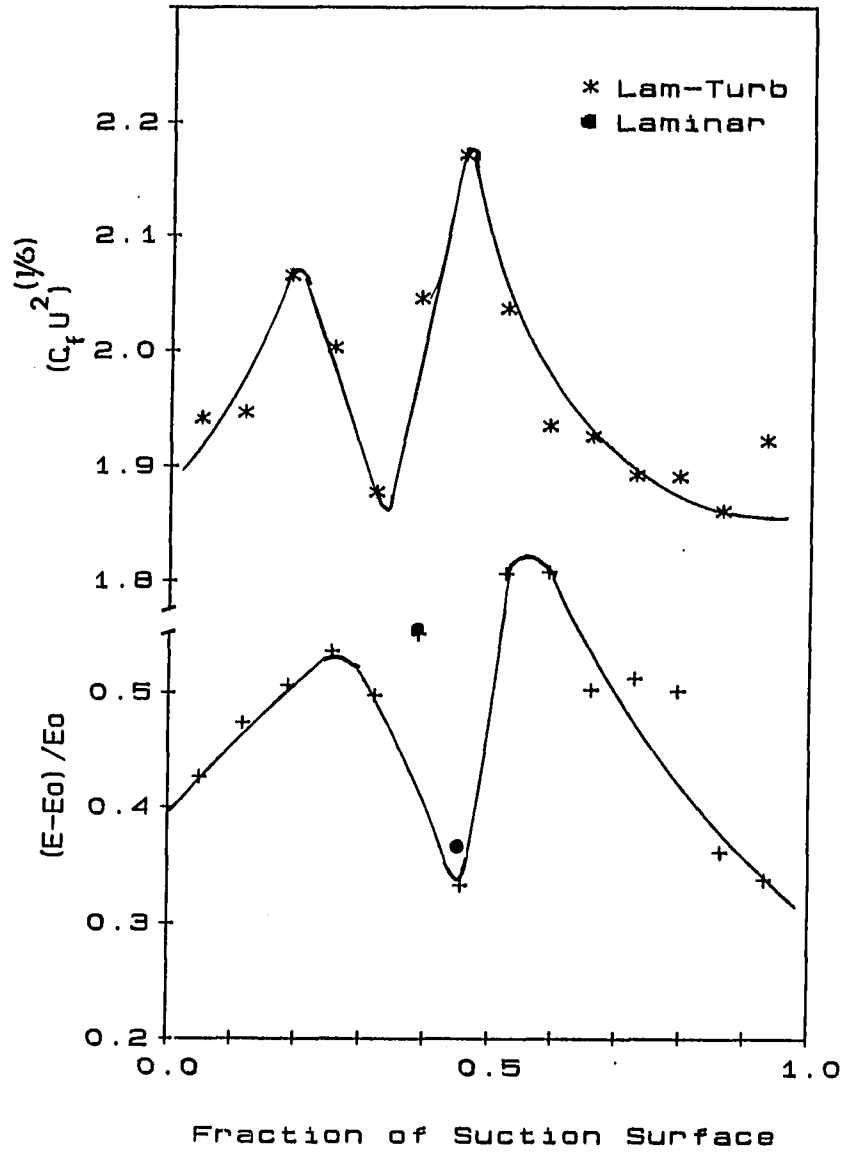


FIGURE 153. Comparison of hot-film signal and predicted shear-stress distribution for $\beta_1 = 45^\circ$, RE1, NGRID

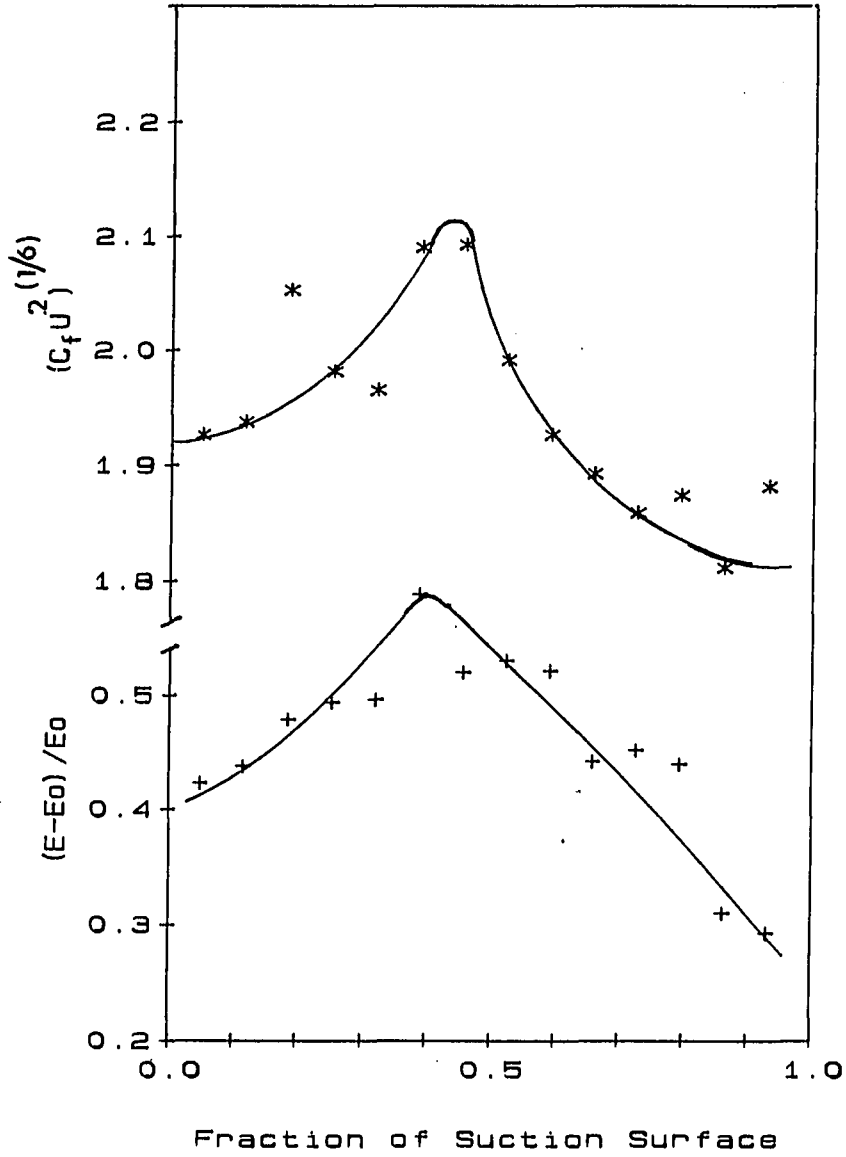


FIGURE 154. Comparison of hot-film signal and predicted shear-stress distribution for $\beta_1 = 45^\circ$, RE1, GRID2

assumptions involved in using the relation $I^2R \propto \tau_w$ for the hot-film gage.

Results from heat transfer measurements on heated airfoils by Graziani et al. [60], Turner [61], Hylton et al. [62] show a decrease in heat transfer coefficient from the leading edge onwards unlike the present results which show an initial increase up to 40% along the suction surface. This anomaly can be explained by recollecting that the thermal boundary layer for a hot-film gage begins only at the gage, and that its thickness over the gage is considered to be less than that of the viscous sublayer. Whereas, for a heated airfoil, the thermal boundary layer develops from the stagnation point on, and its thickness is of the same order as the velocity boundary layer.